Synthesis and 3D Printing of Hydroxyapatite Scaffolds for Applications in Bone Tissue Engineering

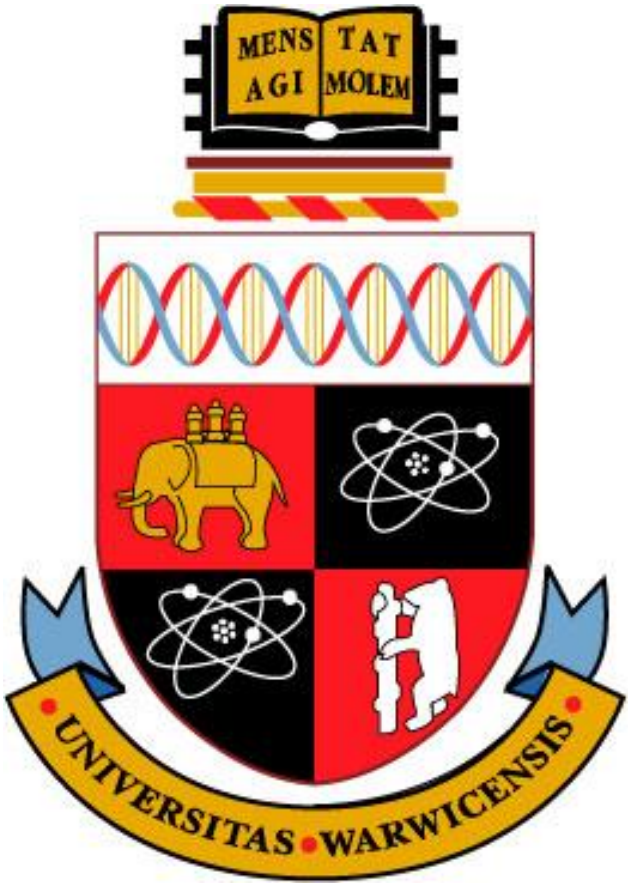

Sophie Constance Cox
WMG
University of Warwick

A thesis submitted for the degree of
Doctor of Philosophy
September 2013

This thesis is dedicated to my grandfathers,
Ernst Cox and John Port

Table of Contents

List of Figures

List of Tables

Acknowledgements

I would like to thank my supervisor Dr Kajal Mallick for his support throughout this project and his confidence in my ability. I also must acknowledge and extend my gratitude to Professors Richard Walton and Liam Grover, Dr Greg Gibbons, Dr Stuart Coles and Dr Ben Douglas for the facilities they so kindly provided as well as their invaluable comments and feedback that helped to direct this work. Further thanks to Tom Skelhon and Adam Morgan for assistance with particle size, zeta potential and surface area measurements. Richard Williams is also recognised for his help with the cellular internalisation experiments. The University of Warwick Chancellor's Scholarship is acknowledged for funding this project.

Special recognitions must be made to Martin Davis and Parastoo Jamashidi. Martin has on so many occasions been the person I went to when I did not know where else to go and has always gone that extra mile to help me, which I am truly grateful for. Paras and I went on a journey to complete and understand the reported cell work. Throughout she offered me unrivalled professional support and a compassionate ear, thank you Paras.

I would also like to extend my appreciation to Dr James Meredith who has offered me support throughout this project, invaluable careers advice and helped me organise an internship with Ceram. Thanks to Dr Phil Jackson and Ben McCarthy at Ceram for formulating such a challenging and enriching placement that has been an instrumental part of my career to date.

Personally, I would like to thank all of my colleagues in room 359, close friends, and Warwick Judo who have supported me throughout this time, offered me 'proactive' procrastination and kept a smile on my face.

Mum, Dad, Sam and Sami, thank you for giving me the belief, guidance and love that I have needed. And of course, Thomas, you're the best and Squidger would not be where she is today without you.

Declaration

This thesis is the original work of the author and is submitted to fulfil the requirements of the degree of Doctor of Philosophy (PhD). The research was performed at WMG of the University of Warwick and the School of Chemical Engineering of the University of Birmingham between October 2010 and September 2013, under the supervision of Dr Kajal Mallick. This thesis has not been submitted in whole or in part as consideration for any other degree qualification at this or any other university. Where other work has been used it has been acknowledged. In accordance with the Degree Committee of the Faculty of Sciences, the length of this thesis is less than 70,000 words.

Sophie Constance Cox
WMG
University of Warwick
September 2013

Publications

Journal articles:

- Cox, S. C., Jamshidi, P., Grover, L. M., and Mallick, K. K., "Preparation and characterisation of nanophase Sr, Mg, and Zn substituted hydroxyapatite by aqueous precipitation", *J Maters Sci and Eng Part C*, 2013
- Cox, S. C., Jamshidi, P., Grover, L. M., and Mallick, K. K., "Low temperature aqueous precipitation of needle-like nanophase hydroxyapatite", *J of Maters Sci: Maters in Med*, 2013

Conference proceedings:

- Cox, S. C. and Mallick, K. K., "Preparation of nanophase hydroxyapatite via self-propagating high temperature synthesis", *Ceramic Transaction Book Series*, Ed: Roger Narayan, Wiley-VCH, 2012
- Cox, S. C. and Mallick, K. K.: "Preparation of porous hydroxyapatite scaffolds using yeast as a pore forming agent", *Ceramic Transaction Book Series*, Ed: Roger Narayan, Wiley-VCH, 2011

Book chapters (peer reviewed):

- Mallick, K. K. and Cox, S. C., "Biomaterial Scaffolds for Tissue Engineering", *Frontiers of Bioscience, Special Edition: Next Generation Biomaterials*, Encyclopaedia of Bioscience, Ed: Roger Narayan, 2011

Oral presentations (peer reviewed):

- MiMe International Conference, Oct 2013, Italy
- Materials and Manufacturing Annual Conference, WMG, May 2013, UK
- Annual Conference, UK Society of Biomaterials, June 2012, UK
- MS&T 2011 Conference, American Ceramic Society, October 2011, USA
- MS&T 2010 Conference, American Ceramic Society, October 2010, USA

Poster presentations (peer reviewed):

- MC11, Royal Society of Chemistry, July 2013, UK
- Annual Conference UK Society of Biomaterials, June 2013, UK
- World Biomaterials Congress, June 2012, China
- Materials and Manufacturing Annual Conference, WMG, April 2012, UK
- Annual Conference, UK Society of Biomaterials, 2011, UK

White paper:

- Cox, S. C., "Synthesis methods of hydroxyapatite", Available online at www.ceram.com

Abstract

It is known that chemical and physical features of bone contribute to its functionality, reactivity and mechanical performance. This knowledge is the fundamental rationale for this project. The aim of this thesis is to study the influence of synthesis conditions on material composition and ultimately the biological performance of hydroxyapatite (HA) as well as to fabricate scaffold structures that physically emulate bone tissue. Concurrent characterisation of physiochemical properties and evaluations of in-vitro cytocompatibility, and the degree of osteoblast proliferation on CDHA substrates precipitated under different reaction conditions provides a novel contribution.

Non-viability of cells seeded on substrates prepared in a solution adjusted to pH 10 (AP07) was confirmed after 1 day of culture. Dead cells were also observed after 3 days on CDHA prepared at 70°C under a controlled pH level of 11 (AP12). XRD found no discernible difference between these samples and CDHA substrates shown to be cytocompatible. The source of cytotoxicity was concluded to be the presence acidic DCPD in AP07, and positive surface charges for AP07 and AP12 that were revealed by FTIR, DTA-TGA and ZP measurements. Control of pH, increased solute concentration, the use of Toluene, and substitutions of 10mol% Mg or 2mol% Zn were shown to enhance the proliferative rate of cells seeded on CDHA synthesised at RT.

CDHA prepared in a 60 Toluene: 40 DI water (% v/v) solvent system with a lower dielectric constant (AP14) exhibited marked XRD peak broadening and 20% larger surface area compared with CDHA prepared in DI water (AP09). These features are suggested to explain the enhanced proliferation of cells on AP14, which was shown to be more than double the fluorescence exhibited for AP09 after 7 days. XRF was used to confirm the presence of Sr, Mg, and Zn that were selected due to their key biological roles in bone apatite. Evidence of lattice incorporation of these divalent cations was supported by XRD analysis that demonstrated shifts of characteristic HA peaks. Mg ions inhibited the crystallisation process, which caused a 45% reduction in the crystallite size, 60% increase in particle surface area and thermal conversion to whitlockite at 600°C. The relatively low crystallinity and larger surface area of Mg and Zn doped substrates is proposed to explain the respective 80 and 40% increase in cell proliferation compared to a pure sample prepared under the same conditions.

Flowability of HA:PVOH precursor materials correlated well with the mechanical stability, microstructure and porosity of 3D printed scaffolds. Anisotropic behaviour of constructs and part failure at the boundaries of interlayer bonds was highlighted by compressive strength testing. A trade-off between the ability to facilitate removal of PVOH thermal degradation products during sintering and the compressive strength of green parts was revealed. The maximum green scaffold strength of 0.85MPa was exhibited by parts that were air or vacuum dried for 6hrs. Critically, the pores of 3D printed constructs could be user designed ensuring interconnectivity and the imperfect packing efficiency of precursor powders created an inherent surface roughness and microporosity within scaffold struts. These features are known to be favourable for osteogenesis, osteoconduction and osteointegration in-vivo.

This work establishes that changes to precipitation conditions cannot be deemed trivial since they may alter material composition, which ultimately determines cytocompatibility as well as the proliferative rate of cells. Due to the highly complex structure of bone there are understandably a number of on-going medical challenges and while the application of 3D printed HA bone tissue scaffolds is promising, the name apatite derived from the Greek ‘απαταο’, meaning to deceive is concluded to be very fitting.

List of abbreviations

3DP	3D printing
ALM	Additive layer manufacturing
ALP	Alkaline phosphatase
ANOVA	Analysis of variance
AP	Aqueous precipitation
BET	Brunauer–Emmett–Teller
BG	Bone graft
CAD	Computer aided design
CAM	Computer aided manufacture
CaP	Calcium phosphate
CDHA	Calcium deficient hydroxyapatite
CHA	Carbonated hydroxyapatite
CSPCS	Citric acid self-propagating combustion synthesis
CT	Computer tomography
DAY	Dried active yeast
DCPA	Dicalcium phosphate anhydrate (monetite)
DCPD	Dicalcium phosphate dihydrate (brushite)
DI	Deionised
DMEM	Dulbecco's modified eagle medium
DTA	Differential thermal analysis
DTG	Differentiated thermogravimetry
EDS	Energy dispersive spectroscopy
FDA	Food and drug association
FDM	Fused deposition modelling
FTIR	Fourier transform infrared spectroscopy
HA	Hydroxyapatite
hrs	Hours
IR	Infrared
JCPDS	Joint committee on powder diffraction standards
M	Mega ($=10^6$)
MCPM	Monocalcium phosphate monohydrate

mins	Minutes
MRI	Magnetic resonance imaging
MTT	3-(4,5-Dimethylthiazol-2-yl)-2,5-diphenyltetrazolium bromide
n	Nano ($=10^{-9}$)
NMR	Nuclear magnetic resonance
OA	Osteoarthritis
OP	Osteoporosis
PBS	Phosphate buffered saline
PVOH	Polyvinyl alcohol
Rpm	Revolutions per minute
RT	Room temperature
s	Seconds
SBF	Simulated body fluid
SEM	Scanning electron microscopy
SLA	Stereolithography
SLS	Selective laser sintering
SPCS	Self-propagating combustion synthesis
SS	Solvothermal synthesis
TCP	Tricalcium phosphate
TEM	Transmission electron microscopy
TGA	Thermogravimetry analysis
TP	Tissue culture plastic
TTCP	Tetracalcium phosphate
USPCS	Urea self-propagating combustion synthesis
UV	Ultraviolet
XPS	X-ray photoelectron spectroscopy
XRD	X-ray diffraction
XRF	X-ray fluorescence
YP	Yeast as a pore forming agent
ZP	Zeta potential

Chapter 1

Introduction

1. Introduction

There is an increasing clinical demand to repair and/or regenerate bone defects since millions of people worldwide are diagnosed with numerous diseases, genetic abnormalities or endure traumatic injuries that compromise or fall outside of the self-healing capacity of this hard tissue. Traditionally bone grafts (BGs), most commonly autografts, have been used to fill or heal such defects. Despite being the 'gold standard' there are several disadvantages of autologous BGs, including painful harvesting surgery, limited supply, and long recovery times. These short-comings have driven the research community to investigate alternative solutions that incorporate the use of synthetic biomaterials.

Specifically, an alternative strategy to traditional BGs is to create a temporary surrogate structure, which guides and encourages tissue regeneration. In order for such a strategy to be successful it is necessary to combine expertise of cells, biochemical factors, and biomaterial science. This interdisciplinary field of research is known as tissue engineering and the structural component of this strategy, referred to as a 'scaffold' is the focus of this project.

Ideally, scaffolds should emulate the chemical and physical structure of the native tissue, thus it is crucial that an understanding of the properties that infer the functionality of bone is developed. Bone is an inorganic-organic biocomposite that largely comprises of nanosized non-stoichiometric carbonated multi-ion substituted apatite particles incorporated in a collagen matrix. These phases deduce the compressive strength and stiffness, as well as the elasticity and fracture toughness of bone, respectively. It is important to note that the porous interconnected 3D structure exhibited by cancellous bone enables mass transfer of nutrients, vascularisation, and migration of bone cells.

Much attention has been given to calcium phosphate (CaP) based biomaterials since generally they are chemically similar to bone apatite. In particular, hydroxyapatite (HA) has been shown to exhibit a comparable crystal structure and is an FDA approved CaP [1-4]. However, this material is known to exhibit poor bioresorbability and bioactivity compared to natural bone mineral due to the high stability of synthetic HA under physiological conditions [5-7]. Substitution of trace elements that naturally

occur in bone and the use of nanosized HA (nHA) have been shown to enhance the solubility, bioactivity and response of bone cells to this synthetic material in-vitro and in-vivo [8-11]. Much effort has been focused on the synthesis of this bioceramic due to the potential applications of HA as a bone replacement material [12-17]. However, the majority of such studies are restricted to the preparation and structural investigation of HA without an evaluation of biological performance [18].

Numerous authors have reported the fabrication of pure or composite HA scaffold structures using a variety of techniques [19-23]. In recent decades focus has been directed to the use of additive layer manufacturing (ALM) systems to manufacture such constructs since they can be user defined, which inherently improves reproducibility and enables the creation of patient-specific products. It is relatively common that commercially purchased HA is used as a precursor material and as such the motivation of such studies is narrowed to the influence of physical attributes. That is despite the fact that the reactivity of bone mineral is largely determined by its composition and crystal structure, which is determined by the synthesis method and reaction conditions [2].

This thesis focuses on understanding the effect of both the synthesis technique and reaction conditions on characteristic material properties of HA, including crystallinity, surface charge, chemical composition, and thermal behaviour. Novelty and contribution to knowledge is gained through relating any observed physical, chemical, or crystallographic changes with the results of acellular and cellular in-vitro tests. An investigation of the potential to fabricate scaffold structures suitable for use in the repair and replacement of cancellous bone by 3D printing (3DP) is also presented. This section serves as a basis for future work that aims to ‘optimise’ the scaffold by combining enhanced self-synthesised HA and 3DP.

Objectives

1) To experimentally assess the feasibility of selected synthesis techniques to produce nHA

2) To synthesise nHA using the selected methodology under various conditions

3) To characterise the physiochemical properties of the synthesised HA, assess the cytocompatibility and ability of substrates to support cell proliferation

4) To experimentally assess the feasibility of selected fabrication techniques to construct a scaffold structure that mimics the physical properties of cancellous bone

5) To recommend ‘optimised’ synthesis conditions for future bulk production of nHA to use in combination with the selected fabrication process

Thesis outline

The introduction in Chapter 1 provides a summary of the research background and presents the objectives as well as outline of this thesis. Relevant background literature is discussed in Chapter 2, which has been divided into three parts concerning the structure of bone, calcium phosphates (CaPs), and scaffold fabrication techniques to reflect the organisation of the experimental chapters and project objectives. Attention is focussed on bone mineral, pure as well as substituted HA, synthesis of HA via aqueous precipitation, and 3DP of bone tissue scaffolds.

Chapter 3 presents a feasibility study to determine the most appropriate synthesis technique and the conclusions drawn set the foundations for further experimental work. Chapters 4 – 6 focus on the synthesis of HA via aqueous precipitation. Specifically the influence of pH, temperature and solute concentration were assessed in Chapter 4. Chapter 5 presents an investigation of the effects of different solvent systems, namely containing Toluene and/or Ethanolamine in combination with DI water, on the physiochemical properties of HA. In an effort to emulate natural bone mineral more closely substitution of Sr, Mg, and Zn into HA was explored in Chapter 6. Acellular and cellular in-vitro tests were performed on HA prepared under the various conditions reported in Chapters 4 – 6.

From Chapter 7 onwards the research is focused on the fabrication of HA bone tissue scaffolds. Initially the viability of producing appropriate structures via a novel non-aqueous salt leaching technique utilising yeast as a natural pore forming agent was compared with a promising ALM method, namely 3DP. Chapter 8 extends the 3DP method introduced in Chapter 7 and a more detailed characterisation of the scaffold properties is presented, including compressive strength.

The overall project conclusions and recommended future work are discussed in Chapters 9 and 10, respectively.

Chapter 2

Literature review

2. Literature review

Literature reviewed in this thesis has been split into three parts for clarity and to reflect the structure as well as rationale of this project. Part one provides the clinical perspectives of bone as a hard tissue, covering: the clinical need for bone replacement or repair strategies, common bone diseases and defects, the physical, chemical as well as crystallographic structure of bone, and clinical solutions. In summary, this section describes the clinical motivation of this thesis. Literature presented in parts two and three contain background information as well as scientific rationale for the experimental chapters. Specifically, part two summarises key aspects of the group of materials used in this project, CaPs. Sub sections include: HA, synthesis methods, and the thermal behaviour of CaPs. Finally, part three presents selected literature concerning the fabrication of bone tissue scaffolds, which encompasses a discussion of common conventional and ALM methods used to manufacture CaP constructs.

Part one - clinical perspectives of bone as a hard tissue

2.1 Clinical need

Bones perform several vital functions within the body, primarily structural support and protection of bodily organs. The ability of bone to self-repair and remodel to meet different mechanical demands makes it a unique structural composite material [24, 25]. Bone also serves as an: attachment site for muscles to enable limb movement and joint mobility, a reservoir for minerals (e.g. calcium and phosphorous), and the primary site for the synthesis of blood cells.

The capacity of bone to function healthily can be affected by pathological conditions, diseases, and it is also well known that bone degenerates with age [26]. Furthermore, the ability of bone to self-repair is limited by what is known as the ‘critical size defect’, defined by Schmitz and Hollinger as “the smallest intraosseous wound in a particular bone and species of animal that will not heal spontaneously during the

lifetime of the animal" [27]. The 'critical' size is dependent on a number of patient specific properties such as age, bone health and defect location. This makes it difficult to comprehensively define an explicit 'critical' size. It has been proposed that defects ≥1cm in length and ≥50% of the diameter of the dense outer bone layer (i.e. cortical bone diameter) can be deemed critical [28].

Major alterations in bone structure due to injury or disease can lead to discomfort and a reduced quality of life [29], and defects outside of the limitations of natural self-repair may require surgical intervention, thus creating a demand for appropriate clinical strategies. However, due to the highly organised and complex structure of bone this clinical need presents an on-going medical challenge.

2.2 Bone diseases and defects

Millions of people in the UK are affected by bone tissue related diseases, such as osteoporosis (OP) or osteoarthritis (OA). Cancerous primary and metastasised bone tumours can also occur but are less common with only 500 cases reported in 2011 [30, 31]. Furthermore, osteomyelitis, infection of bone or bone marrow can lead to significant tissue destruction. This bacterium or more rarely fungus, most commonly originates from a skin wound or a bone fracture site. In chronic cases tissue necrosis may occur, which requires removal and replacement. An average of 7,000 adults are treated in the UK each year for osteomyelitis [31].

Complex interactions between genetic and environmental factors throughout the lifespan of bones causes them to age and after the fourth decade of life this is accompanied by a substantial loss of matter [32, 33]. There are a number of factors involved in these age related changes, including: imbalance between resorption and formation of bone, adjustments in architecture, accumulation of microfractures, localised inconsistency in the concentration of deposited minerals, and changes in bone tissue mineral deposits as well as protein content [34]. As a result, the mechanical integrity and resistance of bone to bending stress is compromised making them more susceptible to fracture [35, 36]. Occasionally, these changes can progress to a stage where they significantly affect normal functioning.

OP and OA are the most common chronic degenerative bone diseases and the leading causes of musculoskeletal morbidity in the elderly [37, 38]. The NHS has reported that

3 and 10 million people in the UK are affected by OP and OA, respectively [31, 39]. OP is characterised by low bone mass and micro-architectural deterioration of bone tissue, leading to enhanced bone fragility and as a consequence increased risk of fracture [40]. OA can be defined as a heterogeneous group of conditions that lead to joint symptoms and signs, which are associated with defective integrity of articular cartilage relating to changes in the underlying bone at the joint margins [41].

The capacity of bone to heal may be compromised by the conditions described above as well as many other diseases and genetic abnormalities. Furthermore, defects caused by trauma are common and nearly 350,000 bone fractures were reported in the UK between June 2009 and May 2010 [31]. All of these issues create a clinical need for bone repair or replacement strategies. Before potential clinical solutions are considered an understanding of the physical structure, chemical composition, and crystallographic arrangement of bone must be developed.

2.3 Bone tissue

2.3.1 Physical structure

Bone is a hierarchical composite that exhibits an irregular heterogeneous and anisotropic structure that comprises different components at a range of length scales [42]. These can be divided into well-defined domains: macrostructure (>500μm), microstructure (1 – 500μm), and nanostructure (<100nm – 1μm).

2.3.1.1 Macrostructure

Macroscopically bone is distinguished into cortical, otherwise known as compact, and cancellous, also referred to as trabecular or spongy bone. Cortical and cancellous bone can be easily distinguished by their degree of porosity: 4 – 28%, and 40 – 95%, respectively [43]. The denser structure of cortical bone forms the outer region of all types of bone, the diaphysis (shaft) of long bones, and flat bones providing protection and support for the inner regions. In contrast, cancellous bone exhibits macro-sized pores, filled with bone marrow, which is found in the centre of all bones. The respective densities of cortical and cancellous bone are 1.8 – 2Mg/m^3 and 0.07 – 0.97Mg/m^3 [44]. The structure of the femur, a typical long bone, comprising cortical and cancellous bone is illustrated in Figure 2.1.

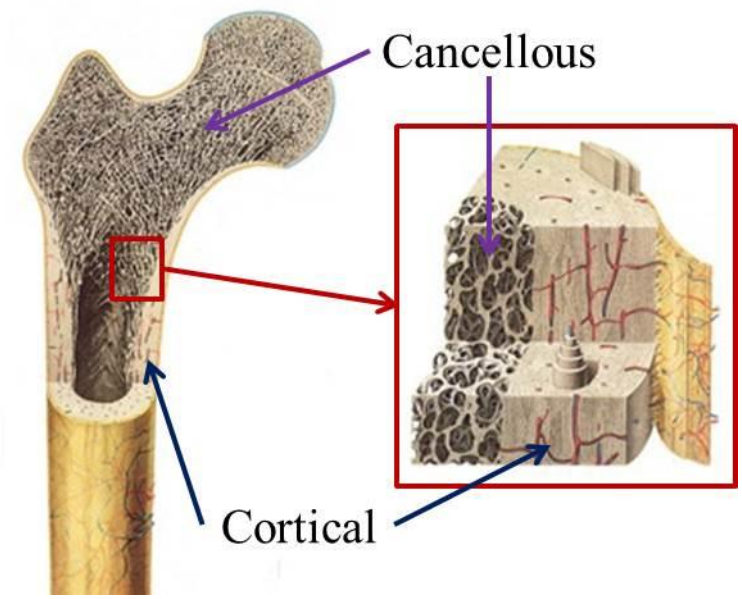

Figure 2.1: Structure of the femur illustrating regions of cortical and cancellous bone [45]

2.3.1.2 Microstructure

Cortical bone is precisely organised into lamellar Haversian systems, otherwise known as osteons (microscopic cylinders of bone matrix). Osteons are typically 200 – 250μm in diameter and run roughly parallel to the long axis of bone. At their centre are Haversian canals, which have a diameter of approximately 50μm and encompass blood and lymphatic vessels, as well as nerves [46]. Surrounding these canals are concentric rings of lamellae, a hard intercellular substance made up of mineralised collagen fibres 3 – 7μm thick [47]. Between the lamellae are spaces, called lacunae, which contain osteocytes (mature bone cells). Waste products and nutrients are transported to and from osteocytes by a branching network of microscopic channels, called canaliculi, which are connected to adjacent lacunae. Osteons communicate by Volkmann's canals, that contain blood vessels which join with the vessels in Haversian canals and this arrangement is shown in Figure 2.2 [48].

In contrast, the structure of cancellous bone is an irregular honeycomb lattice of thin plates of trabeculae 50 – 400μm thick and the cavities between are filled with bone marrow. Nutrients are received by blood vessels embedded in the marrow and osteocytes, osteoclasts (bone resorbing cells), osteoblasts (bone forming cells), and lamellae make up the trabeculae (Figure 2.3).

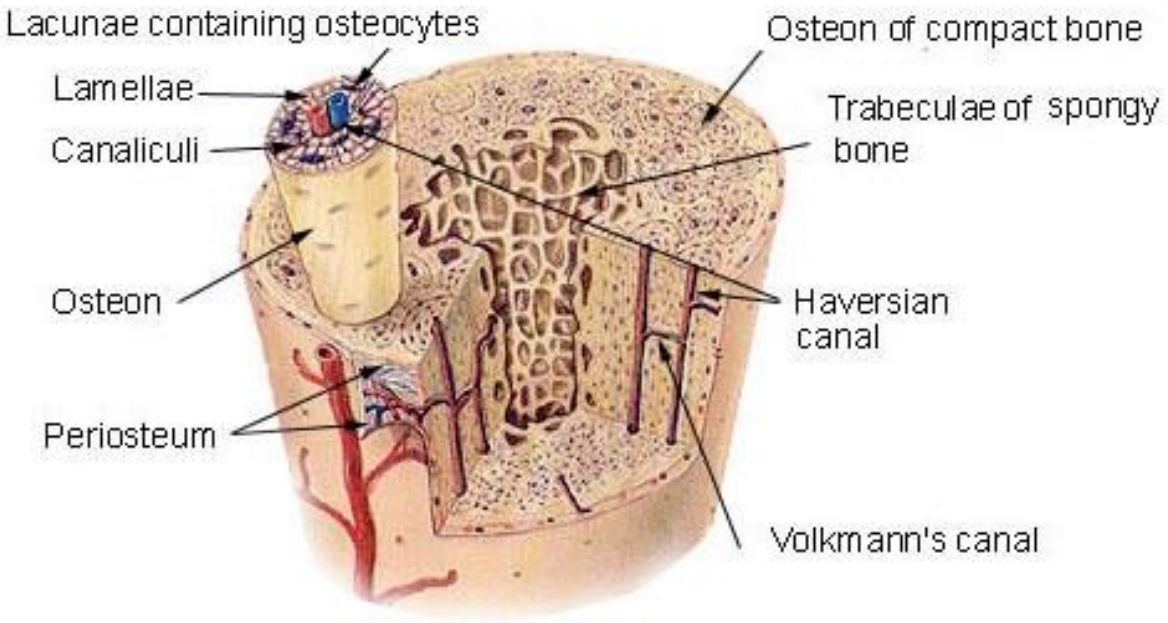

Figure 2.2: Key microscopic features of cortical bone [49]

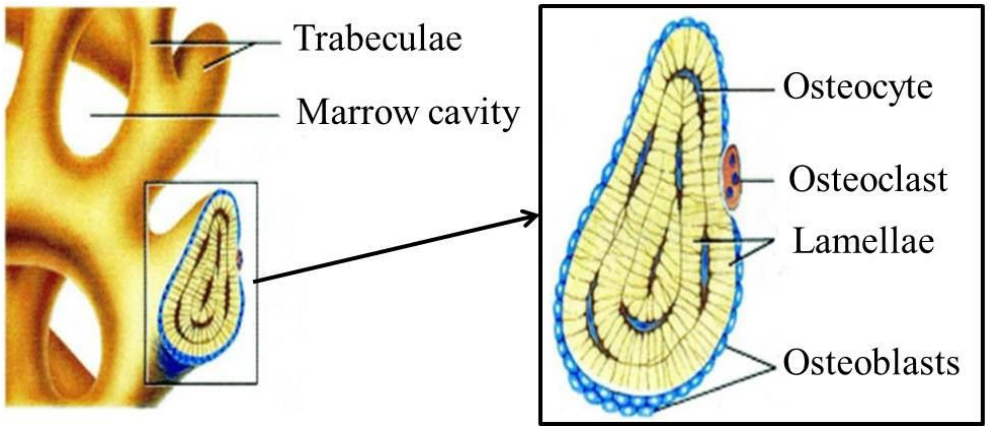

Figure 2.3: Microstructure of cancellous bone adapted from [50]

2.3.1.3 Nanostructure

At the nanoscale osteons are predominantly composed of collagen fibres 0.2 – 12μm in diameter, which consist of bundles of collagen fibrils. Collagen consists of arranged arrays of tropocollagen molecules, typically 300nm long and 1.5nm wide [51]. These molecules are composed of three left-handed helices of peptides (monomers of proteins composed of amino acid sequences) known as α-chains, which are bound together in a right-handed triple helix making up the collagen fibril that exhibits an average diameter of 100nm. Fibrils themselves are type I and V collagen and display a repeated banding pattern every 64nm [52].

Found within collagen fibrils in discrete 40nm holes reside bone apatite crystals [53]. These inorganic apatite crystals are in the form of plates or needles and vary in size, characteristically 40 – 60nm in length, 5 – 25nm in width, and 1.5 – 5nm thickness [54, 55]. The assembly of collagen molecules and bone apatite is shown schematically in Figure 2.4.

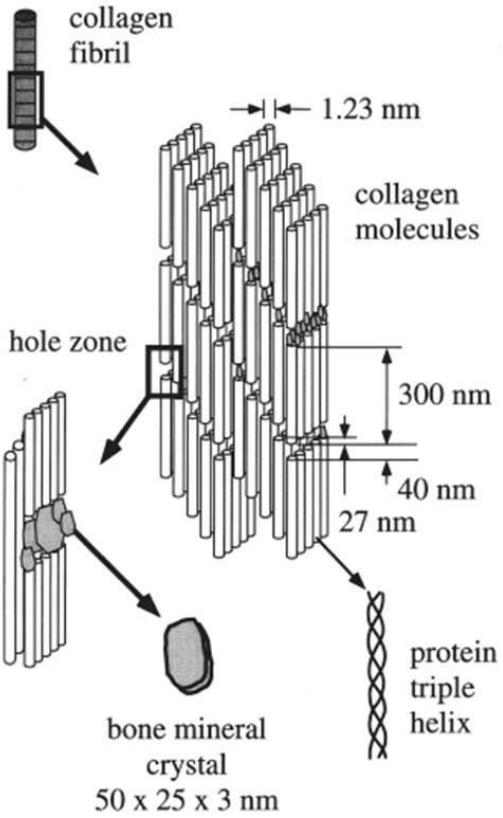

Figure 2.4: Assembly of collagen and bone apatite crystals [42]

2.3.2 Chemical composition

90wt% of bone comprises of its inorganic and organic components, and the remaining 10wt% is attributed to water. Inorganic bone apatite crystals are 65 – 70wt% of the dry weight and contribute to the compressive strength as well as modulus, and stiffness of bone. FTIR and NMR studies have confirmed that bone mineral is a nonstoichiometric carbonated multi-ion substituted apatite with calcium (Ca) to phosphorus (P) ratio between 1.37 and 1.87 [51]. The remaining 30 – 35wt% is composed predominantly of type I collagen (90%) and non-collagenous proteins (e.g. glycoproteins, growth factors) that bind the inorganic phase to the collagen fibres. The organic phase confers the tensile strength, elasticity and fracture toughness of the bone matrix.

2.3.3 Crystal structure and composition of bone apatite

A vast group of ionocovalent compounds, called apatites, are represented by the general formula $Me_{10}(XO_4)_6Y_2$, where Me is a bivalent ion, XO_4 a trivalent ion, and Y a monovalent ion [2]. Bone mineral can be described as a non-stoichiometric apatite that exhibits a similar crystal structure to hydroxyapatite [$Ca_{10}(PO_4)_6(OH)_2$ – HA]. Figure 2.5 illustrates the crystal structure of HA that exhibits a hexagonal arrangement. Two ion channels (3Å diameter) run parallel to the *c* axis [17]. The first is filled with Ca^{2+} (Ca(I) site) and the second with OH^-. Six Ca^{2+} (Ca(II) site) and six PO_4^{3-} tetrahedra are arranged hexagonally around the hydroxide channel. This system enables partial or total replacement of ions, and in bone apatite numerous biologically relevant ionic substitutions occur (Table 2.1), thus contributing to the typical low degree of crystallinity. Divalent cations (e.g. Mg^{2+}) and monovalent cations (e.g. K^+) can substitute for Ca^{2+}, and anions such as fluoride (F^-) or chloride (Cl^-) may substitute for OH^- groups. Furthermore, some ions such as carbonates can substitute for OH^-, PO_4^{3-} or both, which are referred to as A, B and AB type substitutions, respectively [2]. Therefore an appropriate formula for bone apatite can be expressed as (Ca, $X)_{10}(PO_4, CO_3, Y)_6(OH, Z)_2$ with X as substituting cations, and Y and Z being the substituting anions, with the indices 10, 6 and 2 changing according to the degree of stoichiometry [56].

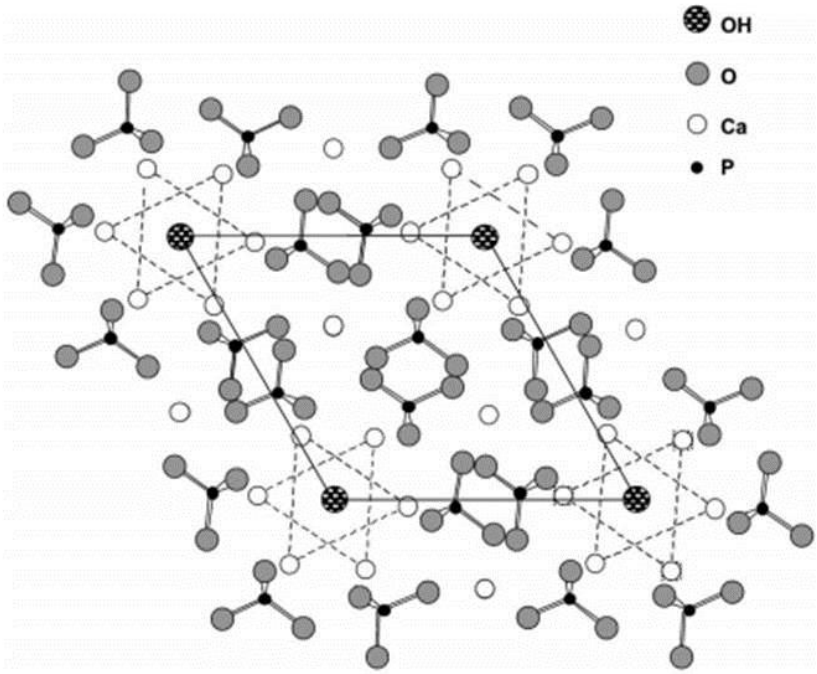

Figure 2.5: Structure of HA projected onto the (001) plane [2]

Table 2.1: Comparative composition and unit cell parameters of bone apatite and stoichiometric HA adapted from [11, 57]

Composition	Bone	Bone	HA
Calcium (wt %)	34.8	36.6	39.6
Phosphorus (wt %)	15.2	17.1	18.5
Carbonate (wt %)	7.40	4.8	-
Sodium (wt %)	0.90	1.0	-
Magnesium (wt %)	0.72	0.6	-
Chloride (wt %)	0.13	0.1	-
Pyrophosphate (wt %)	0.07	-	-
Potassium (wt %)	0.03	0.07	-
Fluoride (wt %)	0.03	0.1	-
Strontium (wt %)	-	0.05	-
Zinc (ppm)	-	39	-
Chromium (ppm)	-	0.33	-
Cobalt (ppm)	-	<0.025	-
Manganese (ppm)	-	0.17	-
Silicon (ppm)	-	500	-
a axis (Å)	9.410	-	9.430
c axis (Å)	6.890	-	6.891

X-ray diffraction (XRD) patterns of bone apatite confirm that the lattice arrangement is consistent with HA standards but peak broadening and intensity vary due to the difference in crystallite size, crystallinity and ionic substitutions. Figure 2.6 shows typical XRD patterns of: (a) bone apatite, (b) crystalline HA with nanosized crystals, and (c) well-crystallised HA. The marked broadening of the characteristic (211), (112), (300) and (202) peaks in patterns (a) and (b) indicate a small crystallite size and the large amorphous fraction of bone apatite is signified by the relatively low intensity above background. When compared with stoichiometric HA (=100), bone apatite exhibits a crystallinity of 33 – 37 [57].

There are a number of reports in the literature that propose the surface of bone apatite exhibits a structured hydrated layer [58, 59]. This model is suggested to be responsible for the high reactivity and ion exchange capacity of biological apatites. Mobile ionic species are contained within this layer, including non-apatitic environments such as HPO_4^{2-} and it is possible that precipitated synthetic apatites may also exhibit this structural model [2, 60].

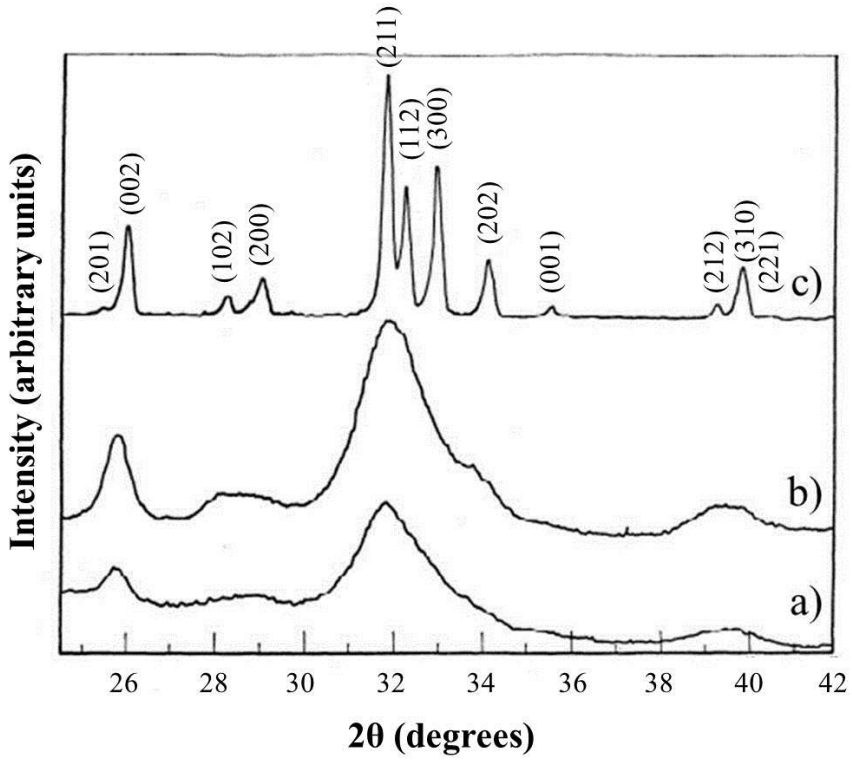

Figure 2.6: XRD patterns of (a) powdered human bone femur, (b) crystalline HA with nanosized crystallites, and (c) well-crystallised HA illustrating the difference in crystal size and crystallinity between bone apatite and HA [1]

2.4 Cellular functions of bone

Three cells are important in the maintenance and remodelling of bone: (1) osteoblasts (bone forming cells), (2) osteocytes (mature bone cells), and (3) osteoclasts (bone resorbing cells). Each is highly specialised, differentiated and generally does not replicate [51]. Instead less differentiated cells, known as stem cells, control cell population. Bone stem cells are normally referred to as osteogenic cells and originate from the mesenchymal bone marrow stromal cell line. Local osteogenic cell populations are increased when biochemical signalling molecules are stimulated during bone remodelling and fracture healing. Depending on the vascularity (i.e. the availability of nutrients and oxygen) of the local environment different differentiation routes can be undertaken by osteogenic cells. A highly vascularised environment is required for bone to form since it cannot diffuse oxygen over long distances due to its dense mineralised structure. Bone relies on an internal vascular network to circulate vital oxygen and nutrients, which are then diffused over short distances [51]. If a differentiating osteogenic cell is surrounded by a highly vascularised environment it will differentiate into an osteoblast, which will produce bone.

Osteoblasts are connective tissue cells found at the surface of bone and once enclosed can be stimulated to proliferate and differentiate into mature osteoblast cells known as osteocytes, which are derived by a complex change of form and activity. Osteocytes are involved with the maintenance of local bone, specifically metabolism, and the exchange of nutrients as well as waste products by blood. In contrast, osteoclasts perform the opposite function of osteoblasts and are responsible for the majority of resorption as well as degradation of existing bone. Specific signalling proteins cause the migration of mononuclear monocytes to resorption sites that may fuse with each other to establish multi-nucleated macrophages, which differentiate into specialised osteoclasts [61]. Monocytes and macrophages are involved in bone resorption during remodelling and fracture repair [62].

2.5 Mechanical properties of bone

Mechanical properties of bone at the macrostructural level vary from one bone to another as well as within different regions of the same bone [63-65]. This has been attributed to differences in microstructure [66]. Ageing and diseases can also affect the mechanical integrity of bone [26]. Table 2.2 provides a summary of the mechanical properties of human cortical and cancellous bone.

2.6 Clinical solutions

2.6.1 Bone grafts

A bone graft (BG) is the transplantation bone from one location to another and can be used to fill skeletal defects, bridge joints, or promote union at a site of delayed union, non-union or fracture [67]. An estimated 2.2 million bone grafting procedures were undertaken worldwide in 2005 [68]. Due to the ageing of the world population, increasing life expectancy, and the growing dynamism of life this number is only expected to increase [69].

Table 2.2: Summary of the mechanical properties of human cortical and cancellous bone (F) = Femur, (T) = Tibia, (Fi) = Fibula, (H) = Humerus, (R) = Radius, (U) = Ulna, and orientation is longitudinal unless otherwise stated

Property	Cortical bone	Cancellous bone	Reference
Compressive Modulus (GPa)	**15.2 – 35.3** (15.2-18.1 (F), 17 (F), 11.5 (F, transverse), 25.9-35.3 (T))	**0.0011 - 9.8**	[63, 70, 71]
Compressive Strength (MPa)	**114.8 – 213** (150.3-209 (F), 158.9-213 (T), 122.6 (Fi), 132.4 (H), 114.8 (U))	**0.15 – 22.5** (0.15 – 22.5, 3.36 – 11.36 (F))	[63, 70-73]
Tensile Modulus (GPa)	**11.5 – 29.2** (15.6-19.4 (F), 17 (F), 11.5 (F, transverse), 18.0-29.2 (T), 18.5 (Fi), 17.2 (H), 18.5 (R), 18.4 (U))	-	[70, 74]
Tensile Strength (MPa)	**120 – 161** (120 – 161 (F), 140.3-161 (T), 146.1 (Fi), 122.6 (H), 149.1 (R), 148.1 (U))	**1.47 - 2.99**	[70, 75]
Torsion Modulus (GPa)	**3.17 – 5.0** 3.3-5.0 (F), 3.17-3.58 (F)	-	[70]
Fracture Toughness (MPa $m^{0.5}$)	**1.77 – 14.8** (5.0-6.4 (F), 2.12-4.32 (T), 1.88-14.8 (T), 1.77 (H))	**0.04-0.6 (F)**	[76-79]

There are four essential elements of bone regeneration: (1) osteogenesis (the ability for cells to survive transplantation, proliferate and differentiate into bone cells), (2) osteoinduction (activation and stimulation of host cells), (3) osteoconduction (facilitation and alignment of blood-vessels), and (4) osteointegration (surface bonding between host and grafting material). To qualify as a bone graft, the material must provide at least one of these functions [80]. Table 2.3 summarises the three types of bone grafts: (1) allogeneic, (2) autologous, and (3) xenogeneic. Autografts, bone taken from another part of the patient's body, have been regarded as the 'gold standard' for many years because they provide osteogenic, osteoconductive, and osteoinductive properties. Hence they are considered the benchmark for other BGs or synthetic substitutes. However, supply of autologous bone is limited and harvesting is connected with numerous complications, such as revision surgery and sensory loss. Furthermore, it has been reported that autografts can fail in clinical practice as osteogenic cellular elements may not survive transplantation [81].

2.6.2 Tissue engineering

The issues associated with current BGs have created the need for the development of alternative clinical solutions to replace or repair bone tissue. Tissue engineering is an

interdisciplinary field that aims to combine the knowledge of cells, biomaterials, and suitable biochemical factors to create a surrogate structure to guide and regenerate new tissue [82]. Ideally, the structural 'scaffold' component should be made from appropriate biomaterials and fabricated so as to mimic the physical and chemical structure of the host tissue.

Table 2.3: Summary of current graft types [83-85]

Cells	Donor - receiver	Advantages	Disadvantages
Allogeneic	Human - human	• Provides structural stability • Osteogenic behaviour	• Immunogenic response to foreign tissue • Graft rejection leading to inflammatory reaction • Disease transmission • Donor shortages • Risk of additional surgeries
Autologous	Human - human	• Avoids possibility of transfection • Osteogenic behaviour	• Donor site morbidity • Limited harvesting sites • Harvesting is expensive and painful • Unpredictable resorption characteristics
Xenogeneic	Animal - human	• Range of sizes and shapes available	• Risk of immunological reactions/infections • Risk of additional surgeries

2.6.2.1 Tissue engineered bone scaffolds

In addition to the essential bone regeneration elements (section 2.6.1) there are a number of specific features and properties that a scaffold must exhibit to be successful in bone tissue applications. However, due to the complexity and variability of native bone there are many aspects that are not yet fully understood.

Porosity

The porosity of native bone allows the migration and proliferation of osteoblasts and mesenchymal cells in-vivo, which facilitates ingrowth of new tissue. To ensure uniform distribution, survival, proliferation, and migration of cells in-vitro it is recognised that bone scaffolds must exhibit a highly porous surface and bulk structure [86]. Using a rat model Kuboki et al. demonstrated direct osteogenesis on porous structures whereas no formation was observed on solid particles [87]. In addition to bulk or macroporosity (pore size >50μm), microporosity (pore size <10μm) has also been reported to facilitate the attachment of osteoblasts and is considered vital for

capillary ingrowth [88]. It is critical that nutrients and gases be readily diffused and metabolic waste be removed, both of these processes are expedited by the degree of scaffold porosity and pore interconnectivity [89]. A porous surface has been found to improve mechanical interlocking between the scaffold and surrounding bone tissue [90], which reduces interfacial mechanical instability. A bulk increase in porosity notably leads to an overall reduction in the mechanical strength and therefore an upper functional limit of porosity should be considered.

Pore size and distribution

Scaffold pores provide a surface and space for cells to adhere and for bone to form in. Early studies by Hulbert et al. suggested a minimum pore size of 100μm [91], since below this limit pores can become occluded by cells and prevent cellular penetration as well as neovascularisation of the inner structure [19]. More recently, experimental research has led to the general acceptance that pore sizes should range between 200 and 900μm. Larger pores have been found to favour direct osteogenesis as they enable a vascular network to form throughout the structure leading to high oxygenation [20, 84, 92, 93]. Narrower ranges of 150 – 800, 100 – 400, 150 – 500, and 250 – 300μm have also been reported [92, 94-97]. Conversely, Holy et al. recommended larger pores ranging from 1.2 – 2.0mm offering the benefit of a higher surface to volume area despite the reduced mechanical strength resulting in limited applications [98]. Table 2.4 summarises the distribution of pore sizes required for full bone regeneration reported by Salcedo et al. [99].

Table 2.4: Hierarchical pore size distribution of an ideal bone tissue scaffold [99]

Scaffold pore size (μm)	Biochemical effect/function
> 1	Interaction with proteins Responsible for bioactivity
1 – 20	Type of cells attracted Cellular development Orientation and directionality of cellular ingrowth
100 – 1000	Cellular growth Bone ingrowth Predominant function in the mechanical strength
> 1000	Implant functionality Implant shape

Despite several reports of contradictory pore size ranges it is indisputably accepted that the size and distribution of scaffold pores are crucial features for bone

regeneration, which should be balanced with the necessary mechanical attributes of the scaffold required for the intended clinical application [100-102].

Interconnectivity

The benefits of scaffold porosity and pore size are constrained if the structure is not interconnected since discontinuous pores limit blood vessel invasion, cell migration and mass transport, in particular to the core of the structure [103]. Cell necrosis or decreased metabolic activity may result if cells are more than 200μm away from a blood supply [104]. Klawitter and Hulbert recommended a minimum interconnection size of 40 – 100μm for blood vessels to anastomose (diverge and reconnect) and 5 – 15μm to facilitate mineralised bone ingrowth [105].

Surface properties

Surface characteristics including area, morphology, topographical features and physiochemistry can influence and control protein adsorption, cellular adhesion and proliferation, as well as tissue formation [106, 107]. Rough surface topography, with nano to macro scale features provide cells with more secure fixation points in comparison to smooth surfaces and results in improved osteoconductive properties [108, 109]. Initial stability and bone to scaffold shear strength also correlate positively with an increasing degree of surface roughness [110, 111]. It is well known that surface charge plays a key role in the adhesion process of cells and the morphology of adhering cells has been shown to depend on the sign of any charge [112].

Mechanical

It is vital that scaffolds provide adequate temporary mechanical support to withstand the continuous loading of bone, therefore it is crucial that structural integrity is not compromised during optimisation [113]. The scaffold must function in tandem with the host tissue sharing mechanical demands and infiltration of cells is known to improve mechanical strength. Specifically, Sopyan et al. reported an increase in compressive strength from 2 to 20MPa over a 3 month period for a porous HA scaffold [96]. In regards to degradation of the scaffold, it is necessary for the kinetics to be tuned to the rate of new tissue growth in order to ensure that mechanical stability is maintained throughout the lifetime of the construct [114].

Part two - calcium phosphates

2.7 Chemical biomimetics

The majority of the dry weight of bone comprises inorganic nanocrystals of nonstoichiometric apatite (section 2.3). To ensure similar properties to native bone the strategy used for this thesis is to fabricate an appropriate scaffold structure from a material that chemically mimics the composition and physiochemical characteristics of the natural apatite structure. Due to the chemical and crystallographic similarity of CaPs to native bone mineral they are commonly used in bone replacement applications. Their popularity is based on their ability to form chemical bonds with native bone tissue (i.e. bioactive), as well as support the adhesion, proliferation and differentiation of osteoblasts (i.e. osteoconductivity) [115].

2.8 Calcium phosphates

Stoichiometric CaPs are formed from different precursor phosphates, such as ortho- (PO_4^{3-}) and pyro- ($P_2O_7^{4-}$) phosphates. The degree of osteoconductivity, bioactivity, and resorbability of these materials differ in-vivo due to the variation of chemical composition [116]. Resorbability is known to depend on composition, particle morphology, and porosity. CaPs have been utilised for a range of different applications due to the range of mechanical and biological properties exhibited. Table 2.5 summarises the key features of biologically relevant CaPs.

CaPs in the form of $Ca_{10}(PO_4)_6(OH, F, Cl)_2$, for example HA, exhibit an apatitic structure. These bioceramics are ranked very highly due to their excellent biocompatibility, compositional similarity to natural bone mineral, osteoconductivity, and bioactivity [117]. In addition, anionic and cationic substitutions of calcium apatite can readily occur, as exhibited in human bone apatite and may result in improved reactivity (Table 2.1).

With the exception of MCPM, CaP phases exhibit an inverse solubility relationship with increasing alkalinity. Solubility isotherms represent the saturation boundary and suggest the conditions required for synthesis. HA is the least soluble CaP phase above pH 4.5 and below this level DCPA is the stable phase (Figure 2.7). Under

physiological conditions (37°C and pH 7.4) HA exhibits the lowest solubility and thus slowest dissolution rate followed by β-TCP, and α-TCP displays the fastest. Although TCPs display a faster degradation rate in comparison to HA, which in-vivo is resorbed over a number of years, they do not exhibit the same level of osteoconductivity [118]. The dissolution rate of CaPs is not only dependent on composition (Ca:P ratio), particle and crystal size, but notably ionic substitutions and crystallinity also play an influential role [119]. Reduced particle size and crystallinity have been reported to improve the dissolution properties of CaPs [119, 120].

Table 2.5: Summary of biologically relevant CaP [57]

Compound	Formula	Ca:P ratio	Solubility at 25°C, -log(K_{SP})
Monocalcium phosphate monohydrate (MCPM)	$Ca(H_2PO_4)_2 \cdot H_2O$	0.5	1.14
Dicalcium phosphate dihydrate (DCPD)	$CaHPO_4 \cdot 2H_2O$	1.0	6.59
Dicalcium phosphate anhydrate (DCPA)	$CaHPO_4$	1.0	6.9
β-Calcium pyrophosphate	$\beta\text{-}Ca_2P_2O_7$	1.0	-
Octacalcium phosphate (OCP)	$Ca_8(HPO_4)_2(PO_4)_4 \cdot 5H_2O$	1.33	96.6
α-Tricalcium phosphate (α-TCP)	$\alpha\text{-}Ca_3(PO_4)_2$	1.5	25.5
β-Tricalcium phosphate (β-TCP)	$\beta\text{-}Ca_3(PO_4)_2$	1.5	28.9
Amorphous calcium phosphate (ACP)	$Ca_x(PO_4)_y \cdot nH_2O$	1.2-2.2	Cannot be measured precisely
Calcium-deficient hydroxyapatite (CDHA)	$Ca_{10-x}(HPO_4)_x(PO_4)_{6-x}(OH)_{2-x}$ $(0<x<1)$	>1.5, <1.67	85.1
Hydroxyapatite (HA)	$Ca_{10}(PO_4)_6(OH)_2$	1.67	116.8
Tetracalcium phosphate (TTCP)	$Ca_4(PO_4)_2O$	2.0	38 - 44

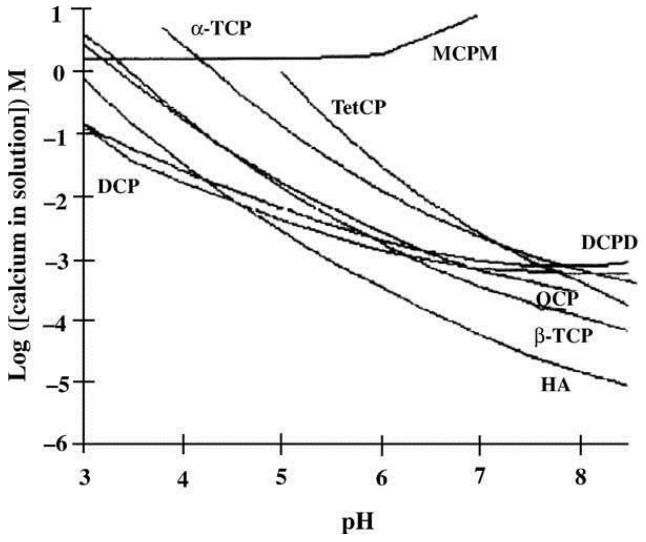

Figure 2.7: Solubility isotherms of CaP phases in water [121]

2.9 Hydroxyapatite (HA)

HA is a stable, dense (3.16g/cm^3) CaP that exhibits chemical and crystallographic similarity to bone apatite, which explains its inherent biocompatibility and bioactivity. This has led to significant research being performed to develop the physical and chemical preparation as well as morphological control of HA. However, due to its brittleness and potential to fail catastrophically, HA is typically used for relatively low loading applications. In addition, if used in a dense form its reactivity is low and exhibits poor bioresorbability [5-7]. To compensate for these shortcomings reinforced biocomposites of HA and polymers may be used. Porous HA constructs that encourage rapid bone in-growth to augment or improve mechanical performance can also be used and have been approved by the FDA for the treatment of bone defects caused by trauma [3, 4]. The use of nanosized HA, compared to micron sized equivalents, has been shown to improve the formation and adhesion of bone cells [8, 9].

Stoichiometric HA has a Ca:P ratio of 1.67 but stable phases are found to exist between 1.3 and 1.8 [122]. A Ca:P > 1.67 indicates the presence of calcium rich or carbonated HA [$Ca_{10}(PO_4)_{6-x}(CO_3)_x(OH)_2$ – CHA]. Whereas, a Ca:P < 1.67 suggests that the apatite is calcium deficient (CDHA) or contains impurities [123].

Of the two known crystal forms of HA – monoclinic and hexagonal – only the hexagonal phase is of practical importance since the monoclinic structure is destabilised by even a small amount of foreign ions [11]. The hexagonal crystal structure of HA was previously described (section 2.3.3) and the unit cell dimensions have been reported as a=b=0.943nm and c=0.689nm [11, 57].

2.9.1 Substituted hydroxyapatite

In order to more closely mimic the composition and crystal structure of native apatite, naturally occurring trace elements can be incorporated into synthetic HA (Table 2.1). As a result in-vivo functions, such as solubility or bioactivity, can be enhanced [10].

2.9.1.1 Cationic substitutions

Bone diseases, such as OP, may lead to changes in the composition of the bone matrix. Termination of bone growth, decreased osteoblast and osteoclast activity, as well as mechanical instability are all consequences of magnesium (Mg) reduction in the bone

matrix [124, 125]. Mg depletion has also been found to adversely affect bone metabolism. Due to the vital role of Mg in native bone apatite many researchers have studied Mg substituted HA [126-128]. Mg is found to inhibit apatite crystallisation in solution and favours thermal conversion to β-TCP. The expected reduction in the lattice parameters of HA, due to the smaller ionic radii of Mg^{2+} (0.065nm) in comparison to Ca^{2+} (0.099nm), is typically observed when Mg is incorporated into its lattice structure. Since Mg destabilises the HA structure an upper limit of 25.4wt% substitution has been reported [129-131]. Mg substituted HA generally exhibits reduced crystallinity, resulting in increased solubility due to the inhibitory effect of Mg on crystallisation of HA [14].

Strontium (Sr) can fully replace Ca in the apatite structure and due to its larger ionic radii (0.12nm) it causes an expansion of the lattice [11]. This destabilises the apatite structure and increases the solubility of HA [132]. Sr concentrations between 0.5 and 1.3wt% have been found to stimulate osteoblast activity as well as differentiation [133] and levels as low as 0.2wt% have been shown to influence osteoclast proliferation [11]. These effects are beneficial in the treatment of bone diseases, such as OP [134, 135].

As well as inhibiting osteoclast differentiation, zinc (Zn) has been reported to promote osteoblast activity, thus resulting in increased bone formation [136]. Deficiency of Zn has been associated with a reduction in bone density and ductility, resulting in an increased susceptibility to fractures [137, 138]. A 30wt% substitution for Ca is possible and a reduction in lattice parameters has been observed up to 15wt%, which is consistent with the smaller ionic radii of Zn^{2+} (0.075nm) [139]. Zn has also been shown to inhibit the crystal growth of HA during synthesis resulting in smaller crystal sizes and reduced thermal stability [140, 141].

2.9.1.2 Anionic substitutions

4 – 8wt% of carbonate (CO_3^{2-}) substitution is found to be abundant in bone apatite [142, 143]. Since carbonate ions can substitute OH^-, some researchers suggest this explains why there is a low degree of hydroxylation in bone apatite [144]. Phosphate groups can also be replaced by carbonate. The substitutions of OH^- and PO_4^{3-} by CO_3^{2-} are referred to as type-A and type-B substitutions, respectively [145]. Synthesis of HA containing similar levels of carbonate (8wt%) to native bone has been reported to

result in structural disorder, which increased solubility and in-vivo dissolution [16, 143, 146]. However, prolonged substitution times of up to 2 months may be required and achieving controlled bulk substitution as opposed to surface absorbance has been described as challenging [147, 148].

Silicon (Si) substituted HA has attracted much interest due to its reported enhanced in-vivo and in-vitro bioactivity in comparison to HA [149, 150]. Incorporation is limited to 5wt% but levels as low as 0.8wt% Si, present as a silicate group, have been found to elicit improvements in the biological activity of HA [151]. Substitution of silicate has also been shown to increase the fraction of amorphous phase and reduce the mean crystallite size of HA. Due to the greater electronegativity of silicate, finer microstructure and increased solubility leading to enhanced dissolution has been observed [7].

Fluorine (F) and chlorine (Cl) are widely considered anionic substitutions for the hydroxyl site of HA and both can fully substitute for OH^- in the apatite structure to form fluoro- or chloroapatite, respectively. However, chloroapatite is not considered an effective biomaterial since it enhances local acidity leading to fast solubilisation of alkaline salts. Full substitution of OH^- with F^- results in decreased lattice constants due to the smaller ionic radii of F^- (0.132nm) in comparison to OH^- (0.168nm). F^- is known to improve the chemical and thermal stability of HA as well as stimulate the proliferation and differentiation of osteoblasts [152, 153]. In contrast, Cl^- may activate osteoclasts due to the potential creation of an acidic environment, and its larger ionic radii (0.181nm) in comparison to OH^- can lead to an expansion of the lattice [154].

2.10 Tricalcium phosphates

Tricalcium phosphates (TCPs) have a Ca:P ratio of 1.5 but do not exhibit an apatitic structure. At ambient conditions there are at least two different phases of stoichiometric crystalline TCP: (1) α-TCP, and (2) β-TCP. Both forms can be prepared by thermal decomposition of other CaPs, such as CDHA. β-TCP may also be prepared by high temperature solid-state reactions but neither α-TCP or β-TCP can be obtained from solution [155]. Due to high temperature preparation TCP particles typically exhibit distinctly different morphologies in comparison to CaPs phases, such as HA, that can be prepared at RT (Figure 2.8).

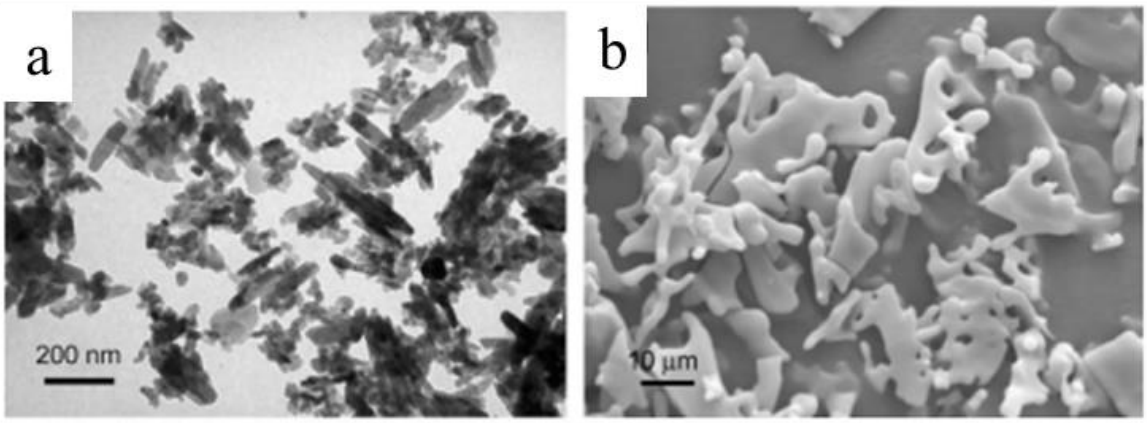

Figure 2.8: Typical particle morphology of (a) HA visualised by TEM, and (b) α-TCP observed by SEM adapted from [11]

β-TCP exhibits a rhombohedral crystal structure and is obtained at temperatures above 800°C. According to the phase diagram for the $2CaO{\cdot}P_2O_5$ system β-TCP is stable up to 1125°C (Figure 2.9). In comparison, the unit cell of α-TCP is monoclinic and is formed from β-TCP at temperatures above 1125°C.

HA, compared to TCP, exhibits slow bioresorbability and this has led to the use of β-TCP as a biodegradable replacement for bone tissue [156]. However, the use of pure β-TCP as a hard tissue augmentation has shown that its rate of biodegradation can be too fast [157]. One solution proposed is to use a composite of HA and β-TCP [86, 158].

2.11 Dicalcium phosphates

Dicalcium phosphate dihydrate (DCPD), commonly referred to as brushite, exhibits a monoclinic crystal structure and its lattice comprises of CaP chains that are layered parallel to water molecules. DCPD has been detected in fracture callus as well as bone and is sometimes considered as a precursor of bone apatite [159-161].

Brushite is metastable and can be converted into dicalcium phosphate anhydrate (DCPA) below pH 6 or HA above pH 7 [121]. DCPA, otherwise known as monetite, is the anhydrous form of brushite and is the most stable CaP at pH levels below 4.5 (Figure 2.7). Monetite is generally formed by the recrystallization of DCPD and, this conversion occurs quickly in water, at high temperatures and under acidic conditions [162]. Both DCPD and DCPA are reported to be biocompatible and biodegradable in-vivo [163, 164].

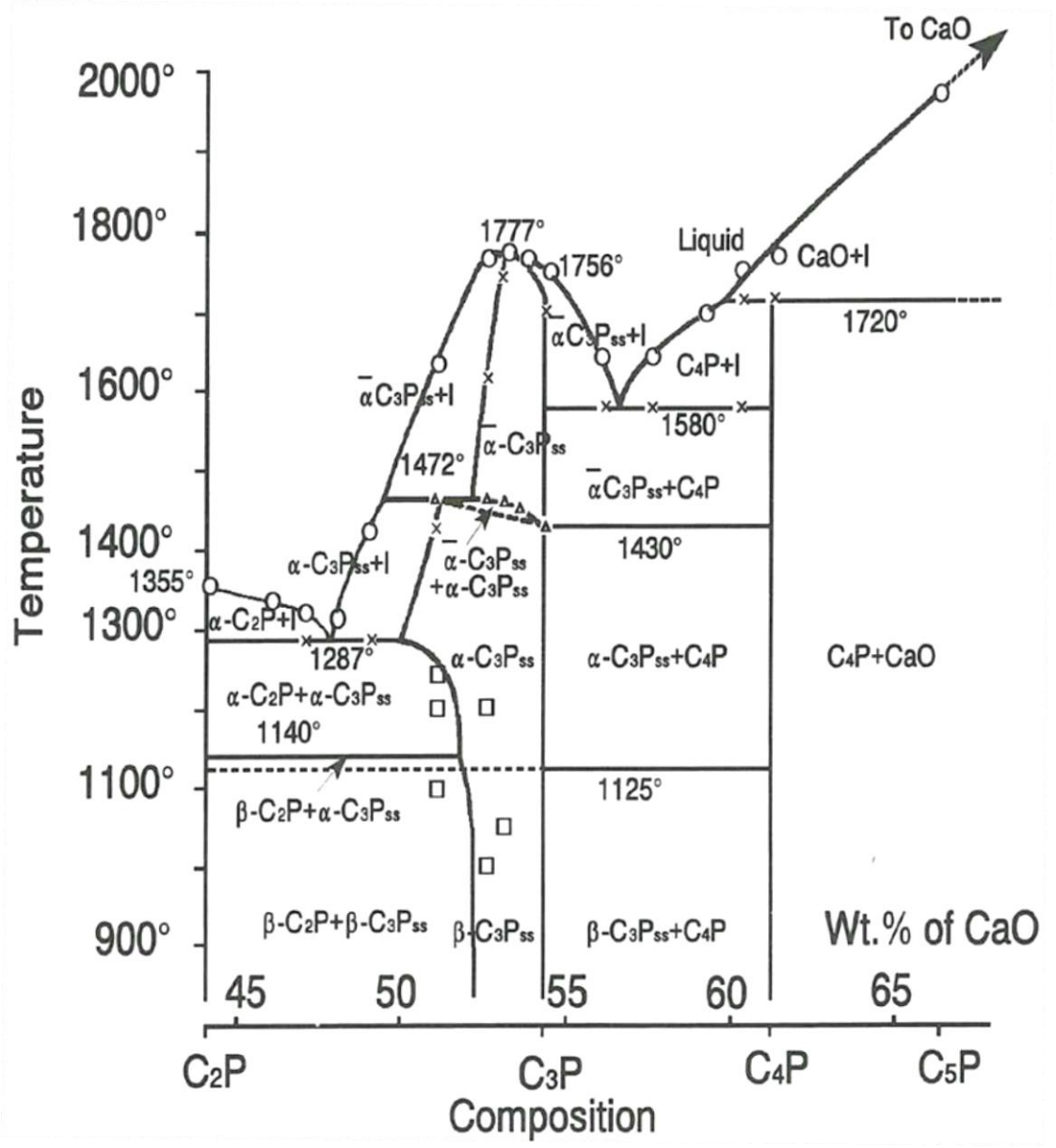

Figure 2.9: High temperature phase diagram for 2CaO·P2O5 system ○ liquidus temperature, Δ temperature of α-TCP to α-TCP transition, x temperature of initial liquid formation, and □ points at which determinations were made by focusing X-ray Guinier camera on quenched specimens, C = CaO, P = P2O5, l = liquid, and ss= solid solution [17]

2.12 Synthesis of synthetic apatites

There are numerous conventional techniques that have been used to synthesise synthetic HA. Notable methods are aqueous precipitation [165-168], sol-gel processing [169-171], solid-state synthesis [172, 173], emulsion or micro-emulsion techniques [174-177], and hydrothermal reactions [55, 178-181]. Other less common techniques, for example self-propagating combustion synthesis (SPCS) and

solvothermal synthesis (SS) have also been explored. Table 2.6 summarises these synthesis methods and highlights key process and product features, such as temperature and particle size.

2.12.1 Solid-state synthesis

This procedure relies on the solid state diffusion of ions when powdered raw materials are sintered. Relatively high reaction temperatures (1050 – 1250°C) are required to initiate such thermodynamic reactions. This method is simple when compared to other common synthesis techniques but there are a number of physiochemical variables that need to be considered, such as addition of additives, binders or organic vehicles, balling milling to sufficiently reduce particle size and ensure homogeneity, crushing and compaction of samples, as well as the sintering protocol. In some cases it is necessary to repeat process steps, such as sintering, to refine the crystal structure or reduce particle sizes [172].

The production of phase pure HA by solid-state synthesis has been reported, for example Rhee et al. [182]. However, the high reaction temperatures required to initiate ionic diffusion may result in mixed phase products [172]. Any phase changes that occur will result in an irreversible alteration of the bulk chemical (e.g. dissolution behaviour) as well as physical (e.g. mechanical) material properties, and final compositions may be difficult to reproduce.

Table 2.6: Summary of common synthesis methods for synthetic apatite
[a]Cost of 1kg of calcium and 500g of phosphate sources as well as minimal amounts of any additional reagents

Synthesis method	Method description	Particle size (µm)	Process time (</> 24hrs)	Reaction temperature (°C)	Material costs[a]	Scalability	Comments	References
Solid state synthesis	Reactants used in solid forms. Thermal treatment required to start reaction. HA formed via solid-state ionic diffusion	> 2.0	>	1050 – 1250	276%	Medium	Involves long ball milling, drying, compression and sintering steps May need to repeat process steps to improve quality and reduce particle size Slow and difficult to achieve a complete reaction leading to a mixed phase product Poor reproducibility	[172, 173]
Aqueous precipitation	Solutions combined under controlled reaction parameters resulting in nucleation and crystal growth	> 0.1	>	RT – 85	100% (£97.10)	High	Most common method Two step procedure; requires sintering after processing Difficulties with reproducibility due to lack of precise control	[165-168]
Hydro- and solvothermal	Reaction occurs in a closed aqueous system under high temperature and pressure	> 0.05	<	150 – 400	89 – 175%	Medium	Homogeneous crystal shapes and sizes can be produced Single step process to form crystallised HA Cost dependent on particle morphology	[55, 178-181, 183-186]
Emulsion and micro-emulsion	Droplets of immiscible liquids react in a heterogeneous mixture	> 1.0 (emulsion) > 0.005 (micro)	>	RT - 50	163%	Low - medium	Porous particles can be formed High temperature calcination and sintering steps required Highly dependent on oil and surfactants used	[174-177]
Sol-gel	'Sol' solution is formed that evolves into a gel system; a mixture of particles and a polymer network	> 0.001	>	37 – 85	120 – 180%	Low	Molecular mixing improves chemical homogeneity Involves more than 3 processing steps HA prepared exhibits inferior crystallinity and thermal stability	[169-171]
SPCS	Particles formed via temperature induced combustion of a fuel and oxidiser in solution	> 0.45	<	170 – 500	118 – 136%	Unknown	Reaction time <20 minutes Uncontrollable high temperature front can lead to mixed phases Particle morphology dependent on fuel used	[187-189]

2.12.2 Aqueous precipitation (AP)

AP methods are the most common technique used to produce HA due to the use of relatively cheap raw materials, compared with reagents used in other synthesis methods. Low reaction temperatures also incur minimal operating costs [190, 191]. However, AP reactions cannot be regarded as trivial due to the simultaneous occurrence of crystal nucleation, growth, and coarsening and/or agglomeration. These underlying scientific mechanisms are not easy to differentiate and as a result reproducibility as well as the control of particle flocculation remain common factors for improvement [3, 192, 193]. The sensitivity of phosphates and the need to fine tune the experimental conditions (e.g. pH, temperature) of AP reactions is reflected in the literature by the ranging phase purity, particle morphologies as well as sizes, crystallinity, stoichiometry and thermal stability. Despite the shortcomings of AP methods, the potential to produce HA containing various ionic substitutions and its high scalability make it an attractive methodology, particularly for industrial scale production [11].

During the precipitation process specific stoichiometric solutions containing Ca and P ions are molecularly mixed. In order to transform into a suspension of precipitates solution supersaturation must be established. Supersaturation is the driving force of crystallisation and is defined as the difference between actual concentration and the solubility concentration. Once established, ions randomly assemble together forming a molecule that serves as a nucleus for further growth, this process is referred to as nucleation. When the size of the nuclei reaches a critical size grain growth occurs.

Equations 2.1 and 2.2 describe the two most common reagent combinations used in the precipitation of HA: (1) calcium hydroxide and phosphoric acid, and (2) calcium nitrate with ammonium phosphate dibasic and ammonium hydroxide, respectively. Since the only by-product of the first reaction is water and the system contains no foreign elements, generally this reaction is favoured for industrial use [12]. Nonetheless, it has been reported that it is challenging to obtain stoichiometric HA by this method, which may result in the formation of other phases after sintering [194].

$$10Ca(OH)_2 + H_3PO_4 \rightarrow Ca_{10}(PO_4)_6(OH_2) + 18H_2O \quad (2.1)$$

$$10Ca(NO_3)_2 + 6(NH_4)_2HPO_4 + 8NH_4OH \rightarrow Ca_{10}(PO_4)_6(OH)_2 + 6H_2O + 20NH_4NO_3 \quad (2.2)$$

In an effort to optimise the precipitation of stoichiometric HA the influence of a number of reaction parameters have been investigated (Table 2.7). Fundamentally, the solubility of most CaPs, including HA are inversely proportional to pH (Figure 2.7). Other authors have reported the precipitation of HA between pH levels of 7.5 and 12.5. It is important to note the influence of pH on the relative concentration of a number of Ca and P ions in solution (Figure 2.10).

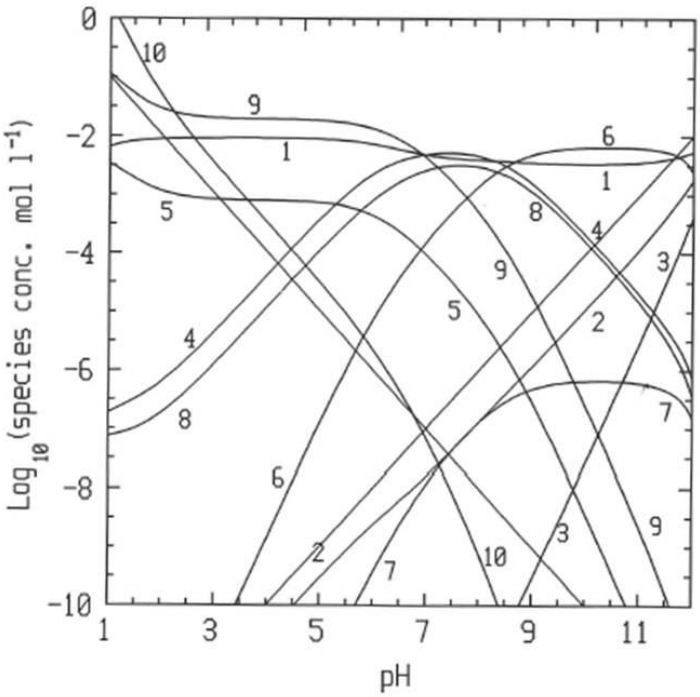

Figure 2.10: Speciation diagram for the $Ca(OH)_2$-H_3PO_4-H_2O system at 37°C (1) Ca^{2+}, (2) $[CaOH]^+$, (3) $[Ca(OH)_2]^0$, (4) $[CaHPO_4]^0$, (5) $[CaH_2PO_4]^+$, (6) $[CaPO_4]^-$, (7) PO_4^{3-}, (8) HPO_4^{2-}, (9) $H_2PO_4^-$, and (10) H_3PO_4. Total Ca concentration is 10mol l^{-1} [17]

Generally, CaPs exhibit an inverse solubility relationship with temperature. Figure 2.11 illustrates a typical solubility diagram for a soluble salt of inverse solubility where equilibrium is represented by the solid line and A represents an equilibrium point. Deviation from equilibrium conditions isothermally (AB), by increasing temperature (AC), or varying both temperature and concentration (AD) may result in metastability. Metastable phases can return to equilibrium; however there is a limit to the extent of deviation defined as the labile region. Precipitation of HA of various degrees of crystallinity and crystallite sizes between temperatures of 15 and 99°C have been reported (Table 2.7).

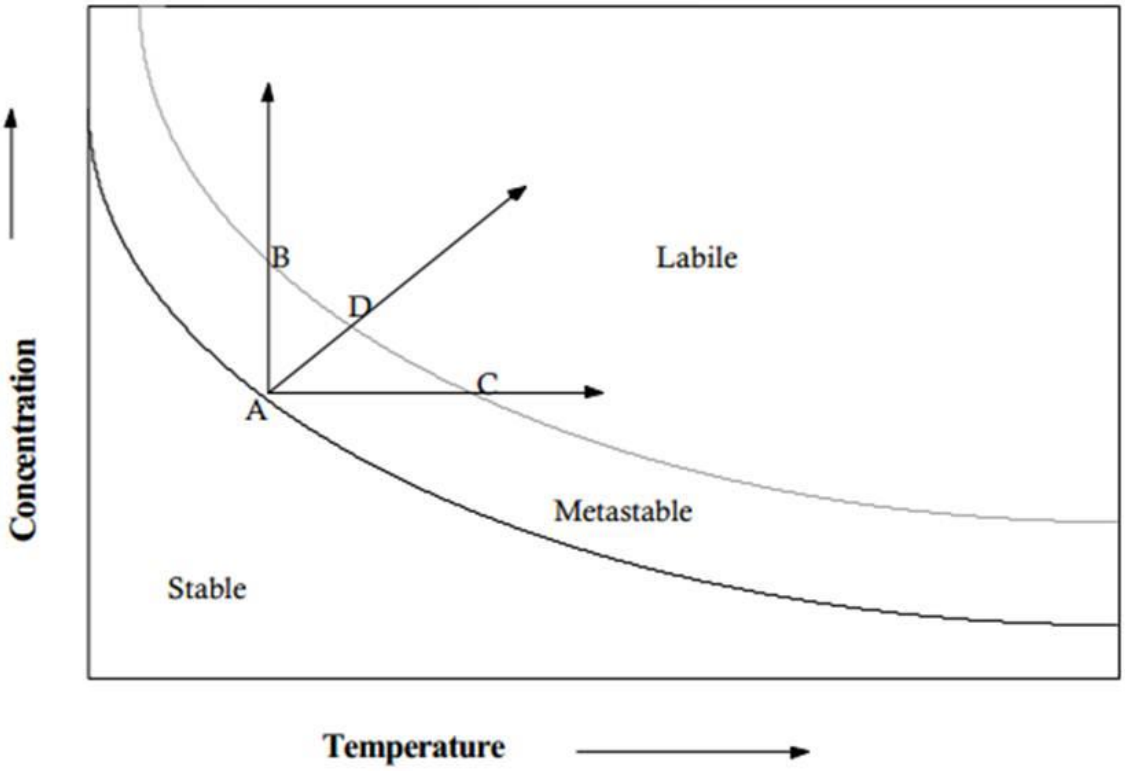

Figure 2.11: Solubility diagram of a soluble salt with inverse solubility [195]

The Ca and P ion concentrations within solution determine the relative degree of the supersaturation of ionic species (e.g. Figure 2.10). At high concentration levels precipitation may occur spontaneously and this can result in the formation of an unstable precursor phase. Composition of this phase is dependent on reaction conditions, at pH>7 ACP is usually formed and DCPD forms under acidic conditions [196-199].

A number of expensive surfactants (e.g. cetyltrimethylammonium bromide) and dispersants, such as polyethylene glycol have been investigated with the aim of reducing particle agglomeration that occurs if surface charges are not great enough to repel neighbouring particles [200-202]. Moreover, alternative solvents to DI water, such as ethanol have been investigated (Table 2.7).

To accelerate the process of crystallisation, commonly ageing and heat treatment protocols are employed to precipitated HA, which typically exhibits low crystallinity [121]. These treatments, in turn, may result in exaggerated crystal growth, changes in density and composition, increased microstructural coarseness, reduced mechanical strength and can also be accompanied by morphological changes [203, 204].

Table 2.7: Summary of reaction parameters reported to be influential in the AP of HA

Reaction parameter	Reported to influence	Reported range	Comment(s)	Reference(s)
pH	Phase	7.5 – 12.5	Generally CaPs exhibit a decrease in solubility with increasing pH OH^- presence in basic pH favours the precipitation of hydroxylated CaP, such as HA HA least soluble phase above pH 4.5	[12, 15, 165, 205-208]
Reaction temperature	Crystallinity, crystallite size and morphology	15 – 99°C	HA exhibits inverse temperature solubility relationship Higher temperatures lead to increased reaction energy resulting in improved crystallinity once these energies are overcome Temperature influences rate of reaction Morphology reported to vary from needle-like to acicular with increasing temperature	[15, 167, 191, 207, 209]
Concentration of reagents	Crystallinity, crystallite and particle size	0.0006 – 0.41M	Increasing reagent concentrations leads to increased supersaturation of solution leading to improved long range order and larger crystals due to prolonged growth	[165, 210]
Solvent	Particle size	N/A	Ethanol reported to effect supersaturation causing particles to grow more quickly	[166]
Surfactants or dispersant	Particle size	N/A	Dispersants are generally charged molecules that attach to particles causing them to repel each other, which has been reported to reduce agglomeration and thus resultant particle sizes of HA Surfactants lower surface tension and may be used as a dispersant to reduce particle agglomeration	[165, 166]
Heat treatment protocol	Crystallinity, particle size	600 – 1250°C	Calcination and sintering leads to improvement in crystallinity and particle coalescence due to an associated reduction of the specific surface area Post-sintered composition greatly influenced by initial Ca:P ratio Stoichiometric HA stable up to 1250°C	[157, 190, 204, 205, 207, 211, 212]

2.12.3 Hydrothermal and solvothermal techniques

Many current synthesis methods of HA are considered too slow and the reaction kinetics difficult to control. Hydrothermal and solvothermal techniques offer a solution to overcome these problems as inorganic nanomaterials can be produced rapidly in a single step and enable a higher degree of control [213, 214].

Hydrothermal and solvothermal processing involve the use of a solvent, which is heated in a sealed vessel. If the solvent used is water the process is defined as hydrothermal synthesis, which is more common than solvothermal methods to produce HA [215]. The temperature of the solvent can be brought above its boiling point since the autogeneous pressure within the vessel exceeds the ambient pressure meaning that experimental variables can be controlled to a higher degree because the solubility and reactivity is increased. This results in a more predictable and thus reproducible reaction. In general, reaction temperatures and times, pH, solvent choice, additives, as well as vessel geometries are parameters that can be readily altered to control the resultant particle size and morphology [3].

Both of these methods are considered environmentally friendly due to the substantially lower reaction temperatures used compared with other techniques, such as solid-state synthesis (Table 2.6). Furthermore, since it is possible to directly form crystalline HA by hydrothermal or solvothermal techniques post-synthesis high temperature treatment, commonly used in other low temperature methods (e.g. AP and sol-gel), may be avoided. Relatively low cost precursor reagents and short reactions times have been reported for these processes [14-18, 21-24]. Despite these inherent advantages, the scalability of these techniques is limited primarily due to the size of the reaction vessel. Selection of appropriate surfactants and solvents require tweaking to optimise this process.

2.12.4 Emulsion and microemulsion techniques

Emulsions can be described as heterogeneous mixtures of at least one immiscible liquid dispersed in another in the form of droplets [175]. These systems are often described as water-in-oil (W/O) or oil-in-water (O/W), and the first phase indicated is dispersed. Generally, O/W systems are used to produce HA. Depending on the size of the aqueous drops (i.e. the size of the reaction domains) this technique can be referred to as an emulsion or microemulsion. Typically, the droplet diameter is 10 – 100nm for

microemulsion and >0.1μm for emulsions. A reaction takes place when two different droplets containing the reactants collide with each other. Nano and micron sized particles of HA have been formed by microemulsion and emulsion techniques, respectively [174-177]. A reported benefit of producing HA by microemulsion methods, compared with emulsion techniques is a reduction in the level of agglomeration [176].

2.12.5 Sol-gel processing

Sol-gel techniques have attracted much attention due to the associated inherent advantages of this method: homogeneous molecular mixing, low processing temperature (<400°C), and the ability to generate nanosized particles. However, the energy saving gained from the low temperatures used is offset by the high cost of the reactants, typically alkoxides and organometallics. Furthermore, in comparison to other low temperature methods, sol-gel techniques have very limited scalability due to the sensitivity of the process to numerous reaction conditions (e.g. hydrolysation and mixing time). If the process is not optimised large fractions of other CaPs, such as β-TCP may be produced [216].

The first stage of this process is to form a 'sol', which is defined as a dispersion of solid particles, otherwise known as colloids in a liquid. This is achieved by mechanically mixing precursor materials (e.g. calcium nitrate and ammonium phosphate) in a solvent at a pH that prevents precipitation. Hydrolysis and polycondensation reactions occur by linking monomer units and forming bonds within the sol. This process, referred to as gelation causes the viscosity of the sol to increase. The result is a 'gel', which can be defined as a diphasic system consisting of solid and interstitial liquid phases. Forming a gel without flocculation can be difficult. The gel is then dried to remove the liquid phase, which is usually accompanied by shrinkage and densification. Lastly, a sintering protocol is employed.

2.12.6 Self-propagating combustion synthesis (SPCS)

SPCS was first reported in the 1980s and since then has attracted much attention due to the ability to rapidly produce nanomaterials at relatively low energies. Conventionally SPCS is performed in a solid state but it can also be accomplished in a solution. The success of the formation of HA by solution based SPCS is dependent on the homogeneous molecular mixing of a suitable fuel with an oxidising agent in an

aqueous medium containing calcium and phosphate ions. Increasing the temperature of this solution initiates a vigorous exothermic redox reaction between the fuel and oxidiser, which causes the gaseous products to spontaneously combust. It is this high local temperature reaction front that causes the formation of a solid powder as it propagates through the sample. Depending on the reagents used, the ignition temperature of this redox reaction is typically 170 – 500°C and full combustion can occur in a matter of minutes (Table 2.6).

The heat energy evolved from the reaction is dependent on the fuel used as well as the ratio of fuel to oxidiser. Citric, tartaric and succinic acids as well as urea, sucrose and glycine have all been used as fuels to form HA by solution SPCS processes [188, 189]. Generally, nitric acid is used as the oxidising agent. Variation of these parameters has been reported to result in the formation of different CaP phases and/or particle morphologies [188, 189]. Depending on the fuel used the HA formed can either be crystalline or amorphous. Nevertheless, SPCS products typically require calcining to remove organic residues and reactions that result in amorphous or low crystallinity products may also need to be sintered.

Viability of using this method on a large scale to produce HA is uncertain, as insufficient work has been carried out to determine the sensitivity of SPCS processes to reaction parameters that are recognised as influential, such as the fuel to oxidiser ratio.

2.13 Thermal behaviour

It is well known that heat treatment protocols, including calcination and sintering can be used to improve the crystallinity of apatites [157, 190, 204, 205, 207, 211, 212]. During such processes high temperature phase changes can also occur as a result of non-stoichiometry or crystal imperfections.

Specifically, DCPD is known to lose its water of crystallisation slowly at ambient temperatures and at 180°C DCPA may form according to Equation 2.3 [217]. Further heating of DCPA yields β-calcium pyrophosphate ($Ca_2P_2O_7$) between 320 and 340°C (Equation 2.4) [217, 218].

$$CaHPO_4 \cdot 2H_2O \rightarrow CaHPO_4 + 2H_2O \quad (2.3)$$

$$2HPO_4^{2-} \rightarrow P_2O_7^{4-} + H_2O \quad (2.4)$$

It is possible that non-stoichiometric HA (i.e. CDHA) may exhibit lattice substitutions of non-apatitic HPO_4^{2-}, for example in the model of $Ca_{10-x}(HPO_4)_x(PO_4)_{6-x}(OH)_{2-x}$ (Table 2.5). Any presence of acid phosphate ions may result in the formation of β-$Ca_2P_2O_7$ according to Equation 2.4, which has been reported to occur slowly between 250 and 700°C [219]. Between 700 to 800°C any formed β-$Ca_2P_2O_7$ can convert to HA and β-TCP according to Equation 2.5 [219].

$$Ca_{10-x}(P_2O_7)_x(PO_4)_{6-2x}(OH)_2 \rightarrow (1-x)Ca_{10}(PO_4)_6(OH)_2 + 3xCa_3(PO_4)_3 + xH_2O$$

$$\text{i.e. } P_2O_7^{4-} + 2OH^- \rightarrow 2PO_4^{3-} + H_2O \quad (2.5)$$

Figure 2.12 illustrates the influence of the Ca:P ratio on the high temperature thermal stability of HA formed via Equation 2.1. This diagram highlights that stoichiometric HA (i.e. Ca:P = 1.67) is thermodynamically stable up to 1250°C. The transformation of calcium proficient HA (Ca:P > 1.67) to HA and CaO above 850°C, and CDHA to HA and TCP above 650°C are also demonstrated. Notably, in-vivo degradation would be increased by the presence of either TCP or CaO phases since they are both less stable than HA under physiological conditions.

Part three - fabrication of bone tissue scaffolds

2.14 Physical biomimetics

Tissue engineered scaffolds are a viable clinical solution to bone defects caused by disease or trauma (section 2.6.2.1). The concept of chemical biomimetics was introduced in section 2.7, i.e. the scaffold structure should chemically mimic the host tissue. In addition there are also a number of key physical features of bone (section

2.3.1) that an ideal scaffold should exhibit in order to be a successful component of the tissue engineering strategy.

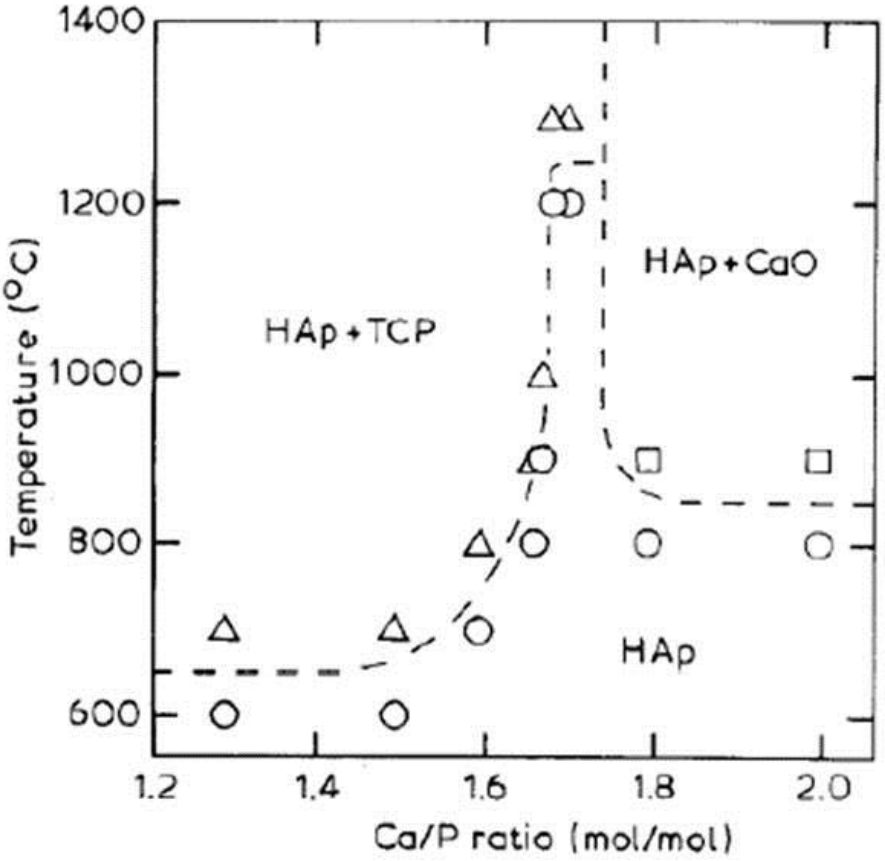

Figure 2.12: Pseudo-phase diagram showing the thermal stability of HA (HAp) [220]

Broadly, scaffold fabrication methods can be grouped as conventional or additive layer manufacturing (ALM) techniques. Notably, ALM is also referred to as rapid prototyping in the literature. As well as bearing in mind the physiochemical criteria, in general the fabrication method should adhere to: (1) does not adversely affect the chemical composition, mechanical properties or cytocompatibility of the material, (2) the technique should be accurate so pore size and morphology can be defined by the user, and (3) minimal variation in physical form between batches (i.e. consistency) [221]. Typical properties of bone scaffolds fabricated by common techniques are summarised in comparison to bone in Table 2.8.

Table 2.8: Comparison of common conventional and ALM techniques used to fabricate bone tissue scaffolds
[a]high = majority of pores interconnected, medium = pores mostly connected, low = few interconnections

Technique	Method	Material(s)	Pore size (μm)	Porosity (%)	Interconnectivity (High, medium, low)[a]	Compressive strength (MPa)	References
N/A	Bone	Composite of organic matrix and inorganic calcium phosphate crystals	1 – 3500	50 – 90	High	0.15 – 230	[63, 222]
Conventional	Solvent casting	Ceramics, polymers	1 – 800	40 – 93	Medium (dependent on salt particles touching)	≤9.3	[223-225]
	Freeze casting	Ceramics, glass-ceramics, polymers	1 – 200	31 – 95	Medium (dependent on temperature gradient achieved during solidification of slurry)	2 – 36	[22, 226, 227]
	Sol-gel techniques	Ceramics, polymers, glasses composites	0.001 – 1000	50 – 88	Medium	2 – 20	[228-231]
	Foam reticulation	Ceramics, glasses, metals	20 – 1000	30 - 98	High (dependent on foam and slurry infiltration)	0.1 – 32.6	[232, 233]
	Gelcasting	Ceramics, polymers, composites	20 – 1000	< 90	Low	4.4 – 32.6	[234, 235]
ALM	Stereolithography	Ceramics, polymers, hydrogels, composites	Features: > 2 Layers: > 1	30 – 80 (defined by CAD model)	Defined by CAD model	1.3 – 30	[236-239]
	Selective laser sintering	Ceramics, polymers, composites	Features: >45 Layers: >76			2 – 50	[240-243]
	3D printing		Features: >45 Layers: >20			16.1 – 31	[244, 245]
	Fused deposition modelling		Features: >260 Layers: >250			2.6 – 15	[246, 247]

2.15 Conventional techniques

Scaffolds of complex shapes with a range of process dependent porosities from 30 – 98% can be produced by conventional techniques (Table 2.8). In contrast to ALM technologies, conventional processes require small capital input but typically scaffolds made using these techniques perform poorly mechanically in comparison to native bone. Reproducibility is another issue associated with these methods due to the inability to precisely control scaffold characteristics, such as pore size, pore interconnectivity and spatial distribution of pores [248, 249]. Conventionally fabricated constructs commonly fail to meet the demand to create highly porous networks necessary for cell growth, flow of nutrients and metabolic waste [23]. Often, these techniques also require the use of organic solvents, such as chloroform, which if any residues remain in the structure may be toxic and/or carcinogenic to cells.

2.15.1 Solvent casting

Solvent casting, otherwise known as particulate leaching is a widely used method for the preparation of scaffolds at RT. The structure is produced by casting a solution of the biomaterial into a mould containing an insoluble porogen (e.g. salt crystals) using either traditional or freeze casting. The final porous network is formed by leaching out the porogen using an appropriate solvent. Resultant pores are dependent on the morphology and size of the porogen and the porosity is reliant on the ratio of porogen to biomaterial.

Although a popular technique, notable disadvantages are the common use of highly toxic solvents, potential crystal deposition, and difficulty in ensuring a homogeneous distribution of interconnected pores.

2.15.2 Freeze casting

This technique, otherwise known as freeze drying, is dependent on the thermally induced separation of a biomaterial slurry. Scaffolding material(s) are mixed with an organic monomer, and both synthetic and natural polymers have been reported [250, 251]. A dispersant may be required and porogens can be used to increase porosity and induce microporosity [252]. The final solution is cast into a precooled mould and the initial green body is freeze dried to induce separation of phases. Once stabilised sublimation can be used to remove the solvent phase and the resultant foam structure

may then be post processed, for example sintering. Similar to scaffolds fabricated by other conventional techniques, freeze cast constructs generally lack mechanical stability. Commonly pores produced are less than 100μm in diameter, which can limit cell ingrowth (Table 2.4). Notably, it is possible to produce highly directional pores by this method [22].

2.15.3 Sol-gel techniques

The principal of the sol-gel process was previously described in section 2.12.5. In order to use this technique to form a scaffold the sol must be cast into a mould before gelation occurs. The gel is then immersed in a liquid and allowed to age until it has developed sufficient strength to resist cracking during the drying phase. The interstitial liquid of the gel is removed during the drying stage to form a porous scaffold and is finally dehydrated as well as chemically stabilised before sintering. Fabrication of nanoscale pores has been reported using this method and porosities as high as, for example 88% [231], have been produced using this technique [253]. The disadvantages of this technique, as mentioned previously, are the high costs of reagents and the difficulty of forming a gel without flocculation.

2.15.4 Foam reticulation methods

The foam reticulation technique is a common method for fabricating open-cell porous ceramics and has been adopted by many to form highly porous (≤98%) scaffold structures [232, 254-256]. This method is performed by impregnating porous open celled foams with a desired biomaterial slurry. Generally, the scaffolding material is dissolved in a solvent with an appropriate binder under stirring conditions to produce the slurry and a dispersant can be added to improve homogeneity. The foam is soaked in the slurry, dried and then burnt out leaving behind the porous scaffold by the process of consolidation achieved by sintering.

Scaffolds with highly interconnected pores (99.9%) and complex architectures have been manufactured by this method from a range of synthetic and natural sponge structures [233, 257]. However, sourcing foams with the correct pore structures to meet the clinical need remains a challenge. More critically, due to the isotropic nature of manufactured polymer sponges the pore size distribution is usually very small, typically at most 200μm. Mechanical strength can also be an issue since the struts formed are hollow and microcracks may develop during sintering resulting in

structural defects. In order to obtain scaffolds with an acceptable strength by this method sintering rate, stirring time, and the concentration of the biomaterial in the initial slurry must be optimised [254].

2.15.5 Gelcasting

Gelcasting was traditionally used for the fabrication of dense ceramics. However, due to the ability to produce a homogeneous structure this method has more recently been used to produce porous (<90%) parts [258, 259]. The process begins with the formation of a slurry containing the scaffolding materials, dispersant, organic monomer binder, and cross-linking agents. This suspension is foamed by adding surfactants, which reduce particle surface energy and generate stable bubbles [260]. Prior to initiation of the polymerisation reaction the solution is casted into a mould. Gelation of the foamed suspension causes particle consolidation, immobilising the scaffolding material in the shape of the mould. Commonly a chemical initiator and/or catalyst are used to initiate the polymerisation process [235]. Finally, the part is unmoulded and dried to obtain a green body, which requires heat treatment to burn out the binder.

Despite high levels of porosity being achieved by this technique typically pores are poorly interconnected with non-uniform size distribution as a result of the volatility of the formed foam. Furthermore, during the gelation and drying stages inner stresses in the mould as well as microcracks can be induced, which may adversely affect mechanical strength.

2.16 ALM techniques

There are a variety of ALM systems that are based on computer aided design (CAD) and manufacture (CAM). These techniques were first used for biomedical applications in the 1990s and can be categorised into three groups: (1) laser, (2) print or ‘ink’, and (3) nozzle systems (Figure 2.13). ALM processes can begin with data generated from a scan (CT or MRI) of the patient, a model created from 3D object digitising systems, or a CAD model, which is converted into stereolithography format that uses triangular facets to represent the surface of the structure. 2D cross sections of the file are then numerically produced and fabricated layer by layer. Desired levels of hierarchical complexity can be built into the part, which is advantageous when trying to mimic the

physical structure of bone. Material composition may also be regulated and in the most advanced ALM systems multiple constituents can be used.

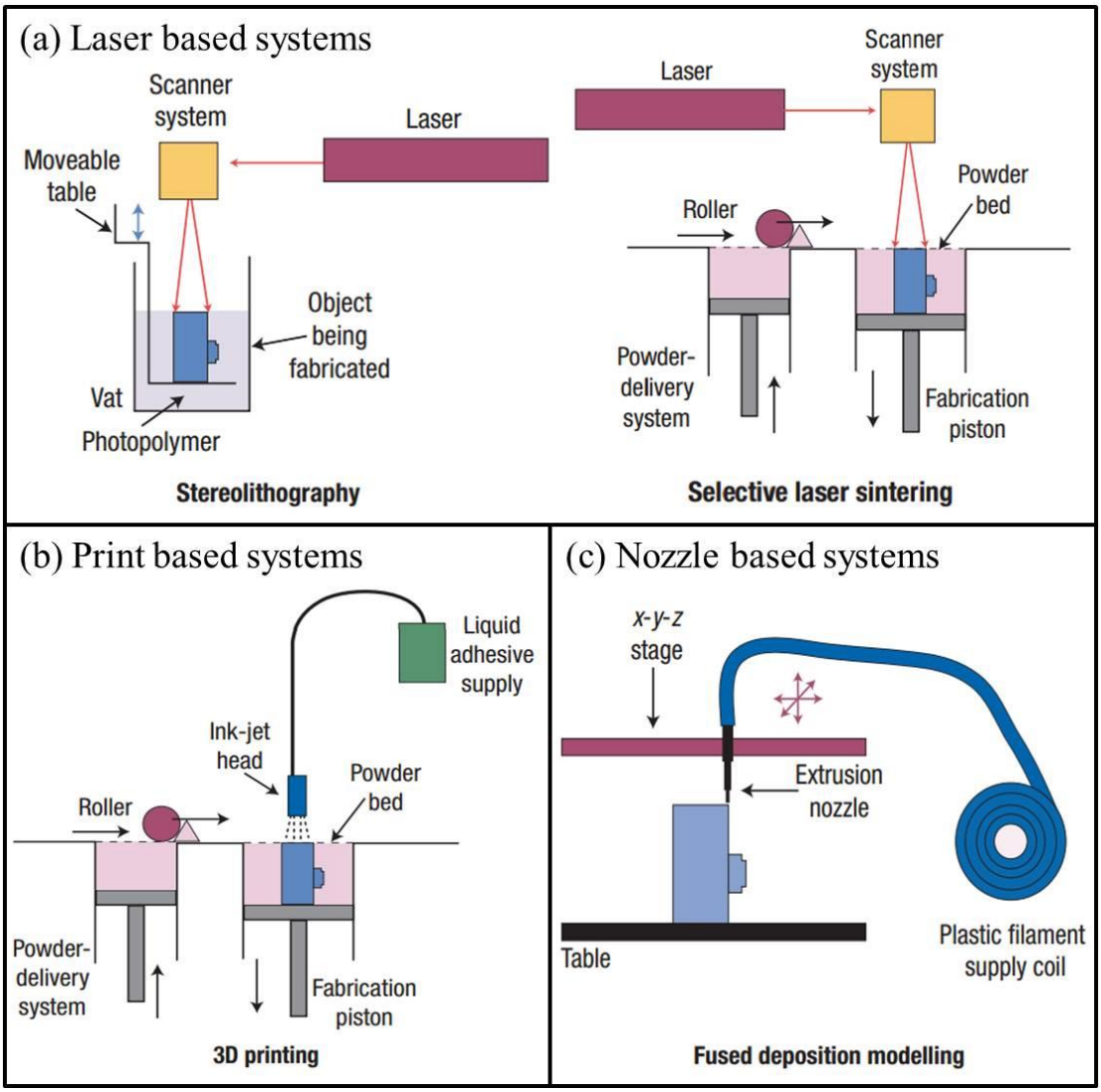

Figure 2.13: ALM systems (a) laser, (b) print, and (c) nozzle adapted from [261]

ALM techniques overcome many of the common limitations of conventional methods, such as lack of geometry control, poor reproducibility and inability to readily customise products. Several also operate without the use of organic solvents. Generally, ALM systems reduce design constraints, enable rapid fabrication of complex structures and reduce manual interaction. Due to the higher level of structural control it is also possible to produce scaffolds with superior mechanical properties in comparison to conventionally manufactured counterparts (Table 2.8). Furthermore, improved bone regeneration has been reported for these designer structures, which has been attributed to a higher degree of interconnectivity [261].

Despite the potential of these processes there are still a number of challenges that need to be addressed. Since each ALM system requires a specific input form (powder, filament, solution) this limits the range of materials that can be used for individual techniques. Processing temperatures may also limit material selection. Surface properties influence cell-scaffold interactions (section 2.6.2), although powder based ALM systems produce rough surfaces, others create structures with a smooth surface that can hinder cell adhesion. Post surface modifications or coating may therefore be required [249]. There are also some inherent disadvantages of ALM systems: resolution is restricted by machine specific parameters, loose powder or liquid can become trapped in internal holes, and the sterility of commercial ALM systems is questionable [262]. Table 2.9 summarises the characteristic resolution, advantages and disadvantages of common ALM systems used to fabricate bone tissue scaffolds.

2.16.1 Laser based ALM systems

2.16.1.1 Stereolithography (SLA)

The ability of photopolymers to solidify when irradiated with an energy source of a specific wavelength is utilised in the SLA process. The part is built up on a table moveable along the y-axis and contained in a vat filled with liquid photopolymer resin. The low molecular weight resins undergo chain reaction to form solid long chain polymers when initiated by a laser, commonly UV. Once the first layer of the structure has been solidified the table is lowered by one cross-sectional thickness and is recoated with liquid photopolymer. This process is repeated layer-by-layer until the full structure is formed. The part is then removed, cleaned and fully cured in a UV oven. The common spot size used in SLA is approximately 250μm but research is currently being conducted on small-spot systems that enable layers of less than 1μm and a resolution finer than 10μm (Table 2.9).

The direct use of bioceramics, such as HA in SLA have been investigated [263]. Generally, the ceramic is mixed with the photopolymer prior to fabrication and the green part is heat treated to remove the polymer as well as sinter the ceramic. Alternatively, ceramic parts can be made indirectly by creating an initial polymer mould [264].

Table 2.9: Comparison of ALM techniques commonly used to fabricate bone tissue scaffolds

ALM system	ALM process	Resolution (elements/mm^3)		Advantages	Disadvantages
		Present	Ultimate		
Laser	SLA	3152	13300000	Established technology High layer fabrication speed capacity High resolution capacity Low imaging specific energy Relatively easy to remove support material Relatively easy to achieve small features	Complex process Requires support Limited to photopolymerisable materials Material creep Expensive materials
	SLS	211	244000	No support required Very little waste material Large number of possible materials Relatively higher part strength Cheap	High imaging specific energy High processing temperature Separate curing step required for some materials Biodegradable materials may degrade in chamber
Print	3DP	1900	244000	Range of materials can be used Self-supporting Low imaging specific energy Minimal heating effect on materials Cost efficient	Low green part strength Post processing may be required De-powdering can be difficult Powder can become trapped inside the part Mechanical anisotropy
Nozzle	FDM	15200	157000	Low material cost Waste material limited to the support material; no material trapped Low imaging specific energy Multiple materials possible in same object or layer	Poor surface finish and grainy appearance Thermoplastic polymer required Limited to materials with low melting point High processing temperatures Mechanical anisotropy

2.16.1.2 Selective laser sintering (SLS)

During the SLS process a laser is passed over powdered material, which raises the local surface to the glass transition temperature resulting in the fusion of neighbouring particles in the working layer and those in the layer below. Generally, IR lasers are used due to their high power density. The build platform is then lowered by the thickness of one layer and a counter-rotating roller applies a new coat of powder on top. Typically, the powder particles used are 80 – 120μm in size and the estimated overall resolution of the technique is 24400elements/mm^3 when a minimum energy laser beam of 16μm diameter is used [265].

Limitations of SLS include the power of the laser and the thermal diffusion of the material, specifically the glass transition temperature must be considered. Despite exhibiting lower dimensional accuracy and porosity in comparison to SLA parts, scaffolds produced by SLS have an inherent advantage since they do not require high temperature post processing. If a ceramic part is to be produced it must be mixed with a polymer that acts as a low melting point binder, which may need to be burnt out after fabrication if it is not biocompatible. Furthermore, since powdered stock materials are used the surface of SLS parts is much rougher and this is considered as advantageous for adhesion of osteoblasts [21].

2.16.2 Print based ALM systems

2.16.2.1 3D printing (3DP)

3DP employs inkjet technology to process powdered materials. Stock material(s) in powdered form are compacted into the powder bed and then a counter-rotating roller spreads a user defined thickness onto a building bed. Liquid binder is propelled onto the powder by a printer head causing adjacent particles of the same and neighbouring layers to bind together. Powder that does not form part of the structure acts as a support during building and must be removed once the final part has dried. Ceramic parts may require sintering after printing. Typically, this procedure is performed at RT.

The minimum resolution of a characteristic 3D printer is 1900elements/mm^3, which is limited by the powder particle size and the adhesive. A number of raw material characteristics (e.g. morphology, particle size distribution, bulk and tapped density, and specific surface area) affect the flowability and wettability of precursor powders,

which are crucial in defining the printability of 3DP systems [266]. Therefore appropriate materials must be selected or created for the 3D printer.

It is essential that the powdered material used has an ability to flow to enable adequate recoating of the part by the counter-rotating roller during layer-based manufacture. Particle size, morphology, and density have been reported to be critical factors in determining powder flowability [266, 267]. A high level of flowability contributes towards an improvement in the resolution of the final part and vice versa. However, if the flowability is too high the powder bed can become unstable. Currently, flowability is typically measured using simple funnel methods, either adopting the approach of measuring the time taken for an amount of powder to exit a defined funnel (ISO 6186) or by calculating the angle of repose by measuring the height of a powder pyramid (ISO 4324). The faster the time to exit the funnel or the smaller the angle of repose the more flowable the powder. More complex alternative methods have also been used, for example Schulze suggested using a ring shear tester [268]. Due to the difficulty involved in experimentally estimating flowability there is on-going research in this area [269].

Wettability of the powder particles by the binder solution is another crucial factor as it influences both resolution and mechanical strength of the 3D printed part. There are a number of parameters that influence powder wetting, including the contact angle between binder solution and powder, binder viscosity, topography of the powder bed surface (which itself is dependent on particle shape and size), and any chemical reactions between the binder and powder [270]. The ballistic and dynamic impacts of binder drops at a high speed on a loose powder bed are complex and difficult to analyse [266]. Powder bed stability has been defined as the capacity of the bed to withstand ballistic impact or deposition of a new powder layer [266]. Binder drop size is a highly critical factor since it determines the ballistic impact on the bed.

Good cell-biomaterial interactions have been reported for 3D printed parts due to the inherent roughness created because of imperfect packing efficiency (i.e.<1) [271, 272]. Numerous authors have reported the fabrication of porous CaP structures by 3DP [273]. Pure CaP powders, for example α- and β-TCP [266], TTCP [274], and HA [275] as well as composites of CaPs mixed with organic polymers, such as poly(L-lactide-co-glycolide)-copolymer (PLGA) [276], have been utilised as stock materials. Material combinations that require the use of organic solvents as a binder, for example

PLGA and β-TCP binded with chloroform [276], have an inherent disadvantage as complete removal of the solvent is rather difficult due to the inherent porosity of 3D printed structures. Despite the numerous studies that have been published on the 3DP of CaPs there is still a need for new biocompatible powder-binder systems that enable accurate printing of porous ceramic scaffolds with sufficient mechanical strength [274].

2.16.3 Nozzle based ALM systems

2.16.3.1 Fused deposition modelling (FDM)

FDM uses a temperature controlled extruder to feed filaments of semi molten thermoplastic into a nozzle, which deposits onto a working area in a continuous strand. This causes the material of the previous layer to soften and solidify as one piece. The polymer is heated slightly above its melting point meaning that there is only a small window where it remains molten. A soluble wax, can be used to fill up any unfilled areas to act as a support during building and is dissolved post fabrication. Typical FDM machines have a droplet diameter of 50μm, which corresponds to a resolution of 15200elements/mm^3. FDM has been used to create pure polymer scaffolds as well as polymer-ceramic composites [246, 247, 277, 278].

2.17 Summary

The physical structure and chemical composition of bone was reviewed in this chapter, and can be summarised as a hierarchical arrangement of organic and inorganic components at different length scales. Specifically, bone mineral is a multi-substituted calcium deficient carbonated apatite. It is this crystal structure as well as nanosized crystallites that are responsible for the reactivity of this biological apatite phase.

A clinical strategy that can be used to replace or repair bone is the use of a construct referred to as a scaffold, which ideally should emulate the chemical composition and physical structure of the native tissue. In relation to the above idea a group of materials, namely CaPs, were reviewed due to their chemical and crystallographic similarity to native bone mineral, as well as their reported bioactive and osteoconductive behaviour. Common conventional and ALM techniques used to

fabricate ceramic scaffolds were described and compared to a number of physical properties of bone that are known to be crucial to the success of the implant.

HA was highlighted as a candidate material since it exhibits an apatitic structure that is capable of incorporating ionic substitutions that play key roles in the response of bone cells. Synthesis techniques were reviewed and the low cost as well as high scalability of AP methods were highlighted. Chapter 3 outlines the criteria and presents the experimental procedures used to select a methodology to prepare HA. The following work concerning HA synthesis explores the influence of a number of reaction parameters reported in this chapter to determine key material properties, such as phase, particle size, and crystallinity.

ALM systems were emphasised as promising fabrication methods since they overcome many of the common issues associated with conventional techniques, such as lack of pore interconnectivity. Specifically, the inherent ability to produce scaffolds with a rough surface via 3DP is advantageous since this may improve osteointegration. The feasibility of producing HA scaffolds that exhibit features highlighted to be vital to the success of bone implants was experimentally investigated (Chapters 7 and 8). Risks associated with the use of organic solvents in conventional fabrication methods were also emphasised in the literature. In an effort to address this issue the viability of using yeast as a natural pore forming agent in a novel non-aqueous salt leaching technique was studied in Chapter 7.

Chapter 3

Feasibility study – hydroxyapatite synthesis

3. Feasibility study - hydroxyapatite synthesis

3.1 Synthesis methodology selection

Native bone apatite is chemically and crystallographically similar to HA. Common methodologies to synthesise synthetic apatites, such as HA, were reviewed in section 2.12. To investigate the feasibility of a number of selected techniques to produce phase pure HA each procedure was rated according to a defined selection criteria.

It is known that osteoblasts proliferate up to 60% more when exposed to nHA in comparison to micron-sized equivalents [279]. Guo et al. reported a significantly higher cell density on nHA after 90min incubation of osteoblasts. The authors concluded that these materials not only promote cell adhesion, attachment and spreading but also improve long-term cell proliferation and differentiation in comparison to micron HA [280]. Therefore, the ability of the reviewed synthesis methods to produce HA with a particle size less than 1μm shall be a product criterion. The degree of crystallinity of HA has also been reported to influence the adhesion of osteoblasts [281]. Hence the synthesis method should ideally enable a degree of control of crystallinity in order to ensure crystallographic similarly to native apatite, known to exhibit a large amorphous fraction. Additionally, the selected techniques should also have the potential to alter the stoichiometry of HA by substitution of elements that naturally occur in bone mineral so as to emulate the native crystallographic structure and reactivity more closely. Table 2.1 presents a summary of the composition of bone apatite in comparison to stoichiometric HA. It is important here to consider the scalability of each synthesis technique to ensure a suitable amount of product can be produced for the fabrication of 3D bone tissue scaffolds.

Besides the product criteria discussed above, the efficiency of each synthesis method was also considered, namely in relation to energy (i.e. reaction temperature) and time (i.e. processing time). In summary, the product criteria used to select feasible techniques were defined as: (1) phase pure HA, (2) particle size <1μm, (3) degree of

control of crystallinity, (4) ability to alter stoichiometry by substituting naturally occurring ionic species into the HA structure, and (5) ease of process scalability.

Each of the synthesis methods described in section 2.12 was rated according to the product criteria outlined above and the results presented in a weighted matrix (Table 3.1). The efficiency of all the methods that met the product criteria were also considered and ranked. Three synthesis methods met all of the product criteria and were selected for experimental investigation: (1) solvothermal, (2) aqueous precipitation, and (3) self-propagating combustion synthesis. Preliminary experimental procedures were designed and conducted to test the feasibility of these techniques to adhere to the outlined product and efficiency criteria.

3.2 Materials and methods

Analar grade reagents were purchased from Sigma Aldrich (UK) and used without further purification unless otherwise stated.

3.2.1 Aqueous precipitation (AP)

HA was prepared by an AP method [279]. 0.025M and 0.015M of calcium nitrate tetrahydrate [$Ca(NO_3)_2 \cdot 4H_2O$ >99%] and ammonium phosphate dibasic [$(NH_4)_2HPO_4$ >99%], respectively were dissolved separately in 50mL of DI water. The pH of both solutions was measured using a pH Tester10 (Eutech Instruments, UK) and adjusted to 10±0.05 using an appropriate amount of ammonium hydroxide [NH_4OH 28 – 30%]. The Ca^{2+} solution was added dropwise to the PO_4^{3-} solution using a burette while being continuously stirred at 300rpm. After 2hrs the solution pH was readjusted to 10±0.05 and stirred for a further 12hrs at 300rpm. The precipitate formed was filtered, washed with DI water twice, oven dried, and finely ground using a pestle and mortar. Samples were heat treated to 600, 900 or 1100°C with a ramping up and down rate of 1°C/min and dwell time of 1hr in an air atmosphere.

Table 3.1: Selection of synthesis methods to produce HA according to defined product and efficiency criteria
[a]Rated 0 – 1 where 0 = no and 1= yes, [b]rated in order where 1 = highest and 3 = lowest, [c]rated in order where 1 = longest and 3 = shortest

Synthesis technique	Product criteria					Efficiency criteria		Efficiency total
	Reported pure HA?[a]	Reported particle size <1µm[a]	Reported crystallinity control[a]	Ionic substitutions reported in literature[a]	Scalability medium/high[a]	Typical reaction temperature[b]	Typical processing time[c]	
Solid State	0.5 Likely phase transition due to high temperatures	0	1	1	1	Does not meet all product criteria		N/A
Aqueous Precipitation	1	1	1	1	1	3	1	4
Hydro/Solvothermal	1	1	1	1	0.5 Limited by reaction vessel size	2	3	5
Emulsion	1	0	0.5 Typically controlled by sintering protocol alone	1	0 Reported to be sensitive processes	Does not meet all product criteria		N/A
Microemulsion	1	1		1				
Sol-gel	1	1		1				
SPCS	1	1		1	0.5 Only reported on small scale for HA but industrially used to produce other materials	1	2	3

3.2.2 Self-propagating combustion synthesis (SPCS)

Two different fuels were investigated for the SPCS process, both in combination with nitric acid as an oxidising agent.

3.2.2.1 Urea self-propagating combustion synthesis (USPCS)

0.025M of $Ca(NO_3)_2 \cdot 4H_2O$ and 0.015M of $(NH_4)_2HPO_4$ were added to 100mL of DI water to form a white opaque solution. An appropriate amount of concentrated nitric acid (HNO_3,70%) was added to make the solution clear while stirring at 250rpm. 12g of powdered urea [$(NH_2)_2CO$ ≥98%] was added to this solution, which was stirred at 250rpm for a further 5mins at RT. The final solution was poured into an alumina crucible and placed in a furnace preheated to 500°C until combustion occurred. Products of combustion were ground using a pestle and mortar and heat treated as described in section 3.2.1.

3.2.2.2 Citric acid self-propagating combustion synthesis (CSPCS)

0.02M of $Ca(NO_3)_2 \cdot 4H_2O$ and 0.02M citric acid ($C_6H_8O_7$, 99%) were dissolved in 50mL of DI water and stirred for 10mins at 250rpm. Solution pH was measured and adjusted to 10±0.05 using an appropriate amount of NH_4OH. A stoichiometric amount of $(NH_4)_2HPO_4$ (0.012M) was dissolved in 50mL of DI water and added dropwise to the Ca^{2+} containing solution while stirring at 250rpm to form a white opaque solution. This solution was made clear by adjusting the pH to 1±0.05 by adding an appropriate amount of HNO_3. The final solution was stirred at 250rpm and 70°C for 2hrs. After transferring into an alumina crucible the final mixture was placed in a preheated furnace at 450°C until combustion occurred. Powdered precursors were calcined at 900°C for 2hrs to remove carbonaceous combustion products and then sintered at 900 or 1100°C as described in section 3.2.1.

3.2.3 Solvothermal synthesis (SS)

HA was prepared by adapting a reported SS method [186]. In a typical process, solution I was formed by dissolving 0.0003M of $Ca(NO_3)_2 \cdot 4H_2O$ into solvent A (0.8mL DI water, 0.8mL n-butanol, and 3.1mL n-octane). 0.8g of cetyl trimethylammonium bromide ($C_{19}H_{42}NBr$ - CTAB) was then dissolved into solution I under stirring conditions (200rpm). Solution II was formed separately by dissolving 0.00018M of $(NH_4)_2HPO_4$ into solvent A. An appropriate amount of 2M sodium

hydroxide (NaOH >97%) solution was added to solution II to adjust the pH to 10±0.05. While stirring at 400rpm solution II was added to solution I, which was then stirred for 30mins, transferred into a 20mL Teflon lined autoclave and placed in a furnace preheated to 160°C for 24hrs.

The formed precipitate was separated from the final suspension by centrifugation (4000rpm for 10mins) and the supernatant decanted off. The precipitate was washed firstly with DI water and then thrice with a mixture of methanol and dichloromethane (1:1 volume). Drying and heat treatment were then performed as described in section 3.2.1.

3.3 Material characterisation

To assess whether the HA produced met the outlined criteria several characterisation techniques were used to determine phase purity, crystallinity, crystallite and particle size, particle morphology, and thermal stability.

3.3.1 X-ray diffraction (XRD)

XRD analysis was performed on ground as-synthesised and calcined samples using a Bruker D5000 diffractometer in Bragg-Brentano geometry with a monochromatic CuK_α radiation (λ=1.54056Å) and aluminium sample holders. The data was collected over a 2θ range of 5 – 60° with a step size of 0.02° and a count time of 5s. Phase identification was achieved by matching diffraction patterns with Joint Committee on Powder Diffraction Standards (JCPDS) using Eva software. Line broadening analysis was performed on the (002) peak of as-synthesised HA samples using Equation 3.1:

$$L = \frac{K\lambda}{B\cos\theta} \tag{3.1}$$

where L = crystallite size, K = Scherrer constant (≈0.9), λ = X-ray wavelength (CuK_α=1.54056Å), B = peak width (in radians), and θ = Bragg angle. The (002) diffraction peak was specifically chosen since it is isolated from other characteristic HA peaks.

3.3.2 Scanning electron microscopy (SEM)

The morphology and size of as-synthesised and sintered (1100°C) particles were analysed using a scanning electron microscope (Zeiss Supra55 FEGSEM) operating at 20kV. Powders were dispersed onto double adhesive carbon tabs attached to an aluminium stub and sputter-coated with a thin layer of gold in an argon-purged chamber for 90s prior to characterisation. Image J software was used to measure the size of particles and an average was calculated (n=5).

3.3.3 Differential thermal and thermogravimetry analysis (DTA-TGA)

The thermal behaviour of dried powders was determined by simultaneous DTA-TGA using a TGA/DSC-1 STARe instrument (Mettler-Toledo, UK) with STARe software. 10±5mg of samples were heated in alumina crucibles from 30 – 1300°C at a constant ramp rate of 20°C/min in flowing air. A reference alumina crucible was used and data collected for an empty crucible under the same conditions was blank-subtracted.

3.4 Results

3.4.1 Crystal structure

XRD patterns were matched to JCPDS reference files and the average crystallite size determined by line broadening analysis (Table 3.2). For clarity, the influence of heat treatment temperature on the average crystallite size is graphically shown (Figure 3.1).

XRD patterns of AP01, AP02, and SS01 – SS04 exhibited all of the major peaks of HA (09-432), including characteristic (002), (211), (112) and (300) peaks at 2θ values 25.88, 31.77, 32.20 and 32.90°, respectively. These samples were not matched to any other CaP phases. Heat treatment of AP samples above 600°C (AP03 and AP04) resulted in the formation of a biphasic mixture of HA and β-TCP (70-2065) (Figure 3.2). In contrast, SS03 and SS04 were matched only to HA (Figure 3.3).

As-synthesised samples prepared by USPCS (U01) and CSPCS (C01) were matched to characteristic peaks of HA and β-TCP. Heat treatment up to 1100°C did not result in any phase change but an increase in the intensity of characteristic peaks of USPCS samples was observed (Figure 3.4). In contrast, no discernible change was demonstrated between samples C01 – C03 (Figure 3.5).

Table 3.2: Influence of heat treatment with respect to phase and average crystallite size of preliminary samples
[a]Calculated using Scherrer equation on (002) peak of HA, [b]sample formed after combustion

Sample	Synthesis method	Heat treatment temperature (°C)	Phase(s) identified	Average crystallite size[a] (nm)
AP01	AP	As-synthesised	HA	25
AP02		600		33
AP03		900	HA, β-TCP	38
AP04		1100		48
SS01	SS	As-synthesised	HA	41
SS02		600		46
SS03		900		48
SS04		1100		58
U01	USPCS	As-synthesised[b]	HA, β-TCP	32
U02		600		34
U03		900		37
U04		1100		60
C01	CSPCS	As-synthesised[b]	HA, β-TCP	64
C02		900		79
C03		1100		80

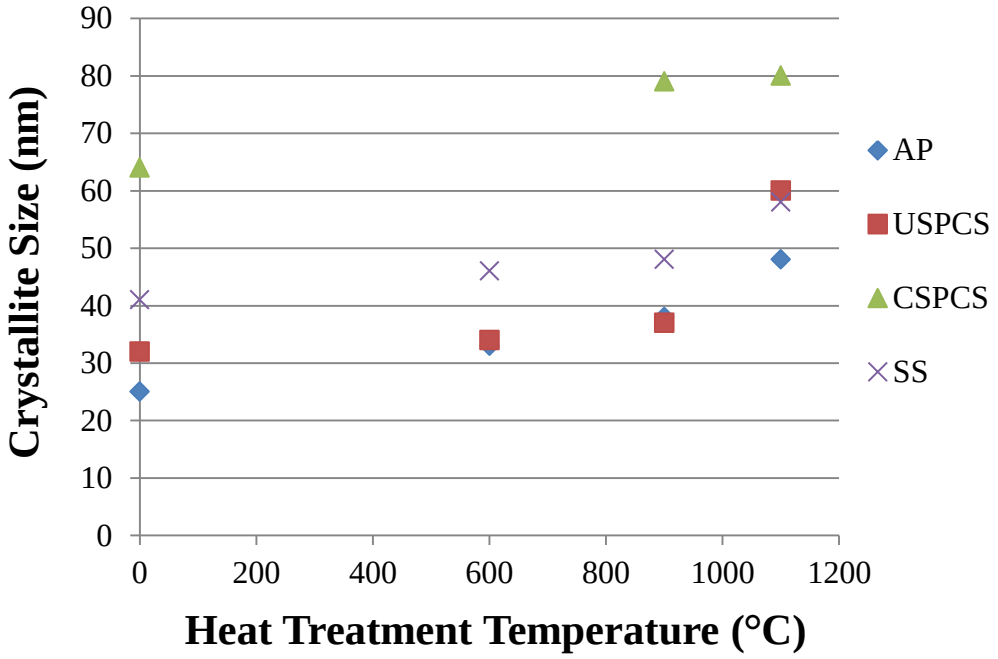

Figure 3.1: Influence of heat treatment on the average crystallite size calculated from XRD line broadening

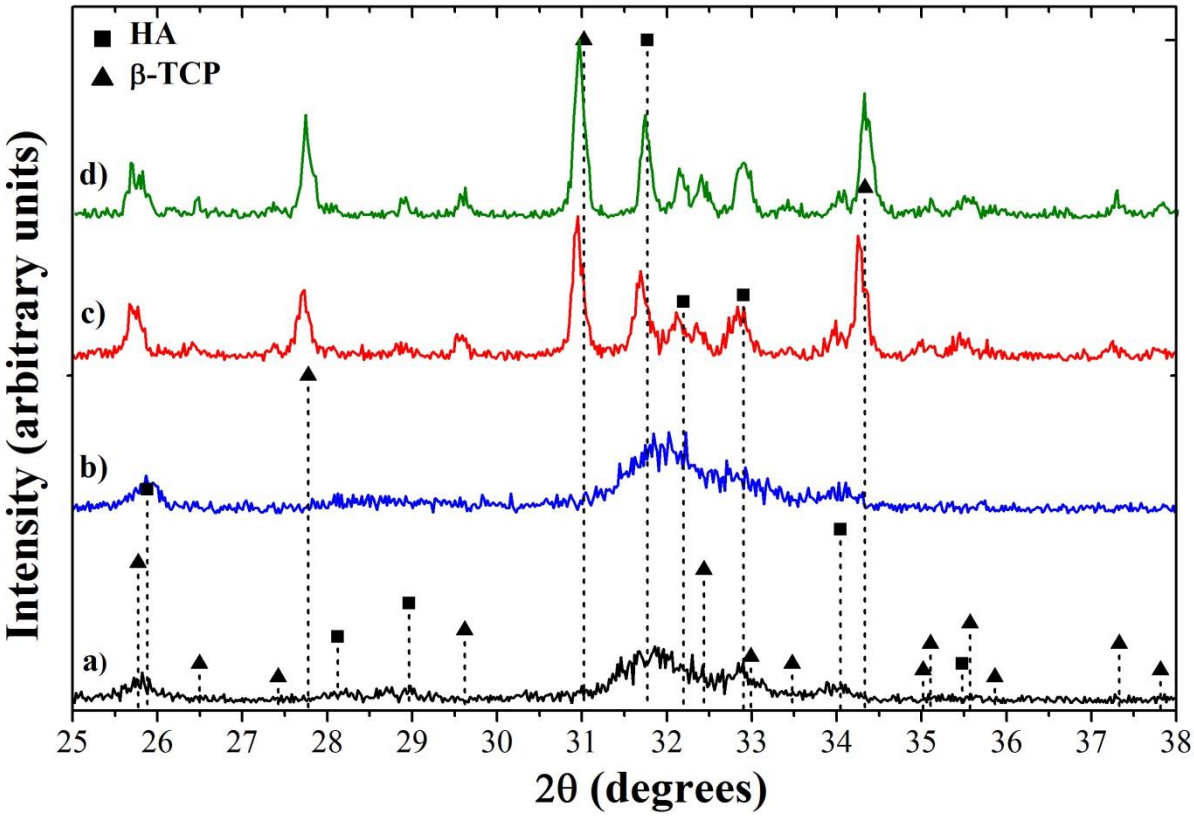

Figure 3.2: XRD patterns of preliminary samples (a) AP01, (b) AP02, (c) AP03, and (d) AP04 produced by AP

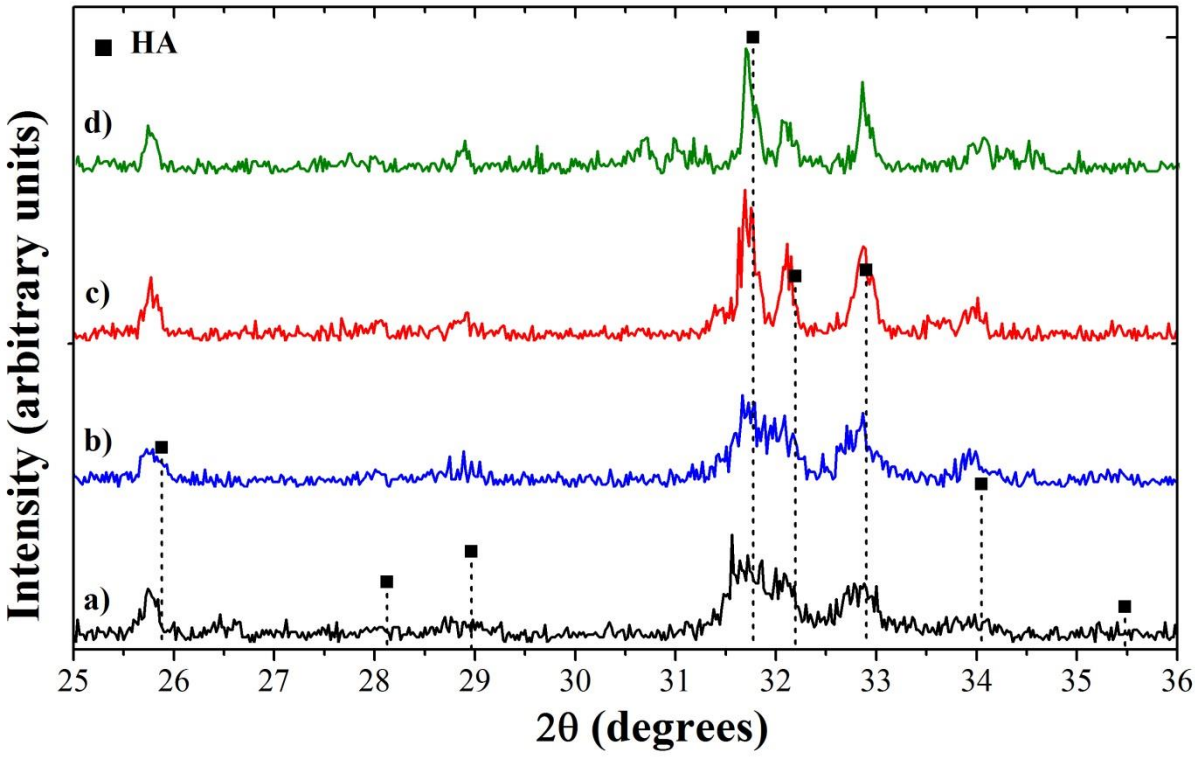

Figure 3.3: XRD patterns of preliminary samples (a) SS01, (b) SS02, (c) SS03, and (d) SS04 produced by SS

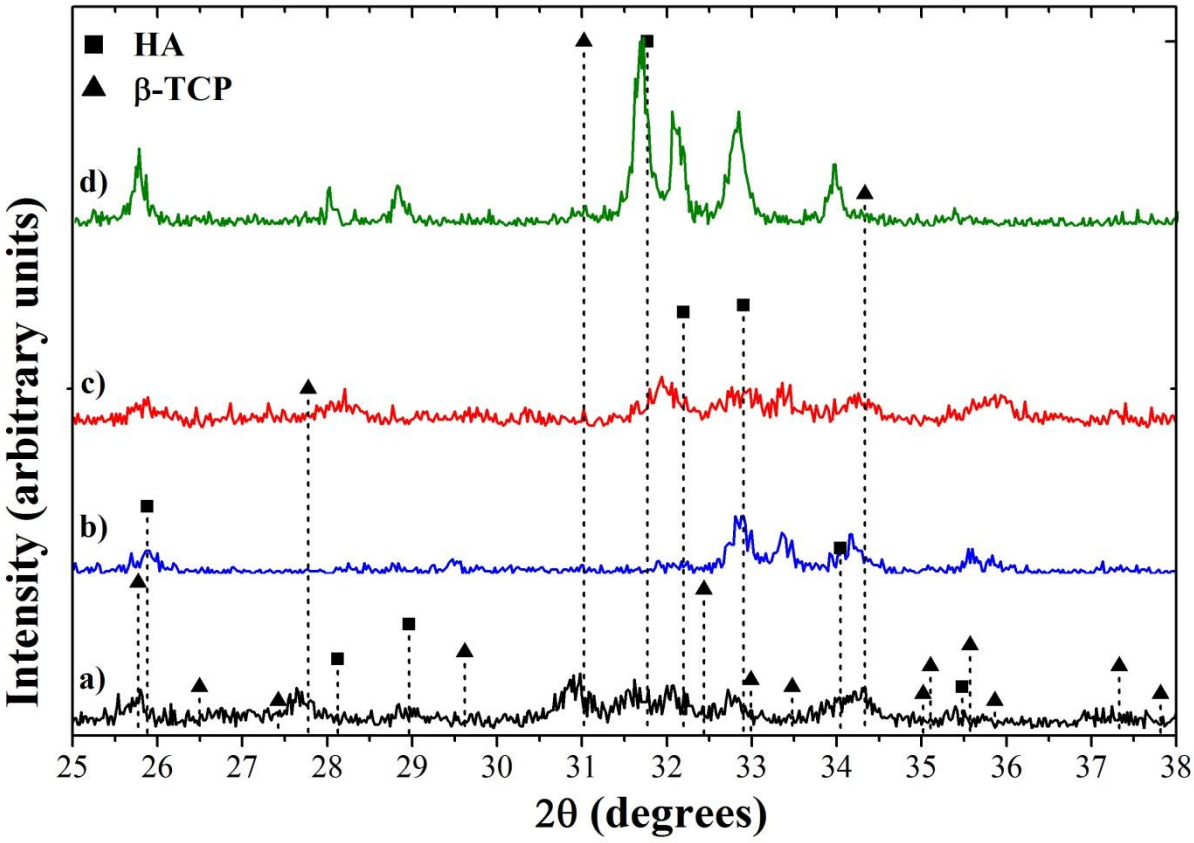

Figure 3.4: XRD patterns of preliminary samples (a) U01, (b) U02, (c) U03, and (d) U04 produced by USPCS

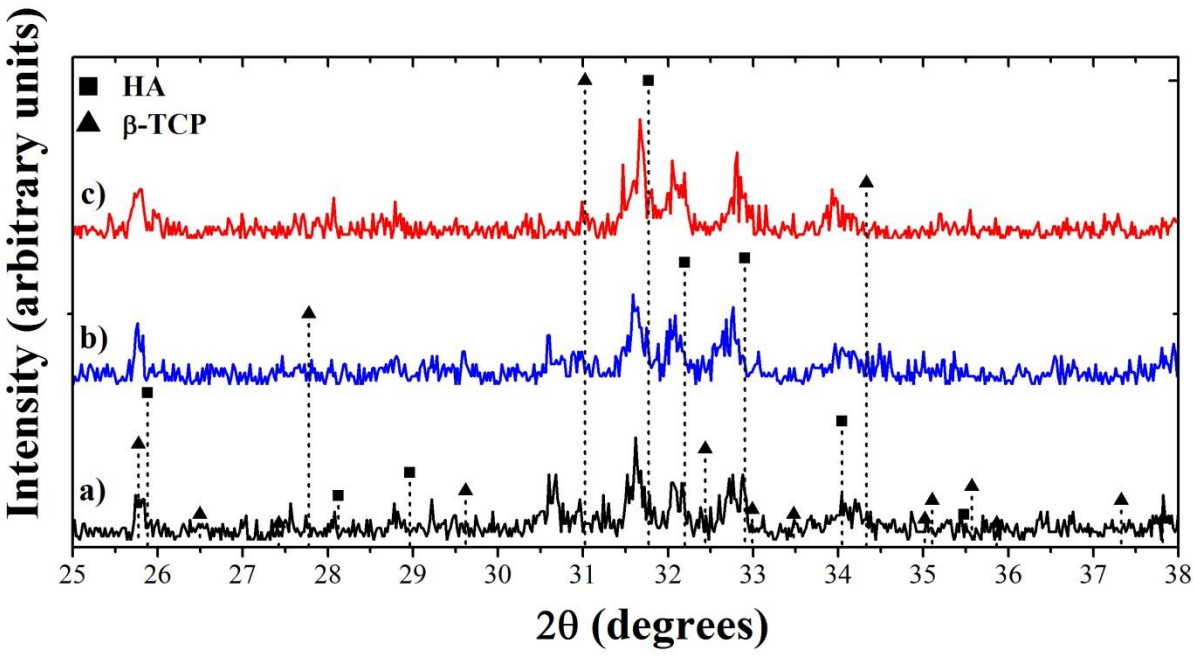

Figure 3.5: XRD patterns of preliminary samples (a) C01, (b) C02, and (c) C03 produced by CSPCS

3.4.2 Microstructural development

The typical morphology of as-synthesised and sintered (1100°C) particles were observed by SEM and average sizes were calculated (Table 3.3). An increase in particle size due to sintering was demonstrated for all synthesis methods (Figure 3.6). Distinct morphological differences were observed amongst synthesis techniques, and between as-synthesised and sintered particles (Figure 3.7). Bulk morphological homogeneity was exhibited for particles, except for those prepared by USPCS that revealed two different morphologies: (1) small globular particles (200 – 400nm), and (2) polygonal shaped agglomerates (12 – 20μm) (Figure 3.8).

Table 3.3: Summary of the average size and typical morphology of particles observed by SEM

Synthesis method	As synthesised		Sintered at 1100°C	
	Typical morphology	Average size (μm)	Typical morphology	Average size (μm)
AP	Single domain, globular, agglomerated	0.57 ± 0.07	Single domain, uniform globular, agglomerated	0.73 ± 0.05
USPCS	Single domain, globular agglomerates	5.81 ± 1.50	Two morphologies: globular and polygonal agglomerates	8.97 ± 6.39
CSPCS	Single domain, polygonal, agglomerated	11.38 ± 5.08	Single domain, polygonal, agglomerated	19.45 ± 2.80
SS	Single domain, globular, agglomerated	2.00 ± 0.19	Single domain, globular agglomerates	4.74 ± 0.84

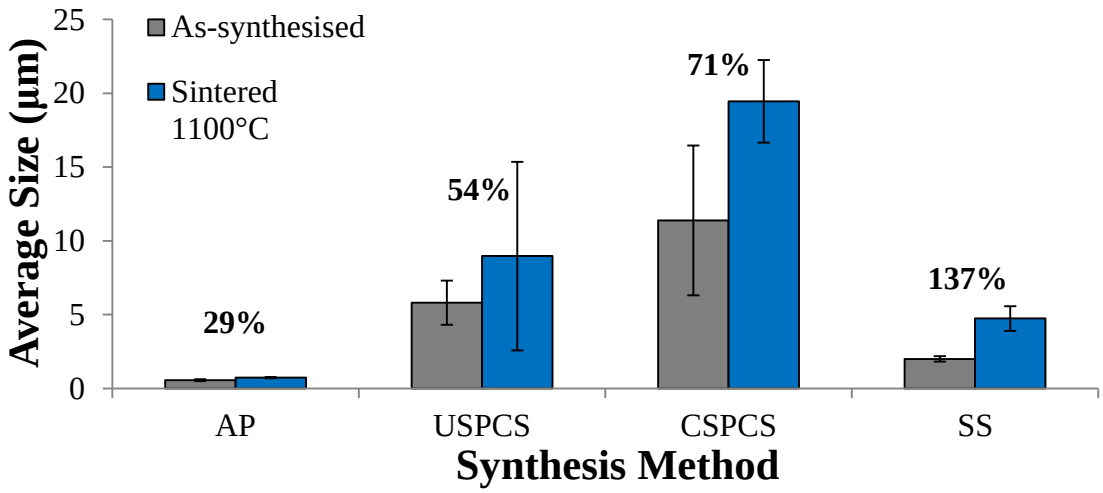

Figure 3.6: Increase in average particle size observed by SEM between as-synthesised and sintered particles produce by preliminary methods

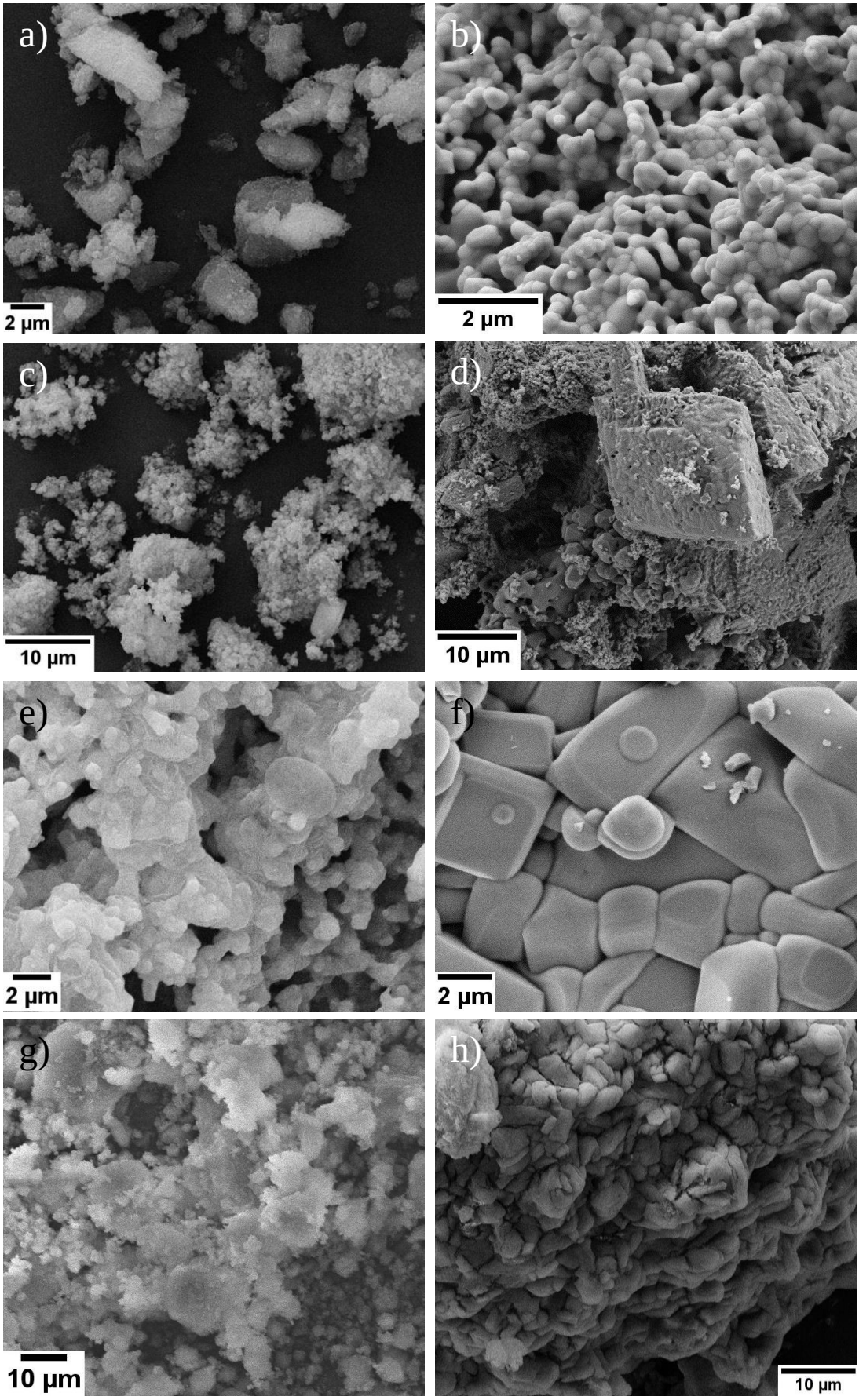

Figure 3.7: Typical particle morphology of preliminary samples (a) AP01, (b) AP04, (c) U01, (d) U04, (e) C01, (f) C03, (g) SS01, and (h) SS04

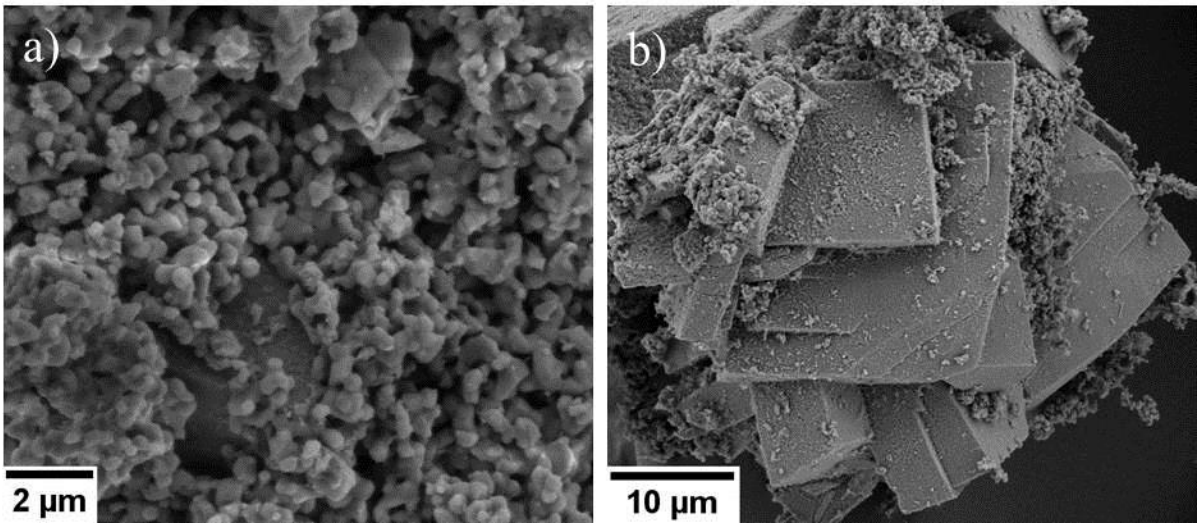

Figure 3.8: Typical (a) globular particles and (b) polygonal agglomerates observed in USPCS samples

3.4.3 Thermal behaviour

A notable variation in the total weight loss recorded between 30 and 1300°C by TGA was observed (Table 3.4). SS01 exhibited a lower than average weight loss, and in contrast U01 and C01 demonstrated a higher than average loss. All samples displayed a weight loss below 100°C corresponding to an endothermic reaction, which is ascribed to the removal of non-bound surface water (Figures 3.9 – 3.12). AP01 (Figure 3.9), C01 (Figure 3.11), and SS01 (Figure 3.12) exhibited an endotherm between 200 and 300°C that is attributed to loss of bound surface water. The weight loss observed in all samples, except SS01, at approximately 500°C, is suggested to be due to the removal of lattice water. Any weight loss after this temperature was attributed to the dehydroxylation of the respective CaP phase(s).

Table 3.4: TGA analysis of as-synthesised preliminary samples

Sample	Total weight loss (wt%)	Residue (wt%)
AP01	9.39	90.61
U01	13.79	86.21
C01	12.08	87.92
SS01	4.53	95.47
Average	9.95	90.05

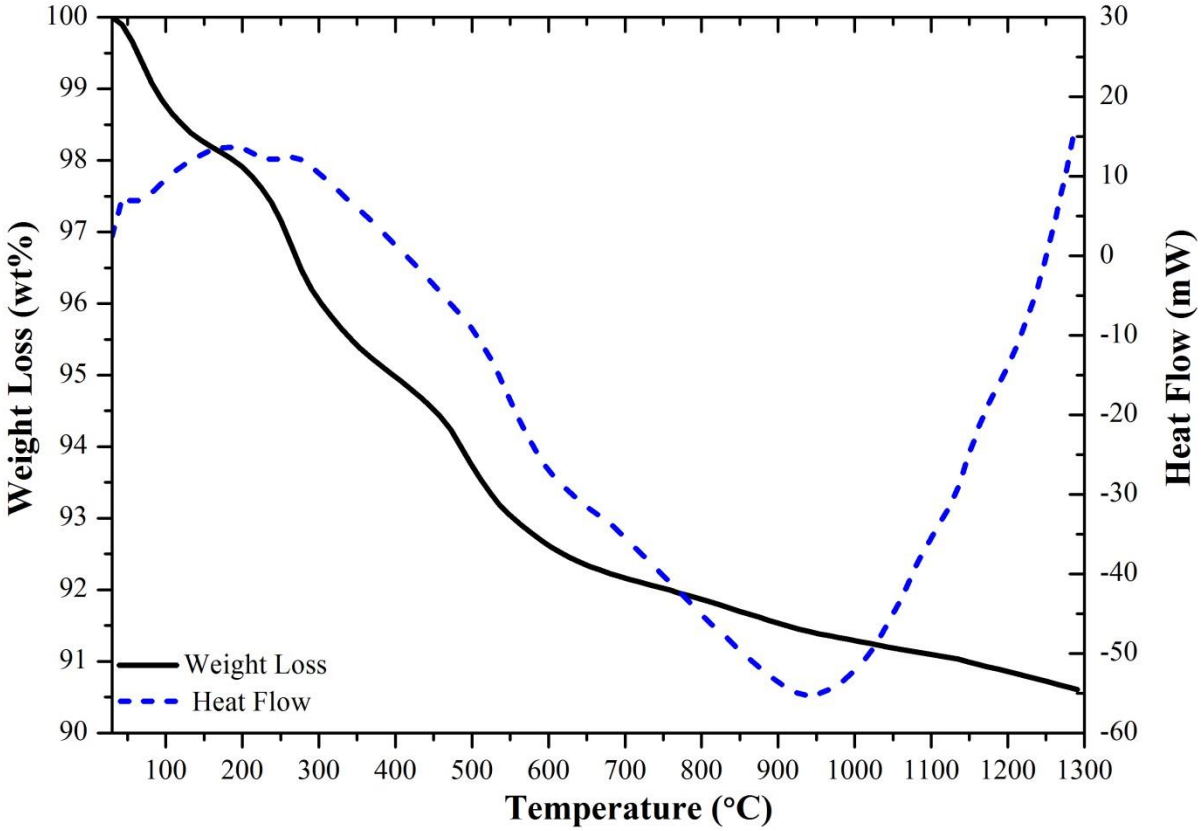

Figure 3.9: Thermal behaviour of AP01

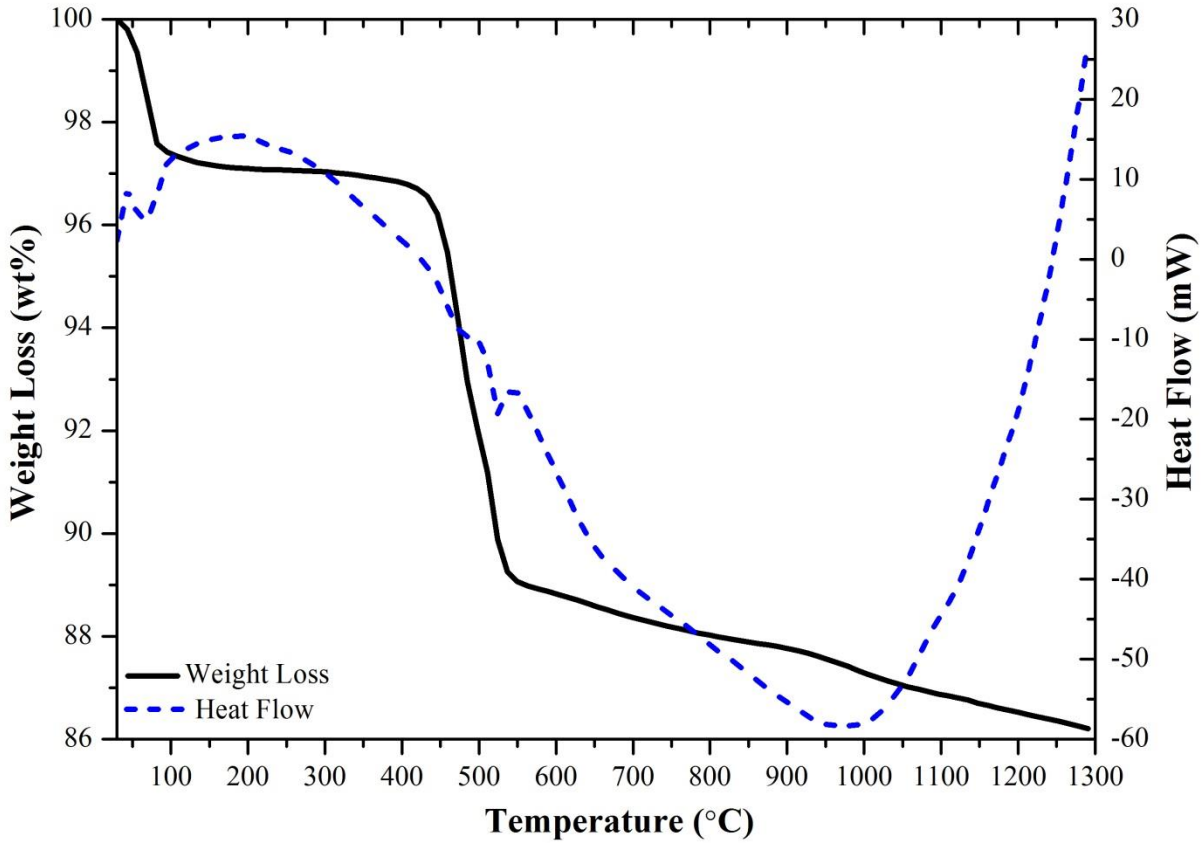

Figure 3.10: Thermal behaviour of U01

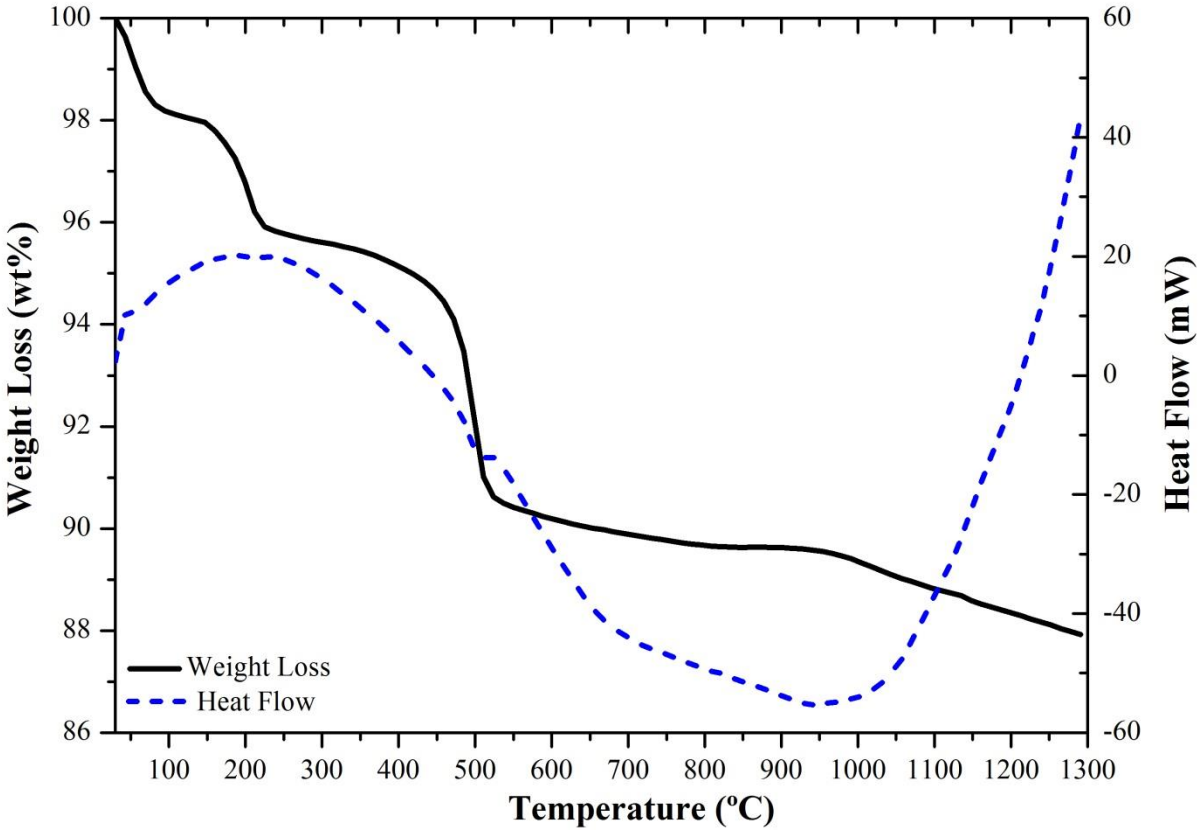

Figure 3.11: Thermal behaviour of C01

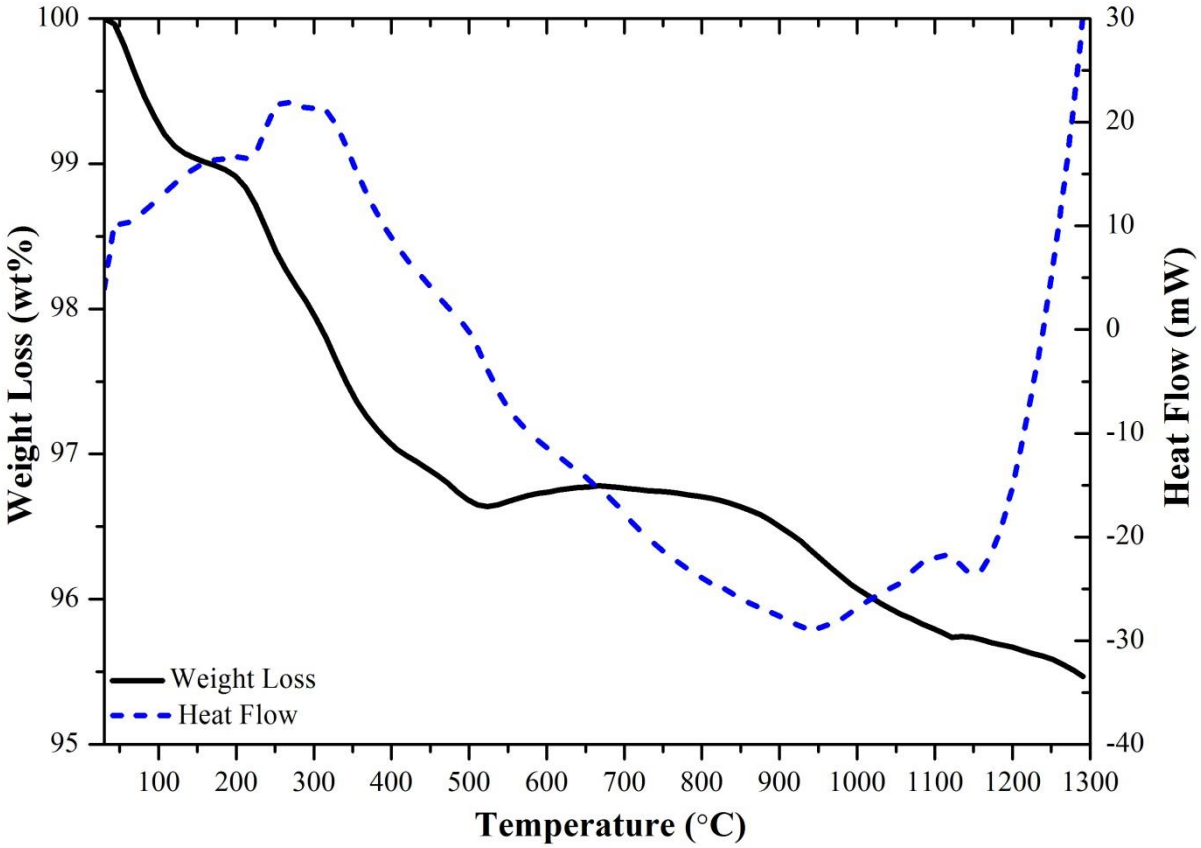

Figure 3.12: Thermal behaviour of SS01

3.5 Discussion

XRD investigations showed that uncalined (AP01 and SS01) and calcined (AP02, SS02, SS03 and SS04) samples produced by the AP and SS methods matched to HA alone and no secondary phases were identified. Uncalcined precipitates exhibited broadened and poorly defined characteristic XRD peaks, which has been reported as typical for HA prepared by AP methods [121]. XRD peaks of as-synthesised samples produced by SS were comparable, in terms of the degree of broadening, to AP01 and this suggests that a higher temperature or longer solvothermal treatment time is required to noticeably improve crystallinity. The heat treatment of AP and SS samples at 600°C increased peak intensity but characteristic (211), (112), and (300) peaks were still observed to overlap. A significant improvement in the refinement of HA peaks resulted at sintering temperatures of 900 and 1100°C for SS samples (Figure 3.3). A steady increase in crystallite sizes was observed for AP and SS samples up to 900°C due to densification of powders (Figure 3.2). Between 900 and 1100°C an increase in the rate of crystallite growth was observed, which is associated to a higher degree of particle consolidation at these temperatures.

Partial phase transition to β-TCP was observed in samples AP03 and AP04, as indicated by the formation of peaks at 2θ values that did not match the standard HA reference pattern (09-432). This thermal instability suggests that the precipitates formed via this preparation method were CDHA, i.e. Ca:P ratio <1.67 (e.g. Figure 2.12). In comparison, corresponding SS samples (SS03 and SS04) were matched to HA alone suggesting a Ca:P ratio closer to the stoichiometric value of 1.67. TGA analysis supports this assertion since SS01 exhibited over 50% less weight loss between 30 and 1300°C compared to AP01, notably stoichiometric HA is reportedly thermodynamically stable up to 1250°C [220]. Equations 2.4 and 2.5 describe reactions that may occur over this temperature range if CDHA is present. Thus the higher weight loss and resultant phase change exhibited for AP samples strongly suggests AP01 is CDHA.

XRD patterns of samples formed after combustion using urea or citric acid as fuels for SPCS suggest they comprised of a biphasic mixture of β-TCP and HA. Since β-TCP is formed from the thermal decomposition of CaPs, such as CDHA above 800°C, these results suggest that the respective combustion reactions of urea or citric acid with

nitric acid formed a high temperature reaction front. A sharp increase in intensity and lower degree of peak broadening was observed between U03 and U04 corresponding to an increase in average crystallite size of over 60%. These changes demonstrate that an improvement in the crystallinity occurred above 900°C, thus suggesting that as-synthesised USPCS powders exhibited a poor long range crystal order. This is attributed to the relatively fast formation of the CaP phase from a solution containing numerous ionic species (e.g. Figure 2.10) due to the instant combustion of urea and nitric acid at the appropriate temperature. In contrast, an increase of only 25% was calculated between the average crystallite sizes of C01 and C03. The degree of broadening and intensity of the XRD peaks were not significantly altered by the heat treatment protocols employed (Figure 3.5). This suggests that the crystal structure was predominantly defined during the initial combustion reaction between citric and nitric acid. The following factors of the SPCS methods are suggested to cause the formation of biphasic CaPs: (1) high reaction front temperatures, (2) volatile molecular dispersion of numerous ionic species within the initial solutions, and (3) spontaneous ignition of the fuel and oxidiser. The importance of the fuel to oxidiser ratio in SPCS methods is recognised as an influential factor since if any constituents are left unreacted undesirable carbonaceous by-products may remain.

Typical SEM micrographs of as-synthesised and sintered samples of AP and SS particles illustrated a similar single domain globular morphology with bulk agglomeration. The CSPCS technique investigated produced monomorphic particles in a polygonal form. In contrast, sintering of USPCS samples resulted in the formation of polygonal agglomerates as well as globular particles as shown by characteristic SEM micrographs of samples U01 and U04. This observation is suggested to explain the increase in the rate of crystallite growth between 900 and 1100°C (Figure 3.1). The agglomeration behaviour demonstrated for particles produced by all methods is linked with the high particle energy associated with nanosized crystallites, which causes them to clump together. However, the higher degree of agglomeration and larger average particle size of as-synthesised particles produced by both SPCS methods is suggested to be due to the high reaction temperatures that occur during the spontaneous combustion of respective fuels and oxidisers. The marked difference in the morphology of particles formed via SPCS methods compared to AP and SS is attributed to the characteristically different morphologies of CaP phases formed at low

and high temperatures (Figure 2.8). Furthermore, the vast differences in particle morphology reflect the differences in material composition. Line broadening analysis confirmed crystallites of all samples were within the nanoregime (Table 3.2).

To complement XRD results the thermal stability of as-synthesised samples was assessed by simultaneous DTA-TGA between 30 and 1300°C. An average weight loss of 9.95% was recorded over this temperature regime and the majority of this is attributed to the removal of surface and lattice water. Removal of surface water is ascribed to any weight loss occurring below 200°C and the loss of lattice water is proposed to take place up to 700°C (Equation 2.4). To reiterate, any reduction in weight above this temperature is owing to the dehydroxylation of CaP phases formed during heating due to non-stoichiometry of HA (Equation 2.5). The thermal stability of powders produced by the SS method is illustrated by the lower than average weight loss recorded by TGA and no detection of secondary phases in XRD patterns of sintered samples. Thus it is suggested that SS01 is predominantly HA. In contrast, both SPCS methods exhibited a larger weight loss below 700°C compared with SS and AP samples, which suggests greater deviation from stoichiometry. Furthermore, a weight loss of 1.61% for U01 between 700 and 1300°C was observed, which was notably greater than other samples and may be linked with further thermal degradation of the CaP phases present. It should be noted that some weight loss of SPCS samples should be attributed to the removal of carbonaceous by-products of the respective combustion reactions.

The feasibility of producing phase pure HA with an average particle size less than 1μm by AP, SS and SPCS methods was experimentally assessed in this chapter. Table 3.5 summarises the ability of each technique to meet the previously defined product criteria: (1) phase pure HA, (2) particle size less than 1μm, (3) degree of control of crystallinity, and (4) ability to alter stoichiometry by substituting naturally occurring ionic species into the HA structure. In addition, those criteria that were not directly measured (i.e. crystallinity control and an ability to alter stoichiometry), as well as scalability, reaction temperature and processing time were commented on.

3.6 Conclusions

XRD analysis of as-synthesised AP and SS samples did not identify any prominent secondary phases and in contrast both SPCS methods resulted in the production of mixed phase CaPs. The sensitivity of the AP process is demonstrated by the relationship observed between the dominate phase and heat treatment temperature, which highlights the need to optimise reaction conditions in an effort to control stoichiometry. The formation of β-TCP above 600°C suggests the phases precipitated were CDHA, which although suggests that the as-synthesised sample was not 'phase pure' HA, a degree of nonstoichiometry is likely to be beneficial since a reduction in the Ca:P ratio is associated with an increase in the rate of dissolution. In order to detect the presence of any HPO_4^{2-} in the suspected CDHA it is recommended an additional characterisation technique would be necessary, for example FTIR.

SEM micrographs confirmed the single domain morphology for as-synthesised and sintered AP, CSPCS and SS samples. In comparison, globular and polygonal particles observed in sintered USPCS samples demonstrated a higher degree of densification. Particles synthesised by the AP methods were the only products less than 1μm in size; however notably a degree of bulk agglomeration was observed.

In conclusion, despite the advantageous short reaction times of the reported SPCS processes due to the volatile and spontaneous nature of particle formation neither method is deemed feasible. Both the AP and SS methods are expected to adhere to the listed criteria after optimisation of influential reaction conditions, such as pH and reaction temperature. However, the SS method is considered unsuitable for further investigation due to the limited ability to control crystallinity and scale up this process. To reiterate, the degree of crystallinity of HA is deemed to be a critical factor due to its reported influence on the adhesion of osteoblasts [281]. Therefore, the AP method was selected for further investigation.

Table 3.5: Feasibility of selected HA synthesis methods according to product and efficiency criteria
[a]experimentally measured, [b]not experimentally assessed

Synthesis technique	Product criteria					Efficiency criteria	
	As-synthesised phase matched to HA?[a]	**Average particle size <1µm?[a]**	**Crystallinity control[b]**	**Ionic substitutions[b]**	**Scalability[b]**	**Reaction temperature (°C)**	**Processing time (hrs)**
AP	Yes No secondary phases identified	Yes	Yes Reaction parameters such as temperature and solute concentration can be controlled throughout precipitation	Yes Numerous reports of incorporation of various substitutions within the literature	High Commonly used industrially	RT	15
USPCS	No Secondary phases present	No	Limited Largely determined by combustion reaction and post heat treatment	Difficult Volatile dispersion of molecules within initial solution could result in inhomogeneous distribution of additional ions in final product	Low Dependent on size of crucibles and furnace. Foreseen difficulty in processing larger batches due to instantaneous ignition. Potential for reactants to remain unreacted	500	1.5
CSPCS		No				450	5
SS	Yes No secondary phases identified	No	Limited Determined primarily by solvothermal treatment temperature and time	Yes Successful reports within the literature	Low Largest autoclave available 50mL corresponding to a HA batch size <1g	160	26

Chapter 4

Precipitation of hydroxyapatite - influence of reaction conditions

4. Precipitation of hydroxyapatite – influence of reaction conditions

4.1 Introduction

The feasibility to produce phase pure HA with a particle size less than 1μm, controllable crystallinity, and an ability to alter stoichiometry by aqueous precipitation (AP), self-propagating combustion synthesis (SPCS), and solvothermal synthesis (SS) methods was experimentally assessed in Chapter 3. Results established that the AP method satisfied these product criteria most closely. Additionally, the ability to produce substantial quantities at relatively low temperatures is another notable advantage of AP methods (Tables 2.6 and 3.5). This technique was therefore selected for further investigation and this chapter explores the influence of various reaction conditions on material properties and the biological performance of HA.

Generally it is accepted in the literature that the value of pH during synthesis affects the phase purity of precipitated CaPs [57, 282]. As summarised in Table 2.7, numerous authors have investigated the influence of other reaction conditions, such as temperature, reagent concentration, addition rate, ageing time, and heat treatment on pure, carbonated, and substituted calcium apatites [15, 60, 167, 209, 283-288].

This chapter presents an experimental analysis of the single factor influence of pH, temperature, and solute concentration on the following properties of HA: (1) phase purity, (2) degree of crystallinity, (3) particle size and morphology, (4) thermal stability, (5) stoichiometry, (6) surface area, and (7) surface charge. Acellular and cellular assessments of bioactivity, cytocompatibility as well as the degree of cell proliferation were also performed, respectively.

4.2 Materials and methods

Analar grade reagents were purchased from Sigma Aldrich (UK) and used without further purification unless otherwise stated.

4.2.1 Aqueous precipitation (AP)

Stock solutions containing Ca^{2+} and PO_4^{3-} were obtained separately by dissolving 0.05M of $Ca(NO_3)_2 \cdot 4H_2O$ and 0.03M of $(NH_4)_2HPO_4$ into 50mL of DI water, respectively. The solution containing PO_4^{3-} was added dropwise to the Ca^{2+} solution while being stirred at 400rpm and RT. During addition the pH was controlled to 11±0.1 using an appropriate amount of aqueous NH_4OH. After addition, the combined solution was stirred for a further 1.5hrs at RT, and solution pH and temperature were recorded throughout.

The precipitate formed was removed from the mother solution and centrifuged four times at 4000rpm for 10mins in a solution of DI water. In between each cycle the supernatant was removed and fresh DI water was added. Washing and filtering was then performed using DI water and a Bucker flask, respectively. The washed precipitate was oven dried at 60°C overnight and ground into a fine powder using a pestle and mortar.

In order to determine the individual influence of pH, temperature, and solute concentration a single factor test method was used, i.e. only one reaction parameter was changed for each sample produced. Variations to the procedure reported above are summarised in Table 4.1.

Table 4.1: Summary of varied pH, temperature and solute concentration conditions
[a]control sample

Sample	Investigated parameter	Parameter value	Comment
AP05	pH	8	pH adjusted before addition of P solution and not controlled during
AP06		9	
AP07		10	
AP08		11	pH adjusted at start and end of addition of P solution
AP09[a]		11	pH controlled during addition of P solution
AP10		10	
AP11	Solute concentration	0.1M Ca reagent	Stoichiometric amount (0.06M) of P reagent was used
AP12	Temperature	70°C	The solution was heated on a magnetic hot plate during addition and stirring

4.2.2 In-vitro test methods

Preparation of as-synthesised powders (AP07 – AP12) for acellular and cellular in-vitro testing is described in this section.

4.2.2.1 Pellet preparation

In-vitro tests were performed on pellets formed from 0.25±0.02g of as-synthesised powder. Samples were pressed into cylindrical pellets (diameter 10mm) using a Simplemet 2 press (Buehler, UK) in combination with a self-manufactured hardened steel die and punch set (Figure 4.1). A uniaxial force of 800N was used to compress the powder, using the process illustrated in Figure 4.2. Pellets were consolidated by heating to 600°C with a ramping up and down rate of 1°C/min and dwell time of 1hr in an air atmosphere.

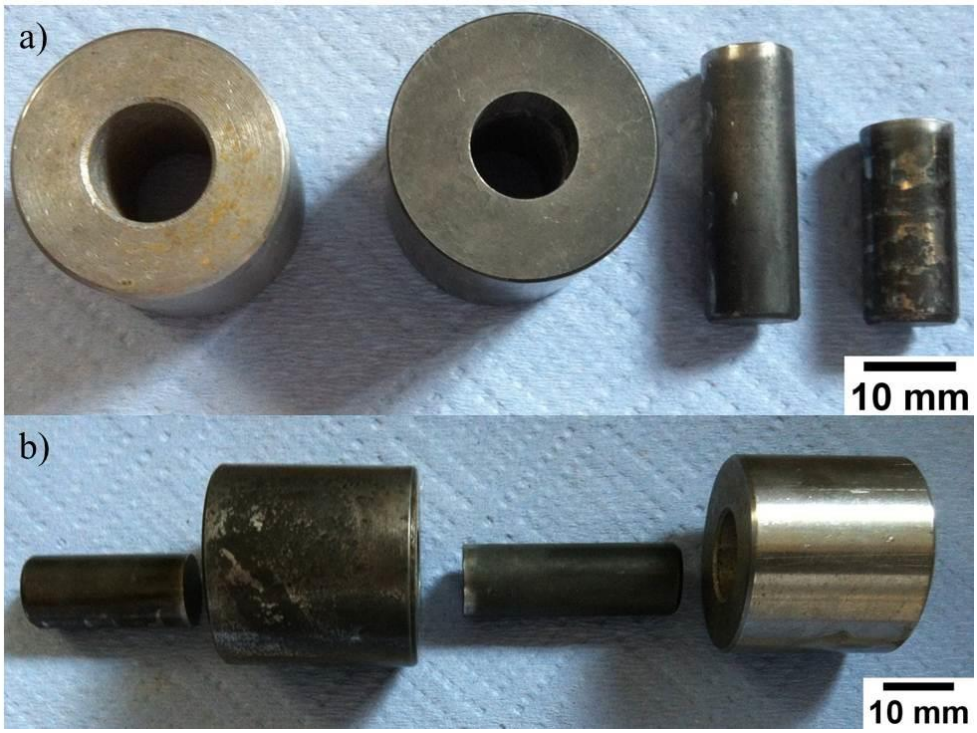

Figure 4.1: Steel die and punch set used to prepare pellets
(a) Top view and (b) side view arrangement in order of application

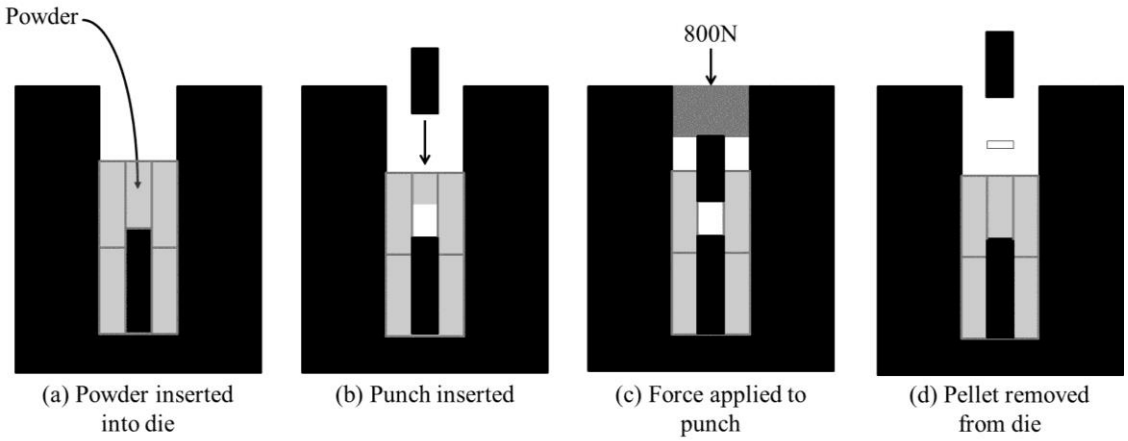

Figure 4.2: Preparation of pellets used for in-vitro tests

4.2.2.2 Simulated body fluid test

As a prerequisite to cellular in-vitro tests the bioactivity of substrates was evaluated by examining the ability of apatite to form on the surface of prepared pellets while immersed in simulated body fluid (SBF), which exhibits ion concentrations nearly equal to those of human blood plasma. SBF was prepared by the method reported by Kokubo et al. [289], in accordance to ISO 23317:2007. During preparation the solution was stirred continuously at 200rpm and the temperature was maintained at 36.5±1.5°C. 4 pellets for each sample were placed individually into glass specimen bottles and immersed in SBF so the entire surface was covered. To avoid evaporation of the solution plastic caps were secured on specimen bottles, which were then placed into an incubator at 37°C until required. A single pellet of each sample was removed, dried, and analysed after 1, 7, 14, and 28 days of immersion.

4.2.2.3 Live/dead staining

MC3T3 osteoblast precursor cells were seeded on to pellets to determine the effect of different substrates on cell viability up to 7 days. Prior to cell culture pellets were sterilised with ethanol (70%, Fisher Scientific, UK) and left overnight under UV light. Well plates were coated with 1.5mL of Sylgard type 184 silicone elastomer (Dow Corning Corporation, US) and left to polymerise for a week before use to provide a non-cell-adhesive surface. Aliquots (50μm) containing $2x10^4$ cells/well were seeded directly on top of the HA pellets in 24-multiwell plates and allowed to adhere for 4hrs. After this time 2mL of DMEM, which was supplemented with 10% fetal bovine serum, 2.4% L-glutamine, 2.4% HEPES buffer, and 1% penicillin/streptomycin, was added to each well and cultures were incubated in 5% CO_2 atmosphere maintained at 37°C. The viability of cells seeded on the surface of HA pellets were analysed using a Live/Dead® Viability/Cytotoxicity Kit after culturing for 1, 3, 5, and 7 days. Live and nonviable apoptotic cells were stained with calcein-AM (1mg/mL, Molecular Probes, UK) and propidium iodide (1mg/mL, Invitrogen, UK), respectively in the dark. Calcein-AM is a green florescent dye that is cell-permeant and converts into intense fluorescent calcein by the activity of an intracellular esterase, an enzyme found in live cells [290]. Propidium iodide is membrane impermeant and is excluded from viable cells. It binds to DNA by intercalating between base pairs.

4.2.2.4 MTT assay

The viability of cells seeded on to the surface of HA pellets was analysed using an MTT assay after culturing for 1, 3, 5, and 7 days. Mitochondria of viable cells reduce the yellow MTT (3-(4,5-Dimethylthiazol-2-yl)-2,5-diphenyltetrazolium bromide) to formazan, which was dissolved by acidic isopropanol after removal of culture medium. Cleavage of MTT occurs only by active mitochondria and therefore the amount of formazan generated is directly proportional to the cell number and activation thus this assay can be used to quantitatively assess cell survival and proliferation [291].

4.2.2.5 Hoechst assay

Cell proliferation on various substrates was also analysed at designated times (1, 3, 5 and 7 days) using a Hoechst 33258 dye that stains DNA. Samples were collected at the appropriate times and washed with PBS. Seeded cells were trypsinized (dissociated) from the surface of substrates and stored at -80°C until the end of the experimental period. All detached cells, from different culture times, were thawed to RT and 100µL of distilled water was added per sample. This solution was incubated at 37°C for 1hr and then stored at -80°C for 20mins and thawed to RT again. 100µL of aqueous Hoechst 33258 in TNE buffer solution was then added to each sample.

4.2.2.6 Florescence staining to visualise cellular internalisation

A stock solution of 5mg Fluorescein-5-Maleimide (Life Technologies, UK) in 1mL of PBS was prepared. 1mg of HA particles was suspended in 500µL of PBS and sonicated for 5mins before adding 400µL of Fluoresceine stock solution. The HA-Fluoresceine mixture was left to react on a thermoblock mixer at 37°C and 1400rpm for 2hrs. The stained particles were finally washed 5 times with PBS.

MC3T3 osteoblast precursor cells were seeded at a density of $3x10^4$cells per quadrant in a 4-segmented live cell imaging dish (Greiner-Bio One Ltd, UK) and incubated overnight at 37°C in supplemented DMEM media. 1mg of HA-dye stock was resuspended in 1mL of supplemented cell culture media and diluted into aliquots of 2.4µg/mL. 500µL of supplemented media and 500µL of the diluted HA-dye solution was added to each quadrant of the imaging dish thus giving a final particle concentration of 1.2µg/mL. Imaging was performed after 24hrs.

4.3 Material characterisation

4.3.1 X-ray diffraction (XRD)

XRD was performed (section 3.3.1) on as-synthesised powders. Samples AP07 – AP10 calcined at 600 and 900°C using a ramp up/down rate of 1°C/min and a dwell time of 1hr were also analysed. Data was collected over the range 2θ = 5 – 60° using a step size of 0.02° and a count time of 15s. Line broadening analysis was performed as previously described using Equation 3.1. The crystalline fraction (X_c) of as-synthesised powders was evaluated using Equation 4.1:

$$X_c = 1 - \frac{V_{112/300}}{I_{300}} \tag{4.1}$$

where I_{300} is the intensity of (300) diffraction peak, and $V_{112/300}$ is the intensity of the hollow between (112) and (300) diffraction peaks of HA, which completely disappears in non-crystalline samples.

4.3.2 Fourier transform infrared spectroscopy (FTIR)

Spectra of finely ground as-synthesised and calcined (AP07-AP10) powders were recorded in Attenuated Total Reflectance (ATR) mode using a Spectrum One FTIR Spectrometer. Specimens were placed onto the sample stage and IR spectra were collect between 550 and 4000cm^{-1} with a 4cm^{-1} resolution averaged over 8 scans using Spectrum software.

4.3.3 Scanning electron microscopy (SEM)

SEM was performed on as-synthesised powders using the method described in section 3.3.2.

4.3.4 Transmission electron microscopy (TEM)

TEM was performed on sample AP07 using a Jeol 2100 LaB6 instrument, operating at 200kV. The specimen was dispersed ultrasonically in ethanol and deposited dropwise onto 3mm lacey carbon grids (Agar, UK).

4.3.5 Differential thermal and thermogravimetry analysis (DTA-TGA)

Simultaneous DTA-TGA analysis was performed using the method reported in section 3.3.3.

4.3.6 Energy dispersive spectroscopy (EDS)

The influence of pH on the Ca:P ratio was determined from elemental analysis performed on a Zeiss Supra55 FEGSEM fitted with a X-max 50mm^2 energy dispersive spectroscope (Oxford Instruments, UK). Preparation of samples was described in section 3.3.2 and involved the use of a carbon tab, as well as gold coating hence the presence of these elements in typical spectra. Three measurements from different locations were obtained and an average value calculated.

4.3.7 X-ray fluorescence (XRF)

The elemental compositions of samples AP07 – AP10 were determined by XRF (S8 TIGER, Bruker Corp, UK). Samples were prepared by mixing 0.5g of HA powder with 0.1g of wax and pressed into pellets. Results were presented as elemental analysis and used to calculate the Ca:P ratio of each sample.

4.3.8 BET surface area measurements

Micromeritics ASAP 2020 surface area and porosity analyser was used to determine the surface area of dried powders using the nitrogen adsorption method [292]. Samples were prepared by heating to 30°C at 1°C/min and evacuated until the pressure reached 10μmm Hg. Specimens were dwelled under these conditions for 10mins.

Nitrogen adsorption data was collected at relative pressures between 0.06 and 0.2, plus a single point at saturation pressure (~1). Free space values were measured using helium prior to analysis. The adsorption took place in a liquid nitrogen bath; saturation pressure (P_0) was measured at intervals and this was used to calculate the temperature of the bath. A value of 0.162nm^2 was used for the area occupied by an adsorbed nitrogen molecule and a non-ideality factor for nitrogen of 5.7 x 10^{-5} was used. BET analysis was carried out on data between relative pressures of 0.06 and 0.2.

4.3.9 Zeta potential (ZP)

Malvern instruments Zetasizer ZS (Malvern, UK) was used to measure particle electrophoretic mobility in DI water and DMEM. Dilute suspensions of particles in the media of interest were prepared at approximately 0.1wt% and loaded into plastic disposable zeta cells. Changes in light intensity fluctuations upon an applied electric field on the zeta cells were measured and employed by the Zetasizer to calculate ZP. Prior to measurement, the cell was agitated in an ultrasonic bath and equilibrated at 25°C for 2mins.

4.3.10 SBF test

Any growth of apatite on the surface of pellets immersed in SBF was visualised by SEM, as described in section 3.3.2. The roughness of the surface of gold coated pellets was profiled using white light interferometry performed on a NT2000 interferometer (Wyco, UK). Average roughness (R_a) was calculated using Equation 4.2:

$$R_a = \frac{(|Z_1|+|Z_2|+|Z_3|+\cdots+|Z_n|)}{N} \quad (4.2)$$

where Z = profile height, and N = number of data points.

4.3.11 Live/dead staining

A fluorescence microscope fitted with a mercury lamp (Carl Zeiss Ltd, UK) was used to visualise live (green) and dead (red) cell cultures on the surface of pellets at magnifications of x20.

4.3.12 MTT assay

The absorbance of coloured solutions was quantified by measuring at a wavelength of 620nm using a microplate reader (BIO-TEK, US), which gave an indication of the cell number at each time point.

4.3.13 Hoechst assay

Fluorescence measurements were carried out using a microplate reader (BIO-TEK, US) with excitation at 360nm and detection at 460nm.

4.3.14 Cellular internalisation

Fluorescein stained samples were imaged with a Zeiss LSM 710 ConfoCor 3 confocal system (Carl Zeiss Ltd, U.K.) attached to a Zeiss Axio Observer.Z1 inverted microscope and equipped with a Zeiss EC Plan-Neofluar x63 NA = 1.40 oil objective lens, 488nm laser diode, 458nm/488nm beam splitter and a 34-channel spectral detector, which was used to divert fluorescence between 500nm and 650nm to a photomultiplier tube detector. Bright field images were obtained simultaneously with the fluorescence images by detecting the transmitted excitation laser light with a second photomultiplier detector [293].

4.3.15 Statistical analysis

It is desired to ascertain whether cell proliferation occurs within the MTT and Hoechst assays. The standard method in the literature is to investigate the variance between and within days 1 and 7 with an analysis of variance (ANOVA) test, for example [294]. A one-way ANOVA was performed, where statistical significance is tested for by comparing the ratio of variance between days 1 and 7 and the variance within days 1 and 7 to the *F*-distribution.

A modified ANOVA test was also used in this thesis (Appendix A). Instead of calculating variance from the mean of day 1 and day 7, linear regression was performed for either days 1 – 3 or alternatively days 1 – 5. Thus the variances were calculated from the straight line fit and the lag cell growth phase was effectively stripped back from the experimental data. It is important to note that since experiment error was random it was therefore assumed that measurements are normally distributed about the true cell number.

The *F* ratios calculated via ANOVA and modified ANOVA analyses were compared with critical *F* values (F_{crit}) to determine any statistical significance. The level of significance was set at $p < 0.05$ (Table 4.2)

Table 4.2: F_{crit} values for data sets collected for MTT and Hoechst assays f_b = between group degrees of freedom, f_w = within group degrees of freedom

Assay	$F_{crit}(f_b, f_w)$	F_{crit} value ($p < 0.05$)
MTT	$F_{crit}(1, 10)$	4.965
Hoechst	$F_{crit}(1, 4)$	7.709

4.4 Results

4.4.1 Development of solution pH

Monitoring the uncontrolled reaction of $Ca(NO_3)_2 \cdot 4H_2O$ (0.05M) and $(NH_4)_2HPO_4$ (0.03M) at RT demonstrated the acidity of the starting solution containing Ca and the final suspension (Figure 4.3). A summary of the solution pH at key reaction stages is presented in Table 4.3 for samples AP07 – AP12.

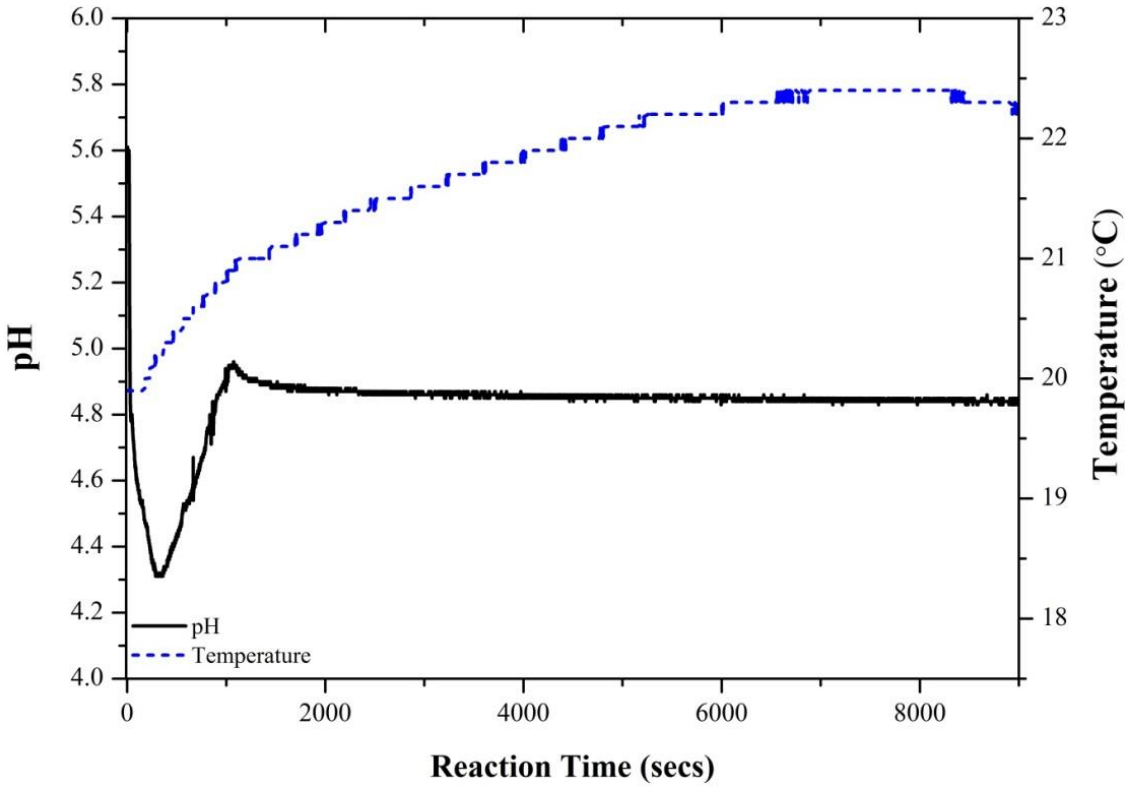

Figure 4.3: Uncontrolled reaction of $Ca(NO_3)_2 \cdot 4H_2O$ and $(NH_4)_2HPO_4$ at RT

Table 4.3: Development of solution pH

Sample	Solution pH		
	Start of addition	End of addition	Removal from mother solution
AP07	10.03	9.14	5.60
AP08	11.00	10.72	10.94
AP09	11.05	10.99	10.78
AP10	10.00	10.00	9.87
AP11	11.10	11.01	10.95
AP12	11.01	11.00	10.38

4.4.2 Crystal structure

Formation of HA was indicated in samples AP07 – AP12 by the characteristic peak occurring at 2θ = 31.77° and verified by matching to the JCPDS pattern for HA (09-432). AP07 exhibited a higher intensity between 2θ = 28 – 30°, which suggests a trace amount of DCPD (09-0077) (Figure 4.4). The influence of temperature and solute concentration is shown in Figure 4.5 with AP09 depicted as a reference.

The different 2θ positions of characteristic peaks observed for samples produced at a starting pH < 10 (AP05 and AP06) were matched to reference patterns for DCPD (09-0077) and DCPA (09-0080) (Figure 4.6).

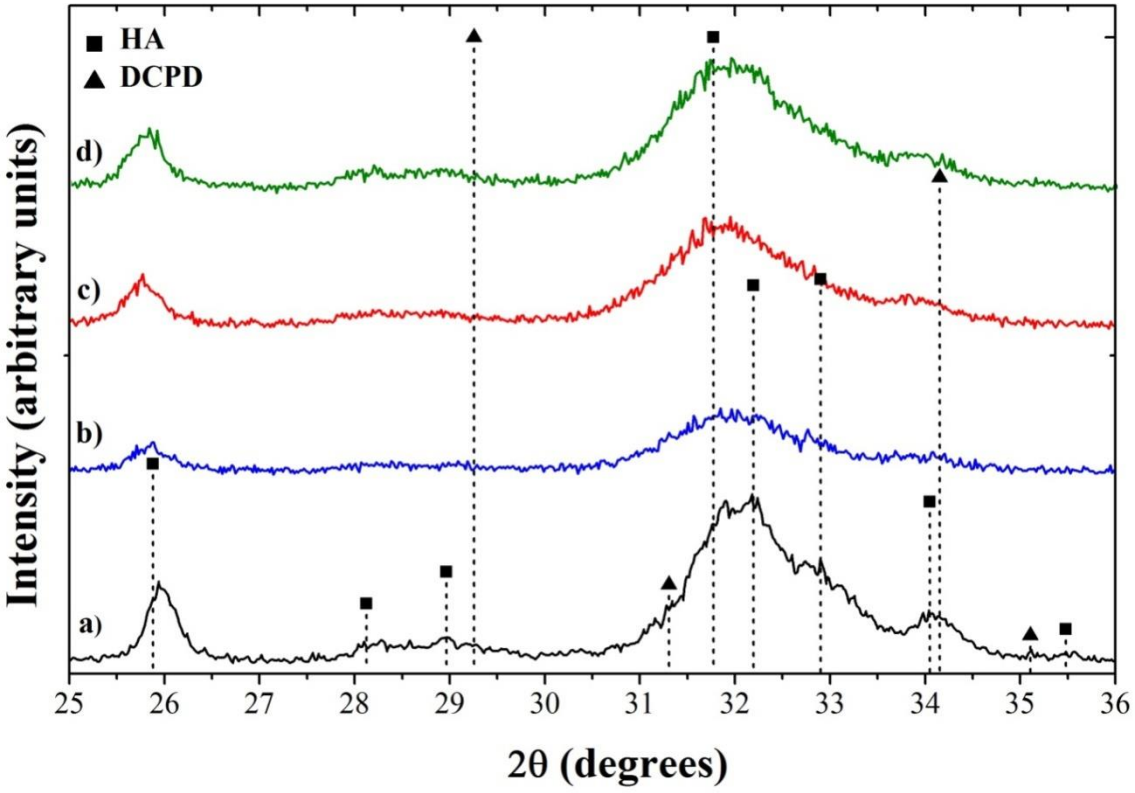

Figure 4.4: Influence of pH value (>10) and control on crystal structure of as-synthesised HA (a) AP07, (b) AP10, (c) AP08, and (d) AP09

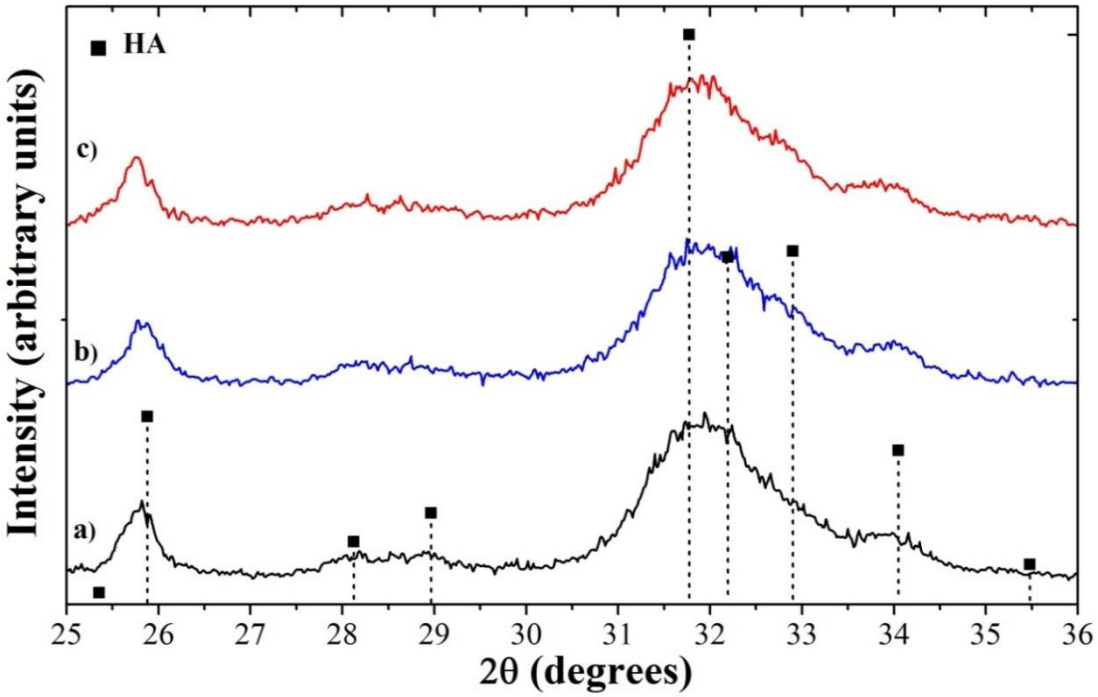

Figure 4.5: Influence of solute concentration and temperature on crystal structure of as-synthesised HA (a) AP09, (b) AP11, and (c) AP12

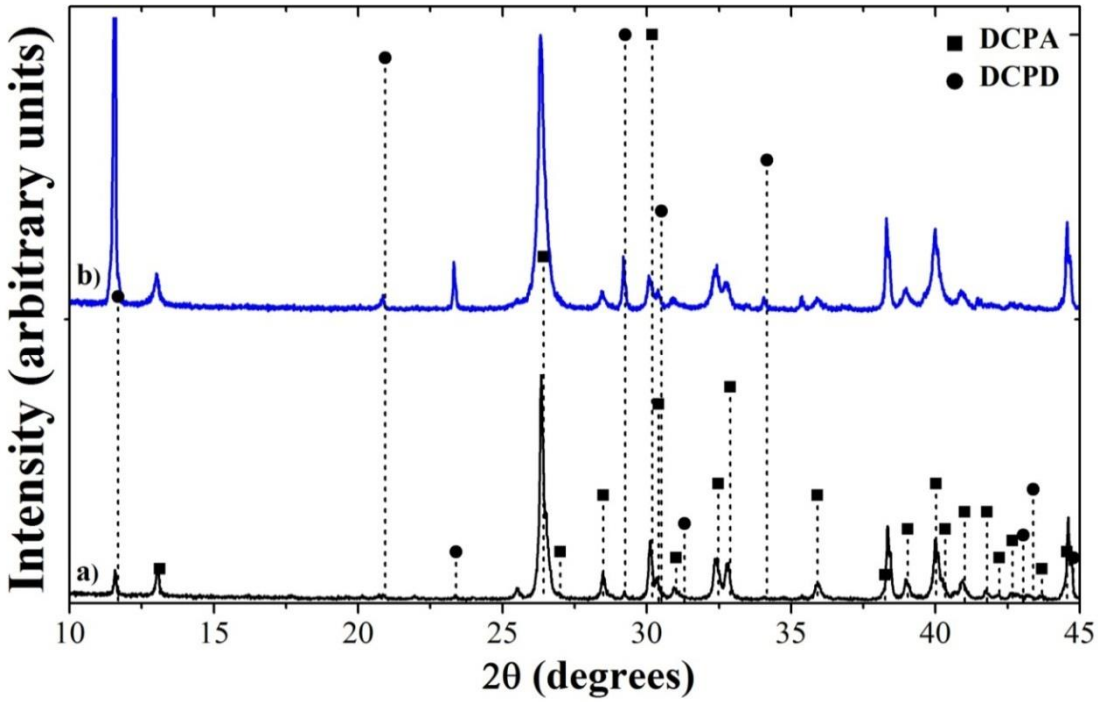

Figure 4.6: Influence of pH on CaP phase formation of as-synthesised (a) AP05, and (b) AP06

Formation of β-calcium pyrophosphate (β-$Ca_2P_2O_7$) is known to occur between 250 and 700°C according to Equation 2.4 if any HPO_4^{2-} is present, i.e. CDHA. However, XRD patterns of samples AP07 – AP10 heated to 600°C did not demonstrate any β-$Ca_2P_2O_7$ (09-346) formation, which suggests no or trace amounts of non-apatitic

HPO_4^{2-} in as-synthesised materials (Figure 4.7) nor did AP11 – AP12 (Figure 4.8). Notably, detection of β-$Ca_2P_2O_7$ was difficult due to the superposition of its peaks with HA ones.

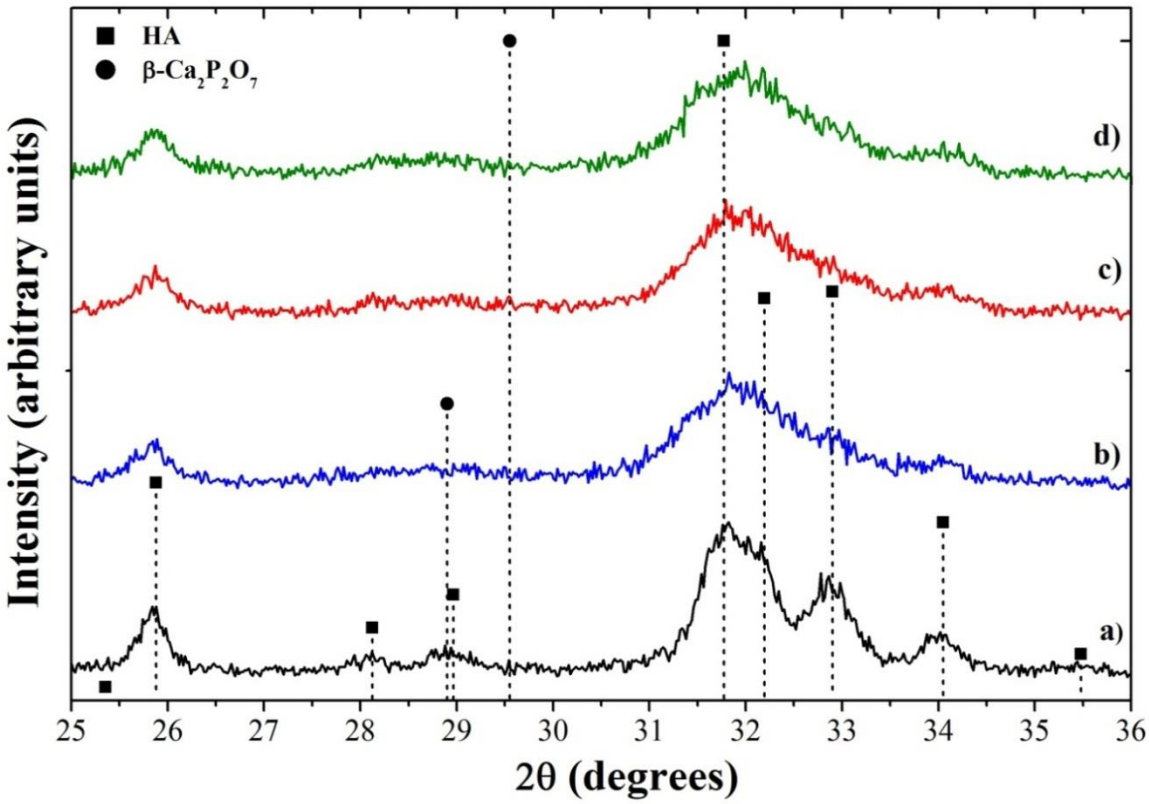

Figure 4.7: Influence of pH on the crystal structure of HA heated to 600°C (a) AP07, (b) AP10, (c) AP08, and (d) AP09

XRD analysis of samples heated to 900°C confirmed the presence of β-TCP. This phase is known to form between 700 and 800°C from $P_2O_7^{4-}$, as a by-product of the condensation of HPO_4^{2-} (Figure 4.9). The intensity of characteristic β-TCP peaks were significantly less and characteristic HA peaks were of a relatively higher intensity in AP07 as well as AP12 compared with other samples. A noticeable peak attributed to β-$Ca_2P_2O_7$ at 28.9° was also observed in these samples.

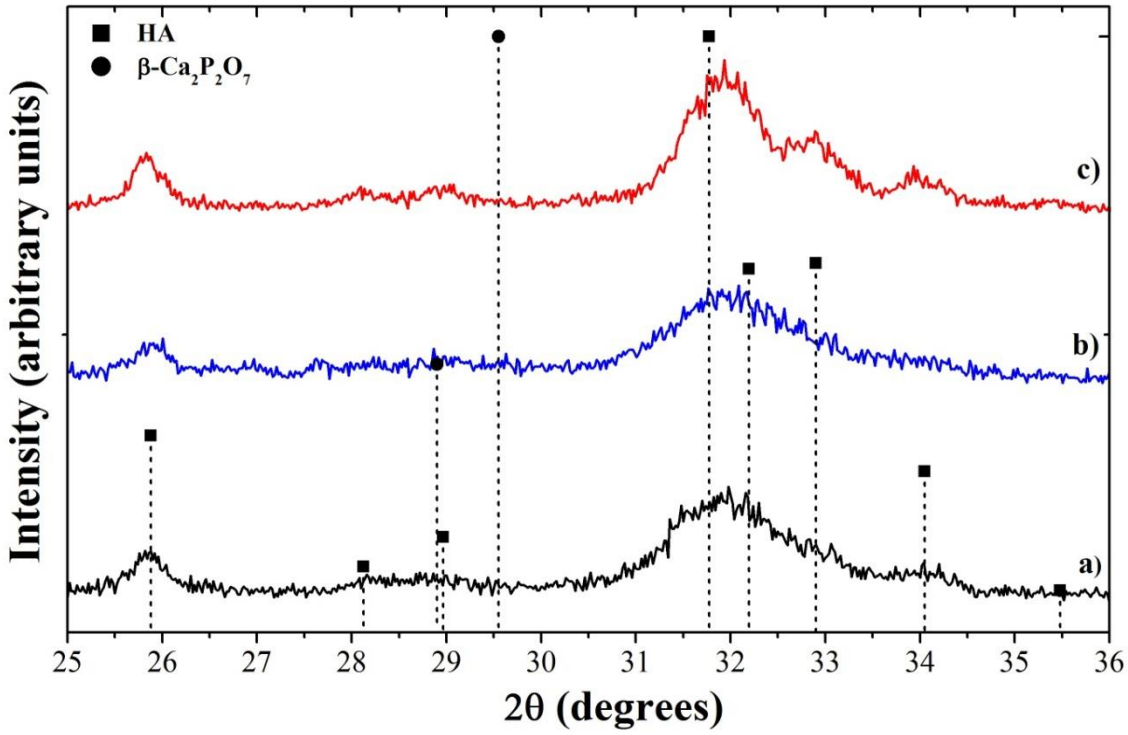

Figure 4.8: Influence of solute concentration and temperature on the crystal structure of HA heated to 600°C (a) AP09, (b) AP11, and (c) AP12

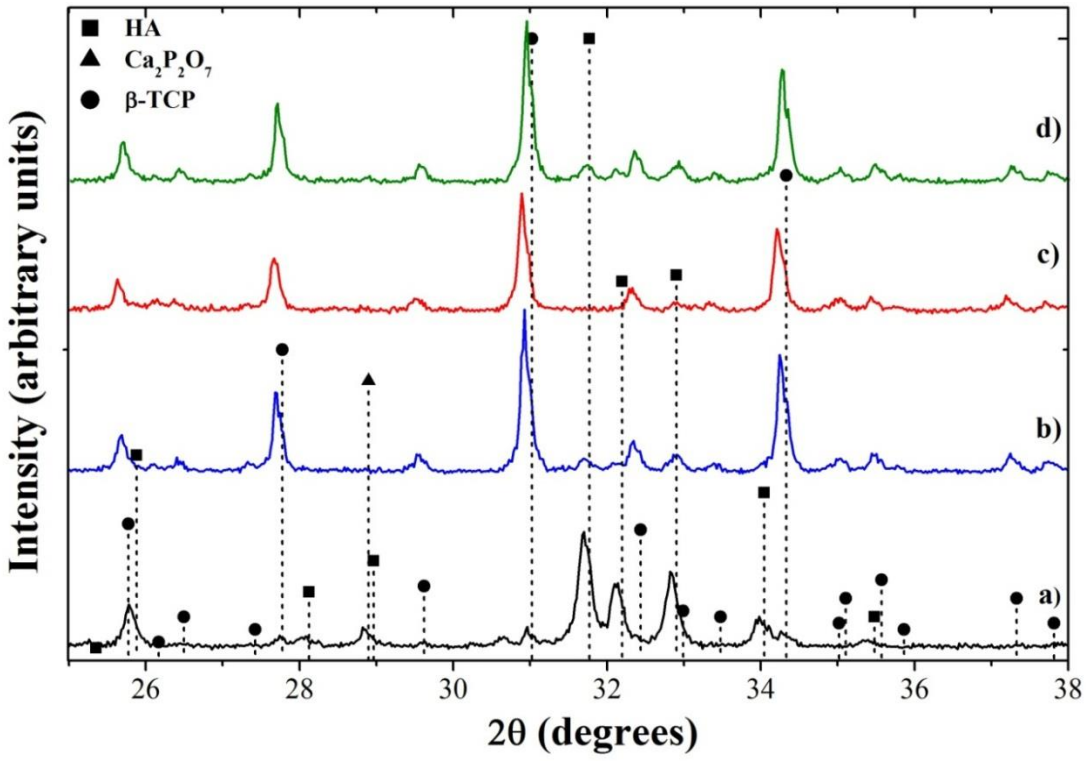

Figure 4.9: XRD patterns of (a) AP07, (b) AP10, (c) AP08, and (d) AP09 heated to 900°C

Line broadening analysis indicated no discernible increase in crystallite size between as-synthesised and powders heated to 600°C (Table 4.4). Heating to 900°C resulted in a significant increase in crystallite size of more than 200%. Equation 4.1 could not be

applied to as-synthesised powders since the hollow between the (112) (32.196°) and (300) (32.902°) peaks was not observed (Figures 4.4 and 4.5). XRD patterns of samples heated at 600°C demonstrate the hollow between the peaks of interest in samples AP07 and AP12 suggesting an increase in crystallinity.

4.4.3 Molecular structure

The samples with XRD patterns matching with HA (AP07 – AP12) were further analysed by FTIR and the major band assignments for HA and CHA are summarised in Table 4.5. OH^- and absorbed H_2O bands between 2500 and 3750cm^{-1} were very weak in all samples and this is suggested to be due to the relatively short ageing time, 1.5hrs (Figures 4.10 and 4.11). A weak band at approximately 875cm^{-1} was observed in all samples, which has been reported to correspond to CO_3^-. However, this attribution was made here since no introduction of carbonate was made during synthesis. Instead, this peak was assigned to HPO_4^{2-}, which can be incorporated into non-stoichiometric HA, i.e. CDHA.

Table 4.4: Influence of pH, temperature, and solute concentration on phase and XRD peak broadening

Sample	Calcination temperature (°C)	XRD peaks matched to	Crystallite size (nm)
AP05	As-synthesised	DCPD, DCPA	83
AP06			80
AP07	As-synthesised	HA	24
	600		27
	900	HA, β-$Ca_2P_2O_7$, β-TCP	54
AP08	As-synthesised	HA	21
	600		23
	900	HA, β-TCP	64
AP09	As-synthesised	HA	20
	600		24
	900	HA, β-TCP	63
AP10	As-synthesised	HA	22
	600		22
	900	HA, β-TCP	65
AP11	As-synthesised	HA	22
	600		23
	900	HA, β-TCP	83
AP12	As-synthesised	HA	21
	600		24
	900	HA, β-$Ca_2P_2O_7$, β-TCP	45

Notably, peaks within the region of 1300 – 1600cm^{-1} were exhibited in AP07, which could be misinterpreted as CO_3^- but due to the previous explanation this peak was attributed to PO stretch associated with DCPD [295].

Table 4.5: IR band assignments reported for HA and CHA [296, 297]

Assignments	Reported vibrational frequencies (cm^{-1})
PO_4 bend (ν_4)	566, 574, 600-604
Structural OH	632-635, 3565-3571
CO_3^- group	873-875
PO_4 stretch (ν_1)	961-963
PO_4 bend (ν_3)	1030-1038, 1090-1098
CO_3^- group (ν_3)	1418-1420, 1480-1487
Absorbed H_2O	1635-1640, 2500-3750
Soluble CO_2 (ν_3)	2331-2335, 2360

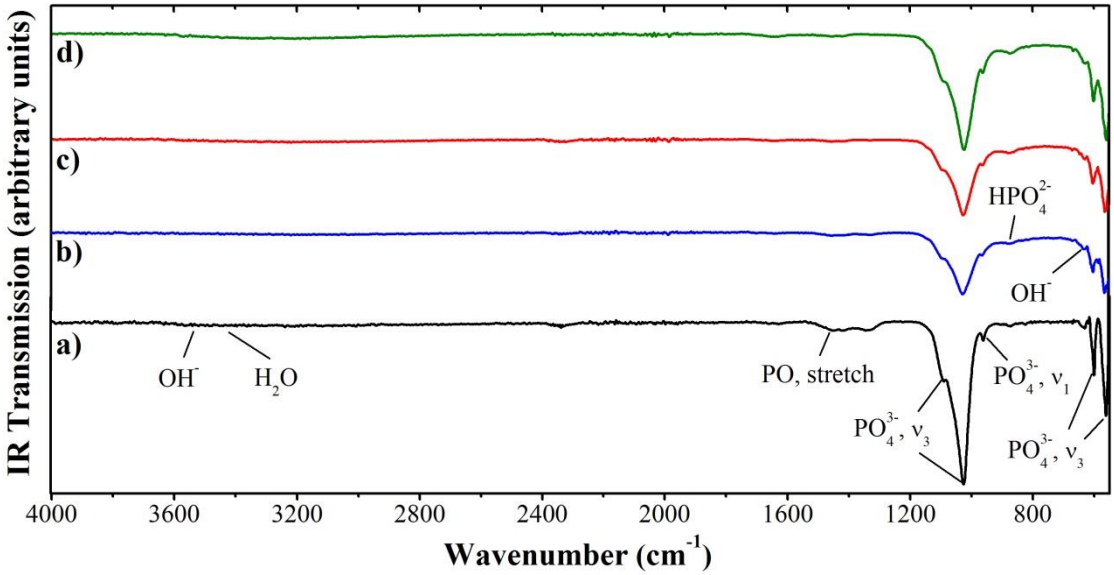

Figure 4.10: Influence of pH on FTIR spectra (a) AP07, (b) AP10, (c) AP08, and (d) AP09

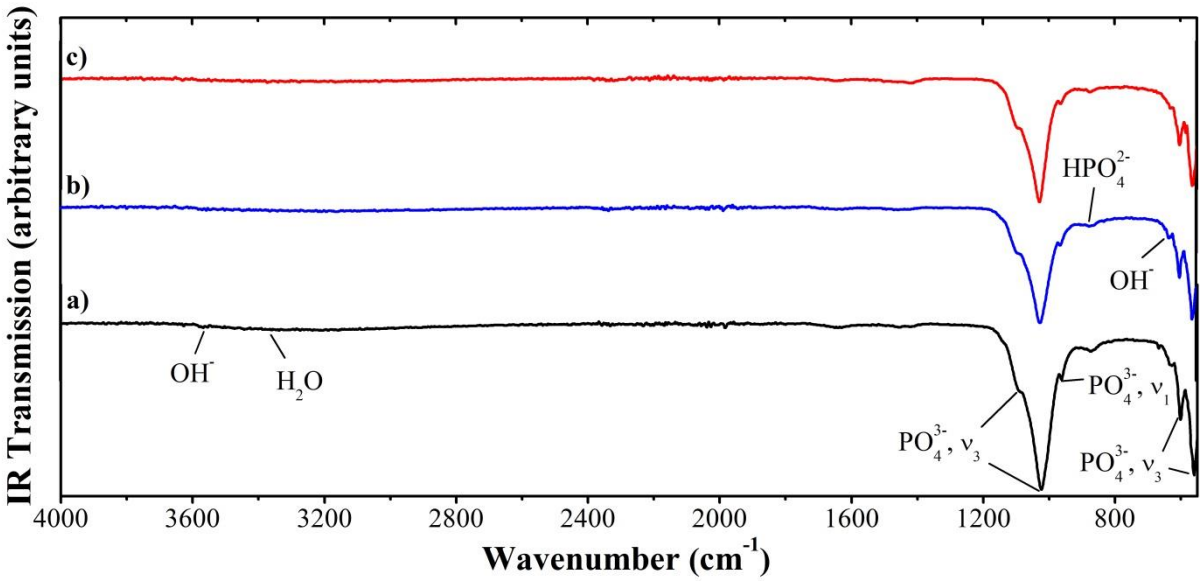

Figure 4.11: Influence of temperature and solute concentration on FTIR spectra (a) AP09, (b) AP11, and (c) AP12

FTIR analysis of samples AP07 – AP10 heated to 600°C revealed the disappearance of the band at 875cm^{-1} attributed to HPO_4^{2-} (Figure 4.12). There is no evidence of structural OH^- bands between 2500 and 3750cm^{-1} in all samples and at 635cm^{-1} in AP08 – AP10. In contrast, a band at 635cm^{-1} was present in spectra for AP07.

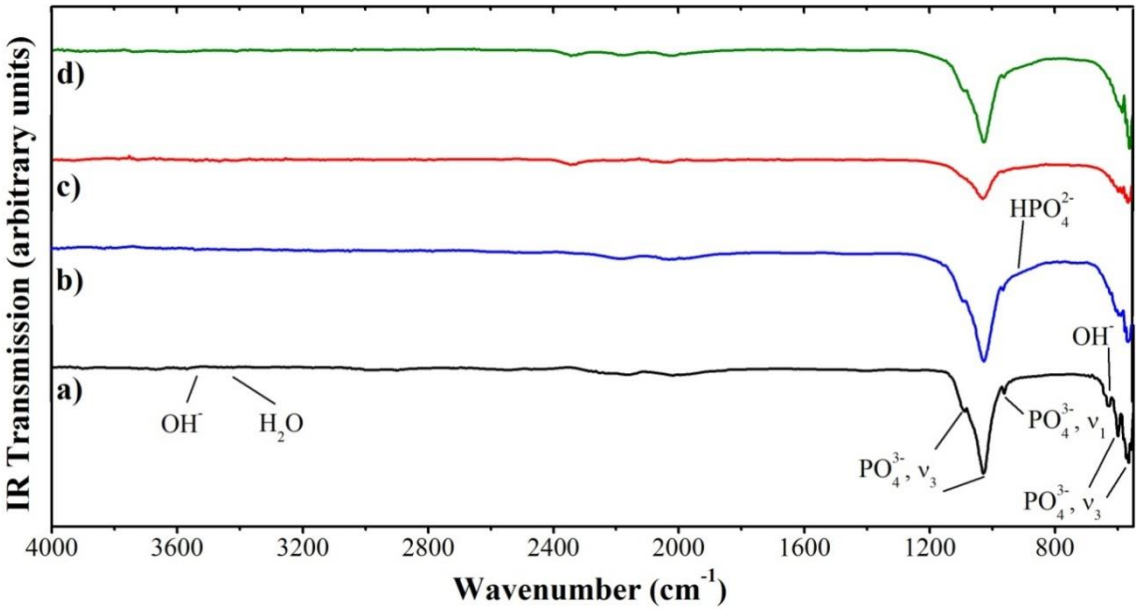

Figure 4.12: FTIR spectra of powders heated to 600°C (a) AP07, (b) AP10, (c) AP08, and (d) AP09

IR spectra of samples AP11 and AP12 demonstrated a difference in intensity and broadening of PO_4^{3-} bands (Figure 4.13).

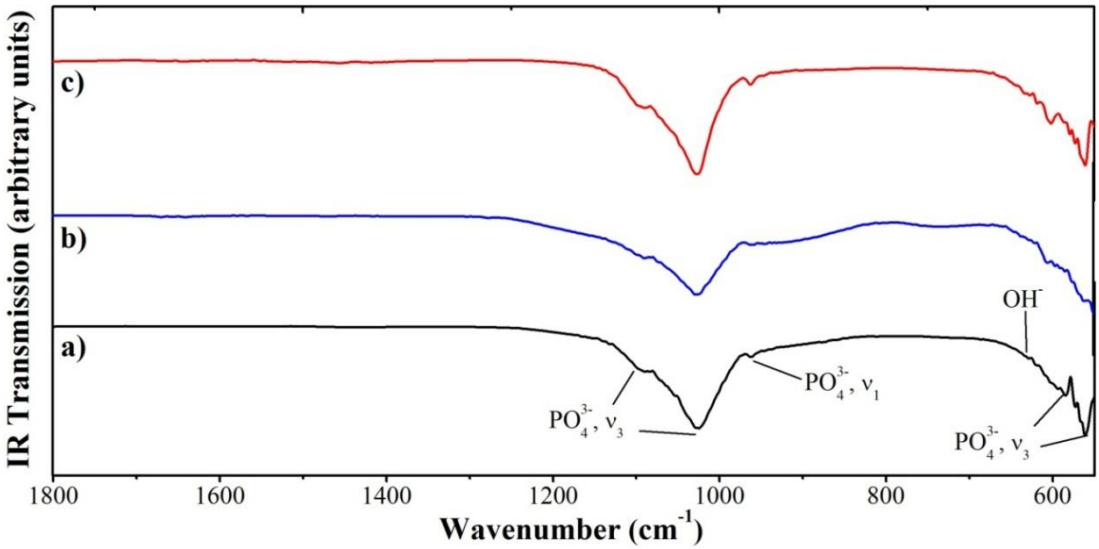

Figure 4.13: FTIR spectra of powders heated to 600°C (a) AP09, (b) AP11, and (c) AP12

AP07 – AP10 exhibited IR spectra typical of β-TCP when heated to 900°C (Figure 4.14). The appearance of the peak at approximately 3700cm^{-1} is associated with O-H stretching within HA and this band was notably absent for the sample AP07.

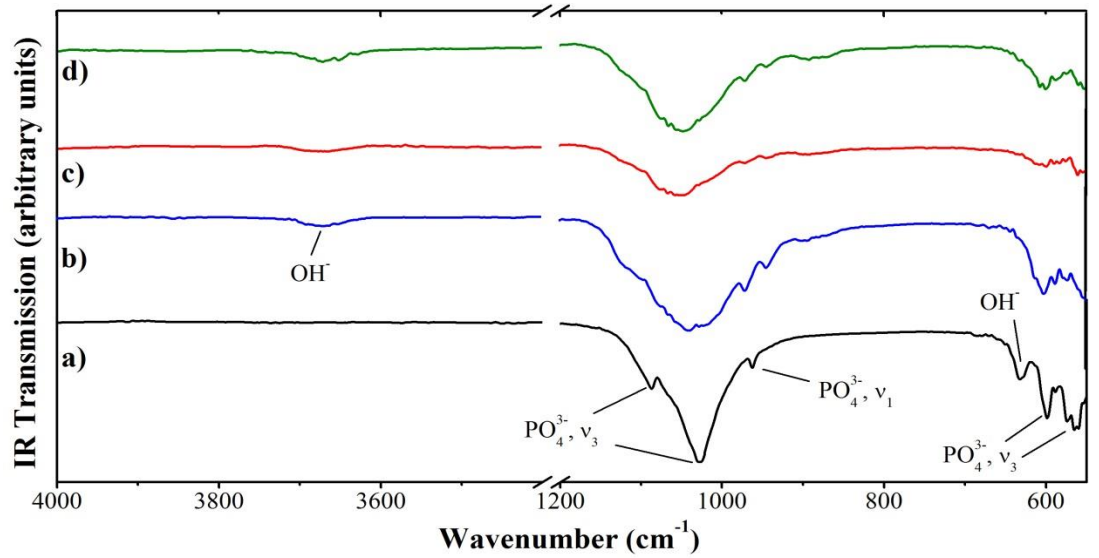

Figure 4.14: FTIR spectra of powders heated to 900°C
(a) AP07, (b) AP10, (c) AP08, and (d) AP09

4.4.4 Microstructural development

SEM micrographs revealed the polygonal morphology of particles of AP05 and AP06 compared with the typically globular morphology of all other samples (Figure 4.15). This difference was attributed to the phase change exhibited in these samples by XRD analysis (Figure 4.6).

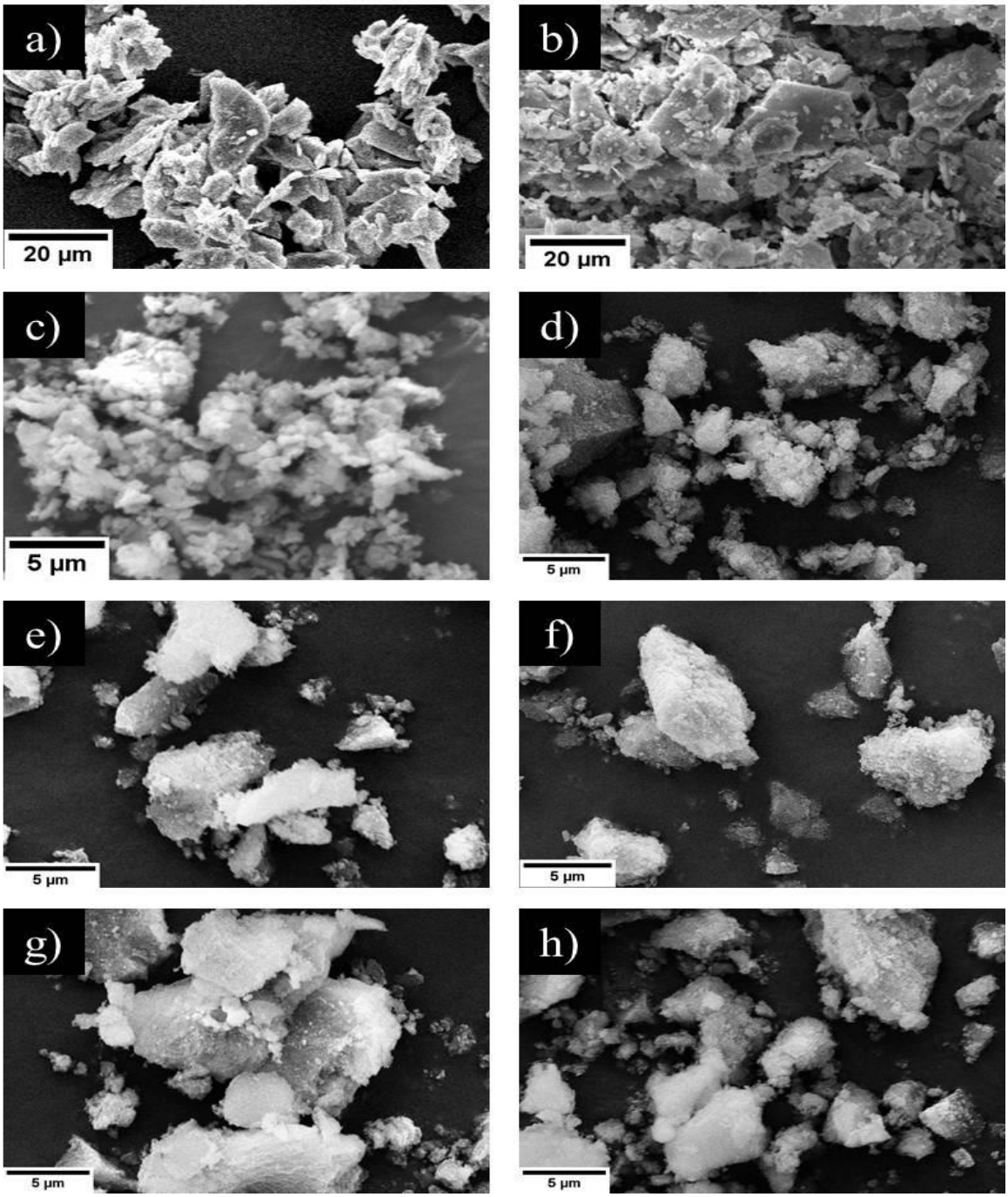

Figure 4.15: Influence of pH, temperature, and solute concentration on typical particle morphology (a) AP05, (b) AP06, (c) AP07, (d) AP08, (e) AP09, (f) AP10, (g) AP11, and (h) AP12

Bulk agglomeration occurred and a significant decrease in particle size was observed for samples AP07 – AP12 compared with AP05 – AP06 (Table 4.7). TEM micrographs revealed a needle-like morphology of AP07 crystallites with an average length and width of 32.8±10.1nm and 5.7±1.2nm, respectively (Figure 4.16)

Table 4.6: Influence of pH, temperature, and solute concentration on average particle and agglomerate size (n=3)

Sample	Average Size (μm)	
	Particles	Agglomerates
AP05	12.7±0.8	17.9±3.4
AP06	15.6±7.7	21.2±3.0
AP07	2.1±0.8	38.4±2.6
AP08	3.2±1.0	34.2±2.4
AP09	2.7±0.5	24.6±4.3
AP10	4.0±1.7	35.5±6.9
AP11	3.6±0.6	31.7±4.2
AP12	7.6±1.9	31.7±2.9

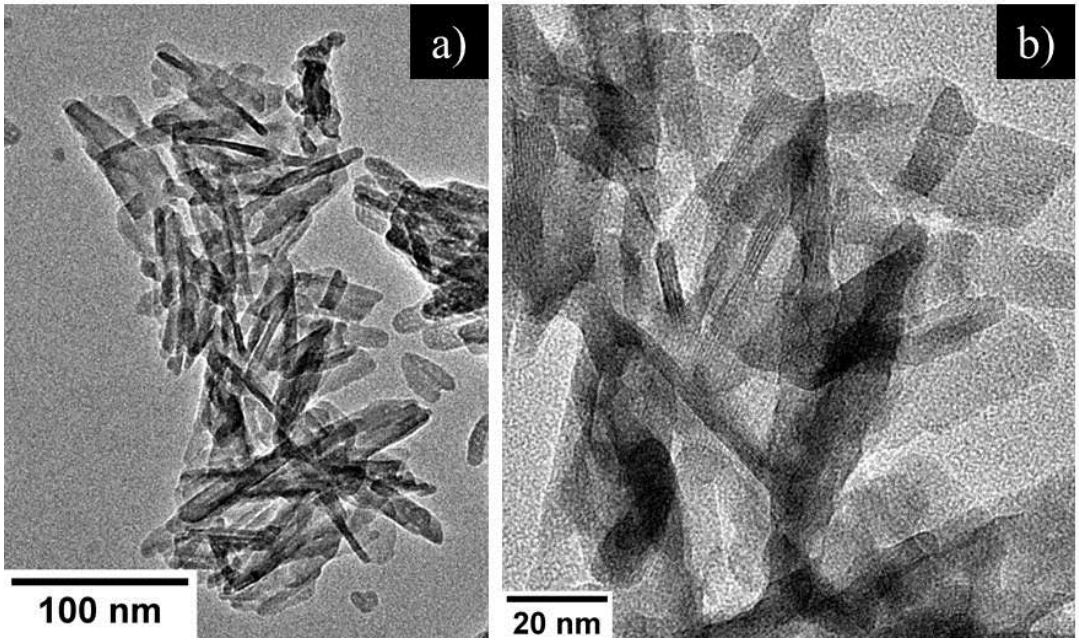

Figure 4.16: Typical crystallite morphology of (a) AP07 100nm scale bar, and (b) AP07 20nm scale bar observed by TEM

4.4.5 Thermal behaviour

Samples AP07 – AP12 were analysed by simultaneous DTA-TGA between 30 and 1300°C. Differentiation of TGA data (DTG) enabled distinctive regions of weight loss to be identified and attributed to previously reported reactions (Table 4.7). Figures 4.17 – 4.20 demonstrate the different combinations of DTG peaks exhibited, which were attributed to loss of water due to the occurrence of the reactions described by Equations 2.4 and 2.5.

Table 4.7: Summary of DTG analysis

Temperature region (°C)	Peak /gradual	DTA peak	Present in samples	Attribution
30 – 200	Peak	Endothermic	AP07 – AP12	N/A
200 – 300	Peak		AP07, AP10	Dehydration of DCPD to DCPA and subsequent condensation to $P_2O_7^{4-}$ (Equations 2.3 and 2.4)
250 – 700	Gradual	No peak observed	AP08, AP09, AP11, AP12	Dehydration of HPO_4^{2-} in CDHA to $P_2O_7^{4-}$ (Equation 2.4)
300 – 700			AP07, AP10	Dehydration of HPO_4^{2-} to $P_2O_7^{4-}$ (Equation 2.4)
700 – 800	Peak	Endothermic	AP08 – AP11	Reaction of β-$Ca_2P_2O_7$ (see above) and HA to form β-TCP (Equation 2.5)

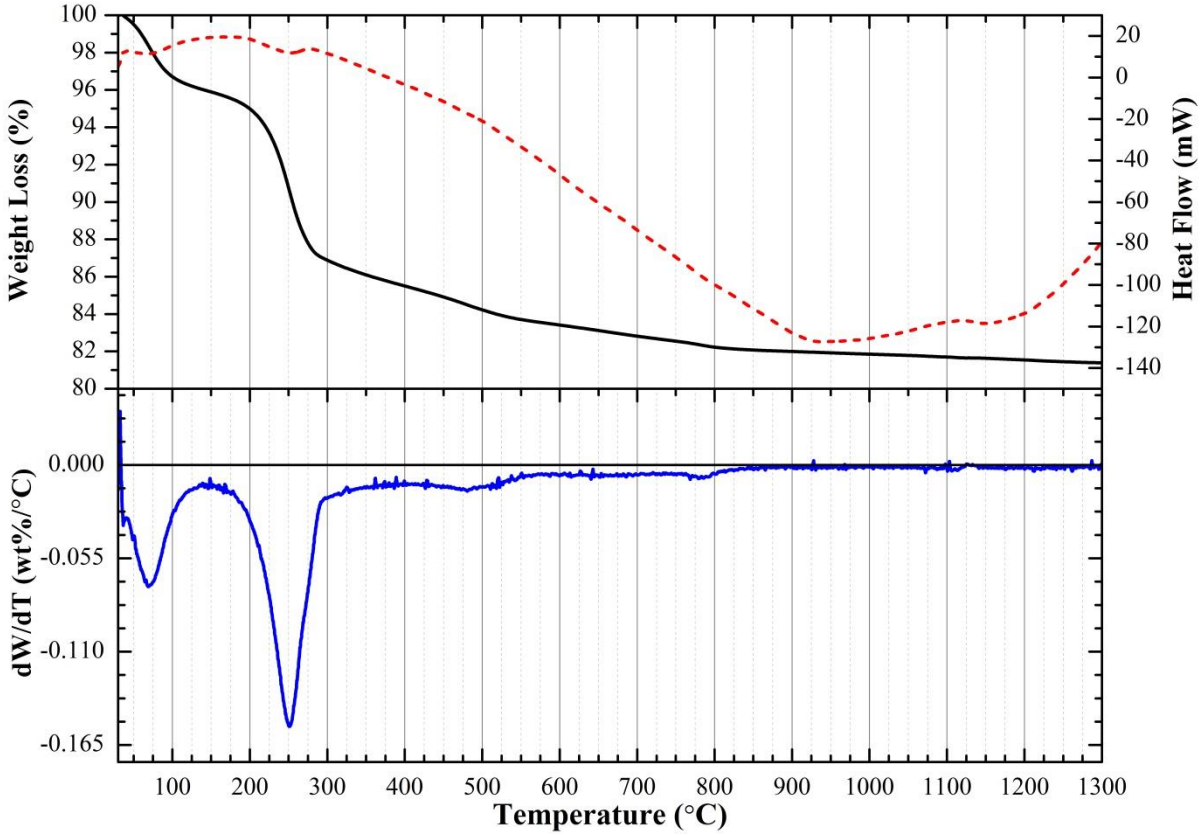

Figure 4.17: Thermal behaviour of AP07
(DTA = dashed red line, TGA = solid black line, DTG = solid blue line)

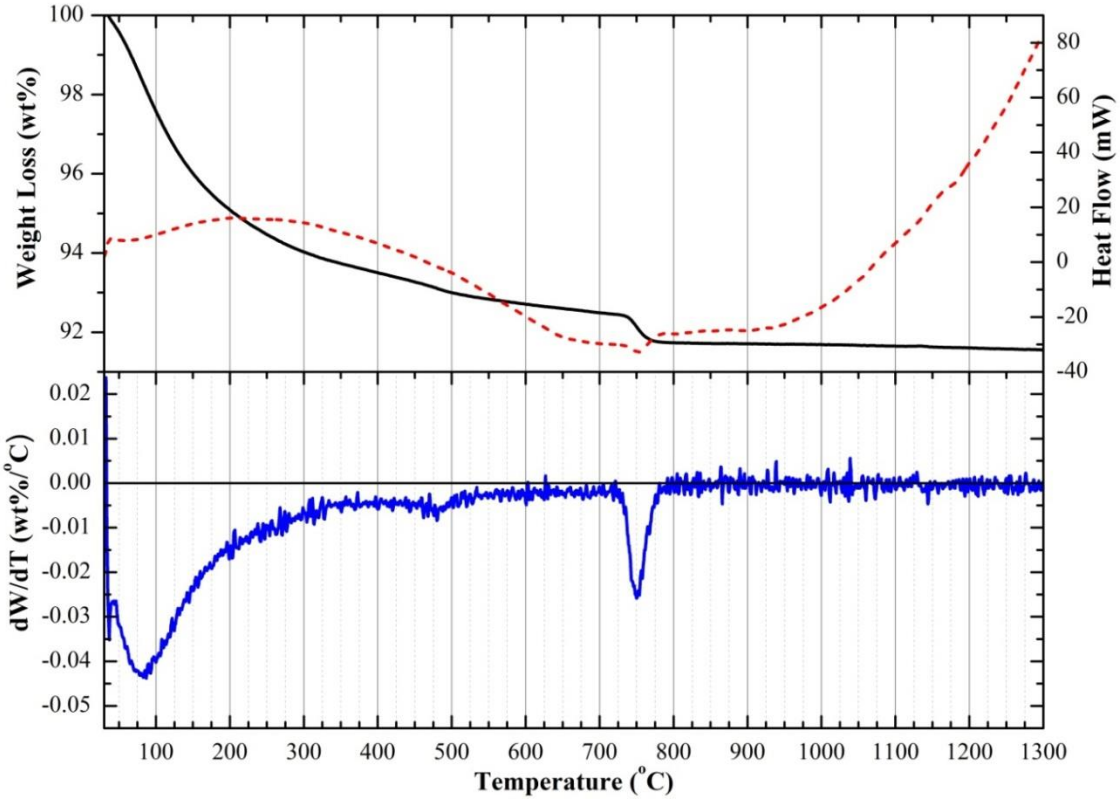

Figure 4.18: Thermal behaviour of AP09
(DTA = dashed red line, TGA = solid black line, DTG = solid blue line)

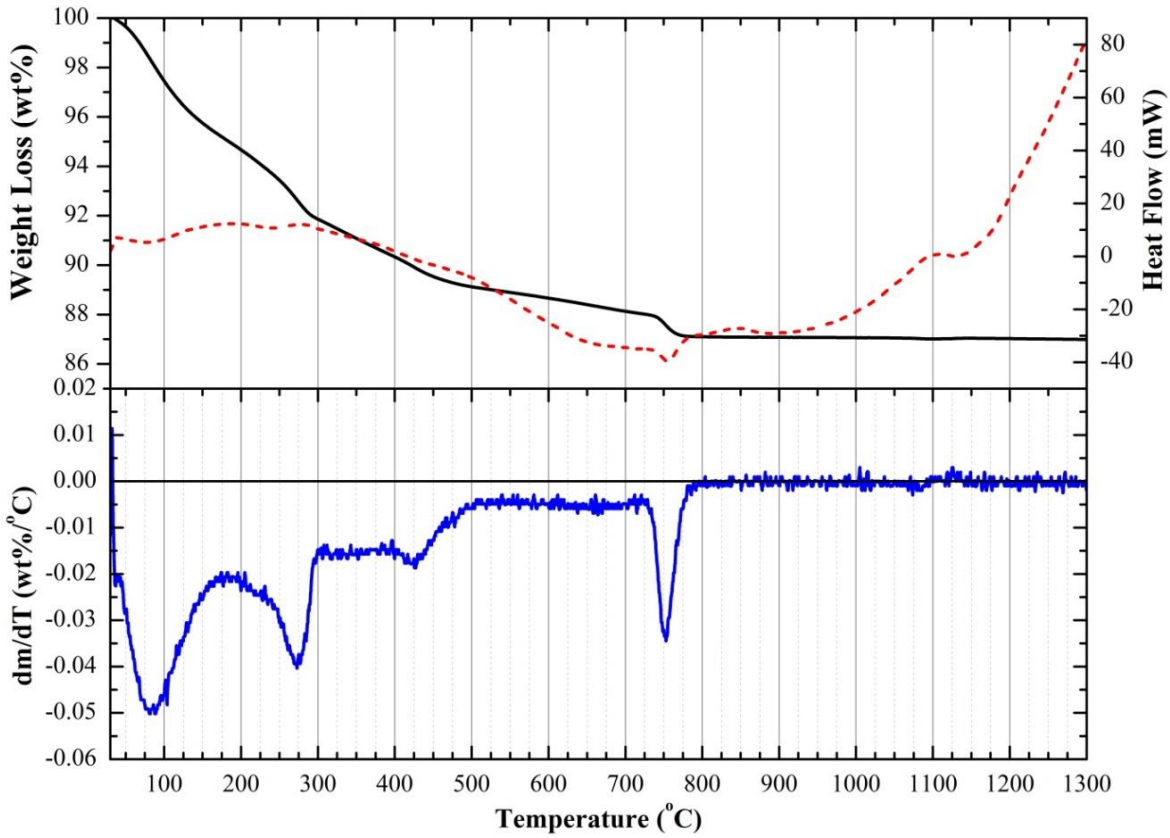

Figure 4.19: Thermal behaviour of AP10
(DTA = dashed red line, TGA = solid black line, DTG = solid blue line)

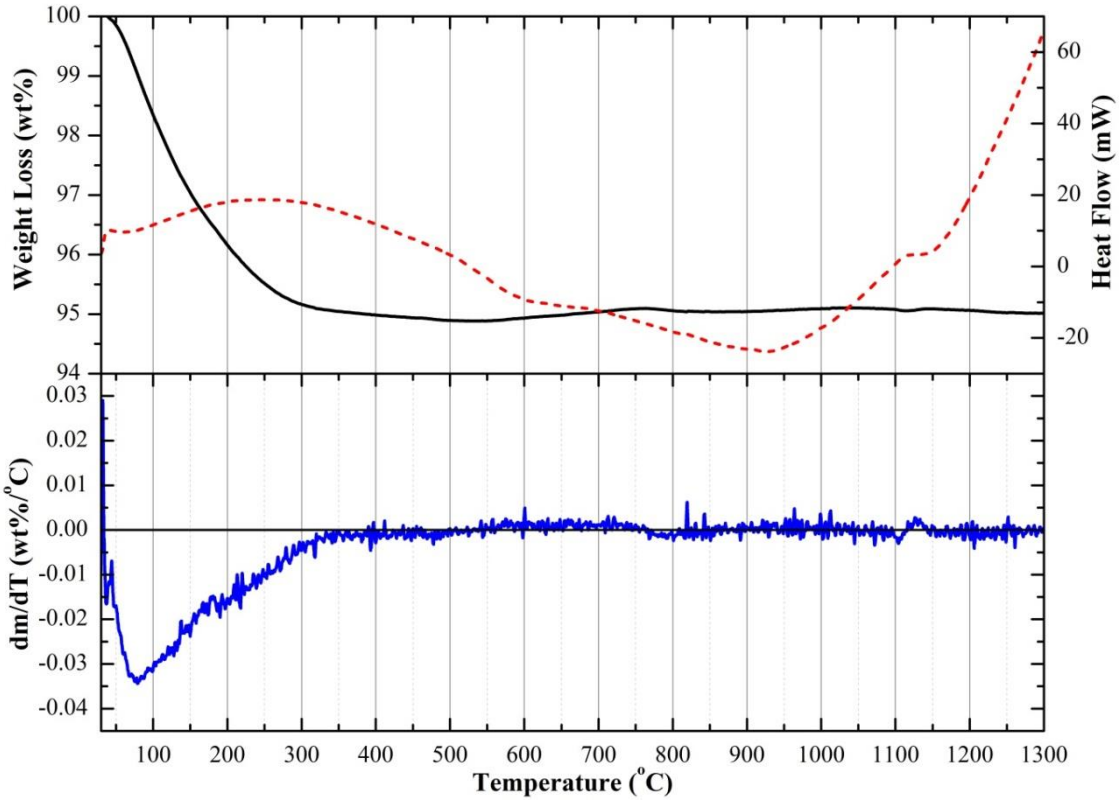

Figure 4.20: Thermal behaviour of AP12
(DTA = dashed red line, TGA = solid black line, DTG = solid blue line)

The amount of water loss within temperature regions associated with the reactions described by Equations 2.3 – 2.5 was determined by integrating the DTG curve with respect to temperature (Table 4.8). These results were used in combination with Equations 2.3 – 2.5 to determine the amount of non-apatitic HPO_4^{2-} and $P_2O_7^{4-}$ sourced from DCPD or CDHA, and the amount of HA and TCP residue at 800°C (Table 4.9).

Table 4.8: Influence of pH, temperature, and solute concentration on the amount of water lost between temperature regions associated with Equations 2.3 – 2.5
[a]temperature region adjusted to 300 – 700°C, [b]peak area between 700 to 800°C analysed, and [c]no DTG peak identified

Temperature region	Water loss (wt%)					
	AP07	AP08	AP09	AP10	AP11	AP12
200 – 300	8.67	N/A		2.81	N/A	
250 – 700	4.07[a]	2.40	1.98	3.73[a]	2.26	0.48
700 – 800[b]	0.59[c]	0.77	0.71	0.91	0.68	0.02[c]
30 – 800	17.78	8.45	8.26	12.90	8.71	4.94

Table 4.9: Influence of pH, temperature, and solute concentration on chemical composition calculated from DTG analysis using Equations 2.3 – 2.5
[a]temperature region adjusted to 300 – 700°C, [b]peak area between 700 to 800°C analysed

Temperature region (°C)	Ion/phase	Source	Weight (wt%)					
			AP07	**AP08**	**AP09**	**AP10**	**AP11**	**AP12**
200 – 300	HPO_4^{2-}	DCPD	18.48	N/A	N/A	5.99	N/A	N/A
250 – 700	HPO_4^{2-}	CDHA	43.37[a]	25.62	21.09	39.74[a]	24.08	5.12
	$P_2O_7^{4-}$		39.30	23.21	19.11	36.01	21.82	4.64
700 – 800[b]	$P_2O_7^{4-}$		5.67	7.42	6.82	8.75	6.54	0.21
	TCP		30.35	39.72	36.46	46.82	35.00	1.12
	HA		51.87	51.83	55.27	40.28	56.29	93.93
HA + TCP residue (mg)			8.20	11.47	8.49	13.28	11.59	8.40
TGA residue at 800°C			8.20	11.47	8.49	13.28	11.59	8.40

4.4.6 Elemental analysis

The influence of pH on the Ca:P ratio of samples AP07 – AP10 was determined by EDS and XRF (Table 4.10). EDS results indicate a non-stoichiometric Ca:P ratio and suggest samples are calcium-rich HA. In contrast XRF data suggests samples are CDHA.

Table 4.10: Infleunce of pH on Ca:P ratio calculated from EDS and XRF analysis

Sample	Ca:P ratio calculated from EDS	Ca:P ratio calculated from XRF
AP07	2.03±0.02	1.66
AP08	2.16±0.04	1.56
AP09	2.17±0.03	1.52
AP10	2.11±0.02	1.57

4.4.7 Surface area

The surface area of AP07 was found to be significantly lower than samples AP08 – AP12. Furthermore, AP12 was observed to be significantly higher than all other samples (Table 4.11).

Table 4.11: Influence of pH, temperature and solute concentration on the surface area of as-synthesised powders

Sample	Surface area (m^2/g)
AP07	72.7±0.1
AP08	100±0.2
AP09	106.7±0.2
AP10	104.1±0.2
AP11	111.1±0.2
AP12	132.3±0.7

4.4.8 Surface charge

The ZP of as-synthesised samples AP07 – AP10, and AP12 were measured in DI water (Table 4.12). A positive ZP was observed as a result of a relatively low uncontrolled pH value during addition of the PO_4 solution (AP07) and an increase in reaction temperature (AP12). Due to the influence of surface charge on cell adhesion the difference in the sign of ZP recorded for AP07 and AP12 is expected to alter the relative morphology of any adhering cells.

Samples AP07 and AP09 were dispersed in cell culture medium (DMEM) and ZP was measured every 30mins over a 60hr period, and after approximately 7 days (Figure

4.21). Over the initial 60hrs no significant difference in ZP was observed. However, after 7 days AP07 was shown to exhibit a less negative ZP value compared with AP09. Linear regression of data demonstrated the same value for gradient but opposite sign, i.e. ZP measurements were increasingly less negative for AP07 and more negative for AP09 over time.

Table 4.12: Influence of pH, temperature, and solute concentration on ZP of as-synthesised particles measured in DI water at 25°C

Sample	ZP (mV)
AP07	0.525
AP08	-16.8
AP09	-21.3
AP10	-19.1
AP12	2.98

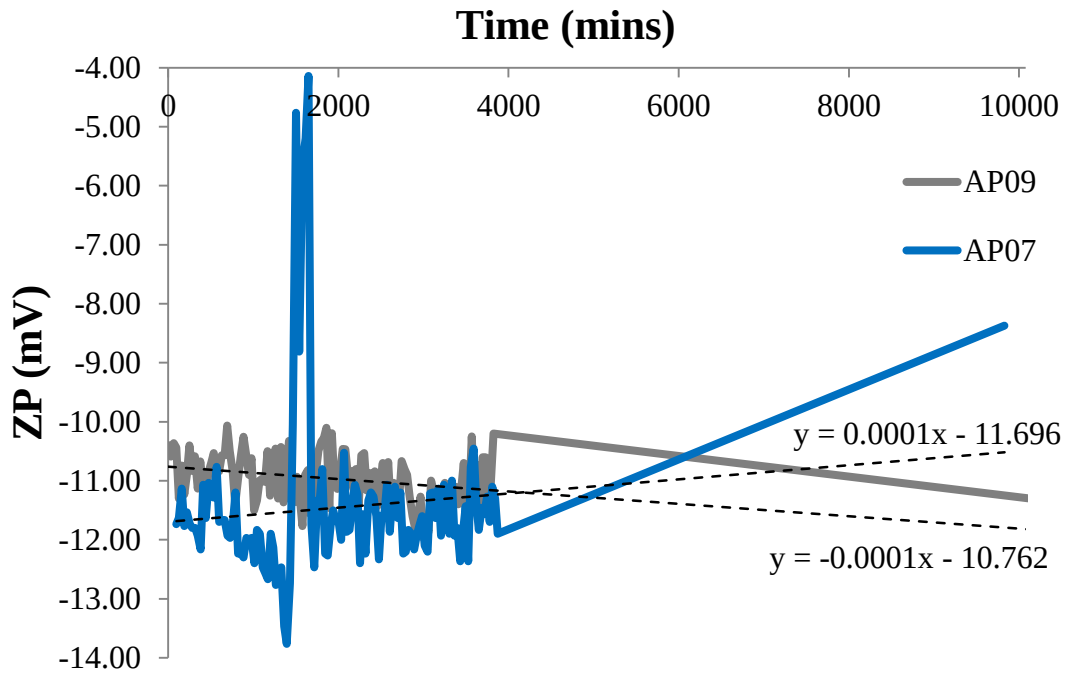

Figure 4.21: ZP measurements over time for samples AP07 and AP09 in DMEM at 37°C

4.4.9 SBF test

Prior to immersion in SBF (i.e. day 0) the surface of pellets formed by pressing powders was visualised by SEM (Figure 4.22) and the surface roughness characterised quantitatively by white light interferometry (Figure 4.23). AP07, AP08, and AP12 were observed to exhibit a lower surface roughness at day 0 compared with other samples. A peak in the degree of surface roughness was observed at day 7 or 14.

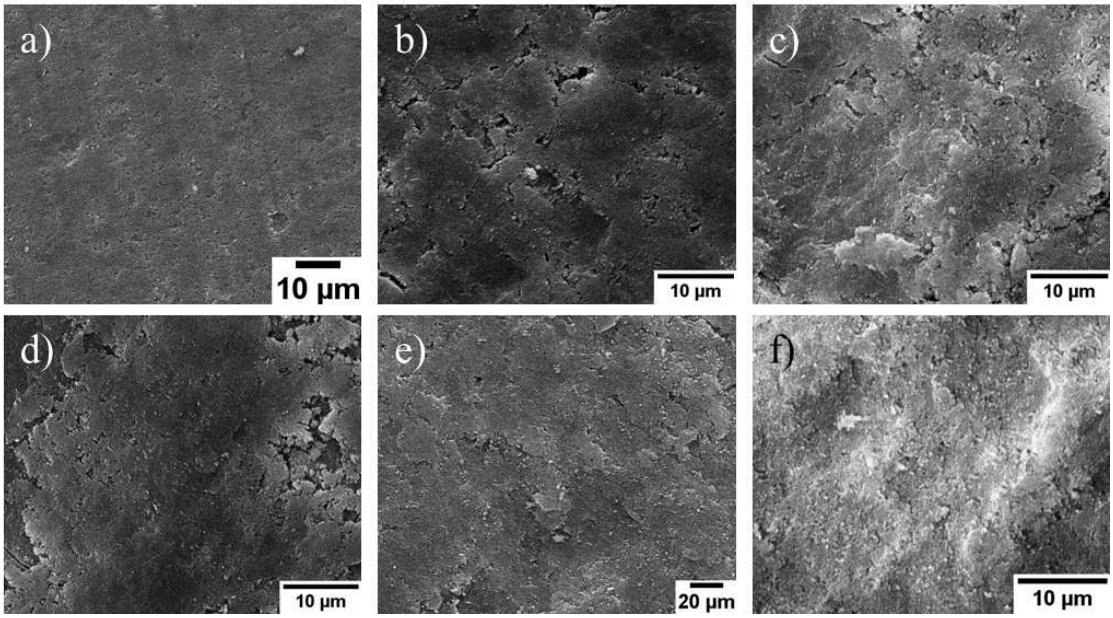

Figure 4.22: Pellet surface prior to immersion in SBF visualised by SEM (a) AP07, (b) AP08, (c) AP09, (d) AP10, (e) AP11, and (f) AP12

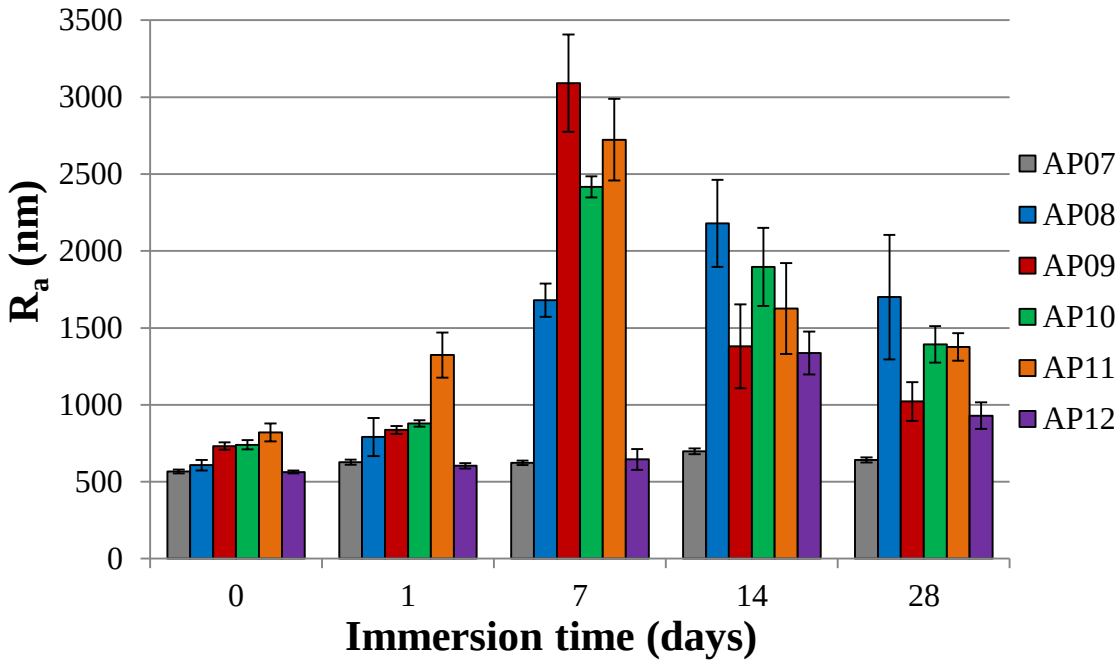

Figure 4.23: Surface roughness (R_a) of pellets immersed in SBF for up to 28 days

SEM images of pellets immersed in SBF demonstrated the growth of a layer on the surface of pellets from day 7 (Figure 4.24 a – dotted blue circle). Typically needle-like particles were observed within this coating (Figure 4.24 b – solid purple circle). After immersion in SBF all samples were shown to exhibit some degradation as indicated by the presence of globular fragments on the surface of substrates (Figure 4.24 a – dashed red circle), which are suggested to alter surface roughness.

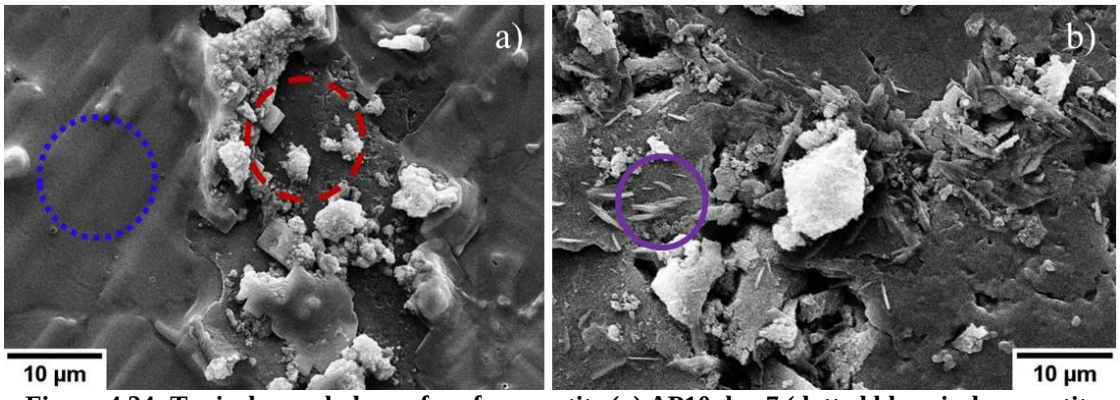

Figure 4.24: Typical morphology of surface apatite (a) AP10 day 7 (dotted blue circle = apatite layer, dashed red circle = pellet surface), and (b) AP12 day 14 (solid purple circle = needle-like morphology of apatite)

4.4.10 Live/dead assay

Fluorescence micrographs demonstrated the viability (green) of MC3T3 osteoblast precursor cells seeded on samples AP08 – AP11 from days 1 – 7 (Figure 4.25). The extent of dead cells (red) observed were minimal and therefore can be associated to the preparation method. The density of live cells on these samples was clearly shown to increase over time and the typical morphology changed from rounded (day 1) to elongated (day 7). These factors are all conducive to the conclusion that these substrates are cytocompatible with osteoblast cells, and support adhesion, spreading, and proliferation.

In contrast, a higher number of cells was observed to be non-viable on AP12 at day 1 and from day 3 onwards the vast majority of osteoblasts were non-viable. The morphology of seeded osteoblasts was found to be rounded, which is typical of apoptotic cells (Figure 4.25). Seeding of cells on AP07 was revealed to result in the death of the cell population at day 1, indicating the cytotoxic effect of this sample on MC3T3 cells. Therefore AP07 was not included in further cell culture studies.

4.4.11 MTT assay

The metabolic activity of live MC3T3 cells seeded on to substrates and tissue culture plastic (TP) was quantitatively measured by MTT assay (Figure 4.26). Results suggest that the control of pH (AP09 – AP11) compared with adjustment (AP08) greatly improves the ability of HA substrates to support osteoblast proliferation over the culture period (Table 4.13). However, it seems that this marked effect is dominated by the influence of an increase in synthesis temperature (AP12). An increase in solute

concentration enhanced the relative proliferative rate and the number of metabolically active cells seeded on AP11, which was notably higher at days 5 and 7 compared with other samples. In contrast, a marked reduction was observed at days 5 and 7 for AP12 compared with other samples prepared under controlled or adjusted pH conditions.

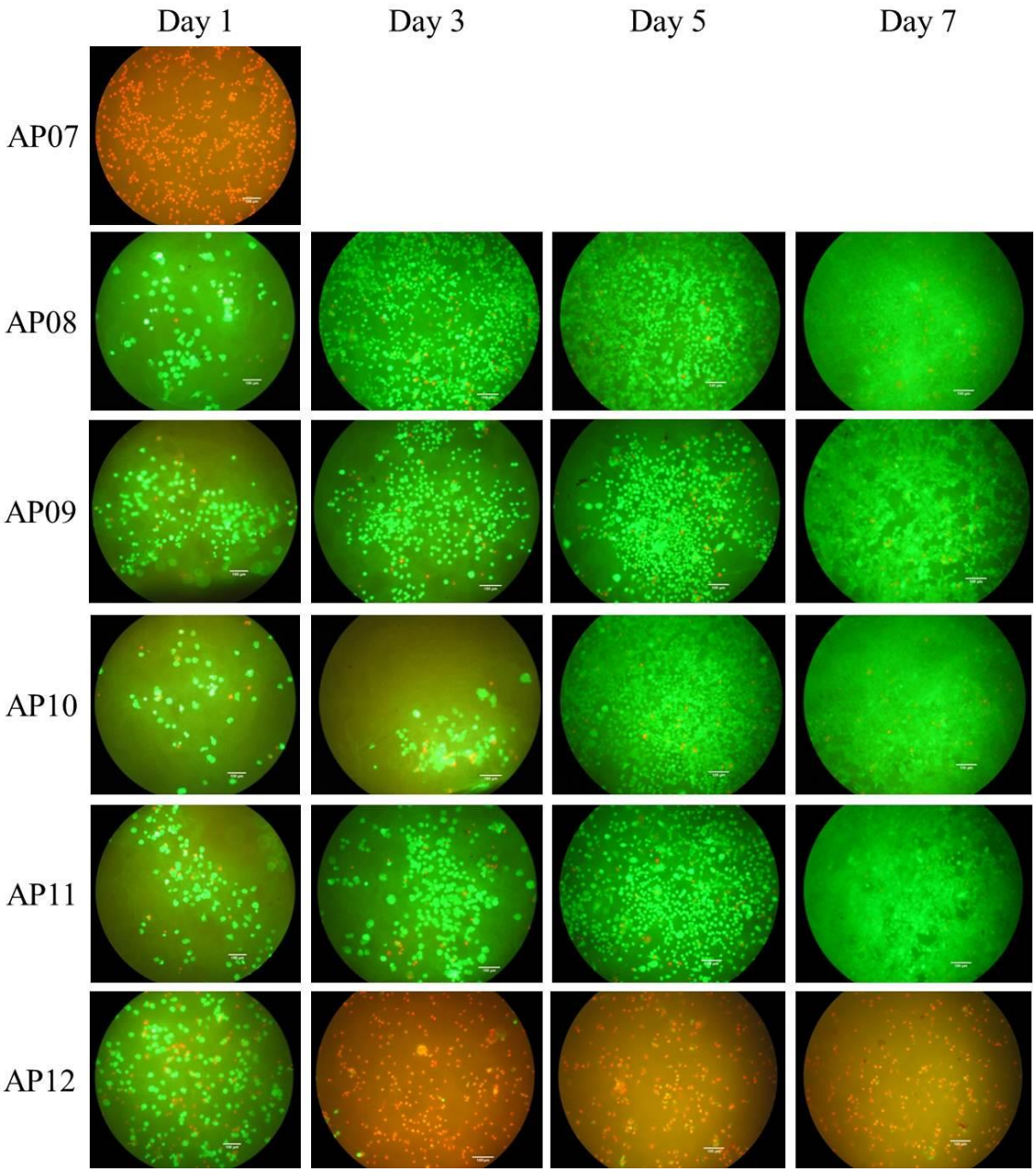

Figure 4.25: Influence of pH, temperature, and solute concentration on the viability of MC3T3 osteoblast precursor cells seeded on substrates (green = live, red = dead)

ANOVA analysis revealed that osteoblasts seeded on substrates and TP exhibited a significant increase in the number of metabolically active cells at day 7 compared with day 1 (Table 4.14). Analysis of significance via the modified ANOVA method was not

conducted on AP08 using a linear trend from days 1 – 3 because regression lines exhibited a negative gradient. In contrast to the standard test, statistical significance was not demonstrated using the modified ANOVA test for AP10 or AP12 at day 7 using either trend line. No samples were revealed to exhibit a significant increase in metabolic activity at day 5 compared with day 1 (Table 4.14).

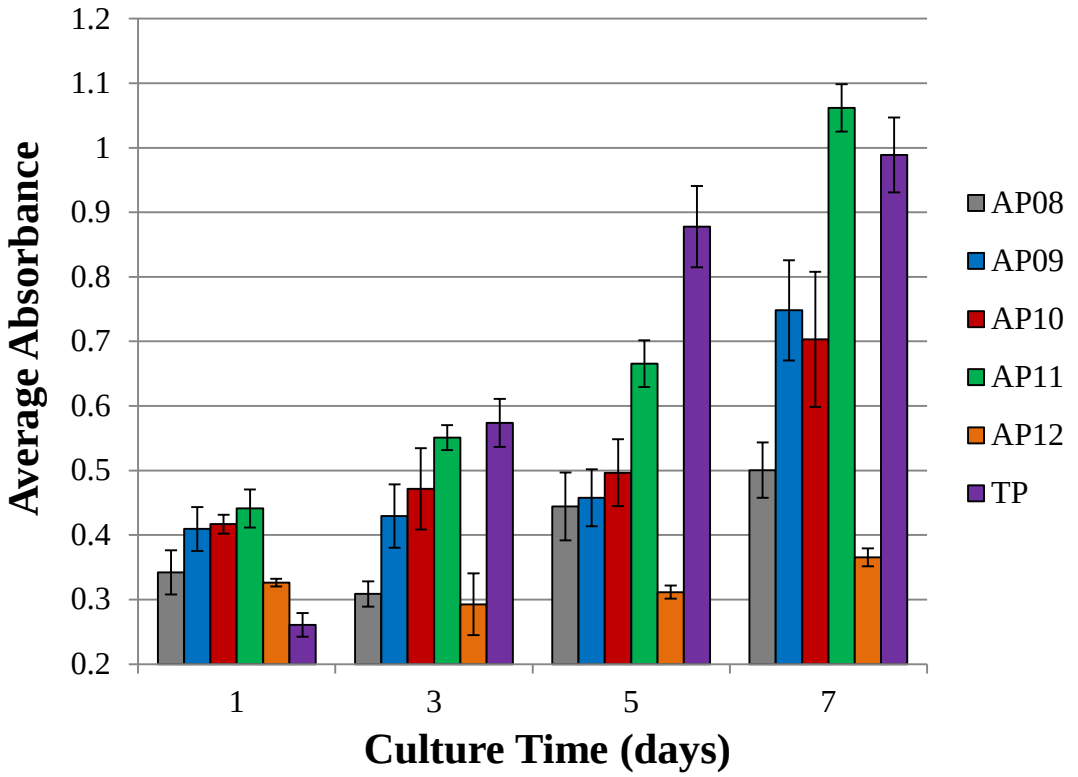

Figure 4.26: Influence of pH, temperature, and solute concentration on the metabolic activity of MC3T3 cells

Table 4.13: Influence of pH, temperature, and solute concentration on the proliferative rate of MC3T3 cells assessed by MTT assay between 1 and 7 days

Sample	Proliferative rate (%)
AP08	46.3
AP09	82.8
AP10	68.7
AP11	140.7
AP12	11.9
TP	279.2

Table 4.14: Statistical analysis of MTT assay samples AP08 – AP12
F_{crit}=4.965 when p<0.05, * = statistically significant

Sample	ANOVA test	Modified ANOVA test		
	Day 7 *F* ratio	Day 7 *F* ratio		Day 5 *F* ratio
		Trend 1-3	Trend 1-5	Trend 1-3
AP08	50.215*	N/A	0.632	N/A
AP09	96.317*	7.237*	6.842*	0.212
AP10	44.015*	2.935	3.662	-0.704
AP11	1043.828*	12.817*	10.697*	0.217
AP12	40.316*	4.481	2.428	1.679
TP	767.697*	-18.333	-5.764	-2.765

4.4.12 Hoechst assay

An increase in the average fluorescence measured using a Hoechst 33258 dye that stains DNA was observed for MC3T3 precursor osteoblasts seeded on samples AP08 – AP11 between day 1 and 7 of culture, which corresponds to an increase in cell number and indicates that these substrates support proliferation (Figure 4.27). AP08 demonstrated a significantly lower proliferative rate compared with AP09 – AP11 (Table 4.15), which may be due to the large experimental variation as indicated by the standard deviation error bars (Figure 4.27). The cell number observed at day 7 for AP10 was shown to be significantly higher compared with other HA substrates. In contrast to other specimens, results indicate that AP12 did not support proliferation since a decrease in cell number was observed at day 7 compared with day 1.

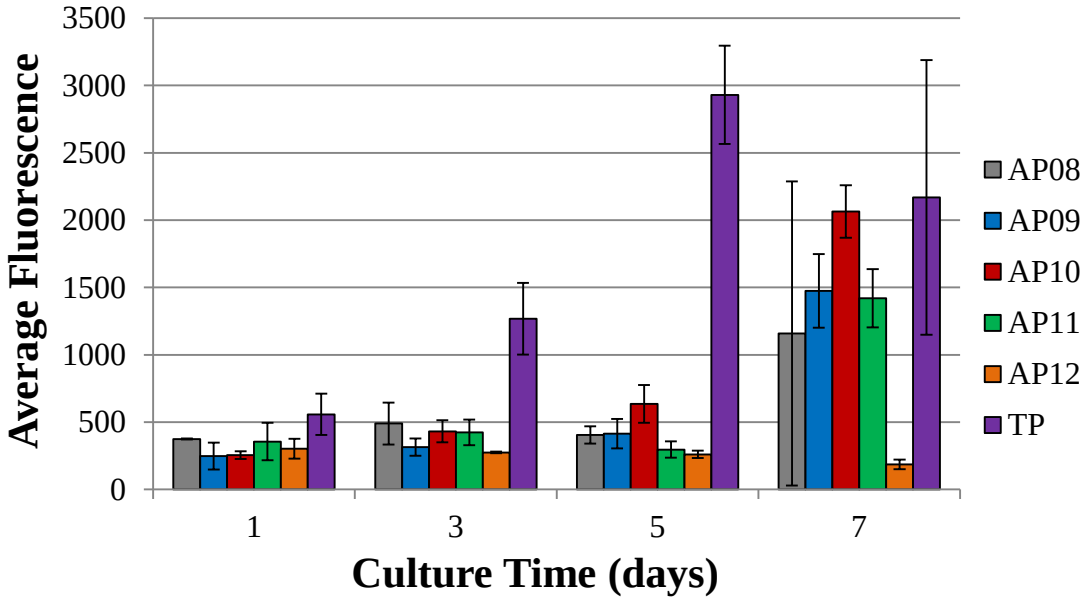

Figure 4.27: Proliferation of MC3T3 cells on substrates prepared under different pH, solute concentration, and temperatures assessed by Hoechst assay

Table 4.15: Influence of pH, temperature, and solute concentration on the proliferative rate of MC3T3 cells assessed by Hoechst assay between 1 and 7 days

Sample	Proliferative rate (%)
	Day 1-7
AP08	42.3
AP09	431.4
AP10	626.0
AP11	256.0
AP12	-21.5
TP	477.2

ANOVA testing revealed statistically significant growth between days 1 and 7 for all samples except AP08 (Table 4.16) and this is attributed to the large variation in experimental data (Figure 4.27). The modified ANOVA method distinguished AP12 as non-significant and the calculated negative *F* ratios reflect the decrease in cell number between days 1 – 5, and 1 – 3. *F* ratios calculated for day 5 using the modified ANOVA method did not indicate any statistically significant differences compared with day 1 data, suggesting that the exponential cell growth phase occurs after day 5. The negative values obtained for AP08 and AP11 indicate that the experimental cell number at day 5 was less than the projected value, calculated linearly from day 1 and 3 data. These observations suggest that the lag cell growth phase occurs up to day 5 (Appendix A).

Table 4.16: Statistical analysis of Hoechst assay
F_{crit}=7.709, where p<0.05, * = statistically significant

Sample	ANOVA test	Modified ANOVA test		
	Day 7 *F* ratio	Day 7 *F* ratio		Day 5 *F* ratio
		Trend 1-3	Trend 1-5	Trend 1-3
AP08	2.887	4.896	7.654	-2.237
AP09	106.892*	14.895*	12.780*	0.508
AP10	507.364*	25.684*	15.947*	0.557
AP11	102.197*	8.855*	11.667*	-2.011
AP12	11.822*	-0.786	-0.547	0.297
TP	14.656*	-2.927	-1.299	-1.253

4.4.13 Cellular internalisation

Combined bright field and confocal fluorescence images of MC3T3 cells exposed to AP07 – AP10 powders for 24hrs revealed the internalisation of particles (Figure 4.28).

Aggregation of internalised AP07 and AP08 particles was detected in multiple cells and the typical morphology of osteoblasts was more rounded compared to elongated MC3T3 cells containing AP09 and AP10.

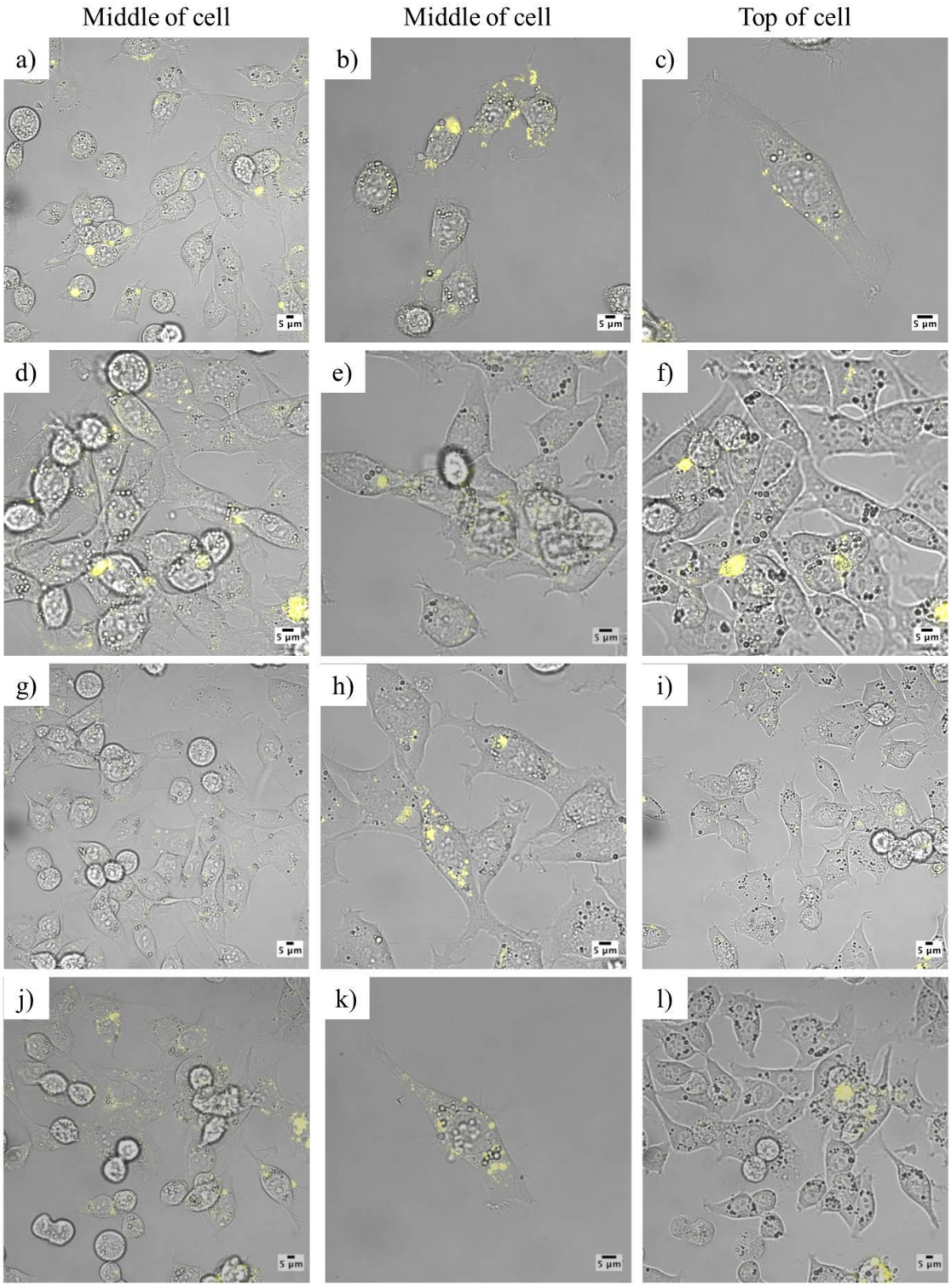

Figure 4.28: Combined bright field and fluorescence images of MC3T3 cells exposed to particle of (a – c) AP07, (d – f) AP08, (g – i) AP09, and (j – l) AP10. Images in columns 1 and 2 are slices from a confocal z stack taken through the middle of the cell, and column 3 at the top of the cell

4.5 Discussion

The attributions made from DTA-TGA analysis revealed a number of endothermic weight loss regions, which were ascribed to the chemical reactions described by Equations 2.3 – 2.5 (Table 4.7). Notably, for samples AP07 and AP10, which were both prepared at pH 10, a rapid endothermic loss of weight between 200 and 300°C was demonstrated by DTG and upon closer inspection it appears that the onset of this peak begins at approximately 175°C. Thus these losses were attributed to the dehydration of DCPD to DCPA and subsequent condensation to β-$Ca_2P_2O_7$, which have been reported to occur at 180°C and 320 – 340°C, respectively [217]. Despite these water losses inferring 18 and 6% content of non-apatitic HPO_4^{2-} ions due to DCPD within AP07 and AP10 (Table 4.9), respectively no obvious traces of this phase were identified in XRD patterns of as-synthesised samples (Figure 4.4). A trace amount of DCPD appeared to be present in AP07 but due to the close proximity to characteristic HA peaks this attribution cannot be made with confidence. In contrast, noticeable peaks in IR spectra, previously associated with DCPD [295], were observed in AP07 but not for AP10 (Figure 4.10). At the lowest pH recorded during precipitation of AP07 (5.60) the solubility of HA and DCPD are relatively close (Figure 2.7), hence it is plausible that this secondary phase could form. Since it is likely that FTIR would detect the HPO_4^{2-} concentration attributed to dehydration of DCPD calculated for AP10 (6%) this suggests AP07 and AP10 were formed via different mechanisms, which is likely due to the observed differences in pH development (Table 4.3). When comparing the DTG plots the major variance between these two samples is the absence of a DTG peak between 700 and 800°C for AP07. Elliott reported that CDHA prepared via the hydrolysis of DCPA would demonstrate weight loss between 250 – 300°C [17]. The combination of weight loss within this region and between 700 – 800°C as well as no presence of DCPD in FTIR or XRD patterns suggests AP10 is a CDHA formed via an intermediate DCPA phase. It has been reported that unstable precursor phases can form prior to HA and the composition of this phase is dependent on pH [196-199]. However, the solubility isotherms for different CaP phases (Figure 2.7) validates that HA is the most stable phase over the bulk solution pH range (9.83 – 10.09) recorded during the precipitation of AP10, and formation of DCPA under these conditions is unlikely. It should however be noted that local pH (i.e. the pH at nucleation sites) might not be equal to

the measured bulk value due to the vast potential number of different ionic species present within the solution. Thus it is plausible that final crystallites of AP10 formed via a transitional DCPA phase.

Interestingly, AP12 did not exhibit DTG peaks between either 200 – 300°C or 700 – 800°C, which explains the calculated lower weight loss (Table 4.8). According to Equations 2.3 – 2.5 these observations infer under these conditions that precipitates do not contain DCPD, form via an intermediate DCPA phase or contain large amounts of non-apatitic HPO_4^{2-}. XRD analysis revealed no presence of secondary phases up to 600°C and notably, compared with AP09 and AP11, (112) and (300) HA peaks were not superimposed when samples were heated to 600°C. Since this was not accompanied with a significant change in the broadening of the (200) peak (i.e. a change in crystallite size) this observation suggests a relatively higher crystalline fraction in AP12. Since no DTG peak was shown between 700 – 800°C for either AP07 or AP12 and β-$Ca_2P_2O_7$ was detected in XRD patterns of samples heated to 900°C this suggests that the reaction represented by Equation 2.5 was uncompleted or did not occur. In the case of AP12 is it likely this phase transformation did not take place since a relatively low content of non-apatitic HPO_4^{2-} was calculated from thermal analysis (Table 4.9) Therefore it is suggested that AP12 exhibits a Ca:P ratio closer to stoichiometric HA compared to CDHA samples prepared at lower temperatures under the same pH conditions, for example AP09.

AP08 and AP09 were both prepared at pH 11 and exhibited DTG peaks within the same temperature regions, <250°C and 700 – 800°C, with a gradual weight loss observed between (Figure 4.18). The absence of rapid weight loss between 200 – 300°C infers neither sample contains DCPD or formed via a DCPA transition phase. XRD and FTIR results support these assertions since no secondary phases were identified in as-synthesised or heated (600°C) HA powders. FTIR bands associated with non-apatitic HPO_4^{2-} were detected in as-synthesised samples and the intensity of PO_4^{3-} and apatitic OH^- peaks were sharper and more intense in heated (600 and 900°C) AP09 compared with AP08. These observations along with the lower weight loss recorded by TGA indicate AP09 is more crystalline and/or contains less HPO_4^{2-} than AP08. Thus, the analysis of samples AP05 – AP10 by XRD, FTIR, and DTA-TGA indicate that it is not merely the starting value of pH that determines the precipitated CaP phase but also stoichiometry is affected by the development of pH throughout

synthesis. Control of pH at 10 during addition led to a reduction in the formation of other phases as evidenced by the comparison of AP07 and AP10, and control of pH at 11 resulted in a lower non-apatitic HPO_4^{2-} content. This is explained in terms of the sensitivity of ionic species (e.g. Figure 2.10), and the ranging solubility of CaP phases according to pH (Figure 2.7).

The influence of doubling the concentration of initial Ca (0.1M) and PO_4 (0.06M) reagents was also considered (AP11). As-synthesised AP09 and AP11 exhibited XRD patterns typical of precipitated HA. No discernible difference was observed in the degree of XRD peak broadening between as-synthesised and heated AP09 and AP11 specimens, indicating a similar nanosized crystallite and crystalline fraction. A band at $875cm^{-1}$ was detected in FTIR spectra of as-synthesised AP09 and AP11, which was attributed to HPO_4^{2-} content, indicating the samples contain CDHA. In comparison to AP09, typical PO_4^{3-} and OH^- bands in AP11 heated to 600°C were noticeably broader and less intense. Differences in the broadening infer a variation in the number and strength of intermolecular interactions and this is common in any sample containing hydrogen bonding. Weaker intermolecular interactions translate to a lower number of chemical environments and narrower IR bands. Hence these spectra suggest stronger or a higher number of PO_4^{3-} and OH^- interactions within AP11 and this may be linked to the higher content of HPO_4^{2-} calculated from TGA analysis (Table 4.9). Since no discernible difference was observed in the size of crystallites it is suggested both reactions generated the same amount of nucleation sites. Therefore the variation in non-apatitic content at a higher solute concentration can be attributed to the solution becoming closer to the relative supersaturation levels of both HPO_4^{2-} and PO_4^{3-} (e.g. Figure 2.10).

Samples AP07 – AP12 exhibited rapid weight loss below 200°C (DTG) and this is attributed to loss of absorbed water since DTA analysis revealed a corresponding endotherm. However, FTIR results contradict this attribution due to the absence of bands associated with unbonded OH^-. It has been proposed that the surface of freshly precipitated apatites comprises of a non-apatitic hydrated layer containing a number of relatively mobile ionic species, which is responsible for the high reactivity of nanocrystalline apatites [2, 58]. Since no change in the crystal or molecular structure was observed at 600°C for samples that exhibited a single DTG peak below this temperature at less than 200°C (AP08, AP09, AP11, and AP12) this weight loss is

associated with the removal of water from the hydrated layer [11, 58]. This structural model and the relatively short ageing time (1.5hrs) clarify the high degree of broadening exhibited in XRD patterns, the presence of non-apatitic HPO_4^{2-} (i.e. a non-stoichiometric Ca:P ratio) and the absence of OH^- bands in FTIR spectra [59].

A marked difference in the morphology of particles prepared below pH 10 was associated with the phase change confirmed by XRD (Figure 4.6). No significant difference in particle morphology was observed by SEM between samples AP07 – AP12. Increase in the size of agglomerates for AP07 – AP12 compared with AP05 and AP06 is attributed to the higher energy associated with smaller crystallites (Table 4.4). Needle-like morphology has been reported within the literature for precipitated HA crystallites and is synonymous to apatite crystals found in hard tissues, including bone [191, 298]. Despite not being stoichiometric HA, TEM micrographs of AP07 (Figure 4.16) demonstrated this typical morphology and illustrated crystallites within the nanoregime, which correlates with the line broadening analysis that confirmed nanosized crystallites for all sample (Table 4.4). Evidently, nanosized crystallites can enhance the proliferation and adhesion of bone cells and therefore the ability to precipitate nHA is considered advantageous [8, 9].

Due to the inevitable agglomeration associated with wet preparation methods typical surface areas exhibited for HA are reported to be between 20 and 60m^2/g [299]. In comparison, the surface areas of samples presented in this thesis are notably higher (Table 4.11). Variation between samples is attributed to the influence of pH (AP07), solute concentration (AP11), and temperature (AP12) on solution supersaturation, which determines the number of nucleation sites. Specifically higher pH, solute concentration, or temperature leads to faster stabilisation since relative supersaturation is increased and therefore smaller crystallites are formed, which corresponds to a larger surface area. Partial evaporation of water due to a higher synthesis temperature of 70°C appears to have the most marked effect on supersaturation since AP12 exhibited the largest surface area (Table 4.11). It is promising that all samples had a relatively high surface area since this will improve sintering kinetics and subsequently increase the mechanical properties of scaffolds fabricated from such materials [13]. It is also advocated that these samples are likely to enhance osteointegration and osteoconduction since a higher surface area provides more fixation points for osteoblasts to adhere [108, 109].

CaPs present a challenge for elemental X-ray analysis due to the high absorption of low energy X-rays in the HA matrix, highlighting the importance of an accurate absorption correction and the potential sensitivity of spectra to roughness effects [300]. SEM micrographs and the relatively high surface area exhibited by samples infer a high surface roughness. This may explain why EDS measurements of Ca:P ratios are substantially higher than what is advocated by FTIR and DTA-TGA analysis, since these results suggest powders are CDHA, i.e. Ca:P ratio < 1.67. In contrast, XRF analysis which was performed on pressed pellets with wax, revealed Ca:P ratios consistent with other characterisation methods that indicate all samples are CDHA. This explains the presence of β-TCP in samples AP08 – AP10 after heating (Figure 4.9). AP07 was shown to exhibit a ratio close to stoichiometry, 1.66, which complements XRD and DTA-TGA analysis that revealed a relatively lower β-TCP content.

Notably, the ZP of as-synthesised samples was negative, except for AP07 and AP12 (Table 4.12). The change in sign confirms the acidity of AP07, which is attributed to the presence of DCPD within this sample. Interestingly a positive ZP was also recorded for as-synthesised AP12 but no secondary phases were detected by XRD or FTIR. This suggests an excess of Ca^{2+} or H^{+}, which is explained in terms of an increase in the concentration of calcium per unit volume due to increased evaporation of water at a higher synthesis temperature of 70°C. This may have resulted in the solution approaching supersaturation of additional cationic species, such as $[CaOH]^{+}$ or $[CaH_2PO_4]^{+}$. Analysis of the ZP of AP07 and AP09 in DMEM revealed a negative value over a 60hr period, which is explained by the buffering effect of ionic salts within the culture medium. However, a positive trend (i.e. decreasing negative value) for AP07 indicates a reduction in colloidal stability over time. This is attributed to the aforementioned acidity of this sample due to the presence of DCPD.

SBF testing was used as a prerequisite to cell culture and in the authors opinion the needle-like morphology of the observed surface coating (Figure 4.24) demonstrates a positive result of bioactivity since it is typical of apatite grown in SBF [301]. In an effort to distinguish between the degree of apatite precipitation, the surface roughness of pellets was measured using white light interferometry. Average roughness was shown to peak between 7 and 14 days, which was not expected since a surface coating was observed on samples up to day 28. Therefore suggesting measurements of surface

roughness do not directly infer the degree of apatite precipitation. This is explained by the dissolution of pellets over the test period, as well as the sensitivity and variability of the SBF solution to any changes in the concentration of ionic species, in particular those containing Ca. Thus, no conclusions can be drawn with certainty from interferometry analysis.

XRD, FTIR, DTA-TGA, XRF and ZP results highlighted a number of distinctive differences in the composition of samples. It was expected that these variations would influence the interaction of cells with the prepared substrates but it was not expected that AP07 and AP12 would be cytotoxic. Since cells were only found to be non-viable on AP07 at day 1 the source of cytotoxicity is likely to be due to the presence of acidic DCPD, which was identified by FTIR, DTA-TGA, and ZP measurements. In contrast, no DCPD or any other secondary phases were identified by XRD, FTIR or DTA-TGA in AP12. However, ZP measurements indicated an excess of surface cations (i.e. acidity), which may explain the death of cells after day 3 of culture. MTT assay results demonstrated a lower proliferative rate for AP12 compared with AP08 – AP11 and for the same sample cell number measured using Hoechst dye to stain DNA was shown to decrease over the culture period. However, ANOVA testing confirmed a statistically significant increase in metabolic activity of live cells (Table 4.14) and cell number (Table 4.16) between days 1 and 7, which contradicts the results of the live/dead assay. This can be explained since the standard ANOVA test does not include all the data, meaning days 3 and 5 are effectively ignored and some information is thereby lost. In, contrast the modified ANOVA method takes into account this data, which explains why this test effectively pulls out this sample as non-significant for MTT results, i.e. the observed increase between days 1 and 7 could have occurred by chance. The negative F ratio for Hoechst assay data of AP12 calculated using the modified ANOVA test indicates that the experimental value at day 7 is lower than the projected cell number at day 7, which is based on the lag growth phase (Appendix A).

MTT and Hoechst assays both demonstrated a lower proliferative rate of MC3T3 cells on AP08 compared with AP09 – AP11. Since no obvious compositional difference was identified using XRD, FTIR, DTA-TGA or ZP measurements attention was focused on the development of pH during precipitation. This revealed that the range of pH values recorded for AP08 was greater than AP09 – AP11 (Table 4.3), inferring that the relative supersaturation of different ionic species in solution was less controlled.

Thus, it is probable that the solution became close to the supersaturation level of a greater number of ionic species due to the lack of control of pH during crystallisation, which may have resulted in trace incorporations of other phases in the final product. Comparison of the proliferative rates of AP08 – AP11 for MTT and Hoechst assays suggests that the degree of variation of solution pH has a greater effect on cell number than metabolic activity. However, it is important to note the larger degree of variation in the fluorescence of Hoechst dye for AP08 (Figure 4.27), thus it is not possible to accurately draw this conclusion from the presented data.

ANOVA testing of MTT data for samples AP08 – AP11 confirmed the significance of growth between days 1 and 7. In contrast, the modified method distinguished samples AP08, AP10, and AP12 as non-significant when the within group variances were compared to the linear regression of day 1 – 5 data (i.e. the proliferation at day 7 is not significantly different from the projected day 7 value). This suggests, assuming that only lag growth occurred between days 1 and 5 that these samples support osteoblast proliferation to a lesser degree than AP09 and AP11, meaning that cells seeded on these substrates will take longer to reach confluency. If this is the case, this supports the assertion that higher pH variability influences material composition to a degree that negatively impacts the metabolic activity of cells, as per the discussion above concerning AP08. The results presented here also advocate that forming CDHA via an intermediate DCPA phase reduces the potential of the substrate to support cell proliferation (AP10).

Recently, the potential of nHA as a vehicle for drug delivery has been explored since such particles can be uptaken by cells and have been shown to exhibit good intracellular release kinetics [302]. It is known that size, shape, and surface charge are key parameters that influence receptor-mediated cellular uptake [303]. Since ZP measurements and SEM studies presented here demonstrated a variation in the sign as well as degree of surface charge, and a range of globular particle sizes, respectively osteoblast uptake of fluorescein stained AP07 – AP10 particles was investigated (Figure 4.28). No distinct change in the affinity for cells was observed between AP07 that exhibited a positive ZP, and negatively charged CDHA particles (AP08 – AP10). Agglomeration of internalised particles was shown, in particular for samples AP07 and AP08 that were prepared in uncontrolled pH conditions. The morphology of cells containing agglomerates of these particles were typically more round compared with

MC3T3 cells that internalised AP09 or AP10, which were shown to exhibit an elongated shape. SEM analysis revealed a smaller average size for AP07 particles compared with AP08 – AP10, thus it appears that the process of internalisation or intracellular behaviour is affected by compositional differences that were shown to alter ZP charge. Chen et al. concluded that positively charged HA nanoparticles were more easily uptaken by MC3T3 precursor osteoblasts, this was attributed to the attractive interaction between the positively charged particles with the negative cell membrane [303]. The average size of AP08 particles was between the sizes demonstrated for AP09 and AP10 therefore the observed intracellular agglomeration of this sample cannot be attributed to the size of particles prior to internalisation. The ZP of AP08 was notably less negative compared with AP09 and AP10. Motskin et al. reported enhanced internalisation of less negatively charged rod-shaped particles compare with colloid nanoparticles of HA [304]. Thus, these results advocate that the degree and sign of particle charge influence the process of internalisation. Increased uptake of particles that release Ca^{2+}, such as HA, has been correlated to toxicity since release can interfere with intracellular homeostasis of Ca^{2+}, which is known to regulate cellular functions such as proliferation and apoptosis [304]. This may explain the elongated morphology of cells that exhibited fewer agglomerates of AP09 and AP10 particles since this shape is indicative of potential cellular adhesion, spreading and proliferation [305, 306].

4.6 Conclusions

The results presented in this chapter highlight the compositional variability of CaP phases under different pH, solute concentrations, and temperature conditions. Numerous authors have highlighted the effects of pH and temperature on a number of powder properties, such as phase and thermal stability (Table 2.7), and the material characterisations presented in this thesis demonstrate the knowledge that is established within the literature. Thus, the novelty of this work is attributed to the associations made between variations in material composition due to different preparation conditions and the effect of these changes on the biological performance of substrates.

Results of in-vitro cellular proliferation studies established that pH and temperature conditions used during synthesis affect material composition to an extent that may determine the viability and proliferative rate of MC3T3 cells. This was explained by

the influence of these reaction parameters on the concentration of different molecular species within solution and this was shown to translate to the chemical composition of the precipitate. Development of a precipitate containing DCPD or excess cations, which created a positive ZP, resulted in substrates that were cytotoxic to MC3T3 cells (AP07 and AP12). Differences in the degree of proliferation of cells seeded on substrates, which were demonstrated to exhibit similar chemical compositions by XRD, FTIR, and DTA-TGA as well as a negative surface charge (AP08 – AP11), was explained in terms of the degree of variation of pH during synthesis. It was found that a greater degree of variation reduced the proliferative rate of osteoblasts measured by metabolic activity and DNA staining using Hoechst 33258 dye. Thus, these results advocate that it is vital to consider the absolute value of pH as well as temperature, and that it is advantageous to control the development of solution pH throughout synthesis in order to develop a substrate that is cytocompatible and supports a higher degree of cell proliferation. Variation in the degree and sign of surface charge as a result of preparation of CDHA under different pH conditions was shown to influence the cellular uptake process of AP07 – AP10.

In summary, the ability of samples AP08 – AP11, that were all suggested to be CDHA by FTIR, DTA-TGA and XRF, to support the proliferation of MC3T3 osteoblast precursor cells was evidenced by the increase in cell number as measured by MTT and Hoechst assays between 1 and 7 days of culture. The relatively higher proliferative rates calculated for samples AP09 and AP11 should be noted and are considered promising since cell proliferation is the first step in the development of bone tissue: proliferation occurs for the first 10 – 12 days of culture, followed by ECM synthesis, maturation, and finally mineralisation [307]. Scaffolds fabricated from such materials are expected to exhibit enhanced osteogenesis and osteoinductivity.

Chapter 5

Precipitation of hydroxyapatite – influence of solvent system

5. Precipitation of hydroxyapatite – influence of solvent system

5.1 Introduction

There are a number of reaction conditions that affect the crystallisation process of HA, which comprises of nucleation and crystal growth mechanisms. The previous chapter highlighted the variability of HA composition under different pH, temperature, and solute concentrations leading to the conclusion that these parameters ultimately define the cytocompatibility and ability of the substrate to support osteoblast proliferation. Other authors have investigated the influence of a number of additional reaction parameters (Table 2.7), including the effect of different solvent systems [166].

Broadly, solvents can be described as either polar or non-polar. The degree of polarity is generally indicated by the dielectric constant, which is defined as a comparison of the ability of the solvent to reduce electric field strength surrounding an immersed charged particle, with the field strength of the charged particle in a vacuum. This term is also sometimes referred to as static relative permittivity. Generally, a solvent is considered to be non-polar if it exhibits a dielectric constant below 15.

The influence of replacing water, the most common solvent used in the precipitation of HA, with two non-polar solvents, namely Toluene and/or Ethanolamine was experimentally investigated to determine the effect on key properties of HA: (1) phase purity, (2) degree of crystallinity, (3) particle size and morphology, (4) thermal stability, (5) stoichiometry, (6) surface area, and (7) surface charge. Corresponding effects of material characteristics on the bioactivity, cytocompatibility, and the ability of HA substrates to support the proliferation of MC3T3 cells was assessed using an acellular SBF test, and cellular MTT and Hoechst assays, respectively.

5.2 Materials and methods

Analar grade reagents were purchased from Sigma Aldrich (UK) and used without further purification unless otherwise stated. The procedure outlined in section 4.2.1 was modified to incorporate the use of Toluene and Ethanolamine as follows.

5.2.1 Aqueous precipitation (AP)

To investigate the influence of Toluene ($C_6H_5CH_3$), 30mL was added to 20mL of DI water to form a 60Toluene:40water solution to which 0.05M of $Ca(NO_3)_2 \cdot 4H_2O$ was added. When Ethanolamine (C_2H_7NO) was used it was added to the Ca^{2+} containing solution under stirring conditions (400rpm) before the adjustment of pH. The remainder of the procedure was kept as described in section 4.2.1. Samples produced using this modified method were compared to a control HA sample, namely AP09, which was precipitated under the same pH and temperature conditions in DI water (Table 5.1).

Table 5.1: Summary of varied solvent conditions

Sample	Solvent system
AP09 (control)	DI water
AP13	5wt% Ethanolamine
AP14	60% Toluene
AP15	5wt% Ethanolamine, 60% Toluene

Toluene was selected to investigate as an alternative solvent since it is non-polar and therefore it is expected to influence the crystallinity of precipitates. Toluene exhibits a lower dielectric constant of 2.38 at 25°C compared to 80.1 for water at 20°C. Ethanolamine was selected for its properties of alkalinity and volatility, suggesting that the solvent would help to maintain a basic environment and be easily removed after synthesis.

5.2.2 In-vitro test methods

The methods described in section 4.2.2 for pellet preparation, SBF testing, dead/live staining, as well as MTT and Hoechst assays were followed.

5.3 Materials characterisation

Sample prepared in different solvent systems were characterised by: XRD, FTIR, SEM, DTA-TGA, EDS, BET, ZP, SBF, live/dead staining, as well as MTT and Hoechst assays using the methods described in section 4.3. XRD was performed on as-synthesised and powders calcined at 600°C using a ramp up/down rate of 1°C/min, and a dwell time of 1hr. ZP was analysed in DI water at 25°C. Statistical analysis of

data collected from MTT and Hoechst assays was performed using the ANOVA and modified ANOVA tests as described in section 4.3.14 (Appendix A).

5.4 Results

5.4.1 Development of solution pH in different solvent systems

No discernible difference in the development of solution pH was observed between samples (Table 5.2). Notably, less NH_4OH was required to control pH when Ethanolamine was added to the solvent system since it is a basic solvent.

Table 5.2: Development of solution pH in different solvent systems

Sample	Solution pH		
	Start of addition	End of addition	Removal from mother solution
AP09	11.05	10.99	10.78
AP13	10.99	11.00	10.80
AP14	11.09	11.00	10.83
AP15	11.09	11.00	10.86

5.4.2 Crystal structure

As-synthesised and calcined (600°C) samples were matched to HA alone (Figures 5.1 and 5.2). Notably a higher degree of peak broadening in as-synthesised samples prepared in solvent systems containing Toluene (AP14 and AP15) was observed. In contrast, the hollow between the (112) and (300) HA peaks was observed for calcined AP14 but not in other heated samples and this is indicative of a higher crystalline fraction. No distinguishable difference in the degree of peak broadening between as-synthesised and heated AP09 or AP13 was demonstrated.

Line broadening analysis showed only a minimal variation in the size of as-synthesised crystallites (Table 5.3). Less than 23% increase was calculated between the size of as-synthesised and calcined crystallites of AP09, AP13, and AP15. However, a relatively high increase of 41% was revealed for AP14.

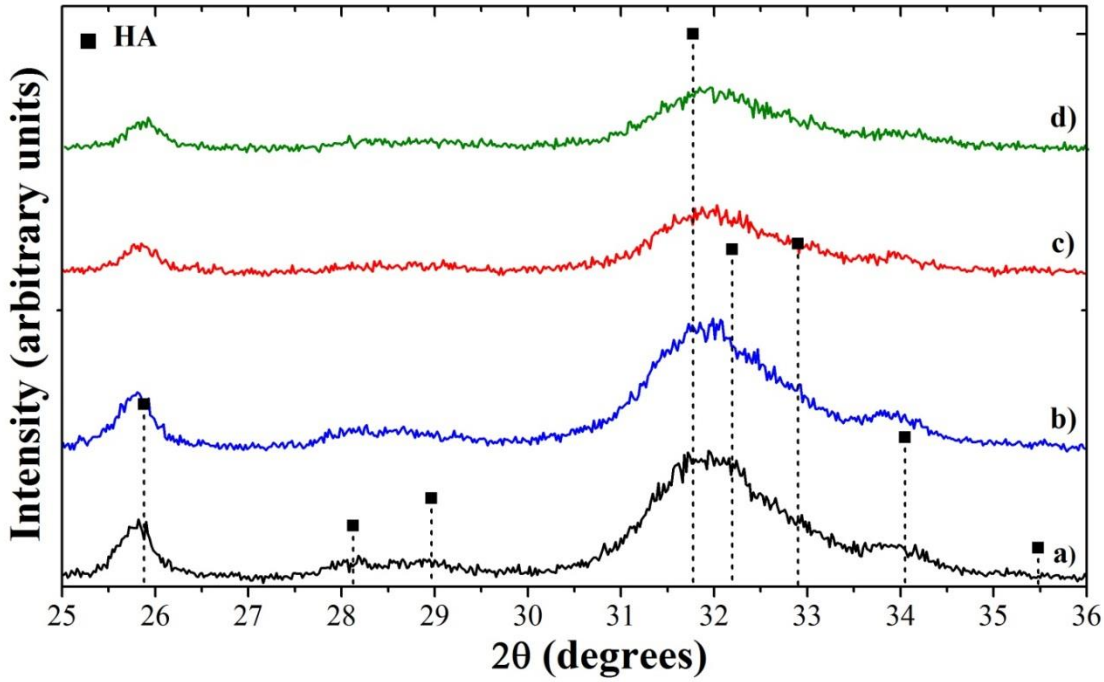

Figure 5.1: Influence of solvent system on as-synthesised crystal structure of (a) AP09, (b) AP13, (c) AP14, and (d) AP15

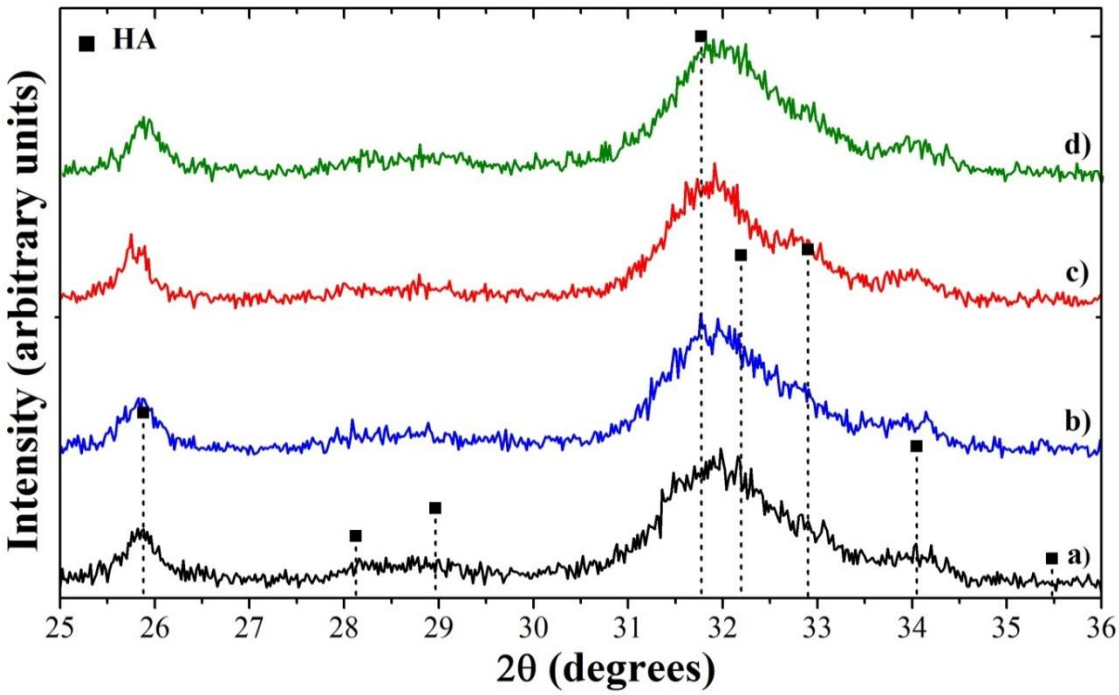

Figure 5.2: Influence of solvent system on the crystal structure of samples heated to 600°C (a) AP09, (b) AP13, (c) AP14, and (d) AP15

Table 5.3: Influence of solvent system on phase and XRD peak broadening

Sample	Calcination temperature (°C)	XRD peaks matched to	Crystallite size (nm)
AP09	As-synthesised	HA	20
	600		24
AP13	As-synthesised		20
	600		20
AP14	As-synthesised		22
	600		31
AP15	As-synthesised		22
	600		27

5.4.3 Molecular structure

The major assignments for HA are summarised in Table 4.5. Strong characteristic bands corresponding to PO_4^{3-} were demonstrated in all samples (Figure 5.3). Weak structural OH^- bands between 632 and 635cm^{-1} were assigned. Similarly to those samples reported in Chapter 4, OH^- and absorbed H_2O bandings 2500 – 3750cm^{-1} exhibited negligible intensity relative to PO_4^{3-} bands. This is suggested to be due to the relatively short ageing time of 1.5hrs. Weak bands at 875cm^{-1} associated with non-apatitic HPO_4^{2-} were also revealed.

IR analysis of samples heated to 600°C revealed the disappearance of the band attributed to HPO_4^{2-} at 875cm^{-1} (Figure 5.4). A significant reduction in the relative intensity of PO_4^{3-} bands was observed in AP14.

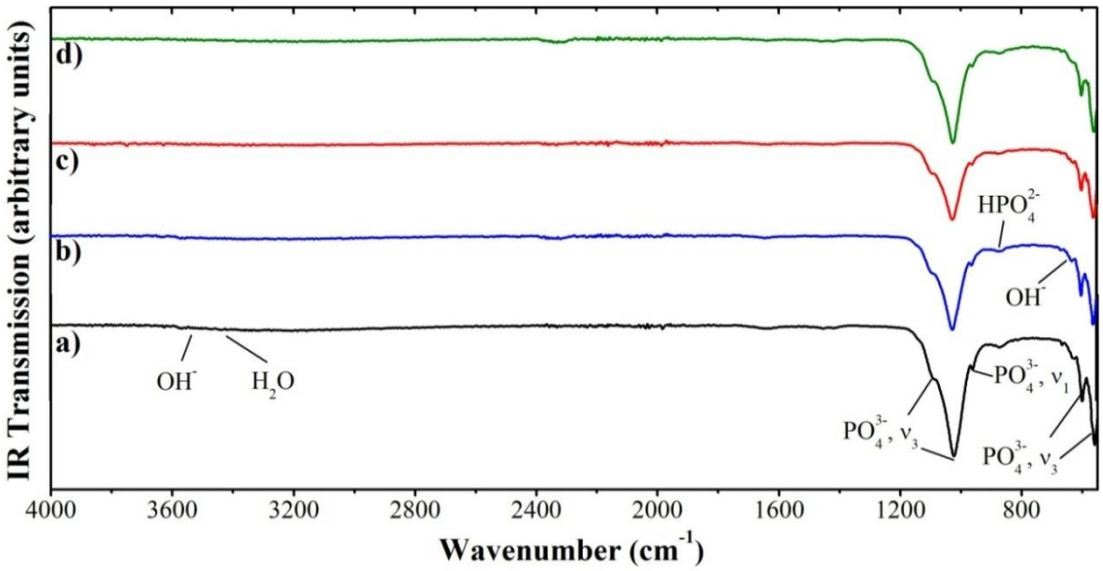

Figure 5.3: Influence of solvent system on molecular structure of as-synthesised samples (a) AP09, (b) AP13, (c) AP14, and (d) AP15

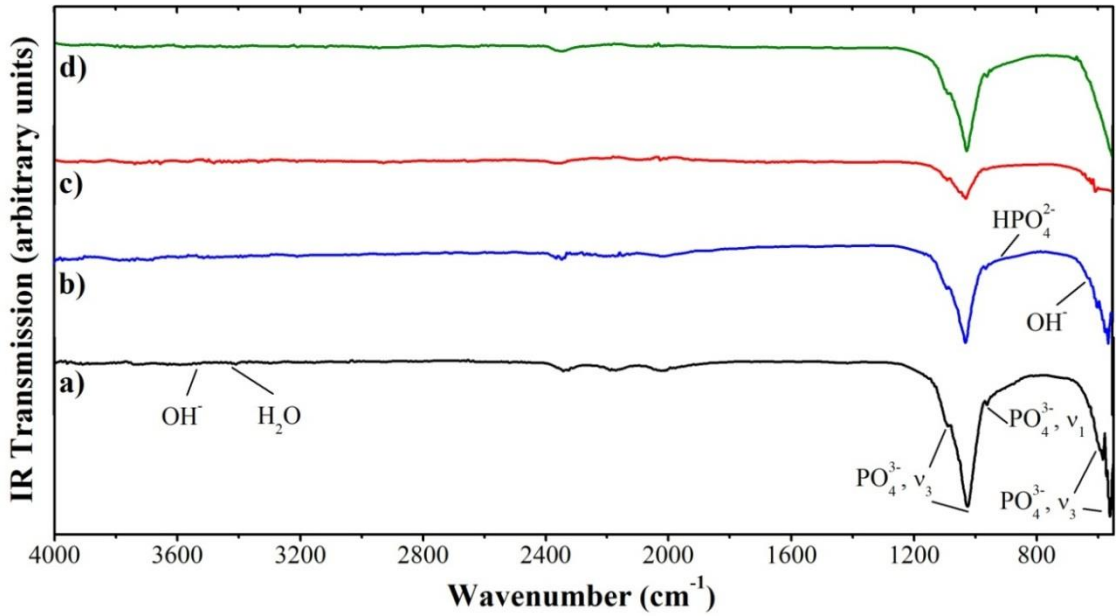

Figure 5.4: Influence of solvent system on molecular structure of samples heated to 600°C (a) AP09, (b) AP13, (c) AP14, and (d) AP15

5.4.4 Microstructural development

Typical micrographs revealed globular particles (Figure 5.5) and bulk agglomeration throughout samples (Table 5.4). The surfaces of particles were observed to exhibit numerous irregularities, which infers surface roughness.

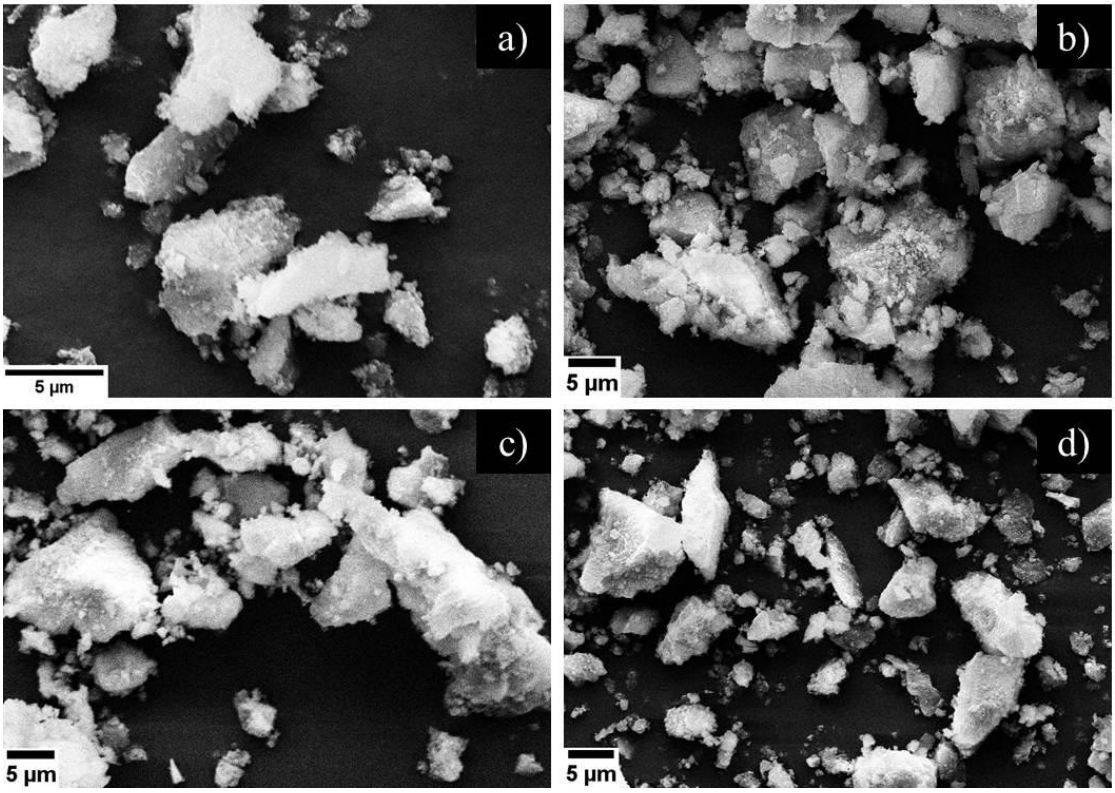

Figure 5.5: Influence of solvent system on typical particle morphology (a) AP09, (b) AP13, (c) AP14, and (d) AP15

Table 5.4: Influence of solvent system on average particle and agglomerate size (n=3)

Sample	Average Size (µm)	
	Particles	Agglomerates
AP09	2.7±0.5	24.6±4.3
AP13	2.2±0.5	39.1±5.7
AP14	2.0±0.2	24.2±5.2
AP15	2.1±0.6	26.6±6.2

5.4.5 Thermal behaviour

Gradual weight loss between 250 and 700°C was observed and attributed to the dehydration of HPO_4^{2-}, present in CDHA, to $P_2O_7^{4-}$ according to Equation 2.4 (Table 4.7). Between 700 and 800°C rapid weight loss associated with an endotherm was demonstrated, which is likely to be due to the transformation of β-$Ca_2P_2O_7$ to HA and β-TCP (Equation 2.5). These reactions are illustrated in Figures 5.6 – 5.8. These water losses were calculated from TGA data (Table 5.5) and used in combination with Equations 2.3 – 2.5 to determine HPO_4^{2-} and $P_2O_7^{4-}$ content (Table 5.6).

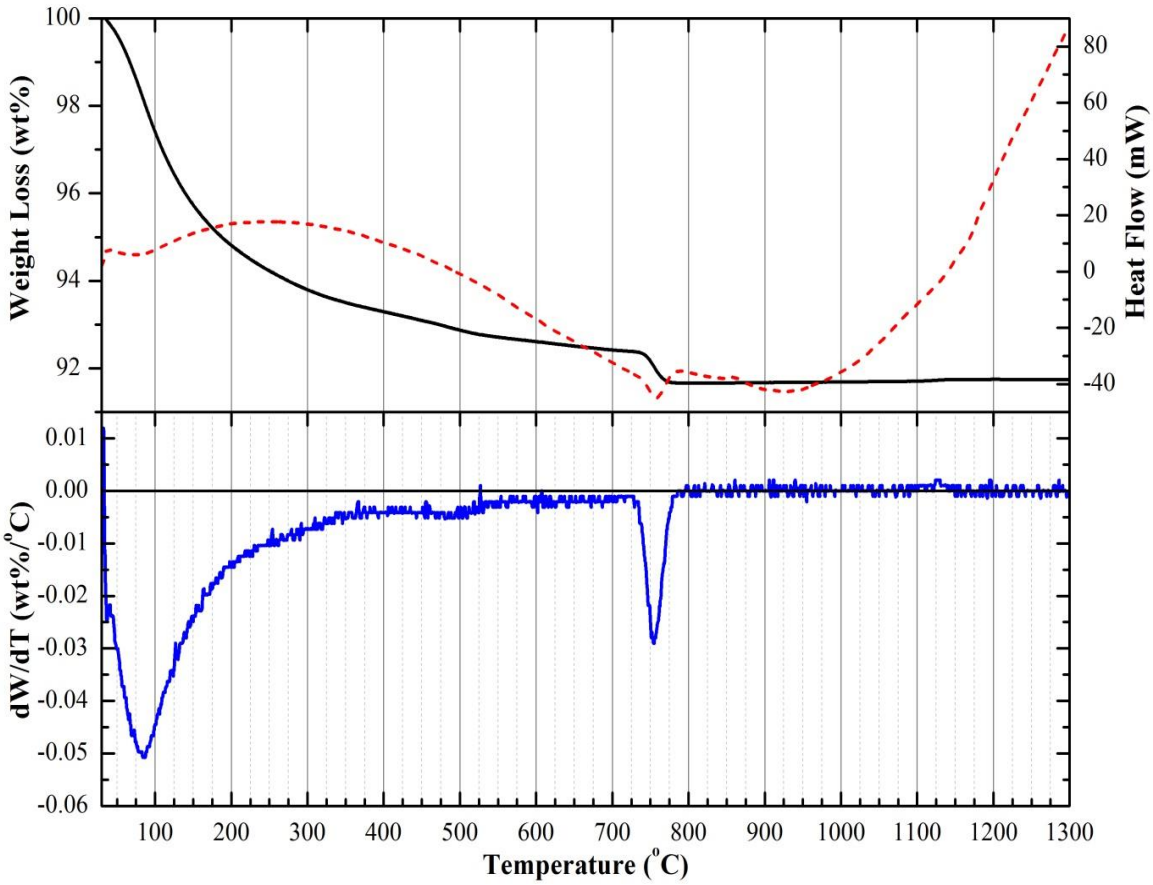

Figure 5.6: Thermal behaviour of AP13
(DTA = dashed red line, TGA = solid black line, DTG = solid blue line)

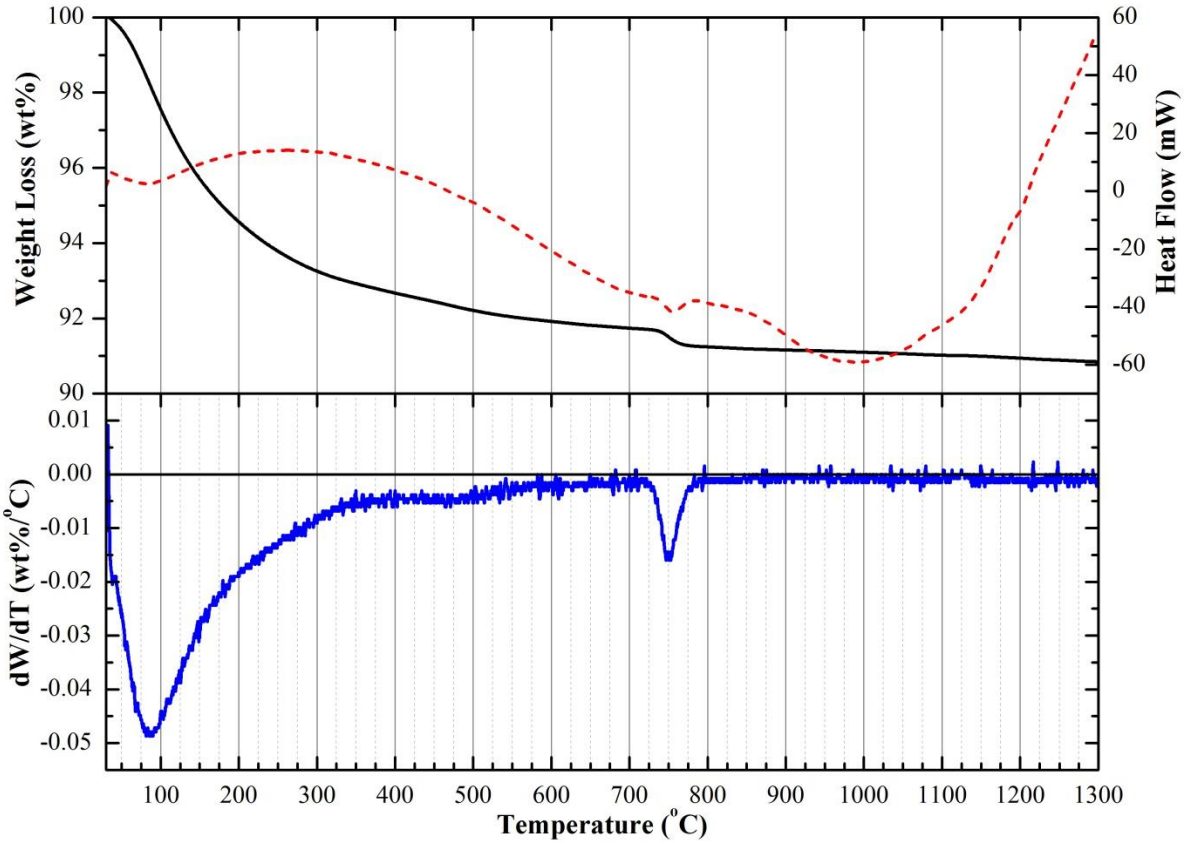

Figure 5.7: Thermal behaviour of AP14
(DTA = dashed red line, TGA = solid black line, DTG = solid blue line)

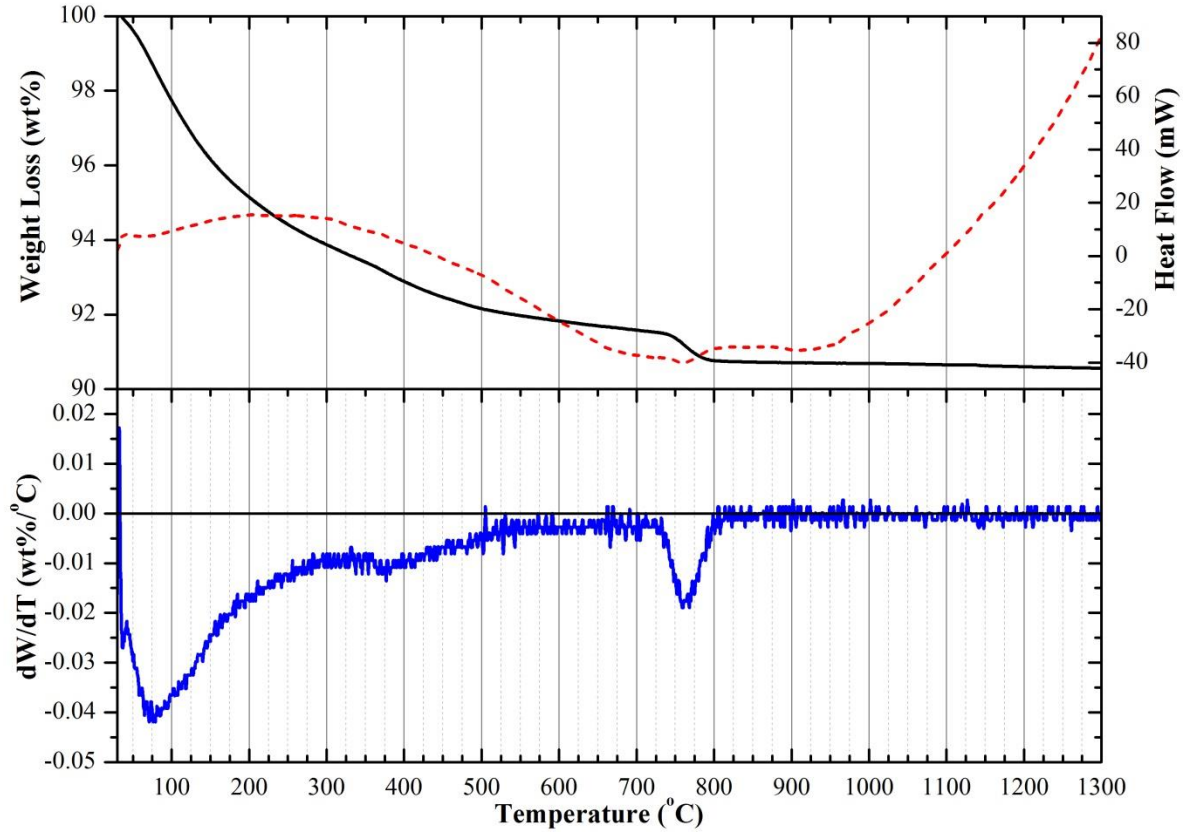

Figure 5.8: Thermal behaviour of AP15
(DTA = dashed red line, TGA = solid black line, DTG = solid blue line)

Table 5.5: Influence of solvent system on the amount of water lost between temperature regions associated with Equations 2.3 – 2.5
[a]peak area between 700 to 800°C analysed

Temperature region (°C)	Water loss (wt%)			
	AP09	AP13	AP14	AP15
250 – 700	1.98	1.809	2.047	2.839
700 – 800[a]	0.71	0.7213	0.4575	0.7827
30 – 800	8.26	8.335	8.756	9.255

Table 5.6: Influence of solvent system on chemical composition calculated from DTG analysis using Equations 2.3 – 2.5
[a]peak area between 700 to 800°C analysed

Temperature region (°C)	Ion/phase	Source	Weight (wt%)			
			AP09	AP13	AP14	AP15
250 – 700	HPO_4	CDHA	21.09	19.28	21.81	30.25
	P_2O_7		19.11	17.47	19.76	27.41
700 – 800[a]	P_2O_7		6.82	6.96	4.42	7.56
	TCP		36.46	37.26	23.63	40.43
	HA		55.27	54.41	67.61	50.32
HA + TCP residue (mg)			8.49	13.27	17.99	10.06
TGA residue at 800			8.49	13.27	17.99	10.06

5.4.6 Elemental analysis

EDS was used to determine the influence of the solvent system on the Ca:P ratio (Table 5.7). These results indicated that samples were non-stoichiometric and calcium-rich HA since the experimental Ca:P ratio was greater than the stoichiometric ratio, 1.67.

Table 5.7: Influence of solvent system on Ca:P ratio measured by EDS (n=3)

Sample	Ca:P ratio
AP09	2.17±0.03
AP13	2.13±0.03
AP14	2.14±0.16
AP15	2.11±0.01

5.4.7 Surface area

Precipitation in a 60:40 Toluene water system (AP14) was found to increase the surface area by nearly 20% compared with particles prepared in DI water (AP09), and a mixture of DI water and ethanolamine (AP13). A smaller increase of <5%, compared

with AP09, was observed when both Toluene and Ethanolamine were used (AP15) (Table 5.8).

Table 5.8: Influence of solvent system on the surface area of as-synthesised powders

Sample	Surface area (m^2/g)
AP09	106.7±0.2
AP13	106.2±0.4
AP14	126.1±0.6
AP15	110.2±0.5

5.4.8 Surface charge

Three measurements of electrophoretic light scattering were taken in DI water at 25°C to obtain an average ZP value (Table 5.9). Precipitation in DI water was shown to result in a relative increase in colloidal stability, i.e. a larger ZP value. Generally speaking a ZP <±20mV indicates that the colloids are liable to flocculation, such as AP13 – AP15.

Table 5.9: Influence of solvent system on ZP measured in DI water at 25°C

Sample	ZP (mV)
AP09	-21.3
AP13	-5.22
AP14	-5.21
AP15	-2.85

5.4.9 SBF test

Figure 5.9 demonstrates the typical surface of substrates before immersion in SBF. After 7 days SEM micrographs revealed the presence of a surface layer (Figure 5.10 a) and in some areas spheroidal nodules as well as needle-like particles were observed (Figures 5.10 b and c). It has been reported in the literature that apatite grown in SBF typically exhibits the morphology described above [301]. Thus these results suggest that substrates are bioactive.

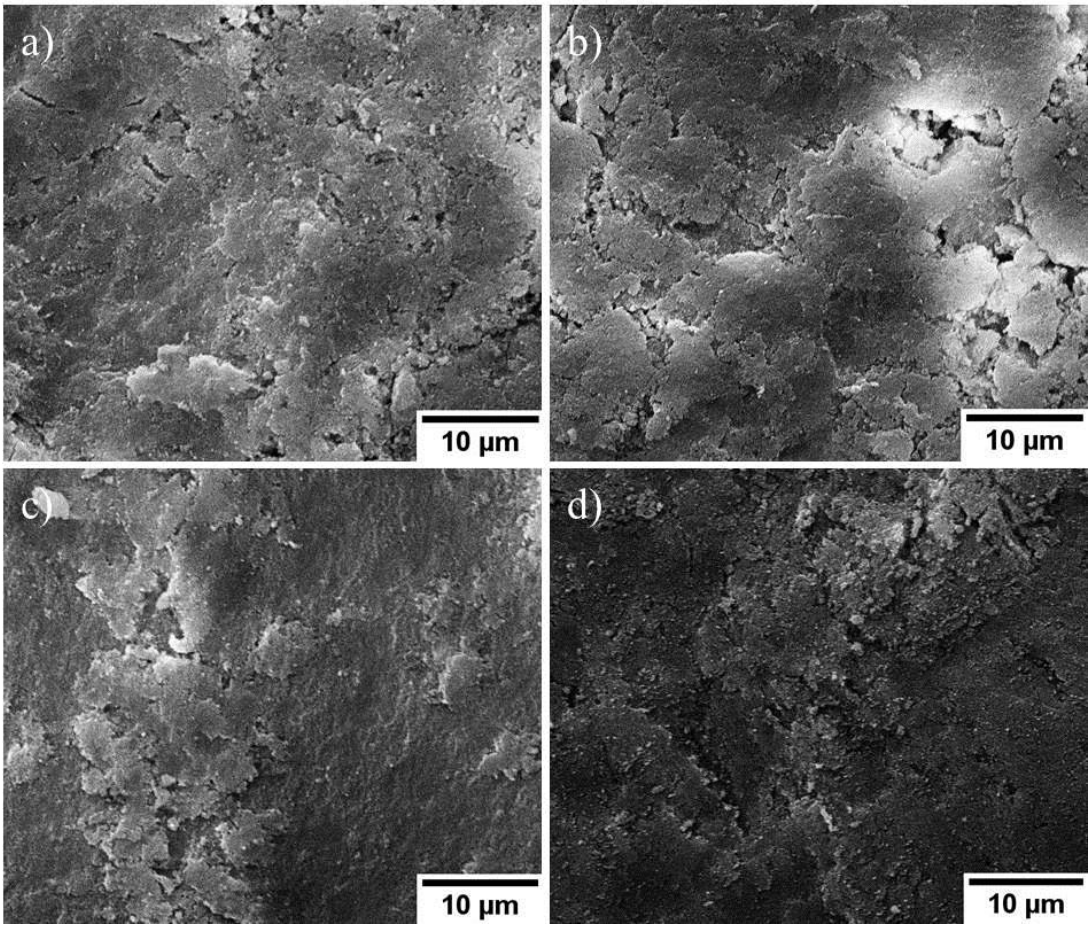

Figure 5.9: Surface of pellets prior to immersion in SBF
(a) AP09, (b) AP13, (c) AP14, and (d) AP15

5.4.10 Live/dead assay

The majority of MC3T3 cells were observed to be viable between 1 and 7 days of culture on samples AP13 – AP15 (Figure 5.11). Very few dead cells were seen and therefore can be attributed to the sensitivity of the culture process. An increase in the density of cells was visually observed over the culture period and the morphology was revealed to change from rounded (days 1 – 5) to elongated at day 7. These results suggest all substrates are cytocompatible and support adhesion, spreading, and proliferation.

5.4.11 MTT assay

An increase in the metabolic activity of MC3T3 cells was observed between days 1 and 7 (Figure 5.12). Proliferative rates were calculated over the culture period (Table 5.9) and the data suggests that substrates supported the proliferation of osteoblast precursor cells, which is consistent with the qualitative assessments drawn from fluorescence micrographs of cell viability staining (Figure 5.11).

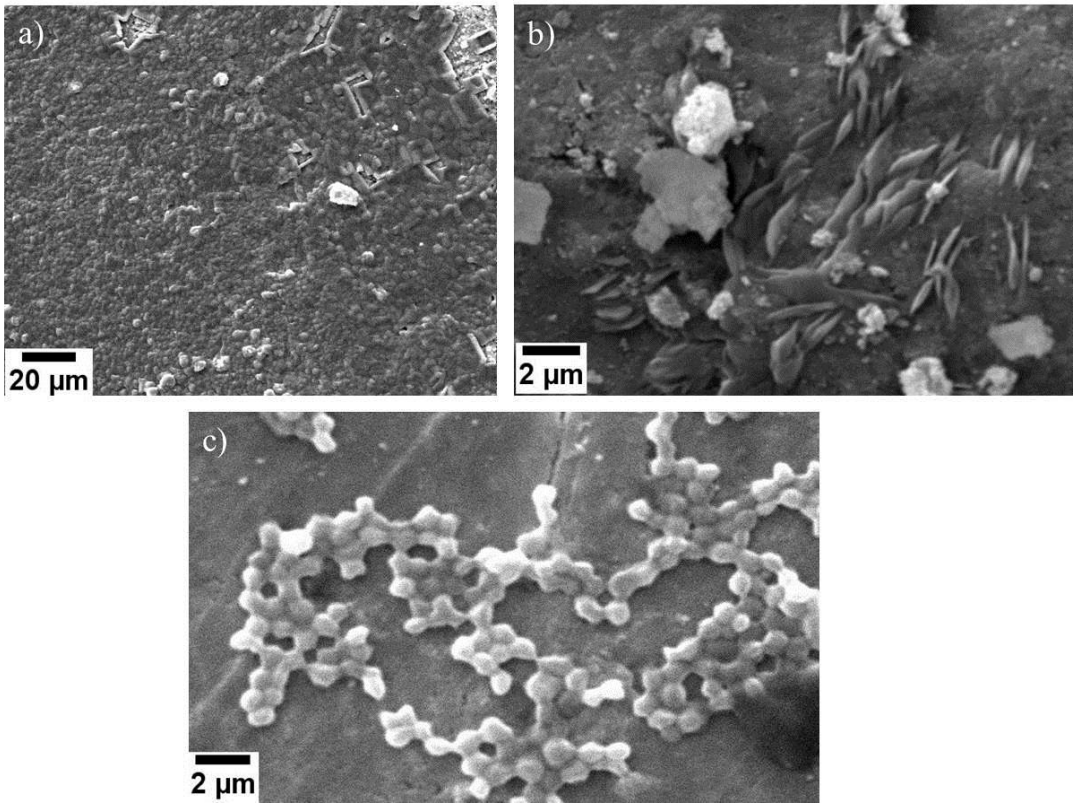

Figure 5.10: Influence of solvent system on the morphology of surface apatite after SBF immersion (a) AP13 day 7 surface layer, (b) AP14 day 14 needle-like surface particles, and (c) AP15 day 7 spheroidal surface particles

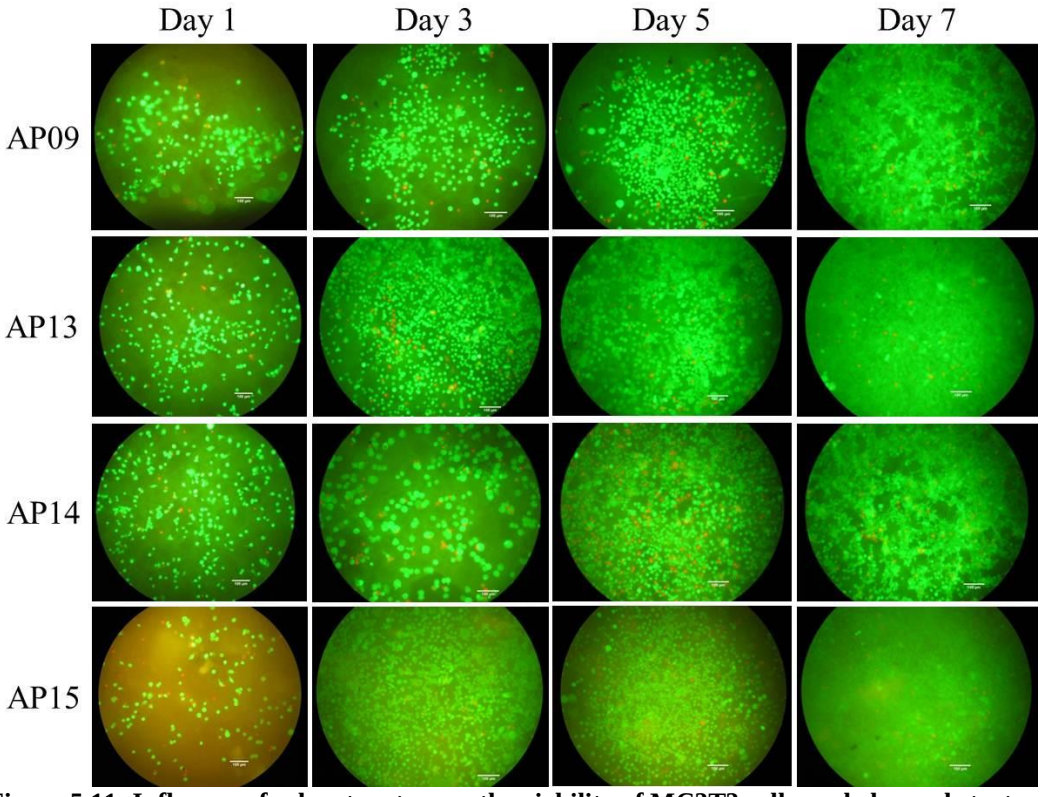

Figure 5.11: Influence of solvent system on the viability of MC3T3 cells seeded on substrates (green = live, red = dead)

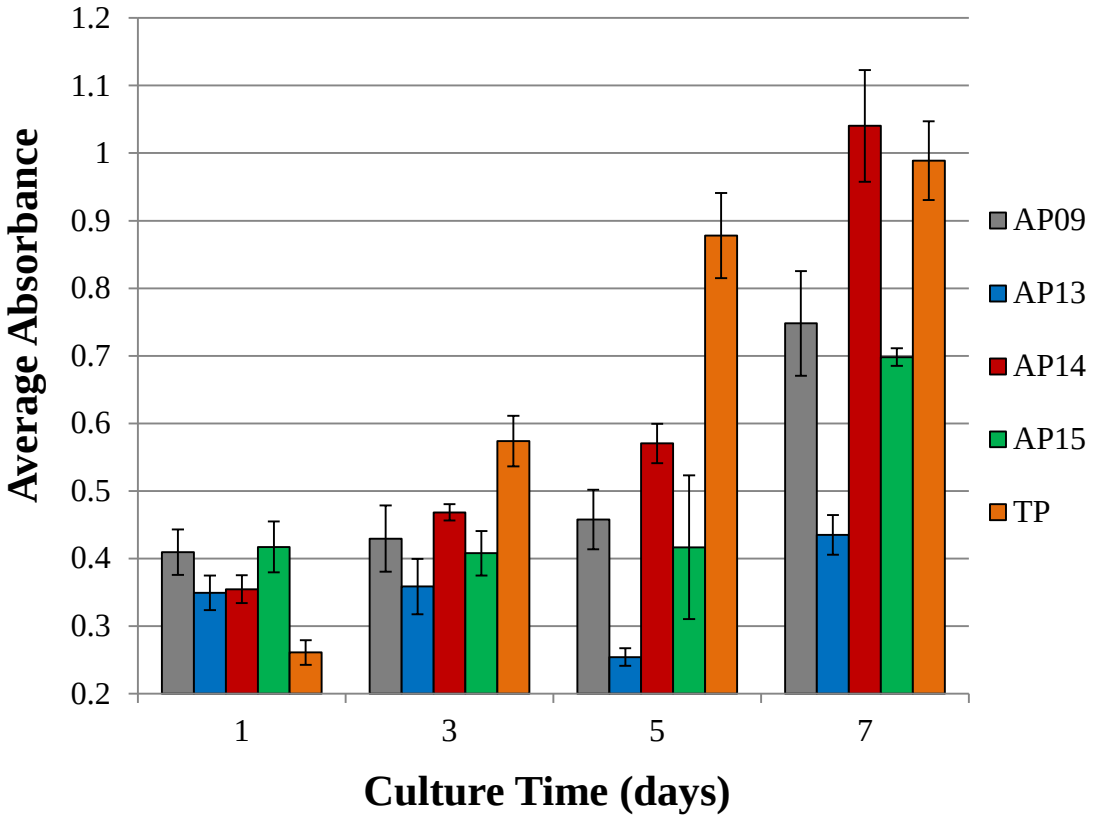

Figure 5.12: Influence of solvent system on metabolic activity of MC3T3 osteoblast precursor cells

Notably, powders produced in a solvent system containing Ethanolamine exhibited a lower proliferative rate compared with AP09, which was prepared in DI water (Table 5.10). In contrast, the proliferative rate more than doubled when precipitates were synthesised in a mixed Toluene and water system (AP14) compared with water alone (AP09).

Statistical analysis using the standard ANOVA method established that all samples exhibited an *F* ratio greater than the critical value, which suggests that a significant increase in cell number occurred between day 1 and 7 (Table 5.11). Day 7 *F* ratios calculated from linear regression of day 1 and 3 data demonstrated statistical significance for all samples except AP13. In contrast, when the same ratio was calculated from a linear trend line of day 1 – 5 data the modified ANOVA method distinguished AP15 as non-significant. Proliferation at day 5 was not shown to be significant compared with projected day 5 data. The negative day 5 *F* ratios for AP13 and AP14 calculated using the modified ANOVA method is explained in terms of experimental values being lower than those projected from day 1 and 3 data. Thus suggesting lag cell growth occurs up to day 5.

Table 5.10: Influence of solvent system on the proliferative rate of MC3T3 cells assessed by MTT assay between 1 and 7 days

Sample	Proliferative rate (%)
AP09	82.8
AP13	24.6
AP14	193.5
AP15	67.4
TP	279.2

Table 5.11: Statistical analysis of MTT assay performed on samples AP13 – AP15 F_{crit} = 4.965 where p<0.05, * = statistically significant

Sample	ANOVA test	Modified ANOVA test		
	Day 7 *F* ratio	Day 7 *F* ratio		Day 5 *F* ratio
		Trend 1-3	Trend 1-5	Trend 1-3
AP09	96.317*	7.237*	6.842*	0.212
AP13	29.069*	1.860	5.575*	-3.656
AP14	388.765*	22.217*	17.924*	-0.747
AP15	297.140*	9.549*	4.583	0.561
TP	767.697*	-18.333	-5.764	-2.765

5.4.12 Hoechst assay

An increase in the number of cells between days 1 and 7 was demonstrated for all samples (Figure 5.13), thus suggesting substrates supported proliferation. In comparison to the proliferative rate for AP09, a smaller increase in cell number was calculated for AP13 as well as AP14, and a greater increase for AP15 was shown (Table 5.12). The proliferation of cells between day 1 and 7 was confirmed to be statistically significant for all samples using the ANOVA test (Table 5.13). In contrast, the modified ANOVA method revealed that the day 7 *F* ratios for AP13 and AP14 were non-significant when experimental values were compared with a linear trend calculated from day 1 – 3 data. However, when linear regression was performed on day 1 – 5 data the modified method suggests a significant increase in cell number for all samples at day 7. The day 5 *F* ratio for AP15 was also found to be above the F_{crit} value and is therefore deemed statistically significant.

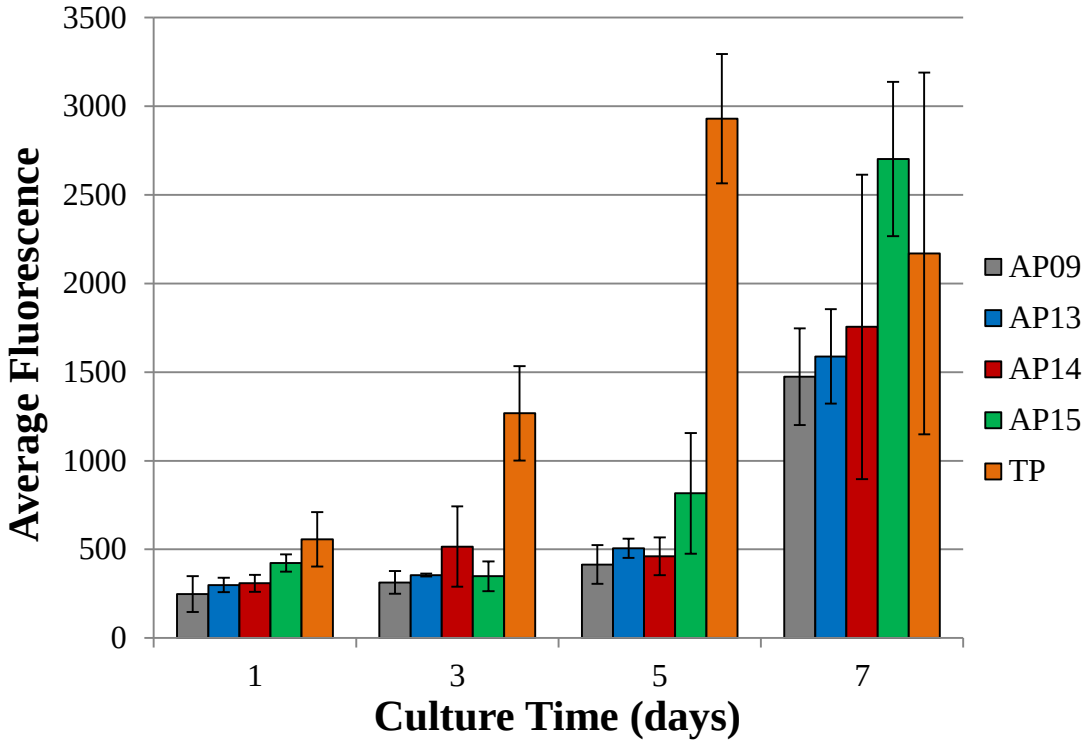

Figure 5.13: Proliferation of MC3T3 cells on substrates prepared in different solvent systems assessed by Hoechst assay

Table 5.12: Influence of solvent system on the proliferative rate of MC3T3 cells assessed by Hoechst assay between 1 and 7 days

Sample	Proliferative rate (%)
AP09	495.7
AP13	431.0
AP14	467.7
AP15	538.9
TP	477.2

Table 5.13: Statistical analysis of Hoechst assay AP13 – AP15
F_{crit} = 7.709 where p<0.05, * = statistically significant

Sample	ANOVA	Modified ANOVA		
	Day 7 *F* ratio	Day 7 *F* ratio		Day 5 *F* ratio
		Trend 1-3	Trend 1-5	Trend 1-3
AP09	106.892*	14.895*	12.780*	0.508
AP13	137.446*	1.860	47.302*	4.005
AP14	16.937*	6.182	8.696*	-1.950
AP15	162.713*	44.683*	8.478*	9.676*
TP	14.656*	-2.927	-1.299	-1.253

5.5 Discussion

XRD patterns of AP13 – AP15 were matched to HA and no secondary phases were identified. Corresponding FTIR spectra revealed the presence of non-apatitic HPO_4^{2-}, which indicates as-synthesised samples are CDHA. This attribution was supported by DTA-TGA analysis that demonstrated gradual weight loss between 250 and 700°C, which is ascribed to the dehydration of HPO_4^{2-} to $P_2O_7^{4-}$ according to Equation 2.4. Further evidence was provided by the subsequent rapid endothermic weight reduction observed 700 – 800°C known to be due to the transformation of β-$Ca_2P_2O_7$ to HA and β-TCP (Equation 2.5). Since all samples behaved similarly under heating, and FTIR spectra as well as XRD patterns were comparable it is concluded that variation of the solvent system did not alter the predominant CaP phase formed.

As-synthesised AP14 and AP15 samples exhibited a notably higher degree of broadening of characteristic XRD peaks (Figure 5.1) suggesting that the use of Toluene influences the crystallisation process. This is explained in terms of a reduction in the polarity of the solvent system causing an increase in the rate of precipitation of polar molecules since the relative supersaturation level is lower. Hence the lower dielectric constant of Toluene resulted in faster precipitation of crystallites, which explains the increase in broadness of characteristic XRD peaks. Assuming a faster rate of precipitation, this may explain the smaller particle size (Table 5.4) and larger surface area (Table 5.8) exhibited by AP14 and AP15 compared with AP09.

In contrast, XRD patterns of samples heated to 600°C exhibited no apparent difference in the degree of peak broadening. This observation suggests that in addition to the aforementioned difference in the degree of crystallinity of as-synthesised materials, samples prepared in different solvent systems may also exhibit a variation in chemical composition. Simply, Le Chatelier's principle states that disruption of a dynamic equilibrium will result in the system countering this by shifting the position of the equilibrium backwards [308]. The large numbers of ionic species within the reported solutions make the equilibrium rather complex (e.g. Figure 2.10). Attention has been focused on the dynamic equilibrium between PO_4^{3-} and HPO_4^{2-} since FTIR and DTA-TGA demonstrated presence of both of these ions (Equation 5.1). Notably, addition of Ethanolamine, since it is an alkali solvent, resulted in less NH_4OH being required to control pH, i.e. a decrease in the amount of OH^- or a relative increase in H^+ within the

system. Thus the equilibrium is shifted to reduce HPO_4^{2-} to counteract this change, which explains the relatively low concentration of this ion calculated for AP13 compared with AP09 (Table 5.6). In the case of AP14, the addition of Toluene decreases the relative concentration of H^+ since it is a non-polar solvent and thus the equilibrium is shifted in the opposite direction, which explains the increase in the amount of HPO_4^{2-} content for this sample (Table 5.6). When Ethanolamine and Toluene are used in combination DTA-TGA results suggest the effect of Toluene is dominant since an increase in HPO_4^{2-} content was calculated for AP15 relative to AP09. Compositional differences (i.e. HPO_4 content) between AP09 and AP13 compared with AP14 and AP15 are suggested to explain the difference in the rate of crystallisation evidenced by XRD patterns of heated samples (Figure 5.2).

$$[HPO_4^{2-}] \rightleftharpoons [PO_4^{3-}] + [H^+] \quad (5.1)$$

A significant reduction in the intensity and increased broadness of FTIR bands associated with PO_4^{3-} was observed in calcined AP14 compared with other samples (Figure 5.4). The broader peaks indicate stronger or a greater number of PO_4^{3-} intermolecular interactions, suggesting that a larger number or smaller critical nucleation size was generated in the formation of precipitates prepared in a mixed Toluene and DI water system. This is associated with the faster stabilisation of crystallites due to the lower dielectric constant of Toluene. As mentioned previously this may also explain why AP14 exhibited a higher surface area (Table 5.8). It is important to note that all samples exhibited a surface area greater than what is typically cited for HA in the literature, 20 – 60m^2/g [299].

No marked difference in particle morphology was observed for samples AP13 – AP15 or for the samples analysed in Chapter 4 (AP07 – AP12). Thus it is suggested that particle morphology is dependent on the crystal structure of the precipitate. This is evidenced by the different morphologies observed for samples AP05 and AP06 that were predominantly matched to different CaP phases, DCPD and DCPA, by XRD analysis. A 60% increase in the average agglomerate size, compared with AP09, was observed for AP13 but in contrast less variation (<20%) in the size of particles was demonstrated. Therefore it is likely the degree of agglomeration is linked not only to particle size but also to the degree of grinding achieved when the dried powders are

crushed using a pestle and mortar. Since each powder was ground for the same period of time this suggests the dried filter cake for AP13 was more resistant to compressive force, which may be due to smaller crystallites creating more grain boundaries. Application of the Scherrer equation (Equation 3.1) confirmed crystallites of all samples were within the nanoregime (Table 5.3).

Similar to the samples analysed in Chapter 4, the Ca:P ratio of AP13 – AP15 calculated using EDS were substantially above the stoichiometric ratio of 1.67 for HA. Since EDS analysis was performed on powdered samples that were observed by SEM to exhibit numerous irregularities and a relatively high surface area, it is likely that this infers significant surface roughness which may have distorted X-ray scattering. This might explain why the calculated Ca:P ratios do not confer with FTIR and DTA-TGA data that clearly suggest powders are CDHA.

Samples AP13 – AP15 all exhibited a negative ZP in DI water at pH 7.4, i.e. a negative surface charge. Particularly, a decrease in the value of ZP was observed for AP13, AP14, and AP15 compared to AP09, which indicates a reduction in the stability of dispersed particles. Colloidal stability is dependent on the balance of repulsive and attractive forces between particles that approach each other within the dispersion. If particles exhibit a mutual repulsion colloidal stability is maintained. However, if there are no or few repulsions the particles are susceptible to instability mechanisms, such as flocculation. Therefore, the lower ZP values of AP13 – AP15 compared with AP09 indicate that these particles are more likely to flocculate in water. It is likely that the negative surface charge of AP09 is created by deprotonation of crystallites in the polar and OH^- rich water system. This would result in a degree of electrostatic stabilisation since deprotonation would create negatively charged particles. The ability of non-polar solvents to influence surface charge is significantly less and this explains why partial replacement of water with a non-polar solvent, such as Toluene results in a lower degree of electrostatic stabilisation of CDHA particles, i.e. a lower ZP value (AP14). Since addition of Ethanolamine resulted in less NH_4OH being required to control pH during precipitation of AP13 the concentration of OH^- within the solvent system was reduced and hence also the degree of deprotonation. AP15 exhibited the lowest ZP value and this is due to the combined effects of Toluene and Ethanolamine, as described above. Particle flocculation during AP synthesis is reported as a common issue [3, 192, 193]. These results advocate that characterisation of ZP is an important

step in the understanding of such instability mechanisms and potential tweaking of the solvent system could reduce this unfavourable effect.

Since the SBF test is relatively cheap and fast compared with cell culture this technique was once again used as an indication of substrate bioactivity prior to cell work. Formation of spheroidal nodules on the surface with a fine needle-like structure is suggested to infer bioactivity. A layer exhibiting this typical morphology was observed on all samples; however coverage was shown to be non-uniformly dispersed across the surface. In this context, it should be noted that the ability to infer in-vivo bioactivity from the formation of apatite in SBF is widely debated within the literature [289, 309, 310]. It is also reported that this test can result in false positive and false negative results due to potential changes in the supersaturation of the solution favouring possible apatite formation. Variability and difficulty in preparing the SBF solution are highlighted in the literature [309]. The author recognises that these issues infer that SBF results are likely to exhibit poor reproducibility as well as inconsistency and therefore since these results are refutable no conclusions are drawn from this test alone.

Live/dead assay revealed that cells were viable on all substrates over the entire culture period (Figure 5.11). Micrographs qualitatively demonstrated an increase in cell density and a change in morphology from rounded to stretched and elongated at day 7, which is indicative of cell attachment and spreading. Hence it can be concluded that the effects of Toluene and/or Ethanolamine on the composition of substrates did not influence cytocompatibility. It may also be inferred that samples support the proliferation of osteoblast precursor cells and this assertion was quantitatively confirmed by MTT and Hoechst assays.

Calculation of the proliferative rate of MC3T3 osteoblast precursor cells seeded on substrates revealed an increase in the number of metabolically active cells over 7 days. In comparison to the reference sample prepared in DI water (AP09), the increase in cell number between days 1 and 7 for AP13 and AP15 was 58 and 15% less, respectively. In contrast, the proliferative rate of cells on AP14 was more than double AP09 (Table 5.10), which may infer improved osteogenesis. AP14 exhibited a relatively high surface area and high degree of XRD peak broadening and therefore it may be considered sensible to assume that either or both of these powder properties influenced metabolic activity. Ribeiro et al., [311] proposed that osteoblast adhesion

and metabolic activity were affected by the surface morphology and roughness of sintered HA substrates. The authors demonstrated a higher level of viability and number of MC3T3 cells on substrates sintered at 1000°C compared to 725°C and attributed this to differences in surface morphology, including larger grain size, higher root mean square roughness, lower surface area and porosity. Unfortunately, the effect of sintering on the chemical composition and crystallinity of HA substrates was not considered in the study conducted by Ribeiro et al. [311] despite these properties being known influence on osteoblast differentiation. Numerous studies in the literature support the assertion that there is an inverse relationship between crystallinity and mineralisation [312, 313] as well as gene expression of osteonectin (a bone specific protein that is suggested to link bone mineral to collagen and initiate active mineralisation) [314], osteopontin (a prominent protein component of the mineralised extra cellular matrices of bones and teeth) [315], and alkaline phosphatase (ALP - an enzyme that dephosphorylates organic molecules and is linked to bone turnover and osteoblast activity) [316]. These observations were explained in terms of improved degradation of less crystalline HA and the ability of these surfaces to provide a dynamic zone for dissolution and re-precipitation [317]. Since the crystallinity of all heated samples appeared to be relatively similar the increased proliferation of metabolically active cells seeded on AP14 is not attributed to this factor. Instead, it is ascribed to the differences in surface properties, namely the higher surface area of AP14 particles, which is considered promising for osteointegration and osteoconduction [108, 109]. To confirm this, additional characterisations of key surface characteristics, such as surface area and roughness, of pellets are recommended in order to help understand the above observations. Aside from this, surface area is known to impact the sinterability of HA generally resulting in increased mechanical strength and thus the higher surface area exhibited by AP14 is considered a desirable property for load bearing applications.

The increase in cell number observed by MTT assay was confirmed to be statistically significant for all samples using the ANOVA test. AP13, showing the lowest proliferative rate, was pulled out as non-significant by the modified ANOVA method when variances were compared to the linear line of best fit calculated from day 1 – 3 data. An observable decrease in cell number at day 5 for AP13 explains why the F ratio for this sample was confirmed as statistically significant when the trend line was

calculated from day 1 – 5 data and negative at day 5 compared with linear regression of days 1 – 3 (Table 5.11). The day 7 *F* ratio for AP15 was calculated to be less than F_{crit} when day 1 – 5 data was used for the modified ANOVA test and is attributed to the relatively large variation in experimental value (Figure 5.12). The modified ANOVA test identified samples that exhibited a lower proliferative rate than AP09 as non-significant whereas these samples were not distinguished using the standard method. This distinction highlights the importance of considering the whole data set (i.e. all time points) as otherwise potentially important information may essentially be overlooked.

In contrast, the proliferative rate calculated for Hoechst assay results demonstrated a larger increase in cell number when MC3T3 cells were seeded onto AP15. Compared with AP09, samples prepared with Ethanolamine (AP13) and Toluene (AP14) alone exhibited a lower increase in cell number between days 1 and 7. Compared to AP09, AP13 and AP14, properties of AP15 that are notable include the greater concentration of non-apatitic HPO_4^{2-} calculated from TGA analysis (30.25wt%) and the reduced colloidal stability measured in DI water. In comparison to the results presented in section 4.4.12 the highest increase in cell number was established on AP10, which also exhibited a relatively high content of HPO_4^{2-} (39.74wt%). Concurrent analysis of these results suggests that a higher non-apatitic content may contribute to a higher increase in osteoblast proliferation as measured by DNA staining. This is explained in terms of the reduction in the Ca:P ratio with increasing HPO_4^{2-} content, and this would improve dissolution, which can be favourable [317]. Statistical analysis using the modified ANOVA method revealed a non-significant increase for AP13 and AP14 at day 7 compared with projected values based on day 1 – 3 data. However, the increase in cell number at day 7 compared to the linear regression of day 1 – 5 data advocates that proliferation was significant on all samples and this was also confirmed using the standard ANOVA test. This analysis suggests the lag cell growth phase occurs up to day 5 of culture for these samples.

5.6 Conclusions

In summary, variation in the dielectric constant of the solvent system used for precipitation was shown to influence the rate of crystallisation. This is explained by a decrease in the relative supersaturation of crystallites in a system containing non-polar

solvents. Hence the rate of precipitation in solvent systems containing Toluene (AP14 and AP15) is likely to have been faster and this explains the higher degree of XRD peak broadening demonstrated for these samples. The above explanation was also used to conclude why AP14 and AP15 exhibited a relatively larger surface area. It is suggested that the substantial increase in surface area observed for AP14 explains the higher metabolic activity of MC3T3 cells seeded on this substrate after 7 days of culture. However, since the surface area of the pellet cannot directly be inferred from particle data further testing is recommended to quantify this properties as well as the surface roughness of substrates.

FTIR and DTA-TGA analysis confirmed the presence of non-apatitic HPO_4^{2-} within all samples suggesting precipitates are CDHA. Notably AP15 was shown to exhibit approximately 10% more non-apatitic content than other specimens. An increase in the number of cells at day 7 was linked to this higher HPO_4^{2-} content. This relationship was also corroborated in section 4.4.12.

Variation in the colloidal stability of powders prepared in different solvent systems was evidenced by ZP measurements and depending on the end use of the powder could be considered an important criterion. In relation to this project particle flocculation is considered a detrimental factor in a number of scaffold fabrication methods. In particular, the resolution and stability of parts fabricated via ALM methods that involve powders or colloids is directly linked with the flowability of stock material and any potential coagulation due to powder or dispersion instability would be unfavourable.

In summary, the uses of Toluene and/or Ethanolamine in the solvent system for HA precipitation was not found to adversely affect the viability of cells seeded on the prepared CDHA substrates. The use of these solvents had mixed effects on composition and physical properties of substrates and this resulted in a varied degree of support for cell proliferation in comparison to CDHA prepared under the same conditions in DI water. In-vitro results for AP14 and AP15 are promising since a relative increase in the number of MC3T3 osteoblast precursor cells seeded on substrates over the 7 day culture period was demonstrated. Overall, these results highlight the potential application of alternative solvents to control and alter chemical as well as physical characteristics that play an important role in determining vital properties, including sinterability, mechanical strength, and biological performance.

Chapter 6

Precipitation of hydroxyapatite – influence of divalent cations

6. Precipitation of hydroxyapatite – influence of divalent cation substitutions

6.1 Introduction

The reactivity of biological apatites, including bone mineral, depends on various parameters one of which is the existence of ionic substituents within the apatite structure [2]. Incorporation of numerous ionic species, generally in relatively small amounts (Table 2.1), exist in bone apatite and explain the different physical-chemical properties of this material compared with stoichiometric HA. Many of these dopants are known to elicit advantageous cellular responses. In an attempt to emulate the performance of native bone apatite researchers have investigated the influence of incorporating biologically relevant ions into synthetic HA.

A number of reports have confirmed that substitution of Sr, Mg, or Zn can influence the crystallinity, solubility, surface charge, and physiological dissolution rate of synthetic CaPs [11]. Each of these divalent cations are known to play important roles in the biological responses of bone cells (section 2.9.1). Despite the synthesis of substituted HA attracting much interest in the biomedical research community to the best of the author's knowledge Sr, Mg, or Zn substituted HA prepared under the same experimental conditions has not previously been reported. Preceding chapters have highlighted that changes in reaction conditions can greatly influence the physical, chemical, and crystal structure of precipitated apatite, which makes it difficult to determine the sole influence of substituents when comparing literature since variations in synthesis conditions, such as pH, temperature, and solute concentration, are common. Hence it is proposed that comparison of samples doped with Sr, Mg, or Zn prepared under the same experimental conditions is a more accurate assessment of the individual influence of these cations. This reasoning serves as justification for the experimental work presented in this chapter. A higher level of Mg doping was selected (10mol%) compared with Sr and Zn (2mol%) since a larger amount of this cation is known to be present in native bone apatite (Table 2.1).

6.2 Materials and methodology

Analar grade reagents were purchased from Sigma Aldrich (UK) and used without further purification unless otherwise stated.

6.2.1 Aqueous precipitation (AP)

To form substituted HA the amount of $Ca(NO_3)_2 \cdot 4H_2O$ used in the procedure outlined in section 4.2.1 was adjusted to reflect the incorporation of 2mol% Sr, 10mol% Mg, or 2mol% Zn. An appropriate amount of strontium nitrate [$Sr(NO_3)_2 \geq 99\%$], magnesium nitrate [$Mg(NO_3)_2 \geq 99\%$], or zinc nitrate hexahydrate [$Zn(NO_3)_2 \cdot 6H_2O \geq 98\%$] was added to the Ca^{2+} containing solution and stirred until the reagents were fully dissolved. No further alterations were made to the precipitation process (section 4.2.1). Substituted HA samples were compared with a control HA sample (AP09) to ascertain the influence of the additional divalent cations (Table 6.1).

Table 6.1: Summary of divalent cation substitutions

Sample	Substitution
AP09 (control)	N/A
AP16	2mol% Sr
AP17	10mol% Mg
AP18	2mol% Zn

6.2.2 In-vitro test methods

The methods described in section 4.2.2 for pellet preparation, SBF testing, as well as live/dead, MTT and Hoechst assays were employed for samples AP16 – AP18.

6.3 Materials characterisation

HA substituted with Sr, Mg, or Zn were characterised by: XRD, FTIR, SEM, DTA-TGA, XRF, BET, SBF, live/dead staining, as well as MTT and Hoechst assays using the methods described in section 4.3. XRD was performed on as-synthesised and powders calcined at 600°C using a ramp up/down rate of 1°C/min, and a dwell time of 1hr. The amount and accuracy of cation substitutions was analysed by XRF. Statistical analysis of data collected from MTT and Hoechst assays was performed using the ANOVA and modified ANOVA tests as described in section 4.3.14 (Appendix A).

6.4 Results

6.4.1 Development of solution pH containing additional divalent cations

A maximum variation of 0.06 was observed between the final solution pH of HA (AP09) and suspensions containing additional divalent cations (Table 6.2).

Table 6.2: Development of solution pH containing additional divalent cations

Sample	Cation substitution	Solution pH		
		Start of addition	End of addition	Removal from mother solution
AP09	N/A	11.05	10.99	10.78
AP16	Sr	11.10	11.00	10.84
AP17	Mg	11.07	11.00	10.81
AP18	Zn	11.00	10.99	10.82

6.4.2 Crystal structure

As-synthesised samples were matched to the standard JCPDS pattern for HA and notably an increase in the broadening of characteristic peaks was observed for AP16 – AP18 compared with AP09, which suggests these samples are less crystalline (Figure 6.1). Calcined samples were matched to HA alone, except AP17 that was confirmed to be a biphasic mixture of HA and β-TCP (Figure 6.2). No distinguishable difference in the degree of HA peak broadening between as-synthesised and calcined samples was observed. However, an increase in the size of crystallites was confirmed by line broadening analysis (Table 6.3).

Positions of characteristic XRD peaks were identified and any shifts observed between samples AP16 – AP18 compared with AP09 were recorded (Table 6.4). In general, a shift of peaks to lower angles was demonstrated for AP16 and, in contrast to higher angles for AP17 and AP18.

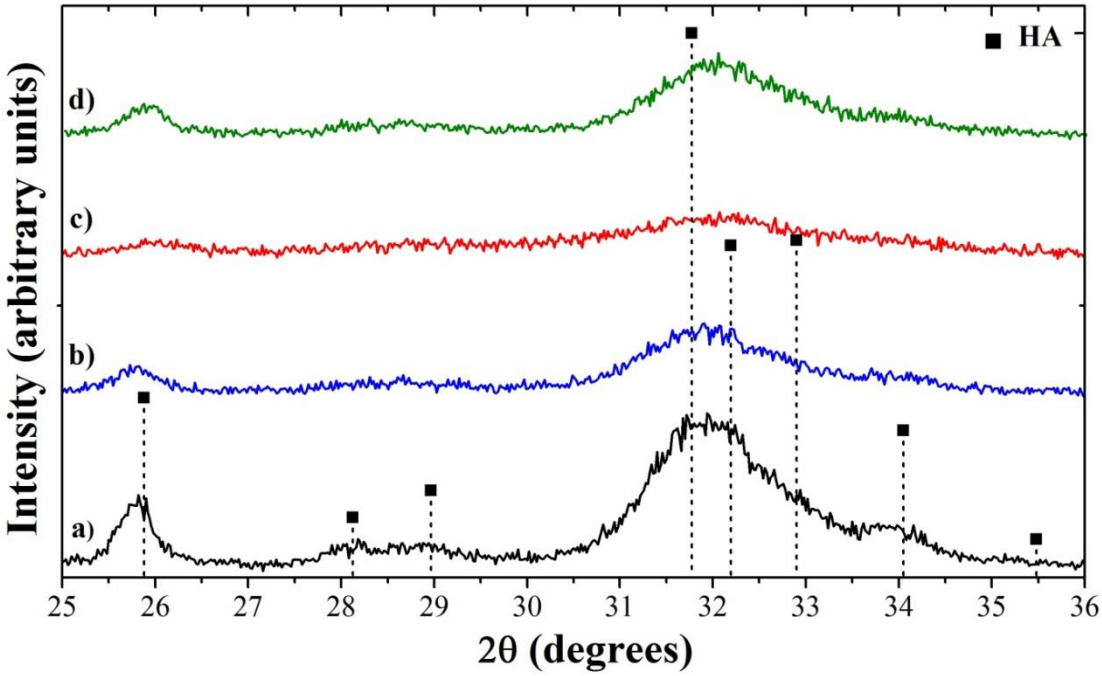

Figure 6.1: Influence of cations on as-synthesised crystal structure
(a) AP09, (b) Sr AP16, (c) Mg AP17, and (d) Zn AP18

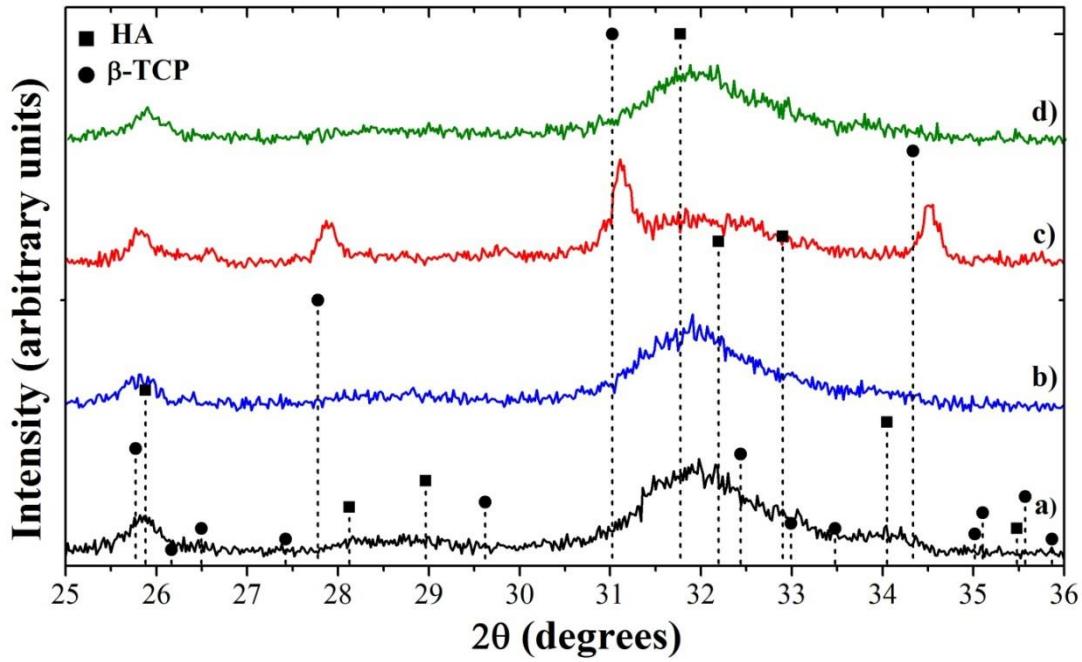

Figure 6.2: Influence of cations on the crystal structure of samples heated to 600°C
(a) AP09, (b) Sr AP16, (c) Mg AP17, and (d) Zn AP18

Table 6.3: Influence of cations on phase and XRD peak broadening

Sample	Cation substitution	Calcination temperature (°C)	XRD peaks matched to	Crystallite size (nm)
AP09	N/A	As-synthesised	HA	20
		600		24
AP16	Sr	As-synthesised	HA	19
		600		21
AP17	Mg	As-synthesised	HA	11
		600	β-TCP	35
AP18	Zn	As-synthesised	HA	19
		600		30

Table 6.4: Influence of cations on the position of characteristic XRD peaks compared with AP09 and HA reference pattern (09-432)

Peak	HA reference (°)	2θ peak position (°)				2θ peak shift (°)		
		AP09	AP16	AP17	AP18	AP16	AP17	AP18
(002)	25.879	25.874	25.823	25.893	25.874	-0.051	0.019	0.054
(102)	28.126	28.129	28.121	28.157	28.122	-0.007	0.028	0.002
(200)	28.966	28.936	28.986	28.970	28.961	-0.280	0.027	0.047
(211)	31.773	31.798	31.762	31.788	31.777	-0.012	0.014	0.043
(112)	32.196	32.199	32.200	32.193	32.185	-0.001	0.021	0.015
(300)	32.902	32.910	32.920	32.911	32.907	-0.006	0.014	0.250
(202)	34.048	34.044	34.045	34.089	34.048	-0.051	0.048	0.022
(001)	35.480	35.523	35.427	35.491	35.495	-0.054	0.009	0.018

6.4.3 Molecular structure

IR band assignments for HA are summarised in Table 4.5. Major bands associated with PO_4^{3-} and HPO_4^{2-} were observed in all as-synthesised samples (Figure 6.3). A band that is associated with structural OH^- was also demonstrated between 632 and 635cm^{-1}.

Corresponding analysis of samples heated at 600°C revealed the absence of a band at 875cm^{-1}, which was attributed to non-apatitic HPO_4^{2-} (Figure 6.4). A reduction in the intensity of all major PO_4^{3-} frequencies was observed for AP16 – AP18 and in addition the shoulder associated with PO_4^{3-} (ν_3) at 1090cm^{-1} was unobservable for AP17 and AP18.

6.4.4 Microstructural development

Typical particles exhibited a globular morphology and a significant variation in size due to agglomeration (Figure 6.5). Measurements were taken of what appeared to be individual particles (i.e. material fractions that were dispersed), and agglomerates to obtain average sizes (Table 6.5). Compared with AP09, samples prepared with Sr and

Zn exhibited larger than average particle and agglomerate sizes. In contrast, an approximate reduction of 40% and 20% was demonstrated between the average particle and agglomerate sizes of AP17 and AP09, respectively.

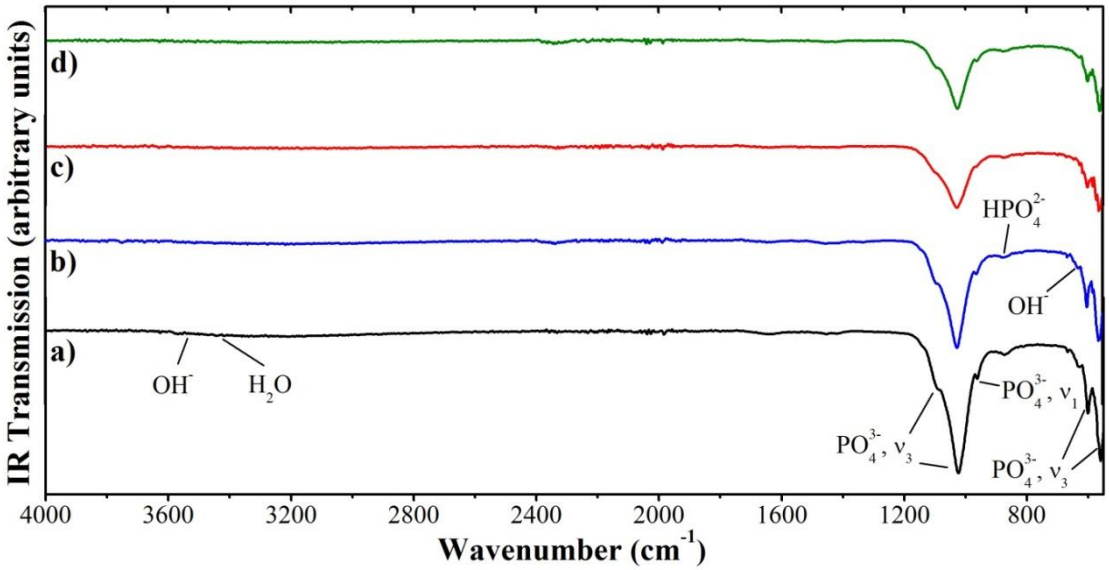

Figure 6.3: Influence of cations on molecular structure of as-synthesised samples (a) AP09, (b) Sr AP16, (c) Mg AP17, and (d) Zn AP18

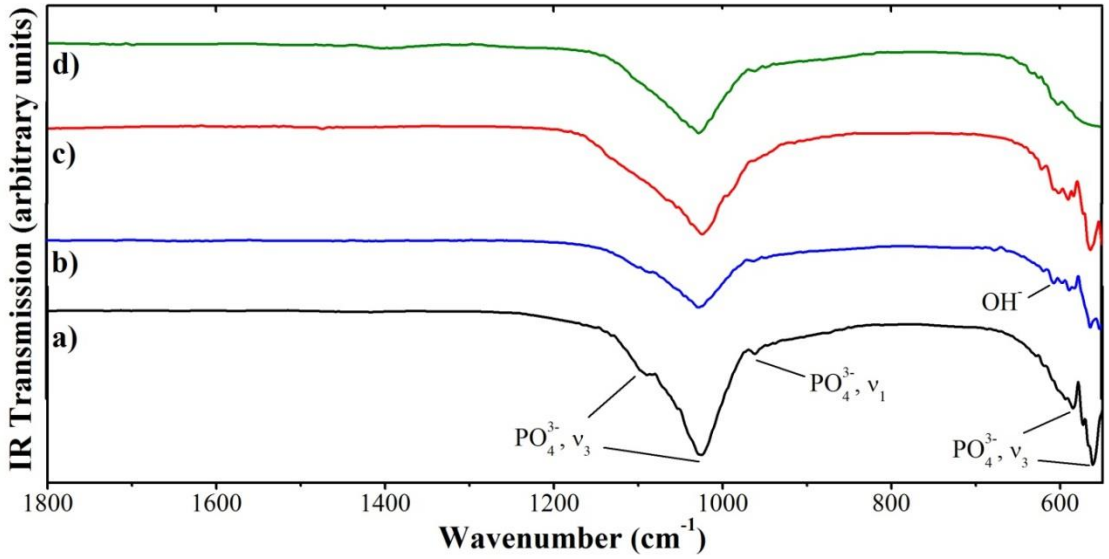

Figure 6.4: Influence of cations on the molecular structure of samples heated to 600°C (a) AP09, (b) Sr AP16, (c) Mg AP17, and (d) Zn AP18

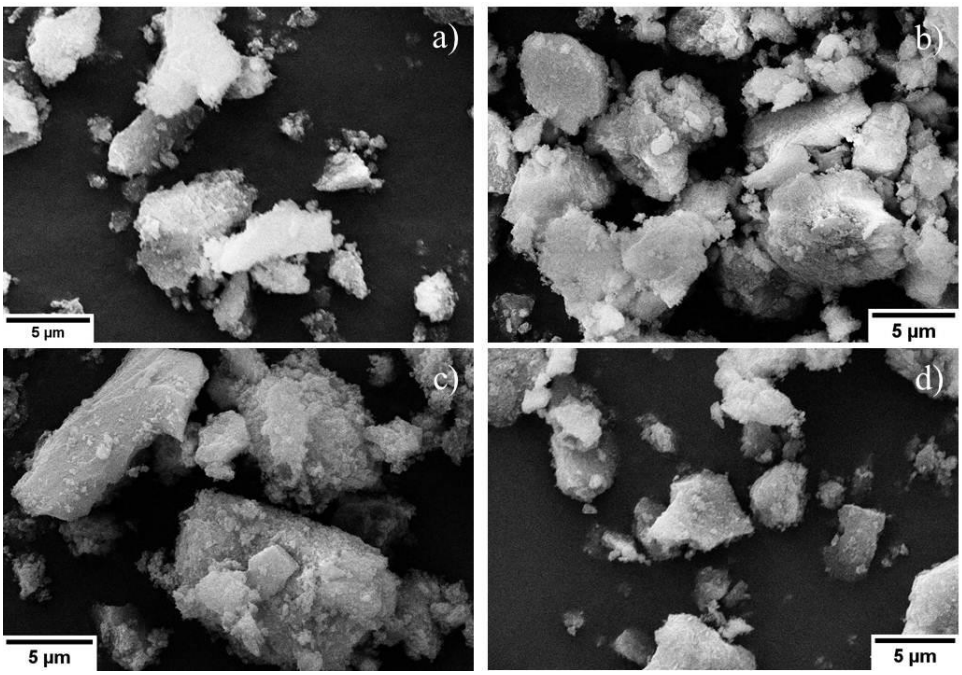

Figure 6.5: Influence of cations on typical particle morphology (a) AP09, (b) Sr AP16, (c) Mg AP17, and (d) Zn AP18

Table 6.5: Influence of cations on the average particle and agglomerate sizes (n=3)

Sample	Cation substitution	Average size (µm)	
		Particles	Agglomerates
AP09	N/A	2.7±0.5	24.6±4.3
AP16	Sr	4.9±0.9	40.5±3.7
AP17	Mg	1.6±0.4	19.9±4.2
AP18	Zn	3.3±0.4	29.5±5.1

6.4.5 Thermal behaviour

The thermal behaviour of samples AP16 – AP18 were analysed by simultaneous DTA-TGA and the results are shown in Figures 6.6 – 6.8. A gradual loss of weight was observed between 250 and 700°C, which is attributed to the dehydration of HPO_4^{2-}, present within CDHA, to $P_2O_7^{4-}$ according to Equation 2.4. An increase in the weight loss within this temperature region was demonstrated for AP16 – AP18 compared with AP09 (Table 6.6).

Differentiation of TGA data (DTG) revealed a distinct rapid weight loss region between 700 and 800°C for all samples except AP17. Reactions within this temperature region can be associated to the transformation of β-$Ca_2P_2O_7$ to HA and β-TCP as described by Equation 2.5. Water losses calculated from TGA data were used in combination with Equations 2.4 and 2.5 to determine HPO_4^{2-}, $P_2O_7^{4-}$, as well as HA and TCP content (Table 6.7).

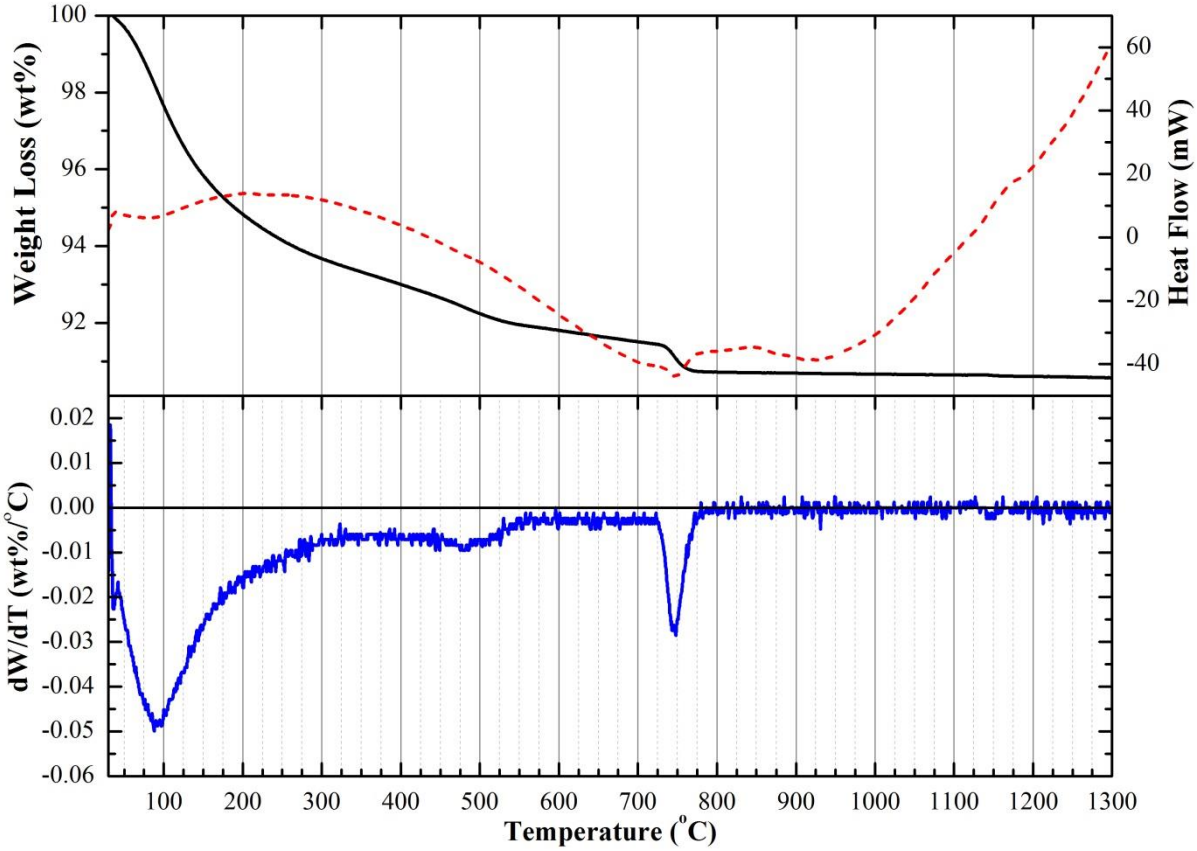

Figure 6.6: Thermal behaviour of AP16 (Sr)
(DTA = dashed red line, TGA = solid black line, DTG = solid blue line)

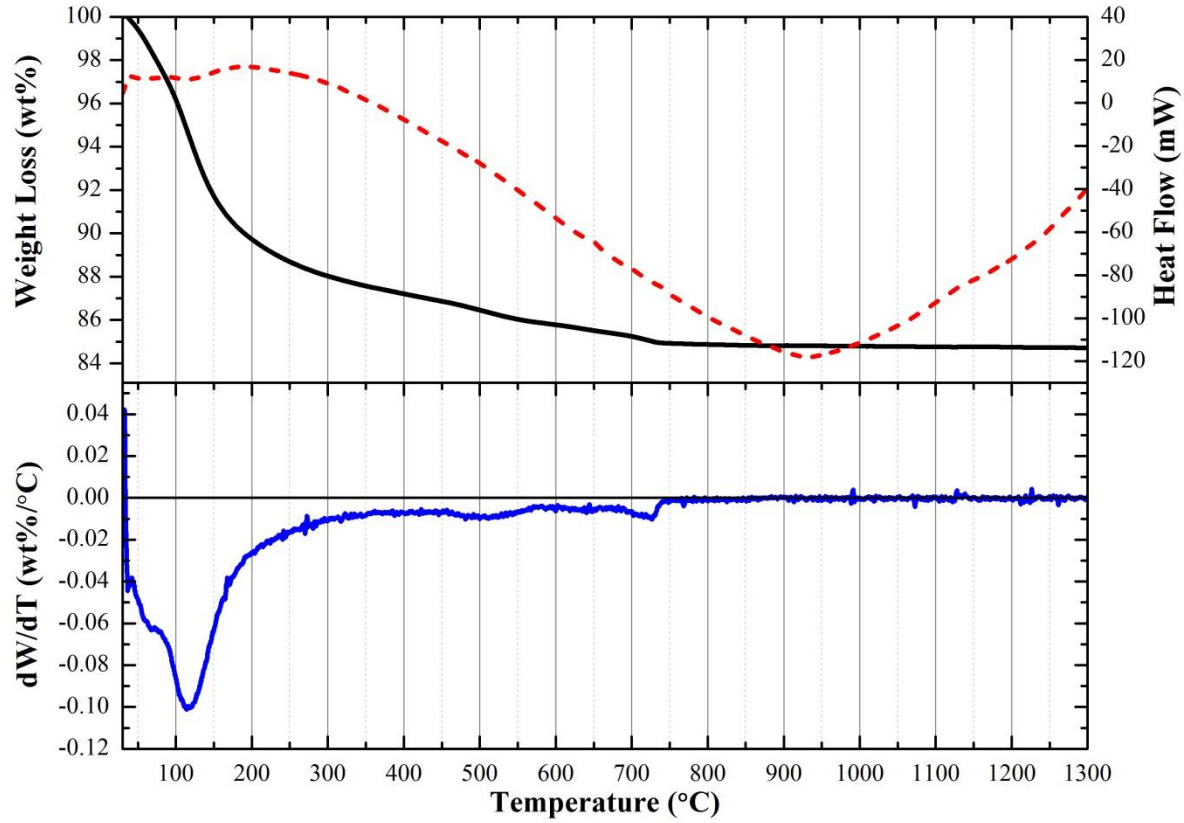

Figure 6.7: Thermal behaviour of AP17 (Mg)
(DTA = dashed red line, TGA = solid black line, DTG = solid blue line)

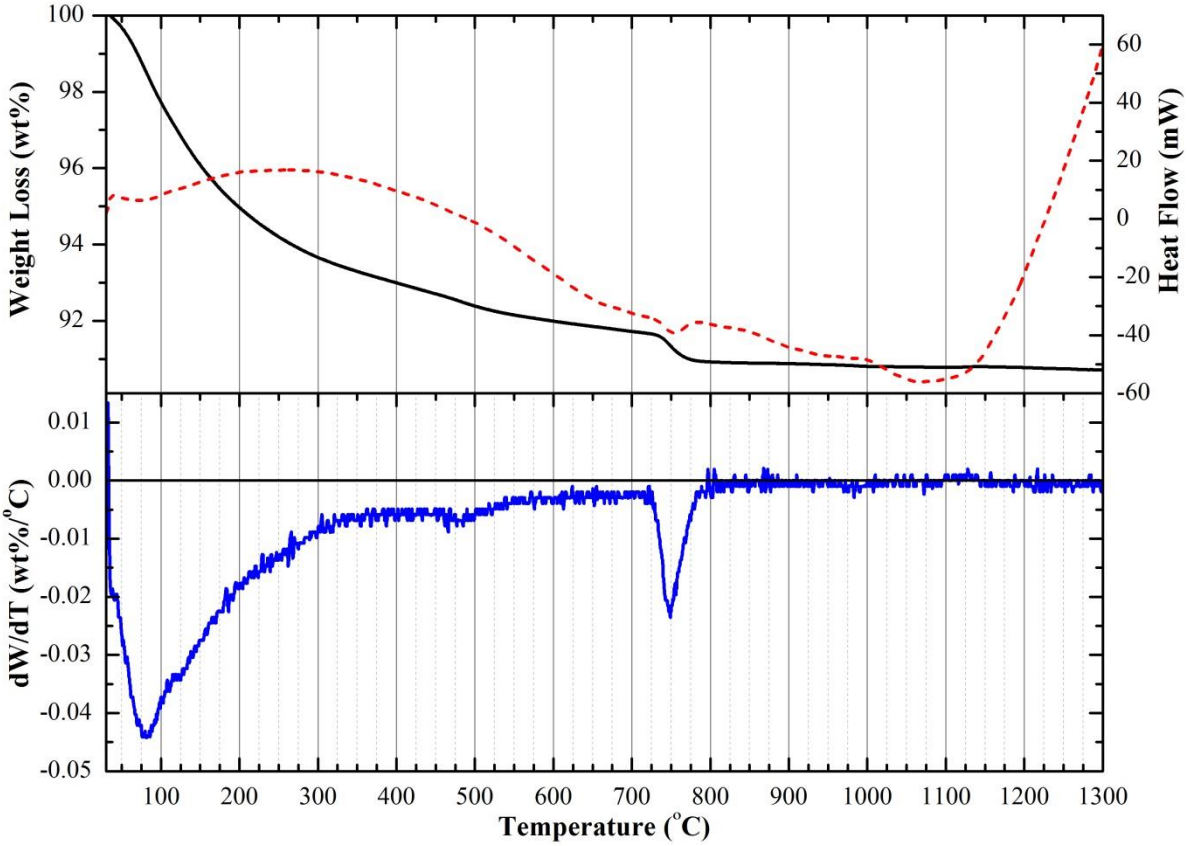

Figure 6.8: Thermal behaviour of AP18 (Zn)
(DTA = dashed red line, TGA = solid black line, DTG = solid blue line)

Table 6.6: Influence of cations on the amount of water lost between temperature regions associated with Equations 2.4 and 2.5
[a]peak area between 700 - 800°C

Temperature region (°C)	Water loss (wt%)			
	AP09	AP16	AP17	AP18
250 – 700	1.98	2.64	3.45	2.48
700 – 800[a]	0.71	0.72	0.31	0.74
30 – 800	8.26	9.28	15.13	9.07

Table 6.7: Influence of cations on chemical composition calculated from DTG analysis using Equations 2.4 and 2.5
[a]peak area between 700 - 800°C

Temperature region (°C)	Ion/phase	Source	Weight (wt%)			
			AP09	AP16	AP17	AP18
250 – 700	HPO_4	CDHA	21.09	28.16	36.72	26.45
	P_2O_7		19.11	25.52	33.27	23.96
700 – 800[a]	P_2O_7		6.82	6.90	2.98	7.18
	TCP		36.46	36.93	15.95	38.43
	HA		55.27	53.79	68.92	52.50
HA + TCP residue (mg)			8.49	11.45	6.92	13.92
TGA residue at 800°C (mg)			8.49	11.45	6.92	13.92

6.4.6 Elemental analysis

XRF was used to identify the presence of additional cations within as-synthesised powders. The accuracy of cation substitution, defined as the experimental amount detected divided by the theoretical substitution, was calculated (Table 6.8). The detected amount of Sr substitution (AP16) was notably the most accurate and over 80% higher than the accuracies calculated for Mg (AP17) or Zn (AP18) doping.

Table 6.8: Accuracy of cation substitution levels measured by XRF
[a]Defined as experimental value divided by theoretical substitution level, [b]Mx cation substitution

Sample	Cation substitution (%)	Cation accuracy (%)[a]	Ca:P	Ca+Mx[b]:P
AP16	1.86 (Sr)	93	1.48	1.53
AP17	1.03 (Mg)	10.3	1.48	1.53
AP18	0.24 (Zn)	12	1.56	1.57

6.4.7 Surface area

Substitution of all the investigated divalent cations was found to increase the measured surface area compared with AP09, which was prepared under the same reaction conditions (Table 6.9). Notably, AP17 exhibited a surface area 60% larger than AP09.

Table 6.9: Influence of cation substitutions on the surface area of as-synthesised powders

Sample	Cation substitution	Surface area (m^2/g)
AP09	N/A	106.7±0.2
AP16	Sr	110.6±0.3
AP17	Mg	170.8±0.8
AP18	Zn	117.1±0.2

6.4.8 SBF test

The surface of pellets were visualised via SEM prior to immersion in SBF (Figure 6.9). Typically, micron sized ridges were observed, which are expected to infer surface roughness. Immersion in SBF solution resulted in the formation of a surface coating after 7 days (Figure 6.10 a and b). This coating did not cover the entirety of the surface but instead was shown to be randomly dispersed. After 28 days a change in the pellet morphology was visualised suggesting that a degree of surface degradation occurred (Figure 6.10 c).

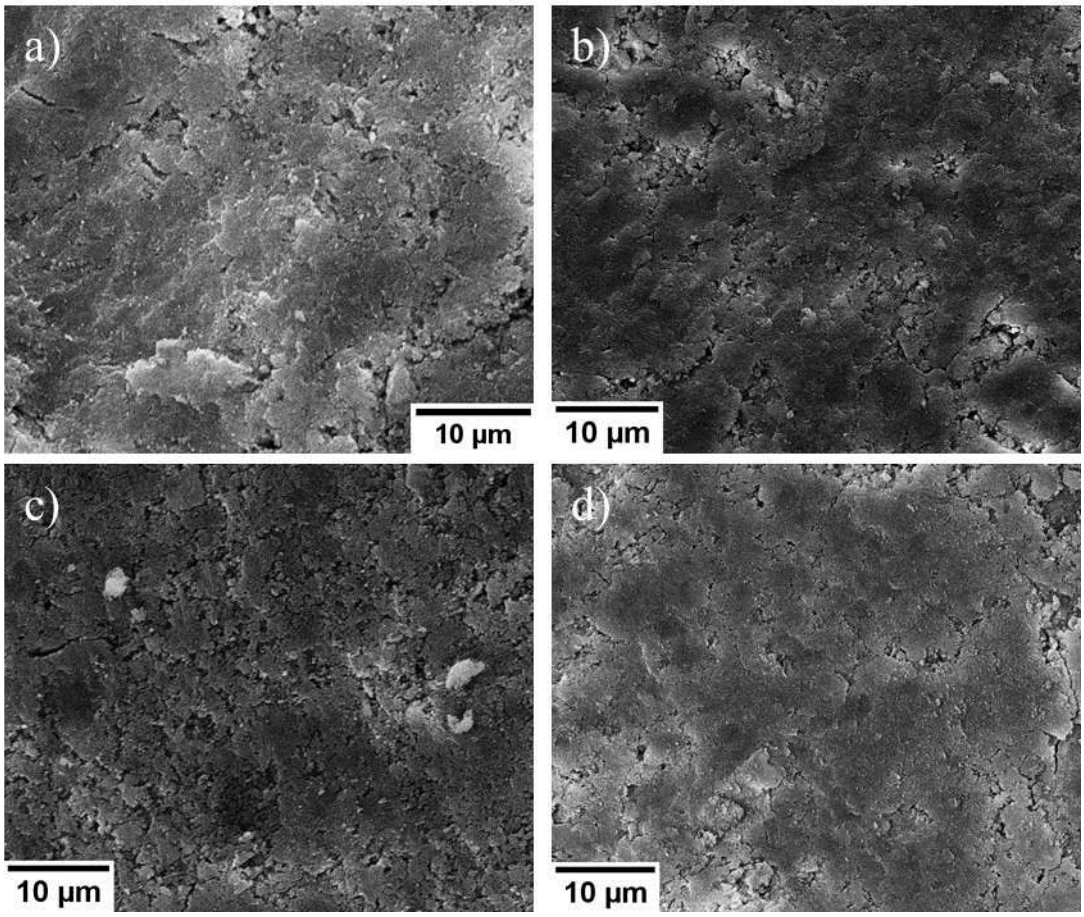

Figure 6.9: Surface of pellets containing cations prior to immersion in SBF (a) AP09, (b) Sr AP16, (c) Mg AP17, and (d) Zn AP18

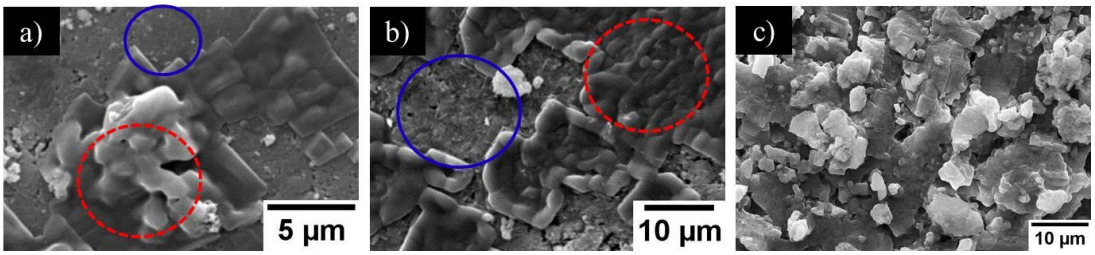

Figure 6.10: Influence of cations on the morphology of surface apatite grown in SBF (a) AP16 day 7, (b) AP18 day 14, and (c) AP16 day 28 (solid blue circle pellet surface, dashed red circle surface coating)

6.4.9 Live/dead assay

Fluorescence micrographs demonstrated the viability of MC3T3 cells seeded on substrates prepared with additional cations, which indicates cytocompatibility (Figure 6.11). An increase in the density of cells was visually observed as well as a change in morphology from rounded to elongated, which indicates that substrates supported adhesion, spreading and proliferation of MC3T3 osteoblast precursor cells.

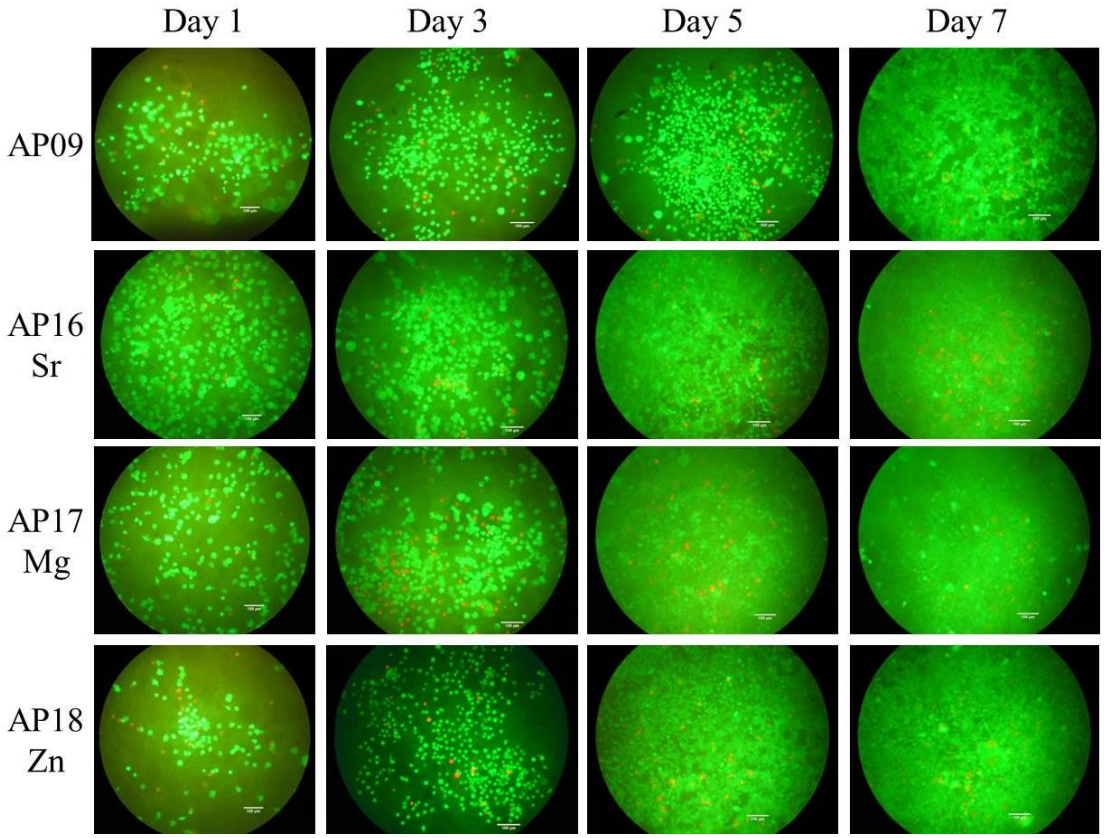

Figure 6.11: Influence of cations on the viability of MC3T3 cells seeded on substrates (green = live, red = dead)

6.4.10 MTT assay

An increase in the number of metabolically active cells was observed on substrates over the culture period (Figure 6.12). Proliferative rates between 1 and 7 days were calculated and in particular, compared with AP09, samples substituted with theoretical concentrations of 10mol% Mg (AP17), and 2mol% Zn (AP18) exhibited an increase of 80 and 40% metabolically active cells, respectively (Table 6.10). In contrast, AP09 and AP16 demonstrated comparable proliferative rates. These results support live/dead fluorescence micrographs since they advocate that substrates are cytocompatible and support the proliferation of cells.

Standard ANOVA testing established that the increase in cell number between day 1 and 7 was statistically significant for substrates (Table 6.11). This assessment was reflected when between group variances were compared to within group variances calculated from the linear regression of experimental data for days 1 – 3. Notably, a negative day 7 *F* ratio was calculated for AP17 when a linear trend line between days 1 and 5 was used, which is due to the significant increase in the number of cells at day 5 skewing the lag growth phase rate. Compared with other samples AP17 exhibited a

much higher proliferative rate between days 3 and 5. Specifically, AP17 was the only sample that showed a statistically significant increase in the number of metabolically active cells at day 5, which suggests that the exponential cell growth phase began between days 3 and 5.

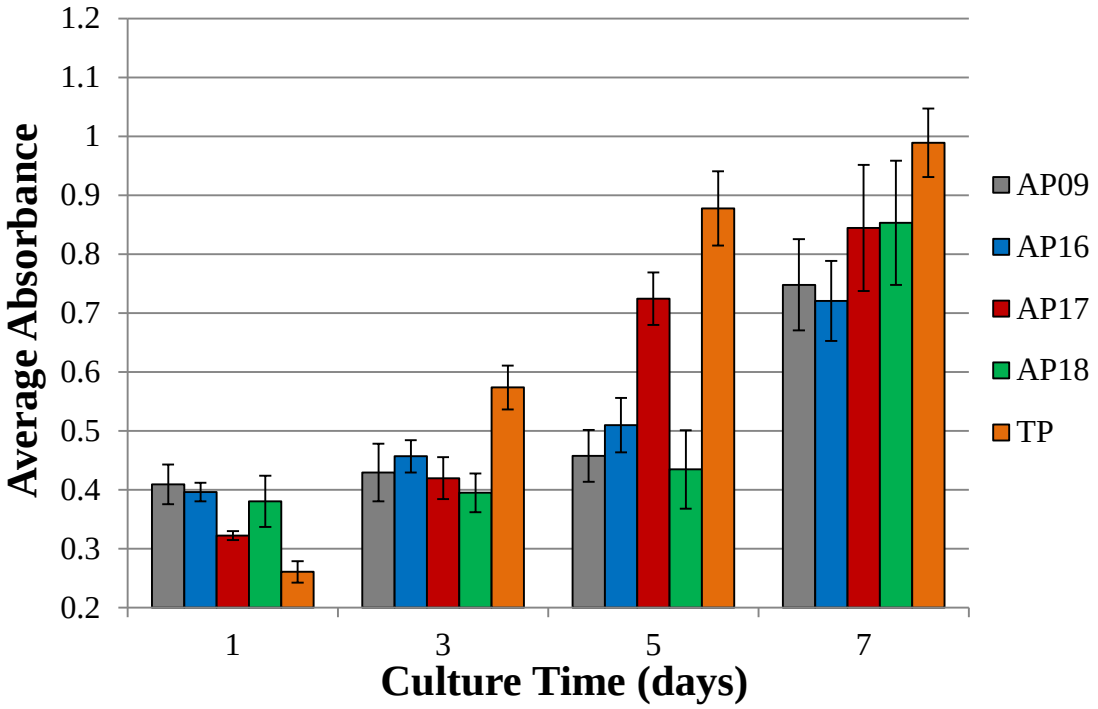

Figure 6.12: Influence of cations on metabolic activity of MC3T3 osteoblast precursor cells

Table 6.10: Influence of cations on the proliferative rate of MC3T3 cells assessed by MTT assay between 1 and 7 days

Sample	Cation substitution	Proliferative rate (%)
AP09	N/A	82.8
AP16	Sr	81.9
AP17	Mg	161.9
AP18	Zn	124.3

Table 6.11: Statistical analysis of MTT assay AP16 – AP18
F_{crit} = 4.965 where p<0.05, * = statistically significant

Sample	Cation substitution	ANOVA test	Modified ANOVA test		
		Day 7 *F* ratio	Day 7 *F* ratio		Day 5 *F* ratio
			Trend 1-3	Trend 1-5	Trend 1-3
AP09	N/A	96.317*	7.237*	6.842*	0.212
AP16	Sr	130.184*	6.975*	5.153*	-0.383
AP17	Mg	142.161*	9.780*	-0.810	8.821*
AP18	Zn	103.221*	12.208*	8.655*	0.720
TP	N/A	767.697*	-18.333	-5.764	-2.765

6.4.11 Hoechst assay

Results for the fluorescence of DNA stained with Hoechst 33258 supported those obtained from live/dead and MTT assays since an increase in the number of MC3T3 cells was demonstrated between 1 and 7 days of culture (Figure 6.13). Calculated proliferative rates revealed a smaller increase in cell number between day 1 and 7 for substrates substituted with any of the investigated cations compared with the control HA sample prepared under the same experimental conditions (Table 6.12).

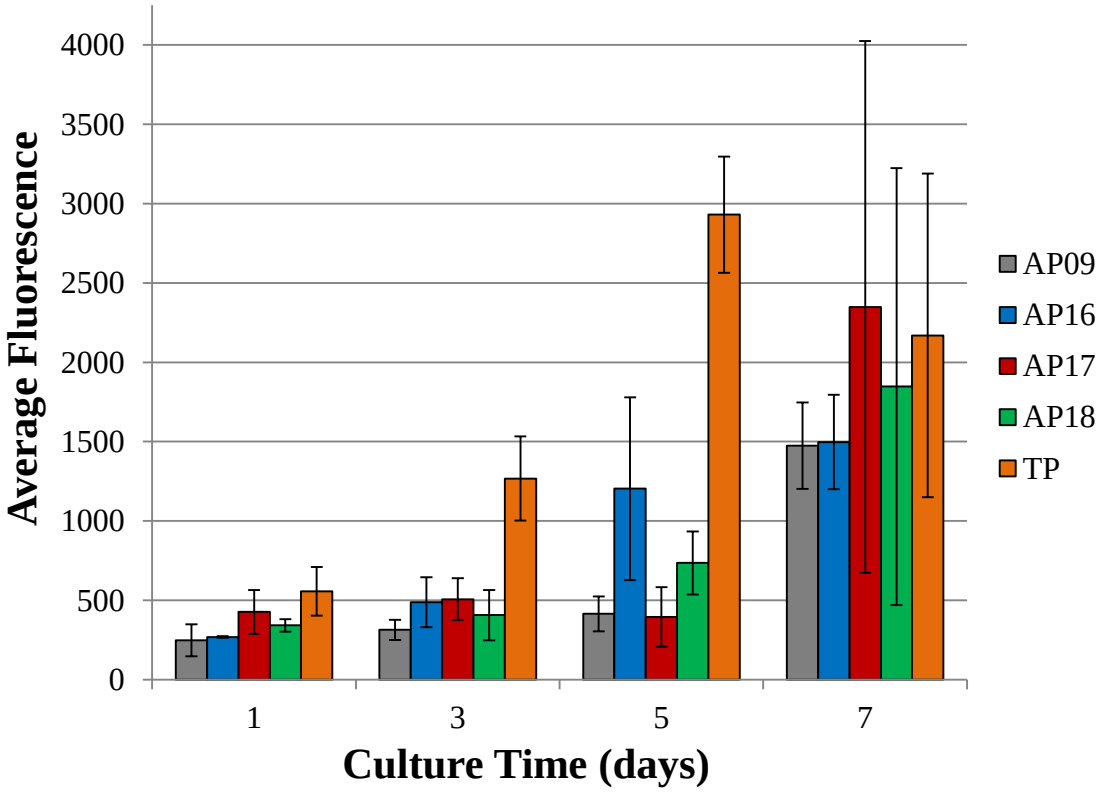

Figure 6.13: Proliferation of MC3T3 cells on substrates substituted with divalent cations assessed by Hoechst assay

Table 6.12: Influence of cations on the proliferative rate of MC3T3 cells assessed by Hoechst assay between 1 and 7 days of culture

Sample	Cation substitution	Proliferative rate (%)
AP09	N/A	495.7
AP16	Sr	457.4
AP17	Mg	450.0
AP18	Zn	439.7

ANOVA using the standard test demonstrated the statistical significance of the increase in cell number between days 1 and 7 for all substrates, except AP18 (Table

6.13). Using the modified method AP16 was pulled out as non-significant using a trend line from days 1 – 3. Furthermore, the day 7 *F* ratios for AP16 and AP18 calculated from linear regression of day 1 – 5 were less than the F_{crit}. Growth in cell number at day 5 was not statistically significant for any sample as determined by the modified ANOVA test.

Table 6.13: Statistical analysis of Hoechst assay AP16 – AP18
F_{crit} = 7.709 where p<0.05, *statistically significant

Sample	Cation substitution	ANOVA test	Modified ANOVA test		
		Day 7 *F* ratio	Day 7 *F* ratio		Day 5 *F* ratio
			Trend 1-3	Trend 1-5	Trend 1-3
AP09	N/A	106.892*	14.895*	12.780*	0.508
AP16	Sr	102.615*	6.247	-0.298	5.432
AP17	Mg	7.839*	15.237*	14.433*	-1.739
AP18	Zn	7.154	13.897*	7.029	2.797
TP	N/A	14.656*	-2.927	-1.299	-1.253

6.5 Discussion

The reactivity of apatites is dependent on their crystal structure and thus substitutions in HA can alter physicochemical properties such as dissolution [318]. It is known that Y^- monovalent ions found within the ion channels can be exchanged readily at high temperature without any crystal alteration, whereas substitutions for trivalent XO_4^{3-} or bivalent Me^{2+} ions that constitute the apatite frame may result in reorganisation of the structure [2]. Notably, a larger degree of XRD peak broadening of as-synthesised AP16 – AP18 compared with AP09 was demonstrated (Figure 6.1). Advantageously line broadening analysis confirmed crystallites of all samples were nanosized (Table 6.3). In particular, a 45% reduction in crystallite size was calculated for precipitates that theoretically contained 10mol% Mg compared with CDHA prepared under the same conditions (AP09). A number of authors, for example [319], have reported that Mg acts as an inhibitor of HA nucleation and subsequent crystallisation, which may explain the above observation as well as the increase in surface area measured for AP17 (Table 6.9). FTIR spectra of as-synthesised samples established the following trend for the sharpness of PO_4^{3-} bands: AP09>AP16>AP18>AP17, which is consistent with the degree of peak broadening observed in XRD patterns and the above assertion that Mg inhibits the crystallisation process (Figure 6.3).

Relative to Ca^{2+} the ionic radii of Sr^{2+}, Mg^{2+}, and Zn^{2+} are 116, 75 and 65% the size, respectively. Shifts to lower diffraction angles were observed for Sr substituted samples (AP16), and in contrast characteristic peaks of Mg (AP17) and Zn (AP18) doped powders were shifted to higher angles (Table 6.4), which suggest expansion and contraction of the lattice parameters, respectively. This advocates that the additional cations partially replaced Ca^{2+} within the crystal structure.

Comparison of XRD patterns of AP16 – AP18 heated to 600°C revealed the presence of relatively sharp peaks that matched with β-TCP in AP17 (Mg), which were not observed in any other samples (Figure 6.2). In addition to the aforementioned inhibitory effect of Mg on nucleation, it has been reported that incorporation of this cation in non-stoichiometric HA favours a thermal transformation to whitlockite [$Ca_9MgH(PO_4)_7$] above 600°C [129]. It should be noted that it is possible to replace up to 15% of Ca^{2+} with Mg^{2+} without changing the β-TCP structure. Since whitlockite and β-TCP exhibit a similar crystal arrangement this explains why XRD peaks were matched to β-TCP [320]. Compared with AP09 the PO_4^{3-} bands for AP17 exhibited a shape synonymous with β-TCP and specifically the intensity of these bands were greater for AP17 compared with AP16 (Sr) and AP18 (Zn) (Figure 6.4).

Variation of the size of globular particles and agglomerates was evidenced by SEM micrographs (Figure 6.5). Specifically, particulates and agglomerates were 80 and 65% larger for Sr substituted precipitates (AP16), respectively compared to AP09. In contrast, a 40 and 20% reduction was observed when Mg was used (AP17), respectively. These observations are consistent with the trend of ionic sizes, i.e. $Sr^{2+}>Ca^{2+}>Mg^{2+}$.

Incorporation of Mg was observed to influence the high temperature behaviour of the prepared apatites between 700 and 800°C (Figure 6.7). Specifically, a significant reduction in the area of the DTG peak within this temperature region was demonstrated and this is linked to the degradation of AP17 to whitlockite below 600°C, as evidenced by XRD analysis. Thermal analysis suggests that the presence of any of the investigated cations led to an increase in the concentration of non-apatitic HPO_4^{2-} compared with AP09 (Table 6.7). This is explained in terms of the additional cations altering the ionic species (i.e. decrease in Ca^{2+} concentration as a result of replacement with Sr, Mg, or Zn) within the initial solution and thus the relative degrees of supersaturation. Gradual weight loss between 250 and 700°C and the

presence of banding associated with non-apatitic HPO_4^{2-} in FTIR spectra suggests substituted samples are CDHA and in the case of AP17 XRD results advocate this specimen is potentially Mg-TCP.

Presence of Sr, Mg, or Zn was confirmed by XRF. Analysis clearly indicated a significantly greater accuracy for Sr substitution in comparison to Mg and Zn (Table 6.8). Other studies have reported significantly higher substitutions of 10% Mg and 20mol% Zn, therefore it cannot be concluded that the lower accuracy of these cations in AP17 and AP18 is due to the respective substitution limits for these elements [139, 321]. Instead, these results are indicative that the process of Mg and Zn incorporation is relatively difficult. In comparison, the higher accuracy of Sr substitution can be linked to the ability of Sr^{2+} to replace Ca^{2+} in the HA structure over the whole range of composition (i.e. 0 – 100%) [11]. These results suggest that the difference in ionic size play an important role in determining the ease of substitution but it is recognised that it would be necessary to investigate a range of substitution levels to clarify any correlation. It should also be noted that these results do not differentiate between surface absorption or lattice substitution, and therefore it is possible that the detected levels of Sr, Mg, or Zn are merely present on the surface of particles. However, since all XRD patterns exhibited shifts consistent with relative ionic sizes this strongly suggests that there is at least a partial substitution of these cations in the lattice structure. The Ca+Mx:P ratios calculated from XRF results indicate all samples are CDHA (Table 6.8), which is consistent with FTIR and DTA-TGA analyses.

The advantages of the SBF test have previously been discussed in section 5.5 and hence justify why this technique has been used again in this chapter as a prerequisite to cell culture. However, the morphology of the surface coating on samples AP16 – AP18 was not shown to exhibit the spheroidal nodules and fine needle-like structure known to be typical of SBF grown apatite [301]. The author does not consider this a false result of bioactivity but instead experimental confirmation of the sensitivity and variability of SBF, which are the underlying reasons why this test is debated within the literature. It is suggested that the noticeable surface degradation of substrates containing additional cations influenced the process of apatite precipitation in SBF. These effects were only noted for samples AP16 – AP18, which explains why SBF results for these samples are different than those presented in other chapters.

Live/dead assay confirmed the viability of cells seeded on samples shown to contain Sr, Mg, or Zn thus indicating that the presence or effect of these additional cations on substrates did not induce a cytotoxic response (Figure 6.11). MTT and Hoechst assays demonstrated the ability of these samples to support cell proliferation between 1 and 7 days of culture. Specifically, compared to the control sample prepared under the same conditions (AP09), substrates containing Mg (AP17) and Zn (AP18) were shown to exhibit a relative increase of 80 and 40% metabolically active cells between days 1 and 7, respectively (Table 6.10). These samples exhibited a greater degree of broadening of characteristic XRD peaks as well as FTIR bands associated with PO_4^{3-}, and a relatively large surface area compared to the control. Thus, it is proposed that these characteristics are responsible for the observed improvement in the ability of substrates to support cell proliferation. This assertion is supported by the literature since numerous authors have reported an inverse relationship between crystallinity and mineralisation, and an increase in the number of osteoblasts on rougher substrates (section 5.5). Therefore it seems that the inhibitory effect reported for Mg as well as Zn on the process of nucleation is beneficial to the ability of substrates to support the proliferation of osteoblast precursor cells, this is explained in terms of the improved dissolution associated with lower crystallinity [319]. As such, scaffolds made from these materials might exhibit improved osteointegration and osteoconduction. SEM micrographs of all substituted substrates after 28 days of immersion in SBF exhibited morphology indicative of surface degradation (Figure 6.10 c), this was not observed in other samples characterised in this thesis. It is recommended that future work include characterisation of substrate dissolution rates since this information could support these suggestions that are based on qualitative observations. Standard and modified ANOVA testing verified the statistical significance of the observed cell proliferation (Table 6.11). The different trend in growth measured for Mg containing substrates (AP17) was distinguished by the *F* ratios calculated using the modified method. This highlights the importance of considering the whole data set to ensure information is not lost. The notable difference in the proliferative trend of AP17 is suggested to be due to the higher HPO_4^{2-} content (Table 6.7), which infers a greater degree of non-stoichiometry and thus a faster dissolution rate. The negative *F* ratio calculated for AP17 based on the linear regression of day 1 – 5 suggests that the exponential growth phase of MC3T3 cells begins between days 3 and 5, whereas for other samples it appears this does not occur until after day 5. Thus it is expected that osteoblasts seeded

on this sample would reach confluency quicker. No discernible difference was demonstrated between the number of metabolically active cells measured on AP09 and substrates containing Sr (AP16). The density of osteoblast precursor cells on HA containing 10mol% Sr has been reported previously to significantly exceed a control sample of pure HA [18], which suggests a higher concentration of Sr may be required to induce advantageous biological effects.

A difference in the degree of proliferation on substrates was revealed between MTT and Hoechst assays, which are to be expected since the two assays measure different cellular properties. In contrast, the proliferative rates calculated from DNA staining using Hoechst 33258 for samples AP16 – AP18 were on average 9.4% lower compared with AP09. In previous chapters Hoechst assay results revealed an improved proliferative rate was associated with an increase in HPO_4^{2-} content, hence the results presented here call this association into question since AP16 – AP18 exhibited a greater concentration of acid phosphate ions compared with AP09. However, due to the large degree of experimental variability, in particular for substrates containing Mg (AP17) and Zn (AP18), average values of these data sets were skewed by anomalous results and thus cannot be used to discount previous assertions. In order to draw a cohesive overall conclusion it is recommended that a larger number of samples are tested in the future so that any outliers can be disregarded. Statistical analysis confirmed the observed proliferation as significant, except AP18 using the standard ANOVA method and this is associated with the larger variability of fluorescence recorded at day 7 for this sample. In contrast, when the observed lag growth phase rate was stripped back, using the modified ANOVA test, the day 7 *F* ratio for substrates containing Zn exceeded the F_{crit} value. The non-significance of cells seeded onto Sr-CDHA (AP16) at day 7 can be explained by the relatively large increase in cell number between days 3 and 5 compared to the increase between days 5 and 7.

6.6 Conclusions

Literature concerning substitutions in HA is vast and numerous biologically relevant cations and anions have been investigated in an attempt to match the reactivity of native bone apatite. In summary, the influence of substituting precipitates with theoretical amounts of 2mol% Sr, 10mol% Mg, or 2mol% Zn on critical physical, chemical and crystallographic properties, which are related to cytocompatibility and

the ability of substrates to support cell proliferation were investigated. Importantly, CDHA substituted with these divalent cations was synthesised under the same reaction conditions (pH, temperature, solute concentration, solvent system) in order to assess the single factor influence of Sr^{2+}, Mg^{2+} or Zn^{2+}.

Shifts of characteristic XRD peaks of HA due to the addition of Sr, Mg or Zn were demonstrated and found to be consistent with the relative ionic sizes of these cations compared to Ca^{2+}. These observations present evidence to suggest that the levels of substituents detected by XRF were at least partially incorporated into the apatite lattice. Thermal conversion of Mg substituted precipitates to whitlockite (exhibiting a similar structure to β-TCP) was corroborated by XRD patterns of samples heated to 600°C. It is concluded that this cation inhibited the nucleation process resulting in a reduction in the average crystallite size, crystallinity, and a 60% increase in the surface area of precipitates. These chemical and physical properties translated to an 80% increase in the number of metabolically active MC3T3 cells after 7 days of culture compared to the control. The effect and incorporation of Zn was also shown to enhance cell proliferation by 40%. In contrast, no marked difference in the ability of Sr doped substrates to support cell proliferation compared to the control was observed.

Use of the modified ANOVA test enabled samples that exhibited a different proliferation trend to be identified since this method considered the whole data set. In general, day 7 *F* ratios calculated using both the standard and modified ANOVA test (using the linear trend of day 1 – 3 data) exceeded the critical value and thus the proliferation observed can be concluded as statistically significant.

Despite the low accuracy of Mg and Zn substitutions the results presented in this chapter suggest effects of these cations on composition and particle surface area translated to an enhanced ability of substrates to support cell proliferation. These features are considered promising since they could help improve in-vivo osteointegration and osteoconduction of scaffold structures. If these results are to be taken further a better understanding of the positioning of these cations in the lattice would be valuable. In order to optimise the substitution level a range of doping concentrations would need to be schematically investigated.

Chapter 7

Feasibility study - fabrication of hydroxyapatite scaffolds

7. Feasibility study - fabrication of hydroxyapatite scaffolds

7.1 Fabrication methodology selection

Cancellous bone tissue exhibits a porous hierarchical structure that facilitates the migration, and proliferation of bone cells (Figure 2.1). Besides the synthesis of appropriate apatite biomaterials that mimic the chemical and crystallographic properties of bone, the structural attributes of bone tissue scaffolds such as pore size distribution as well as interconnectivity, porosity, and surface topography, are known to be vital factors that determine the success of the implant.

A review of common conventional and ALM methods used to fabricate bone scaffolds in relation to the structural attributes listed above was outlined in Table 2.8. In summary, low interconnectivity and poor mechanical strength of structures produced via conventional methods was highlighted. The literature also exposes the limited reproducibility and risk of using organic solvents in conventional techniques, such as salt leaching. In contrast, ALM methodologies generally require higher capital investment. However, this cost can be justified since these techniques enable the user to define scaffold morphology resulting in improved reproducibility, which ultimately could determine the success of the implant. Many ALM systems also operate without using toxic organic solvents and powder based techniques have been shown to produce rough microporous surfaces favourable for bone cell attachment and fluid flow, which can improve dissolution [322].

In the present work, the feasibility of two methods was investigated: (1) yeast as a pore forming agent (YP), and (2) 3D printing (3DP). Firstly, yeast was utilised as a natural pore forming agent since it overcomes the risks associated with using organic solvents in conventional techniques. This method can be described as a non-aqueous salt leaching technique where the by-product of the reaction between yeast and sugar, namely CO_2 was exploited, instead of a conventional salt, to form pores within the scaffold structure. Secondly, in comparison, the viability of using a commercial powder based 3DP system was also selected to evaluate since it is compatible with the

raw feedstock material form of HA, can be performed at RT, does not typically use any organic solvents, and printed parts inherently exhibit desirable physical features, such as surface roughness.

This chapter presents an experimental assessment of the feasibility to fabricate HA scaffolds via these two methods, YP and 3DP, that mimic the physical porous structure of native bone tissue. Scaffolds prepared using both techniques were characterised to reveal a number of features known to be crucial to implant success (section 2.6.2), including porosity, pore size, and interconnectivity. Since reproducibility is known to be an inherent disadvantage of conventional methods the consistency and variation between fabricated scaffolds was also discussed.

7.2 Materials and methodology

Analar grade reagents were purchased from Sigma Aldrich (UK) and used without further purification unless otherwise stated.

7.2.1 Method one - yeast as a pore forming agent (YP)

The principles used in traditional bread making, viz. dough mixing, fermentation, and baking, were followed with the addition of HA as an initial constituent. High purity HA (>90%, Fluka, UK) with a median particle size (d_{50}) of 5μm and a specific surface area of 72m^2/g was used as a precursor material. Gluten derived from wheat (≥80% protein), wheat based starch [$(C_6H_{10}O_5)_n$], and dried active yeast (DAY) were used as active constituents for the bioceramic dough. CO_2 was formed as a by-product of the reaction of sugar, from the starch constituent, and DAY.

20g batches of bioceramic dough were formed with HA loading between 25 and 80wt%. Dry dough components (HA, gluten, and starch) were homogenised in powder form using a ball mill (Glen Creston, UK). To form the bioceramic dough, 1g of DAY dissolved in lukewarm DI water was added in stages to the dry mixture that was then kneaded for 10mins, and left to ferment for 24hrs at RT covered with a moist cloth, which is referred to as proofing. Pre-firing of green bodies was performed at 600°C for 1hr at a ramp up rate of 1°C/min to burn off the gluten and starch constituents. The remaining HA structures were then sintered up to 1300°C, held at this temperature for 3hrs and then cooled to RT in an air atmosphere using a ramp up and down rate of 1°C/min. Variables investigated included, the influence of the gluten to starch ratio

(1:3 – 2:3), degree of grinding of DAY (unground or ground), and the yeast content (0.5 – 2g) (Table 7.1).

Table 7.1: Summary of the reaction conditions used to fabricate scaffold structures via YP method (G = ground, UG = unground)

Sample	HA loading (%)	Gluten:Starch	DAY content (g)	DAY (G/UG)
Y01	25	1:3	1	*G*
Y02	*25*	1:3	1	*UG*
Y03	50	1:3	*0.5*	UG
Y04	*50*	1:3	1	UG
Y05	50	1:3	*2*	UG
Y06	*60*	1:3	1	UG
Y07	60	*2:3*	1	UG
Y08	*70*	1:3	1	UG

7.2.2 Method two - 3DP

Prior to printing scaffold structures, the printability of HA:PVOH (Moiwol 23-88, Clariant, UK) composite powders was assessed by fabricating rectangular blocks of various compositions (50 – 100wt% HA). Prior to use, supplied PVOH was ball milled, passed through a 200μm sieve, mechanically mixed with appropriate amounts of HA, and stored at RT. Optimum binder saturation levels for each composition were visually assessed by considering the influence on part stability. This initial assessment was used to select printable HA:PVOH compositions to fabricate 200% cylindrical scaffold structures (Figure 7.1). Any loose powder was removed from parts after printing using compressed air.

Rectangular blocks and scaffolds were designed using Solidworks CAD software, and converted to stereolithography format prior to printing. Green body parts were printed using a ZPrinter 310 (ZCorp, US) 3D printer in combination with Zb60 binder (ZCorp, US). Layer thickness was defined as 0.1mm.

7.3 Scaffold characterisation

7.3.1 X-ray diffraction (XRD)

XRD analysis was performed on as-received and sintered (1300°C) HA, as well as a 50:50wt% composition of HA:PVOH. Phase identification was performed using the JCPDS database using the scan parameters previously described in section 4.3.1.

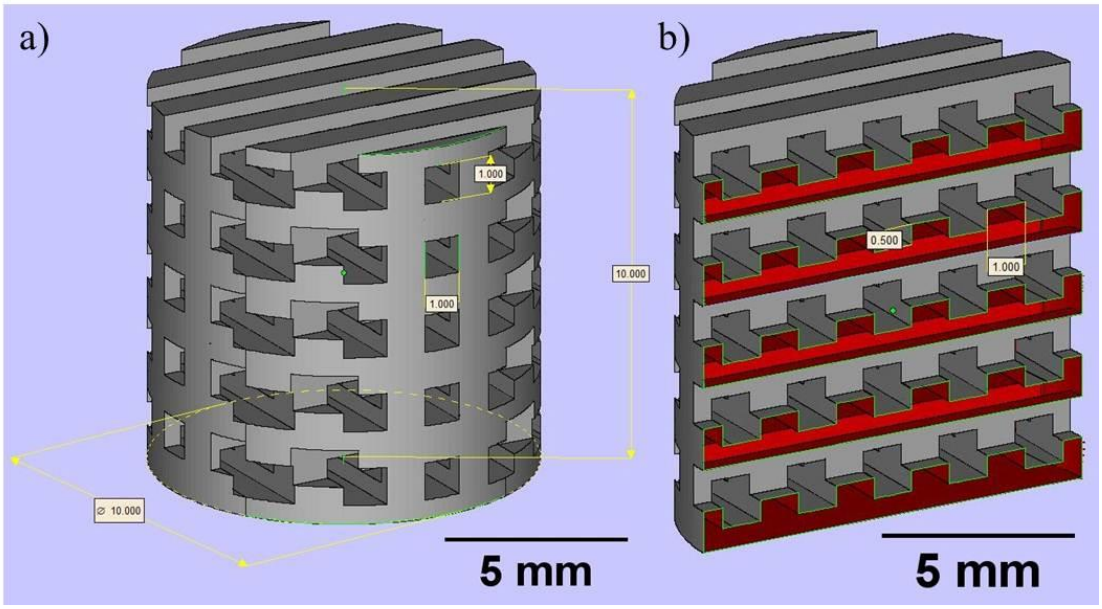

Figure 7.1: CAD design of 3DP cylindrical scaffolds (1mm pores, 10mm height and diameter) (a) External structure and (b) internal structure

7.3.2 Differential thermal and thermogravimetry analysis (DTA-TGA)

Burn out of organic constituents (starch and gluten) used in the YP process was characterised by DTA-TGA (section 3.3.3) by heating 20mg of dry bioceramic dough from 30 to 800°C at a constant ramp rate of 1°C/min in flowing air. The thermal behaviour of as-received HA and ball milled PVOH powders used in the 3DP procedure were also analysed between 30 and 1300°C at a constant ramp rate of 1°C/min in flowing air.

7.3.3 Scanning electron microscopy (SEM)

The method previously described (section 3.3.2) was used to image the surface topography, and microstructure of typical scaffolds. Micrographs were used to measure the average pore size (n=3) and qualitatively assess the degree of pore interconnectivity. Prior to analysis the constructs were attached to aluminium stubs using conducting silver paint and sputter coated with a thin layer of gold in an argon-purged chamber for 90s.

7.3.4 Computer tomography (CT)

A CT scanner (Model XT H 320 LC, Nikon Metrology, UK) was used to capture the volume data of a typical YP construct and visualise the internal structure.

7.4 Results

7.4.1 Characterisation of precursors used in YP and 3DP methods

7.4.1.1 Crystal structure

The phase purity of as-received and sintered HA (used in both YP and 3DP methods), as well as 50HA:50PVOH powders (used in only 3DP method) were analysed by XRD (Figure 7.2). Characteristic peaks of as-received HA and 50HA:50PVOH powders were matched to the JCPDS standard for HA (09-432) and DCPA (09-0080). Notably the peak intensity of the 50HA:50PVOH powder was reduced and a higher background observed. Sintering HA at 1300°C resulted in the formation of β-TCP (70-2065), and α-TCP (29-359) phases (Figure 7.2 c).

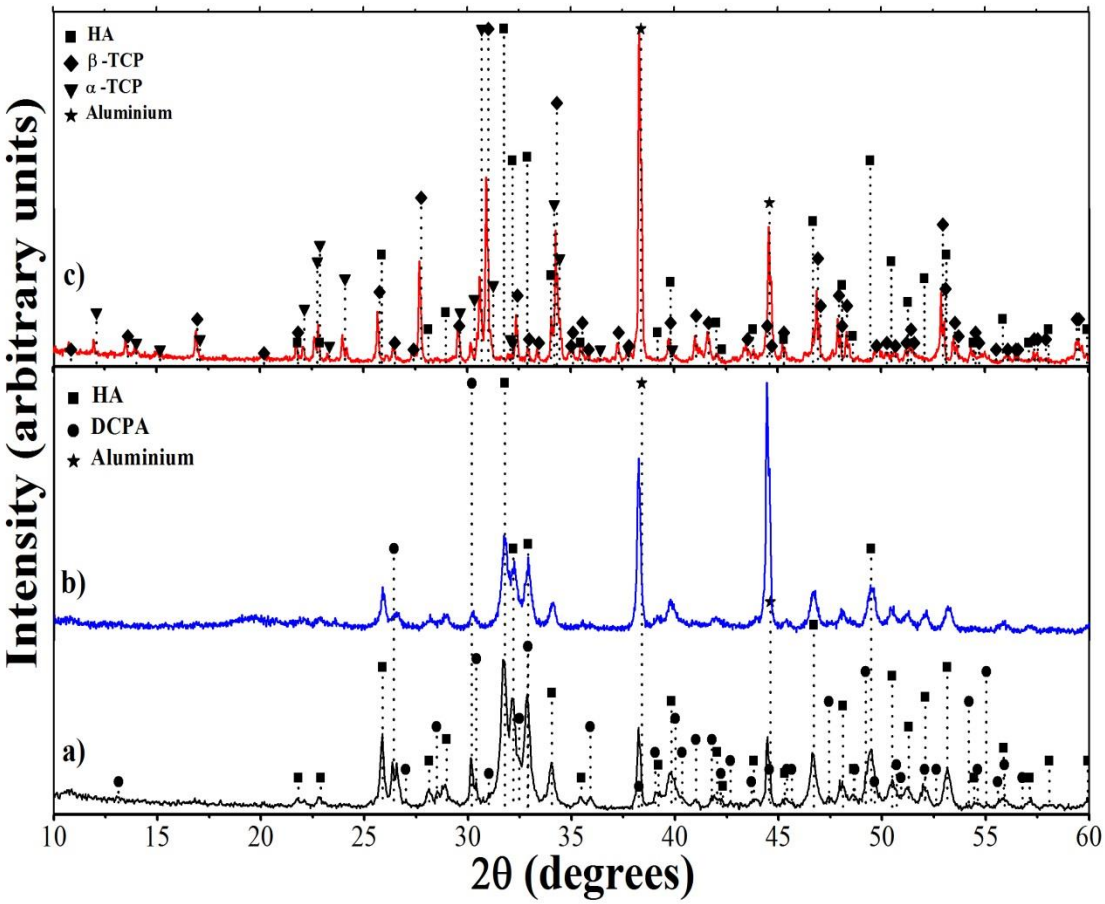

Figure 7.2: XRD pattern of (a) supplied HA, (b) 50HA:50PVOH, and (c) HA sintered to 1300°C

7.4.1.2 Thermal behaviour

Simultaneous DTA-TGA analysis of supplied HA, used in both fabrication processes, was carried out from 30 to 1300°C and the remaining mass was calculated to be 95.42wt% (Figure 7.3). Differentiation of the TGA curve (DTG) revealed the presence of three temperature regions where a significant change in the rate of weight loss was observed: (1) endothermic 350 – 450°C, (2) endothermic 700 – 800°C, and (3) exothermic 1100 – 1150°C. Gradual weight loss associated with an endotherm was also demonstrated below 350°C.

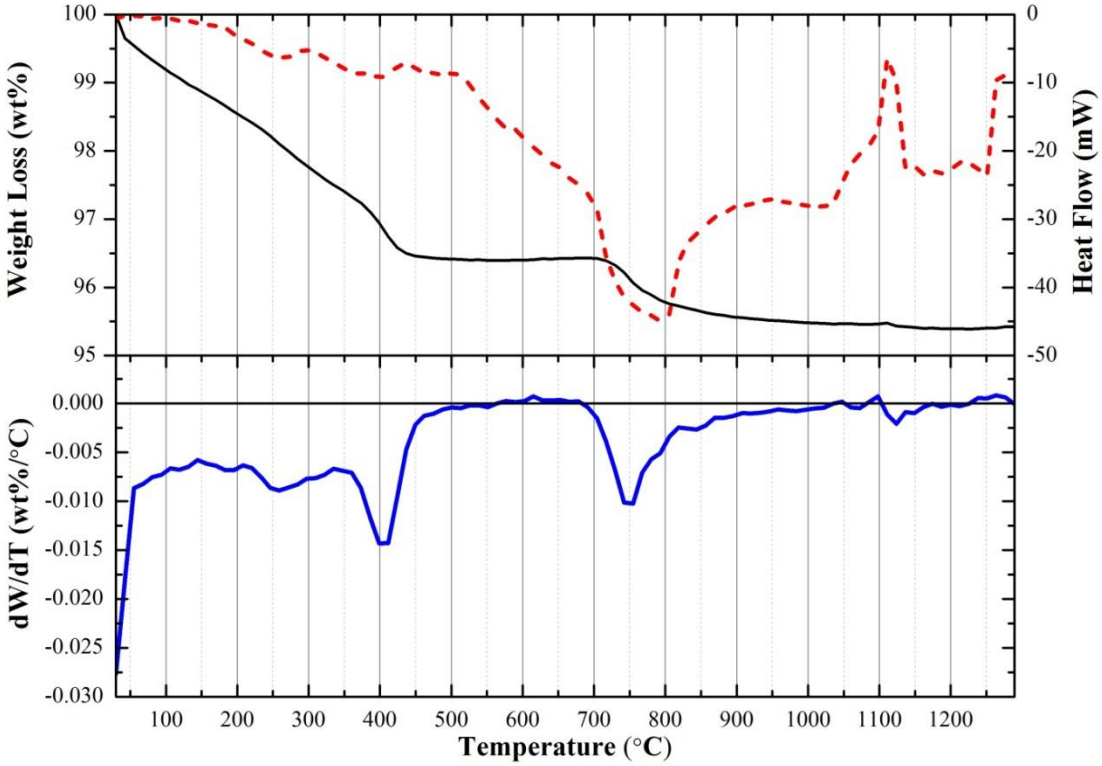

Figure 7.3: Thermal behaviour of as-received HA used in YP and 3DP processes (DTA = dashed red line, TGA = solid black line, DTG = solid blue line)

In comparison, simultaneous DTA-TGA analysis of ball milled PVOH revealed a residue of 0.45wt% at 1300°C (Figure 7.4), which is consistent with the maximum ash content (<0.5wt%) reported by the manufacturer. PVOH was heated above its thermal degradation temperature meaning cross linking of the polymer chain began to be disrupted, i.e. molecular deterioration. Onset of thermal degradation was observed to be approximately 185°C. Holland et al. attributed solid state thermal degradation of PVOH exclusively to the elimination of water [323] and this may account for the observed endothermic peak close to the degradation temperature (Figure 7.4). In contrast, the following were attributed to molten state degradation between 230 and

450°C: (1) elimination of water and chain scission, (2) formation of saturated and unsaturated volatile aldehydes, and (3) formation of saturated and unsaturated volatile ketones. The three exothermic DTA peaks exhibited between 245 and 450°C are attributed to molten state degradation of PVOH. The DTG peak at 260°C was associated to solid state degradation, and the other two regions of rapid weight loss, between 350 and 500°C, were attributed to removal of volatile aldehydes and ketones.

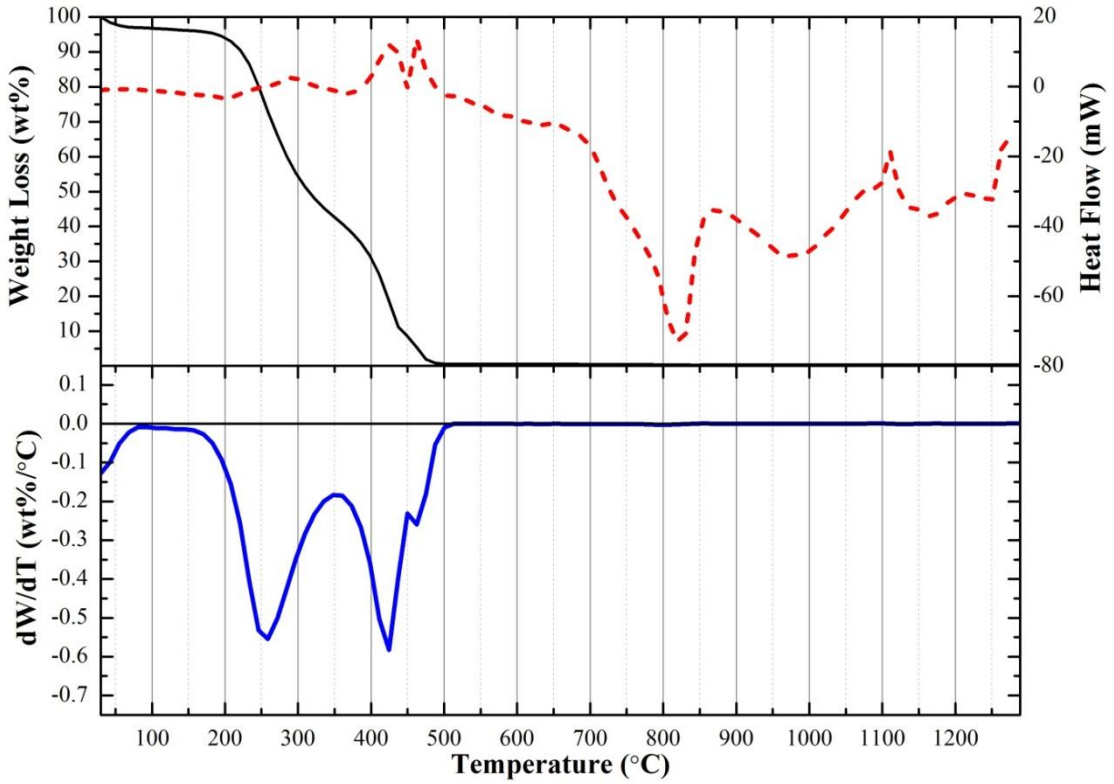

Figure 7.4: Thermal behaviour of ball milled PVOH used in the 3DP process (DTA = dashed red line, TGA = solid black line, DTG = solid blue line)

Burn out of the organic constituents, namely gluten and starch, from the bioceramic dough formed for sample Y02 was analysed by DTA-TGA (Figure 7.5). Three weight loss stages were observed between 30 and 800°C that corresponded to: (1) endotherm peaking at 80°C, (2) exotherm peaking at 340°C, and (3) exothermic reaction peaking at 460°C. These events are attributed to the removal of water, and the burn out of starch and gluten, respectively. A residue of 21.1wt% was calculated for Y02. When the weight loss observed for HA alone over this temperature regime (Figure 7.3) was taken into account (4.19wt%), this total 25.3wt%, corresponded approximately to the HA loading (25wt%) of Y02. This observation suggests that both organic constituents were completely removed from the dough.

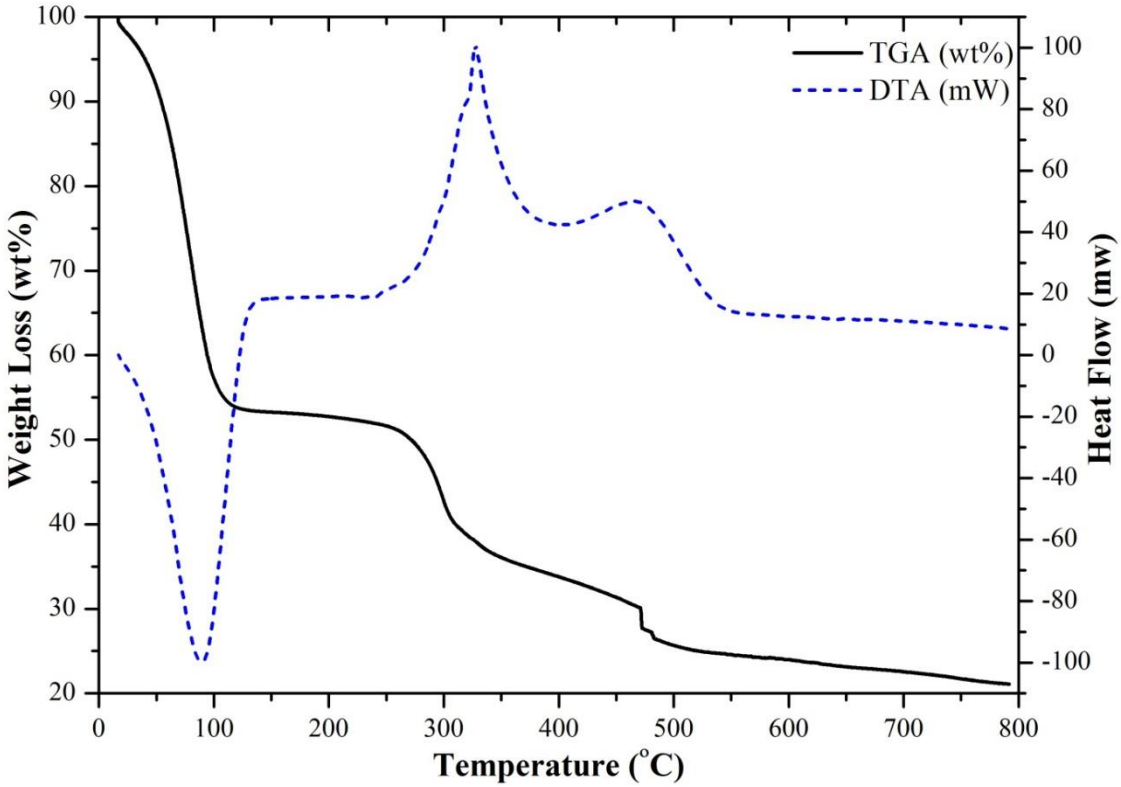

Figure 7.5: Thermal behaviour of Y02 25wt% HA bioceramic dough formed in YP process

7.4.2 Microstructural development of scaffolds

7.4.2.1 Method one - YP scaffolds

It is well known that the by-product of the reaction of yeast with sugar is CO_2 and it is this process that was utilised to form the observed pores in YP scaffolds (Figure 7.6). It is proposed that this process is initiated firstly by evolution of CO_2 from individual DAY granules that results in the formation of micropores. Over time, it seems this reaction propagates and CO_2 it built up within the sample, which leads to the development of macropores.

Micrographs of samples prepared with ground and unground DAY demonstrated a difference in the degree of micropores (Figures 7.6 f and g). Consequently, it is suggested that grinding of DAY fragments pellets to a degree, which resulted in a reduction of the amount of CO_2 evolved from individual granules. This disrupts the previously described sequence of micropore formation. Less than 10% difference was observed in the average pore sizes of Y01 and Y02, which suggests that the development of macropores is not affected by granulation since bulk scale development of CO_2 is not altered (Table 7.2).

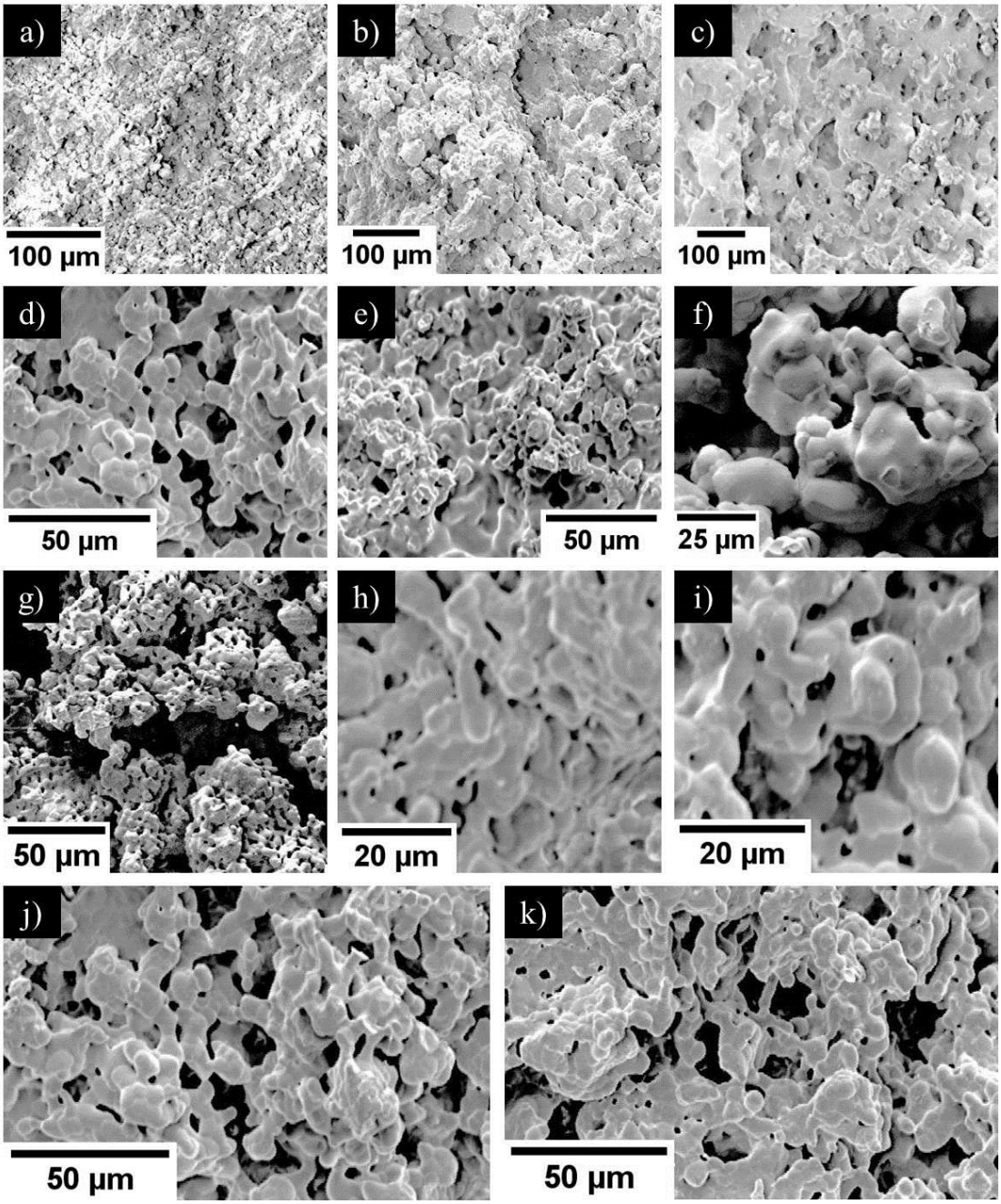

Figure 7.6: Micrographs of scaffolds produced via YP method and sintered at 1300°C (a) Y03, (b) Y04, (c) Y05, (d) Y06, (e) Y07, (f)Y01, (g) Y02, (h) Y02, (i) Y04, (j) Y06, and (k) Y08 Images taken from 'micropore' region (Figure 7.12) of a cross sectional slice

Yeast content was observed to affect the size of pores (Table 7.2). An increase in yeast content from 0.5 – 1g resulted in an increase of average pore size of over 115% and further addition of yeast (2g) caused a 35% growth. This is attributed to a greater amount of CO_2 evolution. Increasing the yeast content, within the ranges assessed, resulted in a roughly proportional increase in the average pore size, which is attributed to a higher proportion of sugar from starch reacting with DAY granules (Figure 7.7).

Table 7.2: Summary of the average pore size of YP scaffolds (n=3)

Sample	Investigated parameter	Parameter value	Average pore size (µm)
Y01	DAY G/UG	G	15.8±1.3
Y02		UG (micropores)	2.5±0.4
Y02		UG and 25wt% HA	17.4±4.7
Y03	DAY content	0.5g	13.8±2.4
Y04		1.0g and 50wt% HA	29.9±5.8
Y05		2.0g	40.5±13.2
Y06	Gluten:Starch	1:3 and 60wt% HA	15.4±4.6
Y07		2:3	10.1±2.8
Y08	HA loading	70wt% HA	14.4±4.8

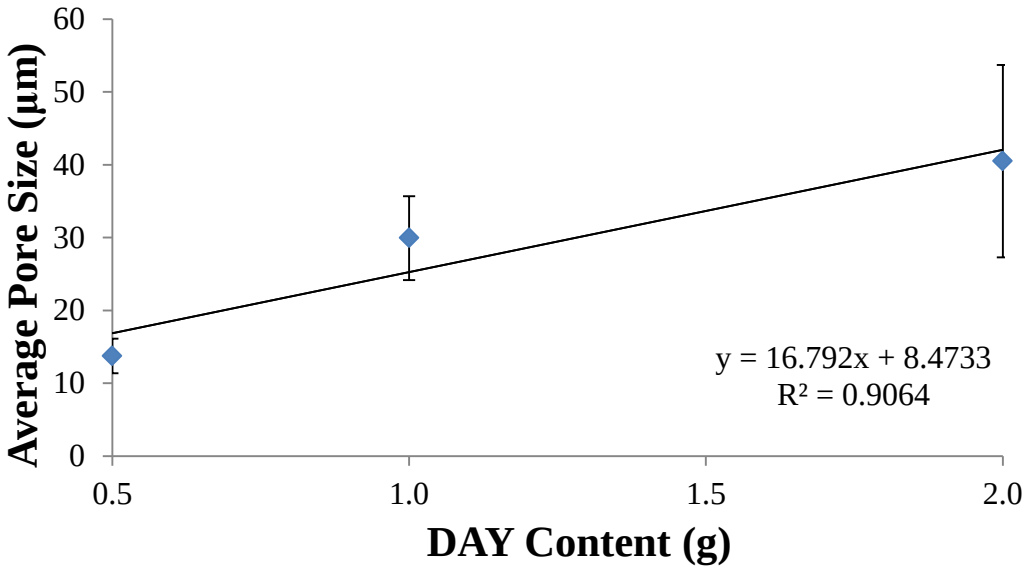

Figure 7.7: Influence of DAY content on average pore size of YP scaffolds

It appears that as gluten content was increased the scaffold structure became less networked (Figures 7.6 d and e). This is ascribed to the viscoelastic properties of typical proteins, such as gluten, which may have resulted in a higher firming rate i.e. lack of pore volume development caused by entanglements and crosslinking of hydrogen bonds between protein fibrils and starch.

The development of porosity and pore size were shown to be dependent on the degree of HA loading (Figure 7.6 h – k). In particular, the observed decrease in average pore size of samples Y06 (60wt% HA) and Y08 (70wt% HA) advocate that the dough has a limited loading capacity, and above this the development of pores is restricted by HA content (Figure 7.8).

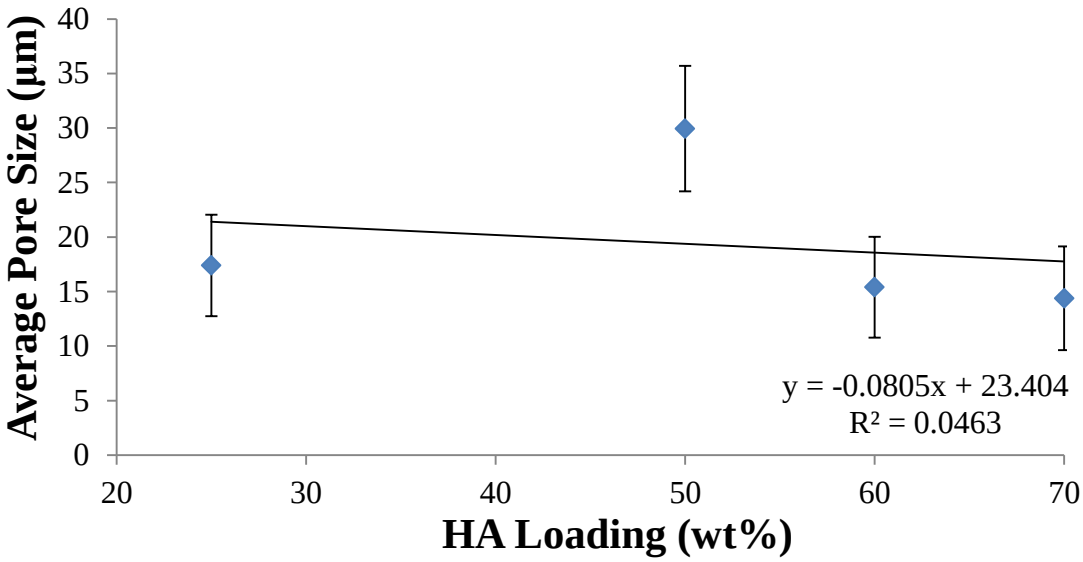

Figure 7.8: Influence of HA loading on the development of pores within YP scaffolds

Typical 2D slices of YP constructs after pre-firing at 600°C confirmed the presence of both micro and macropores (Figure 7.9). In the majority of samples a denser outer region, referred to as 'skin', was demonstrated. This observation is analogous with the crust formed in traditional bread making and is thought to be due to a higher consolidation rate at extremities trapping CO_2. The 'skin' layer is therefore suggested to have contributed to the coalescing of micropores in the inner regions of the sample.

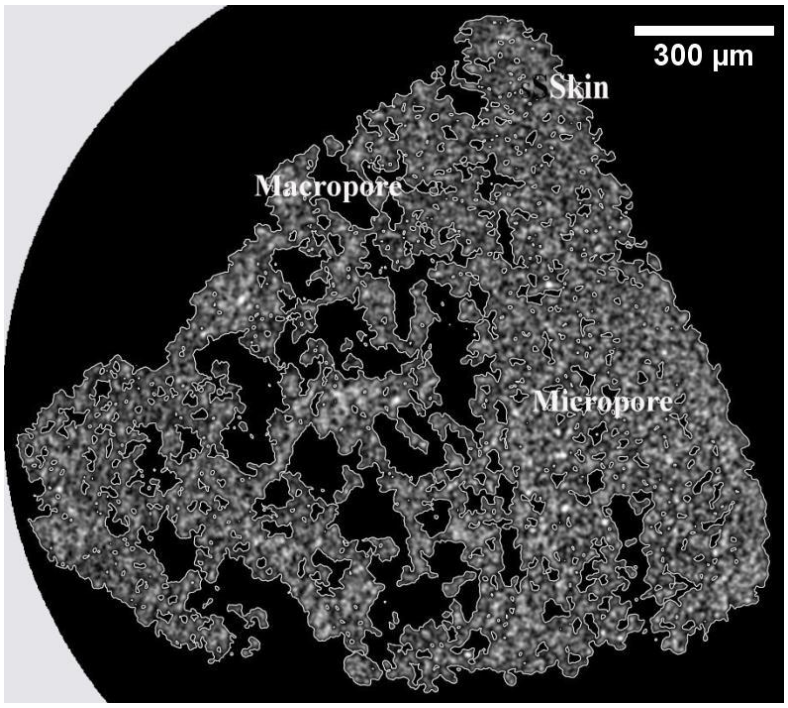

Figure 7.9: Typical 3D distribution of pores in YP constructs

7.4.2.2 Method two - 3D printed parts

The stability of 3D printed blocks of various HA:PVOH compositions were visually assessed, and the large degree of variability observed highlights the importance of selecting an optimum precursor composition (Figure 7.10). These results suggest that the minimum PVOH content required to bind printed layers together was 20wt%, since blocks with less than this value could not be handled. Above this minimum PVOH content all tested compositions (50, 70, and 80wt% HA) exhibited a sufficient flowability to recoat the build bed without compromising bed stability, and interlayer bonding was strong enough to enable parts to be handled. Therefore these compositions were deemed printable. Blocks printed from the 50HA:50PVOH precursor were notably distorted along the axis perpendicular to the direction of spreading, which was attributed to excessive wetting due to the relatively high polymer content.

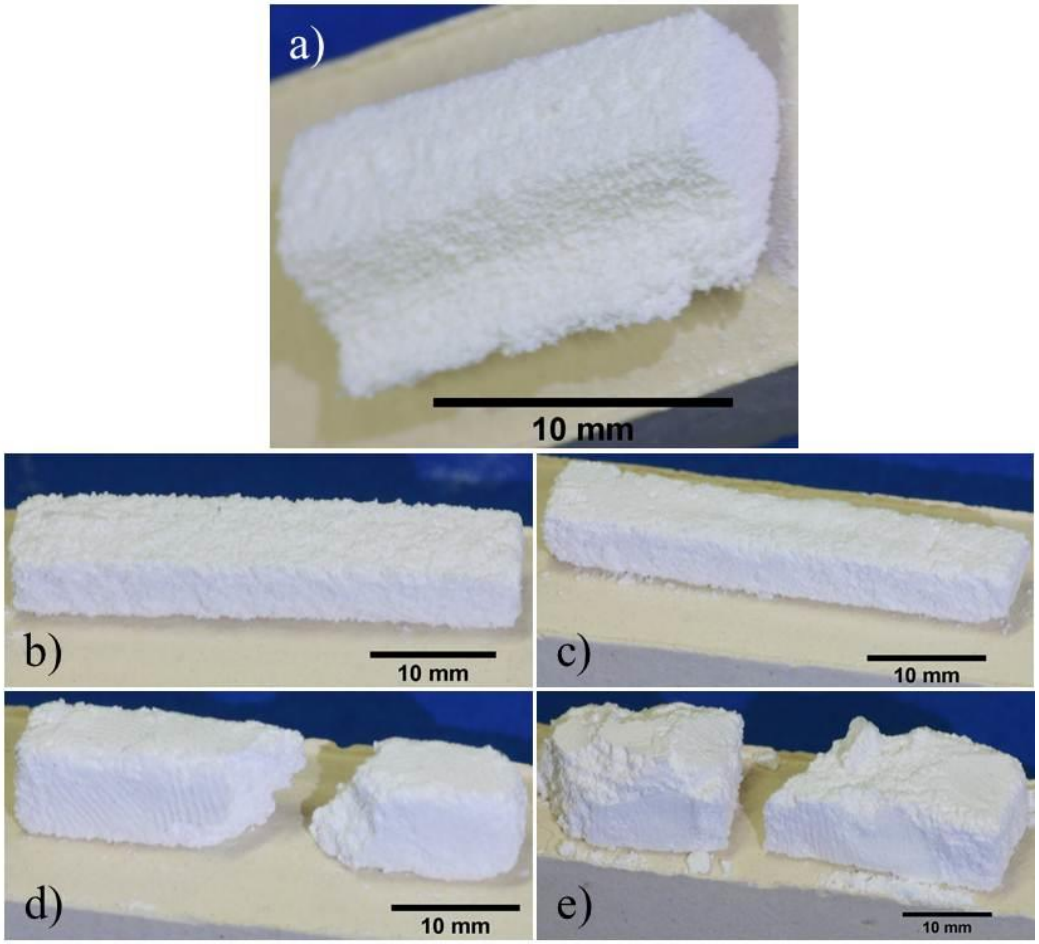

Figure 7.10: Stability of 3D printed blocks
(a) 50HA 100% saturation, (b) 70HA 194% saturation, (c) HA80 194% saturation, (d) HA90 194% saturation, and (e) 100HA 194% saturation

The surface topography of blocks fabricated from printable precursor compositions was assessed via SEM (Figure 7.11). Two distinctly different particle morphologies and sizes were observed within the surface layer of parts that were attributed to HA and PVOH particles. It appeared that smaller HA particles were bonded to the surface of larger PVOH particles, creating a rough surface topography. Surface pores were demonstrated in all green bodies suggesting a degree of microporosity is inherently produced during printing, which is attributed to a packing efficiency less than 1 due to interparticulate voids within spread powder layers.

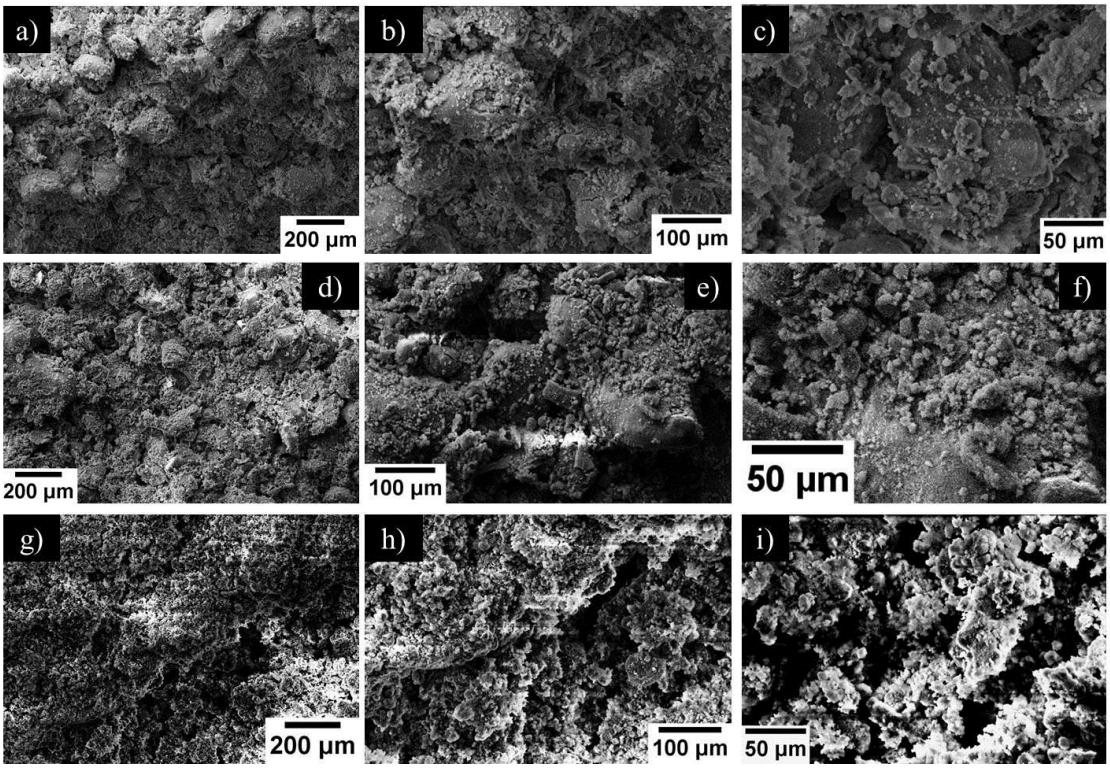

Figure 7.11: Surface topography of 3D printed blocks (a – c) 50wt% HA 100% saturation, (d – f) 70wt% HA 194% saturation, and (g – i) 80wt% HA 194% saturation

Scaffold structures were produced from precursors compositions that were deemed printable (50, 70, 80wt% HA). Remarkably, scaffolds printed from these compositions, except 50HA:50PVOH, were found to be structurally unstable and difficult to handle without causing damage. Fragility of these constructs is attributed to insufficient bonding between powder layers. In contrast, green scaffolds printed from the 50HA:50PVOH precursor powder were easy to handle and could not be crushed by hand (Figure 7.12 a and b). Visualisation of typical green structures validated that designed pore channels were not occluded (Figure 7.12 c), and scaffold struts revealed the layer by layer manufacturing method employed (Figure 7.12 d). A similar

microporous surface topography to block parts was demonstrated (Figure 7.12 e and f). Measurements of pore width and length, as well as strut width of six different samples was used to calculate the reproducibility ratio of green parts, which is defined as experimental size divided by the corresponding user defined CAD dimension (Table 7.3).

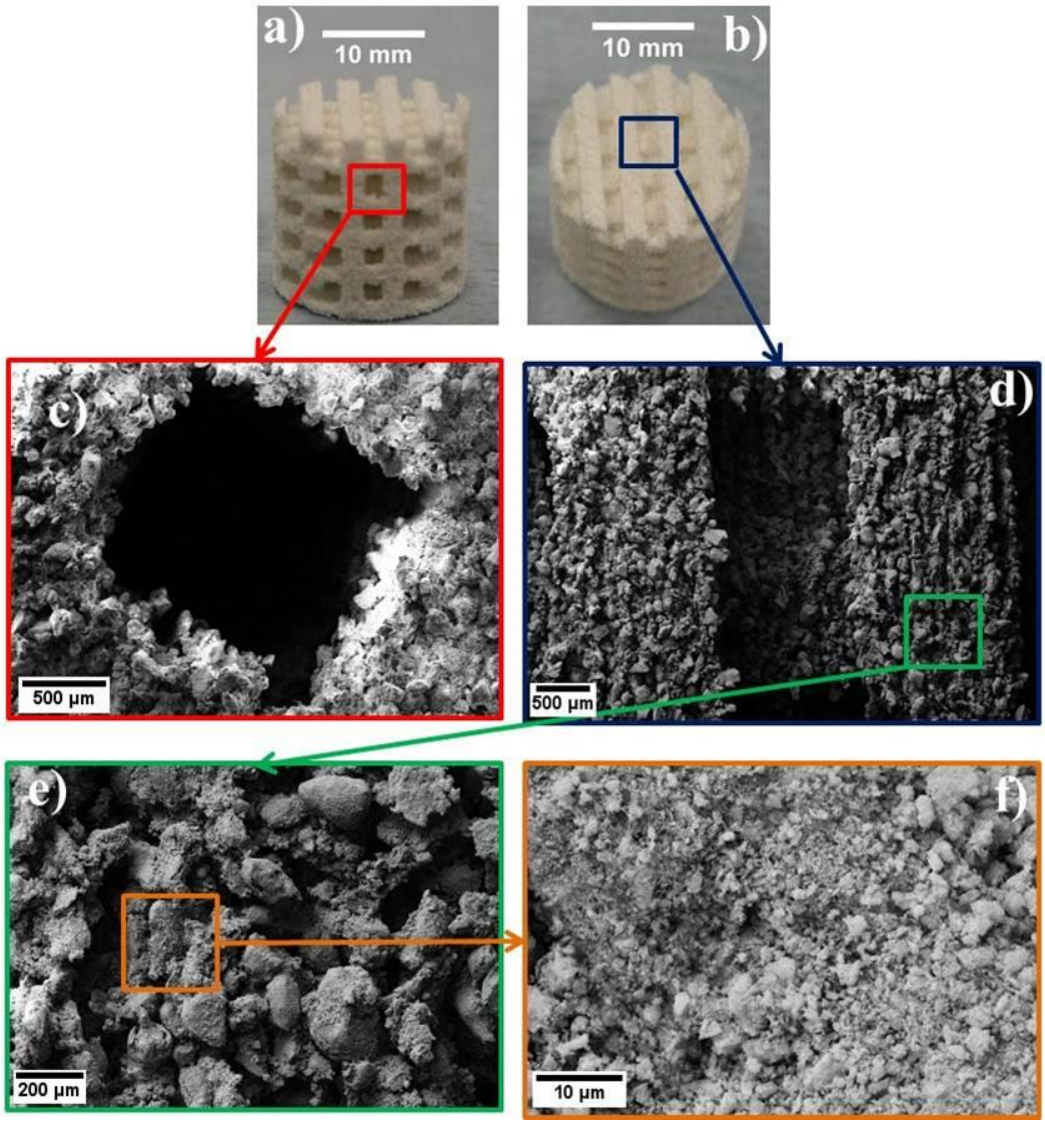

Figure 7.12: 50wt% HA green scaffolds produced via 3DP
(a) Side view, (b) top view, (c) designed pore channel, (d) strut, and (e - f) surface morphology

Table 7.3: Reproducibility of 50wt% HA scaffolds produced via 3DP (n=6)

Feature	Average (µm)	Reproducibility ratio
Pore width	2035±507	101±26
Pore length	1893±538	94.7±27
Strut width	1723±290	86.1±15

7.5 Discussion

XRD analysis of as-received commercial HA powder, used in both fabrication processes, matched to standard patterns of HA and DCPA (Figure 7.2). This result was confirmed by DTA-TGA analysis that revealed weight losses within the temperature region (320 – 340°C), which is associated to the transformation of DCPA to β-$Ca_2P_2O_7$ (Equation 2.4). Further weight loss between 700 – 800°C suggests the commercial powder is CDHA since degradation products of this phase are known to transform to HA and β-TCP within that temperature range (Equation 2.5). This assertion is supported by the presence of β-TCP in the XRD pattern of sintered HA (Figure 7.2 c). Presence of DCPA infers that during synthesis key reaction parameters, such as pH and temperature, were not controlled to a high degree. The exotherm demonstrated between 1100 and 1150°C for HA was attributed to the transformation of β-TCP to α-TCP, which is known to occur at approximately1125°C (Figure 2.9).

The thermal behaviour of a typical bioceramic dough composition formed during the YP process, and PVOH used in the 3DP system were primarily assessed to determine the burn out behaviour of organic constituents. This may be considered as an important prerequisite to the design of heat treatment protocols to remove organics from HA green bodies. The residue after heating bioceramic dough up to 800°C was shown to be approximately equal to the HA loading of samples, which suggests organics were completely removed from the structure. Heating beyond the thermal degradation temperature of PVOH revealed the thermal events involved in its molecular deterioration, which were attributed to reported solid and molten state degradation processes [323]. In order to maintain the structural integrity of sintered 3D printed scaffolds it will be vital that the gases evolved during PVOH degradation do not become trapped within the structure. It is proposed that the inherent micron sized interparticulate voids associated with a packing efficiency less than 1 could help to facilitate gaseous removal (Figures 7.11 and 7.12). However, the author recognises that the effectiveness of the observed surface microporosity to enable gas evolution is greatly dependent on 3D interconnectivity of these pores.

Printing of rectangular blocks proved to be a time efficient way to determine which HA:PVOH compositions were printable. Initial visual assessment of samples suggested the minimum content of PVOH required to bond powdered layers together

was 20wt% therefore suggesting that 50, 70 and 80wt% HA precursors could be deemed as printable. However, of these initial three compositions stable and easy to handle scaffolds could be fabricated only from the 50HA:50PVOH precursor powder. SEM micrographs of the surface of green parts exhibited an inherent surface roughness due to numerous topographical irregularities, which was attributed to the packing efficiency of composite powders. This observation has been reported in the literature as advantageous for fluid flow, resultant remodelling and dissolution [322], which could improve osteoconductive and osteointegrative properties of the scaffold. It is also important to note the microporosity caused by interparticulate voids, since this structural attribute has been reported to facilitate attachment points for osteoblasts and vital to capillary ingrowth [88].

Interconnectivity is known to be a structural property required of bone tissue scaffolds since it is necessary to ensure blood cell invasion, cell migration, and mass transport [103]. A notable inherent advantage of ALM techniques, such as 3DP, is the user can design the scaffold construct so that this critical structural demand is met on a bulk scale. However, it is also important to consider whether the inherent microporosity formed in these 3D printed scaffolds are connected, this could be achieved by CT scanning structures. Previously, other authors have reported that de-powdering 3D printed parts is difficult and therefore loose powder can remain within the structure, which could lead to occlusion of pores. Micrographs of designed pore channels established that this was not the case in this study (Figure 7.12).

2D slices of CT scans of YP scaffolds demonstrated three areas within structures that exhibited different pore sizes and limited interconnectivity (Figure 7.9). SEM analysis of the size of micropores within YP constructs revealed a relatively small range (Table 7.2). It is suggested that the formation of a relatively dense ‘skin’ layer at the extremities during pre-firing is responsible for the inhomogeneous distribution of pores since it may have trapped evolving CO_2 within the structure thus causing a build-up in the inner areas, which explains the larger pores within this region. Since the residue of DTA-TGA analysis of the bioceramic dough corresponded approximately to HA content it seems that the ‘skin’ layer did not prevent the removal of organic constituents. Microstructural development of YP scaffolds was shown to depend on: (1) yeast content, (2) gluten content, and (3) HA loading. Specifically the formation of micropores (2 – 3μm) was linked to the evolution of CO_2 from individual

DAY pellets. YP scaffolds were observed to exhibit surface and bulk porosity, however the interconnectivity of pores were shown to be limited (Figure 7.6) and their distribution inhomogeneous (Figure 7.9). Inhomogeneity is suggested to be due to variation in the thickness (1 – 2mm) of the 'skin' layer trapping evolving CO_2 to different degrees, resulting in poor reproducibility. To understand this process further it would be necessary to assess the kinetics and quantity of CO_2 production and perhaps this knowledge could be used to improve sample consistency.

Overall, a comparison of experimental and CAD dimensions is evidence that the 3DP process enabled accurate translation of the designed model to the green scaffold (Table 7.3). It should be noted that since the resolution of 3DP is partially dependent on the maximum particle size of stock materials, in this case 200 μm, reproducibility is likely to be reduced if scaffold features were scaled down. In comparison, the pore size and distribution as well as interconnectivity of YP constructs were demonstrated to vary as a result of changing any of the investigated experimental variables. These properties are suggested to determine the ease of CO_2 evolution, thus sample consistency and reproducibility is dependent on the ability to accurately control these effects. The high degree of variability of pore size and distribution, as well as interconnectivity was highlighted in this study. These are typical inherent disadvantages reported for conventional methods that result in poor reproducibility due to lack of control over pore development.

7.6 Conclusions

The feasibility of fabricating porous bone tissue scaffolds by two different fabrication processes, namely YP and 3DP, was experimentally assessed in this chapter. The YP process developed in this work demonstrates the possibilities of adapting conventional methods, such as salt leaching, to use alternative natural pore forming agents that do not require the use of common toxic organic solvents. Furthermore, the potential to fabricate user defined constructs with a rough surface topography, known to be favourable for bone cell attachment, via 3DP has also been highlighted. It is important to note that the reported intrinsic advantages of ALM techniques, such as improved reproducibility relative to conventional methods, were evidenced experimentally.

Reported disadvantages of conventional fabrication techniques, such as poor interconnectivity, were highlighted by the characterisations performed on YP scaffolds. To improve this method it would be necessary to develop a better understanding of the evolution of CO_2 and its influence on microstructural development. In order to ensure sample consistency and improve reproducibility it would be necessary to formulate a mechanism to appropriately control CO_2 release and thus pore size distribution.

Scaffolds produced via the 3DP method were observed to exhibit an inherently irregular surface topography and microporosity that are both desirable characteristics, since these features could correlate to improved attachment of bone cells and structural infiltration. These results are a promising foundation to the fabrication of a scaffold that exhibits physical properties considered as advantageous, as well as critical to the success of bone implants, thus justifying the selection of this technique for further investigation.

Chapter 8

3D printing of hydroxyapatite scaffolds

8. 3D printing of hydroxyapatite scaffolds

8.1 Introduction

The feasibility of fabricating 3D porous scaffolds from compositions of HA:PVOH, suitable for use as a component of the tissue engineering strategy was assessed in Chapter 7. This preliminary study highlighted the potential of 3DP to produce constructs that exhibit key structural criteria, such as surface roughness and porosity, which are known to be vital in determining the success of bone tissue scaffolds (section 2.6.2). This chapter expands on previous conclusions and assesses in more detail the experimental viability of printing scaffold structures suitable for use in bone tissue replacement from HA:PVOH precursors.

Previous studies concerning 3DP of CaPs have notably highlighted the influence of a number of powder characteristics, such as particle size distribution, on parameters, namely flowability and wettability, that are advocated to be crucial in defining printability [266, 267]. Flowability, defined as the ability of the powdered raw material system to flow and recoat previous layers, is expected to strongly influence the resolution, mechanical stability, and packing efficiency of 3D printed scaffolds (section 2.16.2). Therefore, prior to printing a number of key precursor parameters were determined experimentally, including flowability, particle morphology and size distribution, as well as bulk and tapped density.

In summary, this chapter demonstrates the influence of precursor characteristics, green part post-processing, and sintering protocols in relation to: (1) macro and microporosity, (2) pore size distribution, (3) pore interconnectivity, (4) surface topography, and (5) mechanical strength of green and sintered scaffolds.

8.2 Materials and methodology

Analar grade reagents were purchased from Sigma Aldrich (UK) and used without further purification unless otherwise stated. As previously described (section 7.2.2), prior to use as-received PVOH was ball milled to form a powder with particle sizes

<200μm. This was mechanically mixed with varying quantities of HA in an alumina crucible. Composite powders were sieved before use to break up any agglomeration formed during mixing or storage.

Prior to printing, the flowability of HA:PVOH compositions were directly assessed using the methods described in section 8.3.1. A number of additional characterisations were performed to obtain a reference composition and assess properties known to affect flowability, for example particle morphology.

A ZPrinter 310 3D printer in combination with a water based commercial binder (Zb60) was used to print 200% cylindrical scaffold structures (Figure 7.1) using powder compositions with a maximum HA content of 80wt%. Precursors were poured into the powder bed of the printer, arranged into a strip, and compacted before printing. The binder saturation level used was 194% and layer thickness was set to 0.1mm. Green parts were left to dry for 1hr, as recommended by the printer manufacturer, before being removed from the build bed. The influences of a number of green part processing variations were investigated: (1) de-powdering method, (2) drying method, and (3) drying time. De-powdered constructs were finally sintered to remove PVOH.

8.3 Scaffold characterisation

For clarity, the characterisations performed have been split into the following sections: (1) precursor materials, (2) green-parts, and (3) sintered constructs. Green and sintered constructs were characterised to determine if scaffolds exhibited vital physical properties (section 2.6.2) namely: (1) porosity, (2) pore size and distribution, (3) interconnectivity, (4) surface topography, and (5) mechanical strength.

8.3.1 Precursor characterisations

Flowability of raw materials and composite powders were assessed by two different funnel methods. In addition, characteristic particle properties that have been reported to affect flowability were also experimentally assessed, including particle morphology, and particle size distribution. DTA-TGA analysis of HA:PVOH powders was performed as a prerequisite to designing heat treatment protocols, and FTIR was used to obtain reference compositions of precursors.

8.3.1.1 Precursor flowability

A Pyrex funnel (60°, 10mm diameter orifice) was held upright 10±0.1cm above a level surface using a clamp, and clamp stand. 10±0.1g of as-received HA, milled PVOH, and composite powders were weighed and reproducibly poured into the funnel while its opening was blocked. The obstruction was removed and the time taken for the powder to pass through was manually recorded using a stopwatch (±0.01seconds). In order to calculate the angle of repose (R) the height and width of the formed powder pile was measured to an accuracy of ±0.1cm (Equation 8.1). This process was repeated thrice for each composition to obtain average values.

$$R = \tan^{-1}\left(\frac{h}{\left(\frac{w}{2}\right)}\right) \quad (8.1)$$

Where R = Angle of repose, h = height of powder pile, and w = width of powder pile (Figure 8.1).

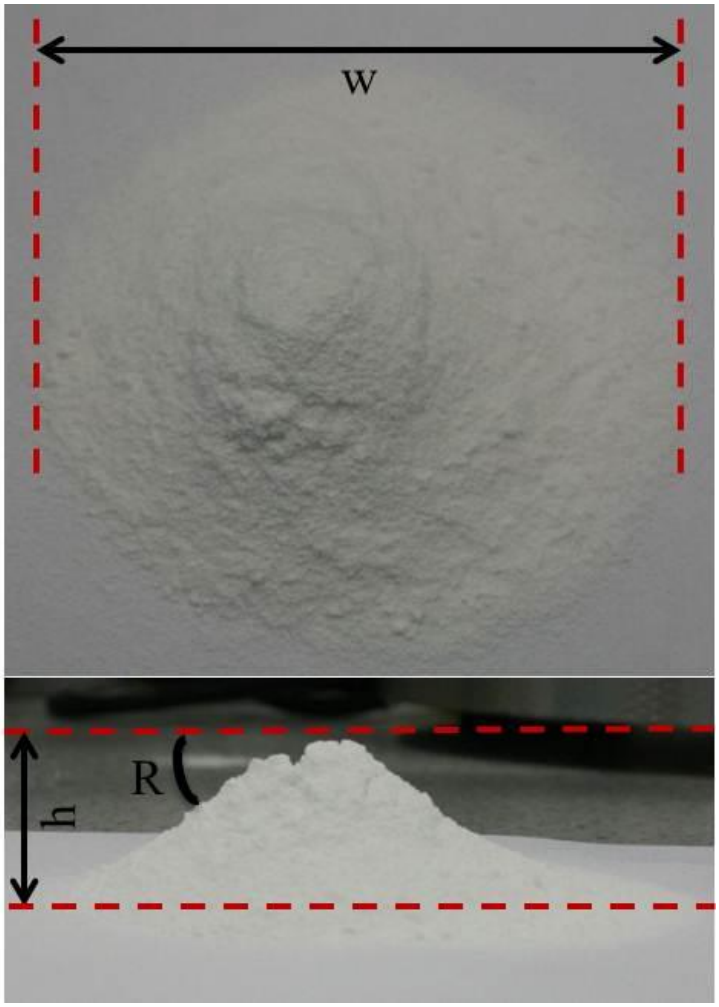

Figure 8.1: Measurements to calculate angle of repose (R) (w = width, h = height)

8.3.1.2 Particle size distribution

Dry particulate size and distribution data was measured by laser diffraction using a Mastersizer 2000 fitted with Scirocco 2000 dry dispersion unit (Malvern Instruments, UK). HA, PVOH, and composite powders were loaded into the dispersion unit and fed through the cell at 1 bar. The laser was aligned to the centre of the cell for optimum intensity and prior to each measurement, a background spectrum was collected to eliminate the presence of contaminants in the data set. Refractive indices from the instrument database for HA and PVOH were used to compile the software scattering model. The final result for each sample was formed from an average of 3 measurements, each of 10s duration, and was transformed from volume average to number average.

8.3.1.3 Bulk and tapped density

The ratio of the mass to volume of an untapped (i.e. unsettled powder), which includes interparticle void volume, is defined as bulk density (ρ_B). Hence, ρ_B is a measure of both the density of the powder and the spatial arrangement of powder particles (Equation 8.2).

To measure ρ_B of as-received HA, milled PVOH, and composite powders 50±0.01g was weighed (m) and poured into a dry 150mL graduated cylinder readable to 1mL. The powder was levelled without compacting, and the apparent volume (V_0) was recorded to the nearest graduated unit in mL. Prior to testing each sample was passed through a 250μm sieve to break up any agglomerates. This process was repeated thrice to obtain an average.

$$\rho_B = \frac{m}{V_0} \tag{8.2}$$

Tapped density (ρ_T) is commonly obtained by using a tapped density analyser, which mechanically taps a container comprising of a powder sample and any changes in volume are recorded until no further significant change occurs, i.e. until interparticle voids are filled. Since a tapped density analyser was not available and an absolute value was not required an ultrasound bath was used to reduce interparticulate voids. After observing ρ_B the cylinder was placed in an ultrasonic bath for 1, 2, and 5mins, corresponding volumes V_{U1},V_{U2}, and V_{U5} were recorded to the nearest graduated unit. Each measurement was repeated three times to calculate an average. Reproducibility

of these results was ensured by 'tapping' a fixed mass of powder over a defined period of time while using the same ultrasound bath.

Using these density measurements the Hausner ratio (H) for each precursor powder was calculated (Equation 8.3). This ratio provides a measure of the propensity of a powder to be compressed, which can be used as a measure of the ability of the powder to settle, and to assess the relative importance of interparticle interactions.

$$H = \frac{V_0}{V_f} \tag{8.3}$$

Where V_f = final tapped volume, in this study $V_f = V_{U5}$. Free flowing powders should exhibit bulk and tapped densities close in value since interparticle interactions are less significant in such materials.

8.3.1.4 Spreadability

An indirect assessment of powder flowability and bed stability was obtained by observing the ability of each powder to be spread from the powder to build bed. HA:PVOH precursor materials were poured into the powder bed of the 3D printer, arranged into a strip, and reproducibly compacted. 5 layers of 0.1mm thickness were spread by the counter-rotating roller and photographs were taken before and after spreading, which were used to measure the maximum and minimum lengths of each bed profile. An average length was calculated from measurements taken in three locations: (1) and (2) 1cm from each edge of the bed, and (3) the centre point (Figure 8.2). This was repeated for the build bed profile and a build:powder bed ratio was calculated. A qualitative assessment of the topography of spread powder layers was also obtained from photographs.

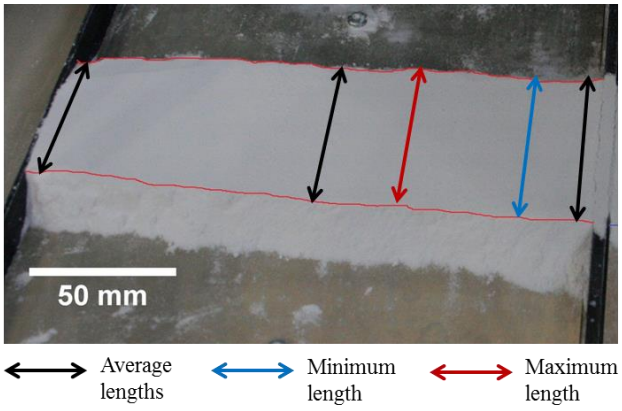

Figure 8.2: Measurements to assess the spreadability of composite powders

8.3.1.5 Particle morphology of precursor materials

The morphology and particle size of as-received HA, milled PVOH, and 50HA:50PVOH powders were analysed by SEM (Zeiss Supra55 FEGSEM) at 20kV. Powders were dispersed onto double adhesive carbon tabs attached to an aluminium stub and sputter-coated with a thin layer of gold in an argon-purged chamber for 90s.

8.3.1.6 Chemical composition of precursor materials

As a prerequisite to determining the chemical composition of post-processed and sintered samples, precursors of different HA:PVOH ratios were assessed by FTIR using the method described in section 4.3.2.

8.3.1.7 Thermal analysis

Burn out of PVOH from HA:PVOH precursors was evaluated as a prerequisite to designing heat treatment protocols for scaffolds. Simultaneous DTA-TGA was performed using the method described in section 3.3.3.

8.3.2 Green body characterisations

8.3.2.1 De-powdering

Post printing it is necessary to remove loose powder from the pore channels of scaffolds. The use of ultrasound treatment for up to 15mins, and compressed air were investigated as de-powdering methods. In order for a thin jet of air to be blown a syringe needle was attached to the end of an AS18K airbrush compressor (Absolute Airbrush, UK), as shown in Figure 8.3. The effectiveness of these techniques was visually assessed from images of constructs, and specifically the ability to remove loose powder from pore channels was noted. The amount of powder removed via ultrasound was determined by weighing scaffolds (±0.0001g) before and after treatment. This process was repeated three times to obtain an average value.

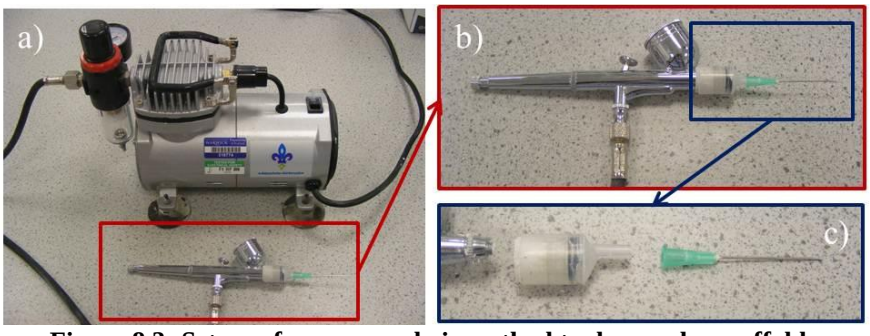

Figure 8.3: Set up of compressed air method to de-powder scaffolds
(a) Airbrush compressor, and (b - c) air brush nozzle with syringe needle attachment

8.3.2.2 Chemical composition

The influence of drying scaffolds in a furnace or vacuum oven, on the chemical composition of HA:PVOH constructs was assessed by FTIR. Prior to using the method described in section 4.3.2 scaffolds were crushed using a pestle and mortar to obtain a fine powder.

8.3.2.3 Surface topography and pore size

SEM micrographs of pore channels, struts, and the surface of constructs were obtained using the method described in section 7.3.3.

8.3.2.4 Mechanical Strength

The yield and ultimate compressive strength of green bodies were measured using an 5800R 100kN static tester (Instron, UK) with a 1kN load cell, and a cross head speed of 10mm/min. Prior to analysis the initial diameter and height of scaffolds were measured using a micrometre. Samples were then placed in the centre of the load cell (Figure 8.4a), the load cell position was adjusted (Figure 8.4b), and the gauge length zeroed. Yield strength and strain were determined from the load and corresponding extension observed before the onset of plastic deformation, i.e. the linear region of the stress-strain curve.

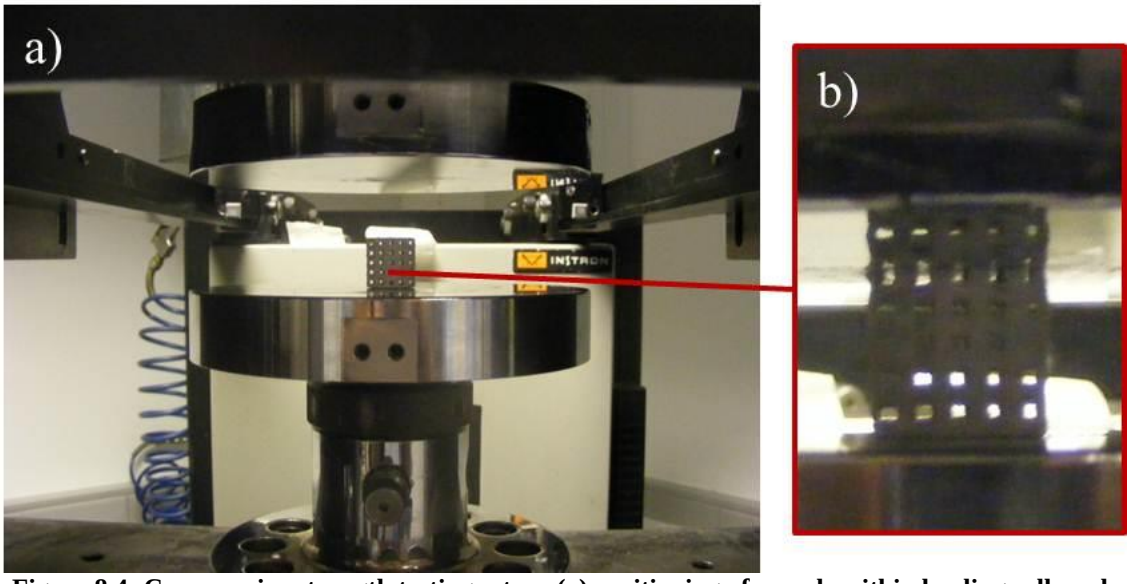

Figure 8.4: Compressive strength testing set-up (a) positioning of sample within loading cell, and (b) adjustment of loading cell

8.3.3 Characterisation of sintered constructs

A number of heat treatment protocols were used to burn out PVOH from green bodies and consolidate the remaining HA scaffold. Any effect of this process on construct stability, composition, size, and microstructure were considered using the methods described in this section.

8.3.3.1 Stability of sintered scaffolds

Scaffolds were visually assessed before and after sintering to determine if the heat treatment protocol had any detrimental effect on bulk stability. Formation of any defects or instability was noted and sintered parts were photographed.

8.3.3.2 Chemical composition

Sintered structures were ground using a pestle and mortar and their composition analysed by FTIR as described in section 4.3.2.

8.3.3.3 Scaffold shrinkage

The height and diameter of constructs were measured using a micrometre before and after heat treatment to determine bulk thermal shrinkage.

8.3.3.4 Microstructure of sintered scaffolds

To enable a comparison of green and sintered parts, the microstructure of heat-treated scaffolds was assessed by SEM as described in section 8.3.2.3.

8.4 Results

8.4.1 Precursor materials

8.4.1.1 Flowability

The results of the two funnel tests performed to assess the flowability of HA:PVOH precursor powders are summarised in Table 8.1. A decrease in both the angle of repose and the time taken to flow through the funnel was observed with decreasing HA content (Figure 8.5). These trends indicate improved flowability with increasing PVOH content.

Table 8.1: Flowability of HA:PVOH precursor powders using funnel tests (n=3)

HA (wt%)	Flow time		Angle of repose	
	Average time (s)	Standard deviation	Angle (°)	Standard deviation
100	4.71	0.24	38.66	0.29
90	2.96	1.09	35.82	0.86
80	2.92	0.26	35.60	0.77
70	2.27	0.27	35.38	0.75
60	1.98	0.24	27.30	0.65
50	1.59	0.08	25.80	0.77
0 (100% PVOH)	0.47	0.03	21.22	2.75

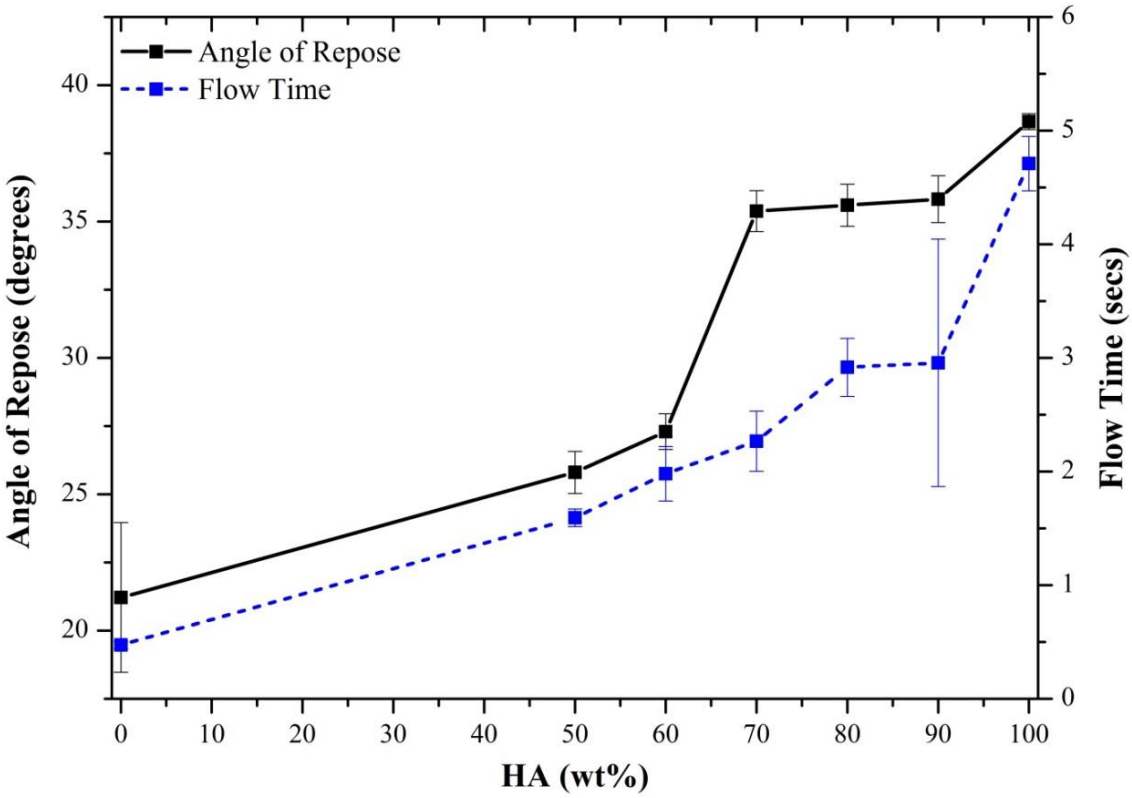

Figure 8.5: Funnel test results for HA:PVOH precursor powders (n=3)

8.4.1.2 Particle size distribution

The particle size distribution for precursor powders containing 100, 90, 80, and 50wt% HA, as well as milled and unmilled PVOH were measured (Figure 8.6). All composite powders exhibited a bimodal distribution comprising of individual HA and PVOH fractions. Intensity was found to vary according to the relative proportion of HA and PVOH, i.e. as HA content was increased the intensity of the HA fraction increased and PVOH decreased. A shift in the PVOH distribution to a larger particle size for composite powders in comparison to the milled PVOH distribution was observed,

which is likely to be due to coagulation with HA particles. The relatively small fraction observed at approximately 1000µm for the milled PVOH precursor is suggested to be due to particles clumping together due to humidity.

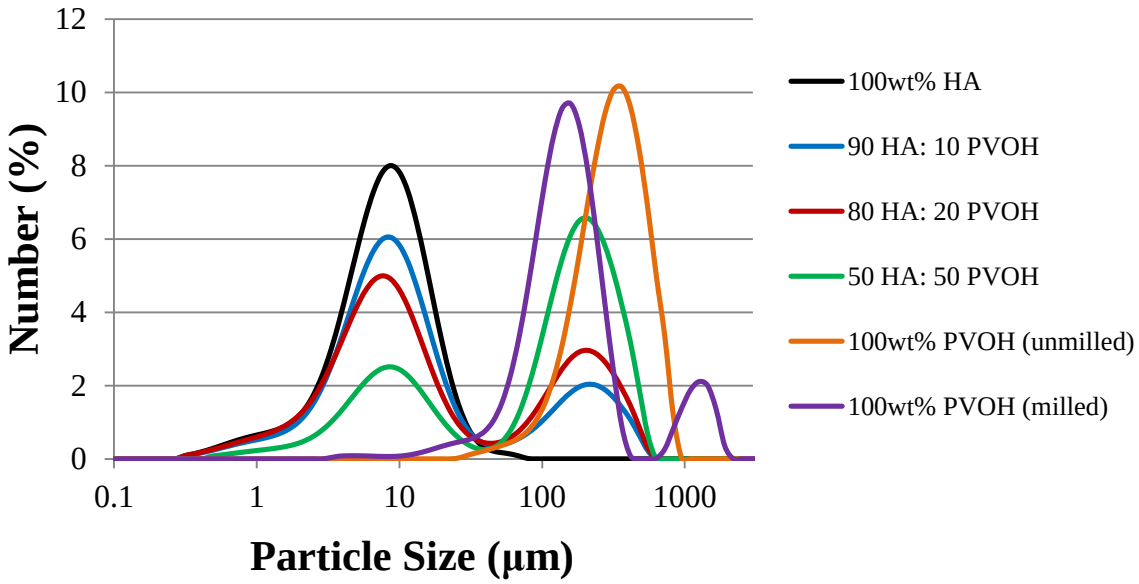

Figure 8.6: Particle size analysis of HA:PVOH precursor powders (ratios expressed as wt%)

Percentile values (d_{10}, d_{50}, d_{90}) for each powder distribution are shown in Table 8.2. The significant increase in the d_{90} value for milled PVOH compared with unmilled is linked with the aforementioned clumping behaviour due to humidity.

Table 8.2: Particle size percentiles of HA:PVOH precursor powders

Precursor powder	Particle size percentile		
	d_{10} (µm)	d_{50} (µm)	d_{90} (µm)
100wt% HA	2.76	8.45	19.27
90wt% HA	3.12	10.5	222.86
80wt% HA	2.84	11.61	268.86
50wt% HA	5.76	144.75	362.38
100wt% PVOH (milled)	71.32	159.85	811.97
100wt% PVOH (unmilled)	133.76	293.79	543.43

8.4.1.3 Bulk and tapped density

An increase in density was observed for all HA:PVOH precursor powders with increasing ultrasound treatment time (Figure 8.7). A reduction in the rate of density increase was demonstrated between 1 and 2mins. After 2mins of ultrasound treatment most samples exhibited less change or plateaued. This suggests that the majority of the

impact of ultrasound treatment on interparticle voids occurs in the first minute of treatment. The corresponding average increase in density calculated between treatment times quantitatively confirmed the above observation (Table 8.3).

The Hausner ratio was calculated from the observed densities and is proposed to be an indication of the ability of each precursor to settle. These results also reveal the relative effect of interparticle interactions on flowability (Table 8.3). PVOH powder was shown to be easiest to compact and is suggested to exhibit fewer interparticle interactions. A larger Hausner ratio was also calculated for as-received HA compared with composite precursors, which suggests particle interactions were more influential in HA:PVOH powders. These samples are therefore likely to be harder to compact or settle.

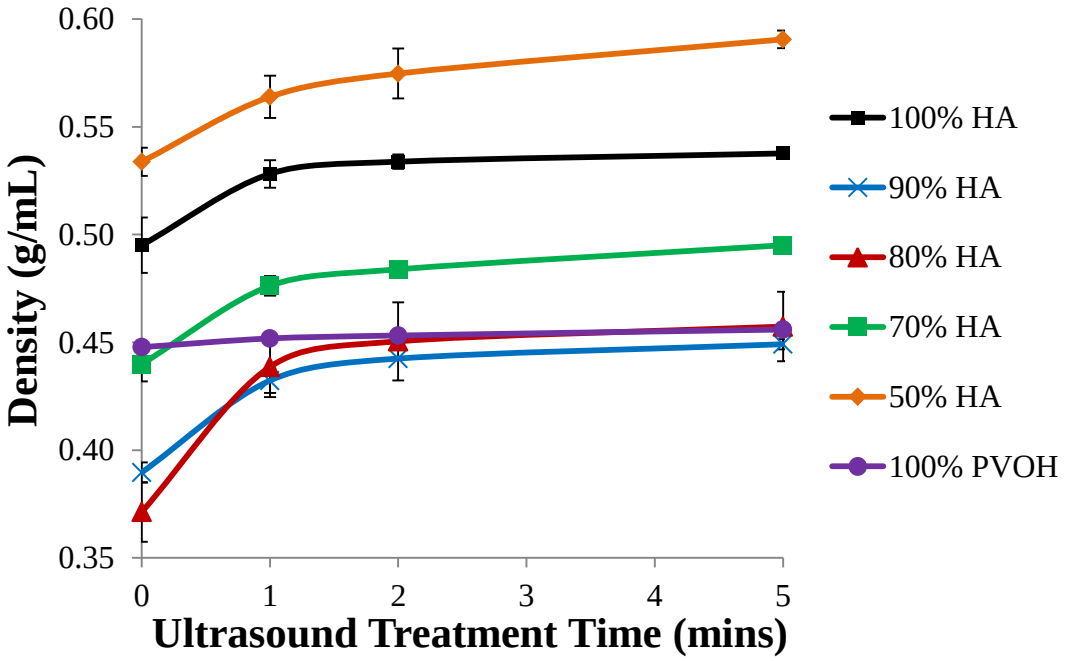

Figure 8.7: Bulk and tapped density of HA:PVOH precursor powders

Table 8.3: Change in density due to ultrasound treatment

HA content (%)	Average change in density (%)			Hausner Ratio
	0 – 1 min	1 – 2 mins	2 – 5 mins	
100	6.69	1.07	0.72	0.921±0.02
90	10.95	2.36	1.50	0.868±0.01
80	18.13	2.70	1.52	0.812±0.02
70	8.25	1.61	2.31	0.889±0.02
50	5.64	1.92	2.76	0.904±0
100% PVOH	0.90	0.30	0.61	0.982±0

8.4.1.4 Spreadability

A typical profile of HA:PVOH powder after 5 layers were spread from the powder to build bed is shown in Figure 8.8. Measurements of each bed (Figure 8.2) were used to calculate minimum, maximum, and average build:powder bed ratios for each composite precursor (Figure 8.9). Since the standard deviation of the average ratio overlaps the corresponding minimum and maximum values in the majority of cases, it is reasonable to assume that this range is representative of the whole bed. Furthermore, since build:powder bed ratios were observed to follow the same trend it is therefore recommended that only a comparison of average values is necessary.

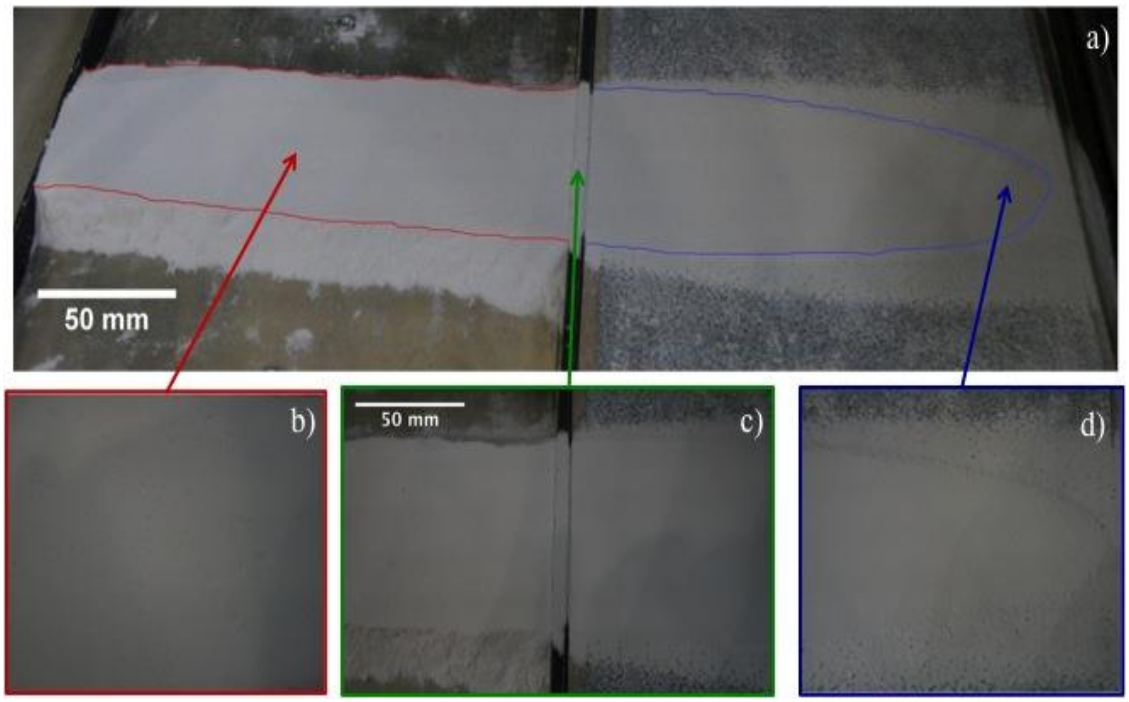

Figure 8.8: Illustration of typical powder distributions for 50wt% HA (a) powder and build beds, (b) powder bed topography, (c) comparison of powder and build bed topographies, and (d) build bed topography

It was proposed that the build:power bed ratio would give a quantitative indication of the spreadability of each HA:PVOH powder, which could be associated to precursor flowability and bed stability. Since the majority of ratios were <1 (i.e. the build profile was narrower compared to the powder bed) it is suggested this indicates bed stability since any instability would likely be associated with widening. Visually no discernible difference in the topography of the build and powder beds was observed for 50HA:50PVOH powder (Figure 8.8). In contrast, clumping of particles was seen for

all other powders, which is expected to reduce the mechanical stability of parts since disruption of the bed could lead to a larger void volume (Figure 8.10).

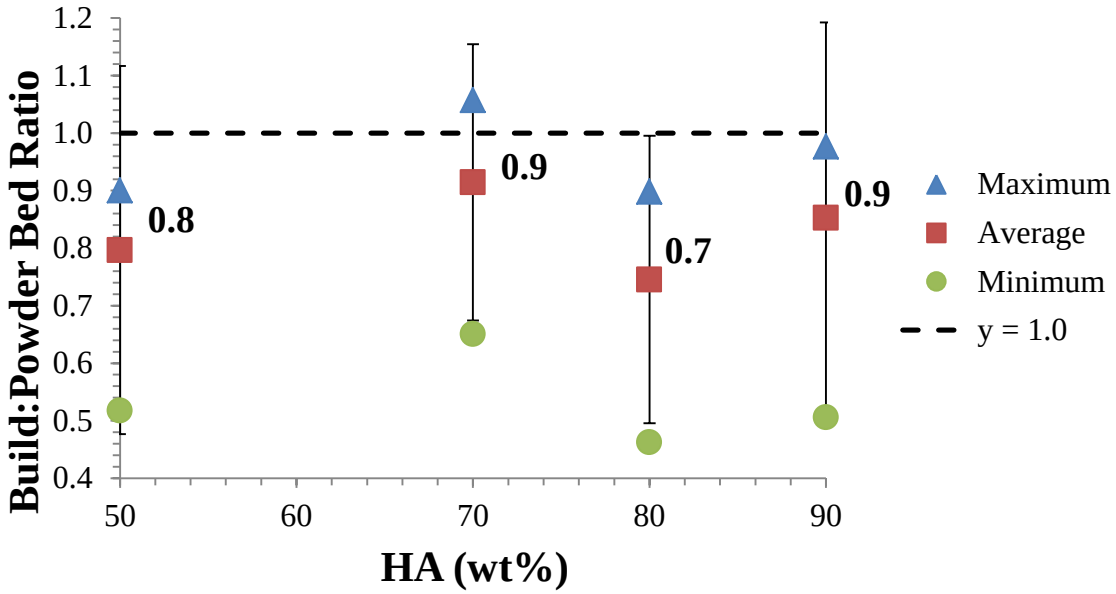

Figure 8.9: Build to powder bed ratios of HA:PVOH precursors

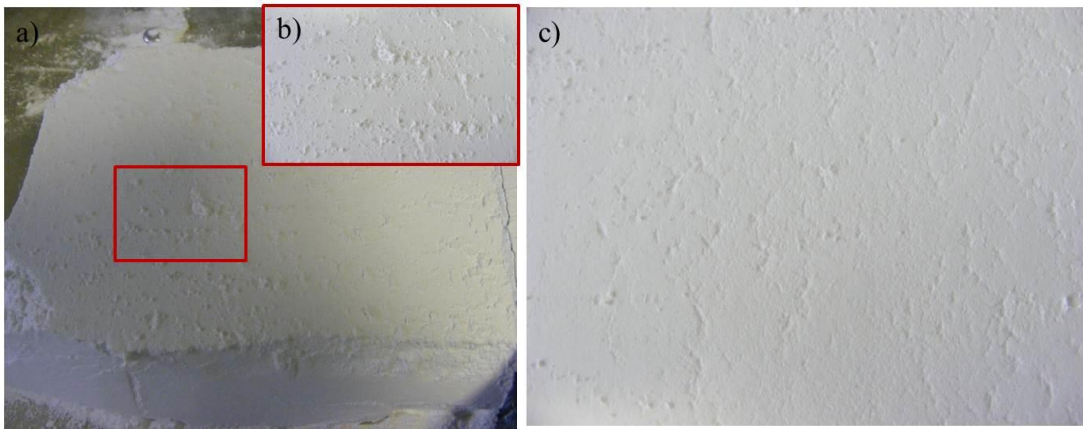

Figure 8.10: Typical clumping behaviour of 60wt% HA precursor (a) powder bed, (b) close up of powder bed, and (c) build bed

8.4.1.5 Microstructure of precursor materials

Typical SEM micrographs of HA, PVOH, and 50HA:50PVOH powders at low (x200) as well as high (x5000) magnifications are shown in Figure 8.11. HA powder (Figure 8.11 b) exhibited a similar globular morphology and agglomeration behaviour to samples self-prepared by AP (Chapters 3 – 6). Higher magnification micrographs revealed the typical topography of HA particles, which in comparison to the slate like PVOH particles appeared to be relatively rough (Figures 8.11 b and f). The average

particle size of 50HA:50PVOH was found to be closer to the average of PVOH particles than HA (Table 8.4). Thus, it is suggested the mechanical mixing of stock HA and PVOH resulted in a degree of agglomeration between materials. This assertion is supported by typical micrographs that demonstrate the presence of HA particles on the surface of larger PVOH fragments (Figure 8.11 c and d).

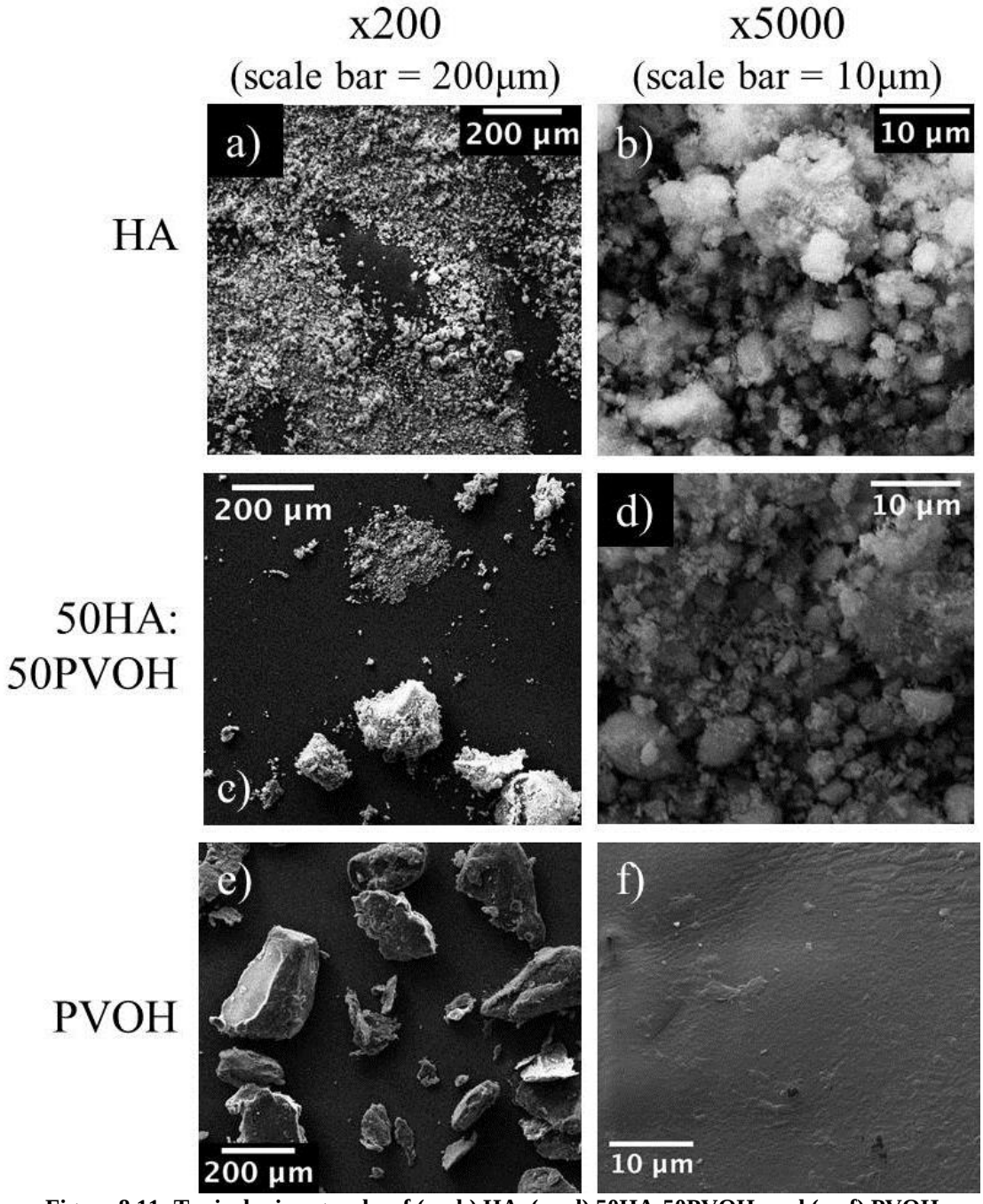

Figure 8.11: Typical micrographs of (a - b) HA, (c - d) 50HA:50PVOH, and (e - f) PVOH precursors

Table 8.4: Summary of typical microstructure observed for HA, 50HA:50PVOH, and PVOH precursors

HA content (wt%)	Average particle size (µm)	Standard deviation (±µm)	Typical morphology
100	3.47	0.92	Largely agglomerated rounded particles Relatively rough surface topography
50	59.76	63.52	Polygonal particles infiltrated with smaller rounded particles
100 PVOH	70.92	28.50	Dispersed slate like polygonal fragments Relatively smooth surface topography

8.4.1.6 Chemical composition of precursor materials

Individual FTIR spectra of HA and PVOH are shown in Figure 8.12. Corresponding plots of HA:PVOH precursors revealed a combination of HA and PVOH band assignments. An increase in the IR transmission of HA peaks was observed with an increase in the nominal content of HA (Figure 8.13). Vice versa a decrease in the intensity of PVOH bands was seen with increasing HA loading.

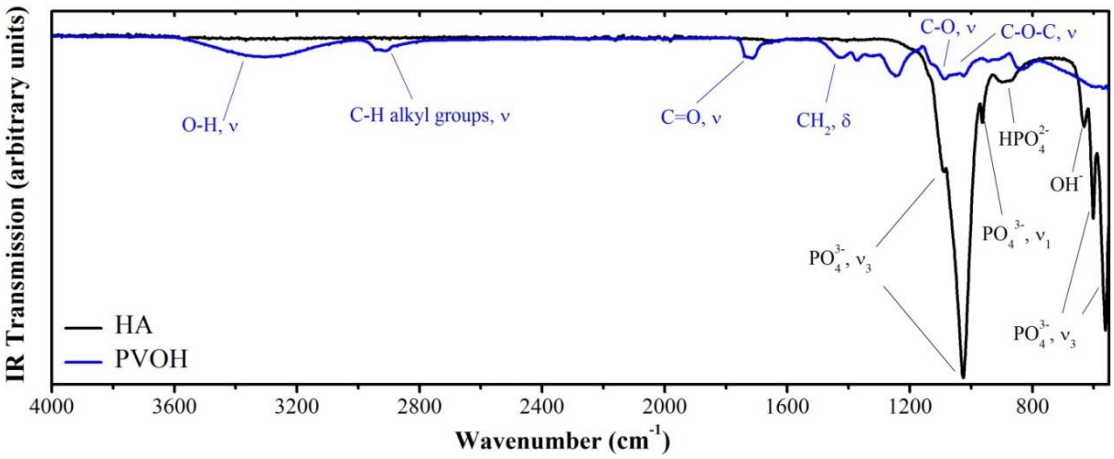

Figure 8.12: FTIR spectra of HA and PVOH raw materials

8.4.1.7 Thermal behaviour of precursors

DTA and TGA results for HA:PVOH powders, obtained simultaneously between 30 and 1300°C, revealed that the majority of the observed weight loss occurred 185 – 500°C (Figure 8.14). These results corroborate the corresponding analysis of PVOH (Figure 7.4), and therefore weight loss in this region is partially attributed to burn out of PVOH. The remaining weight loss is accredited to the degradation of DCPA to β-$Ca_2P_2O_7$ since DTA-TGA analysis of as-received HA confirmed an endothermic reaction within this temperature range. A monotonic relationship between the residue

of HA (i.e. the observed residue of HA:PVOH precursors plus weight loss observed for HA alone), and the HA content of precursor powders was demonstrated (Table 8.5). DTA plots for HA:PVOH samples appear to be a combination of the corresponding data recorded for HA (Figure 7.3) and PVOH (Figure 7.4). However, it should be noted that with increasing HA content the onset of the endothermic reaction, which begins at approximately 800°C for 50HA:50PVOH, is shifted to higher temperatures. For samples containing 80wt% and 90wt% HA this reaction was shown to occur over a larger temperature range up to approximately 1100°C.

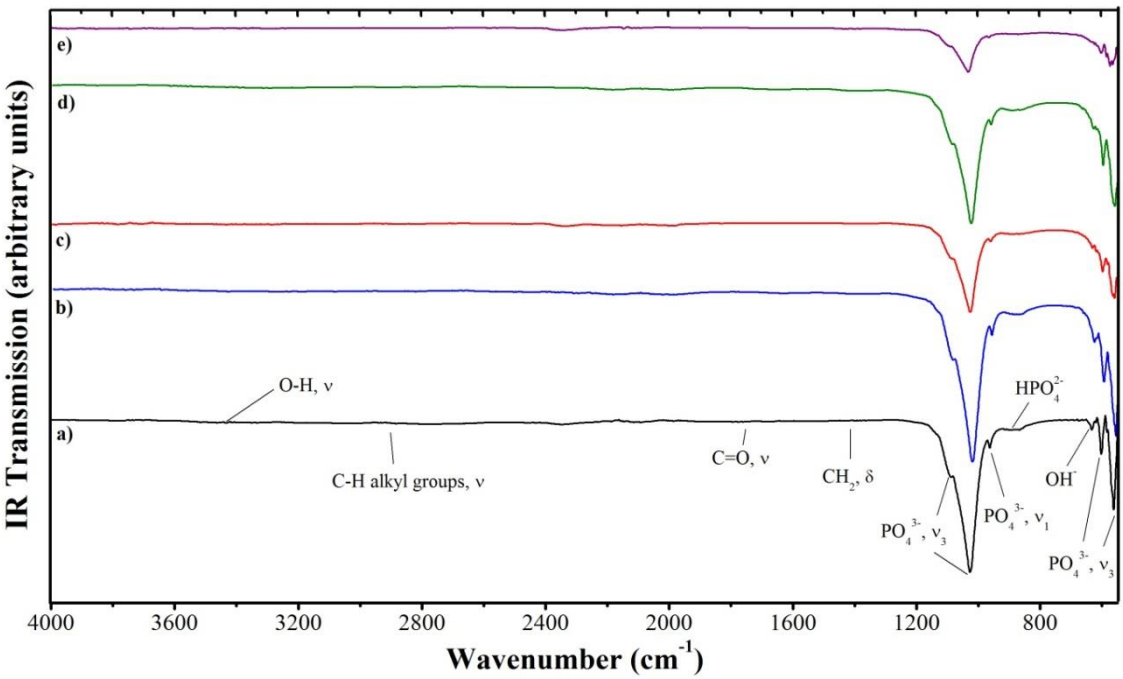

Figure 8.13: FTIR spectra of HA:PVOH precursors (a) 90HA:10PVOH, (b) 80HA:20PVOH, (c) 70HA:30PVOH, (d) 60HA:40PVOH, and (e) 50HA:50PVOH

8.4.2 Green body scaffolds

8.4.2.1 Precursor viability

The results presented for 3DP in section 7.4.3 established that precursors containing a maximum of 80wt% HA were printable and therefore scaffolds of various HA:PVOH ratios within this range were produced. The viability to print scaffolds from each composition was evaluated (Table 8.6). Scaffolds produced from 50 and 60wt% precursors were the only stable compositions and therefore only these structures were characterised.

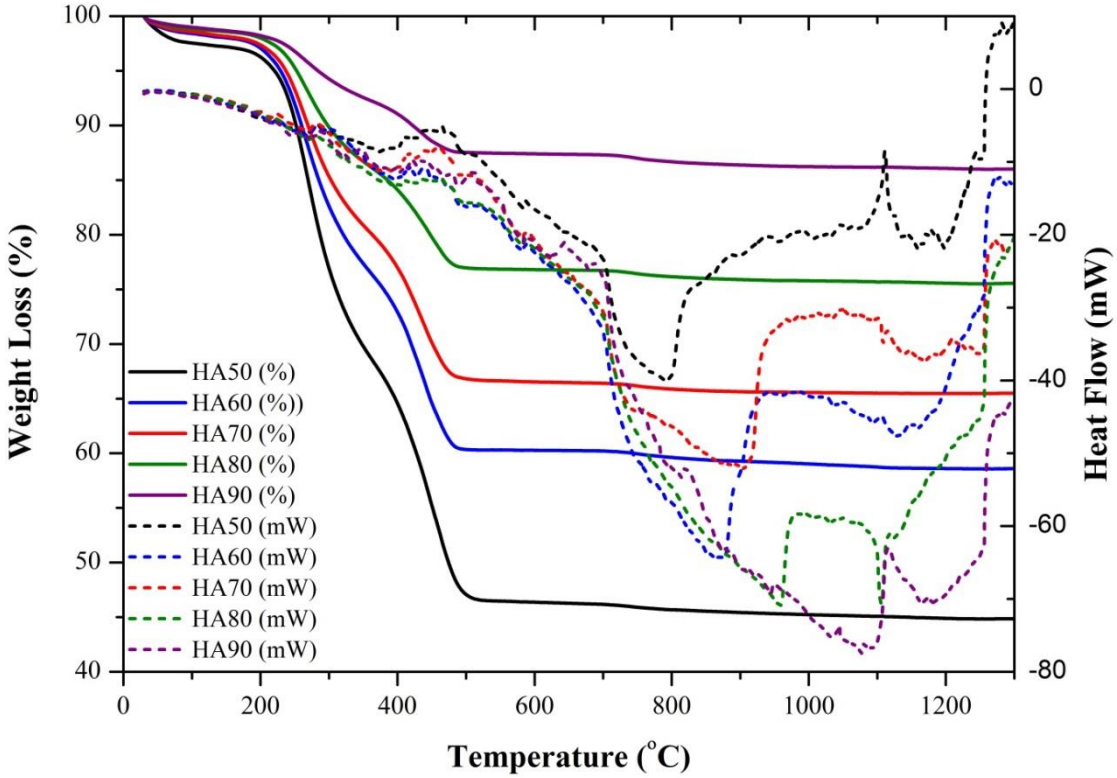

Figure 8.14: Thermal behaviour of HA:PVOH precursors

Table 8.5: Summary of weight loss behaviour for HA:PVOH precursors

HA content (wt%)	Weight loss (wt%)			Residue (wt%)	Residue + HA weight loss (wt%)
	30 – 184°C	184 – 500°C	500 – 1300°C		
50	3.21	49.72	2.22	44.85	49.42
60	2.38	37.28	1.76	58.57	63.14
70	2.21	30.97	1.32	65.50	70.07
80	1.69	21.34	1.41	75.56	80.13
90	1.58	10.89	1.51	86.01	90.58

Table 8.6: Printability of scaffold structures fabricated from HA:PVOH precursor powders

HA content (wt%)	Bonded layers	Ease of handling	Comment
80	No	N/A	Layers were not bonded together leading to scaffold collapse
70	No		
60	Yes	Difficult	A number of printed scaffolds were damaged during removal from build bed Required drying before parts could be removed from the build bed without causing damage
50	Yes	Easy	No damage observed as a result of handling Construct stable straight after printing

8.4.2.2 De-powdering methods

The effectiveness of ultrasound and compressed air to remove loose powder from the surface and pore channels of 50wt% and 60wt% HA green scaffolds was evaluated. Figure 8.15 demonstrates the average amount of powder removed from green parts using ultrasound for up to 15mins. Corresponding images (Figure 8.16) illustrated the limited effectiveness of this method after 5mins and overall the technique was observed to remove loose powder only from the surface of scaffolds. Designed pore channels were shown to remain occluded regardless of treatment time. However, a notable advantage of this technique is that no damage of scaffolds occurred.

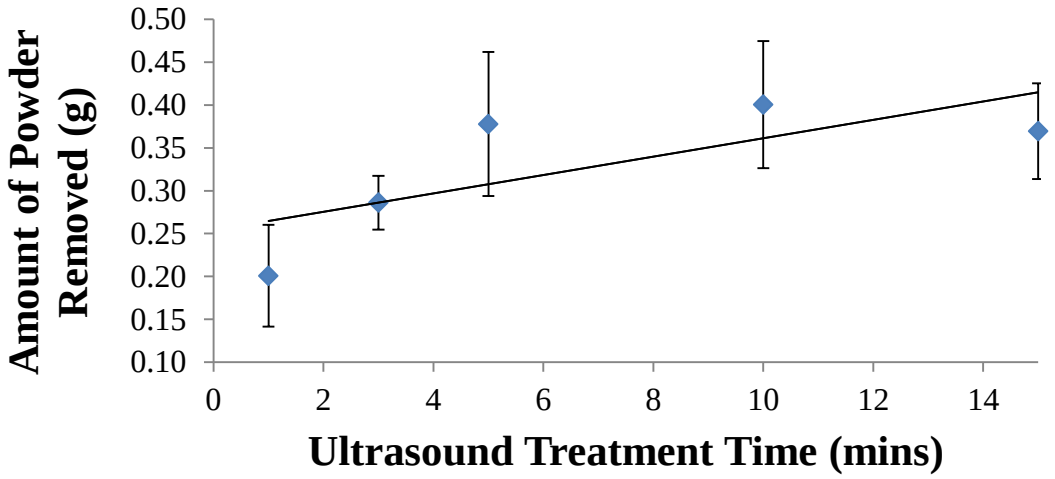

Figure 8.15: Average amount of powder removed from 50wt% HA green scaffolds using ultrasound (n=3)

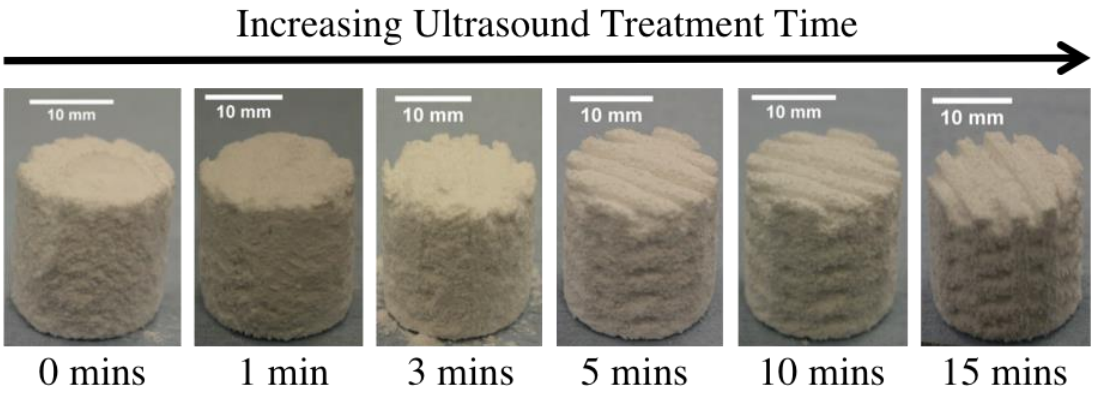

Figure 8.16: Effectiveness of ultrasound treatment to remove loose powder from 50wt% HA green bodies

In comparison, the use of compressed air was observed to effectively remove powder from the surface as well as designed pore channels of green scaffolds (Figure 8.17). Attachment of a syringe needle to the airbrush nozzle enabled a fine jet of air to be directed to areas containing loose powder. This minimised the damage caused to parts during de-powdering. More damage was caused to relatively fragile parts since scaffolds had to be handled during de-powdering, i.e. 60HA:40PVOH. On average approximately 2mins to de-powder a single construct using this method was necessary.

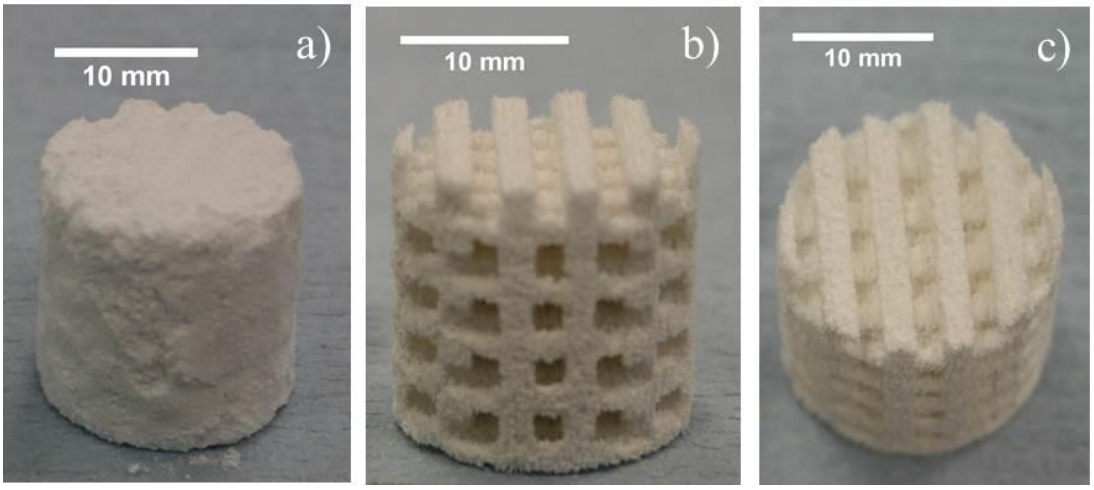

Figure 8.17: Effectiveness of compressed air to de-powder 50wt% HA green bodies (a) printed scaffold, (b) side view of de-powdered scaffold, and (c) top view of de-powdered scaffold

8.4.2.3 Post-processing of green scaffolds

The effect of drying de-powdered green scaffolds at 60°C in a furnace or vacuum oven, for 2 or 6hrs was investigated (Table 8.7). Images of dried green parts were used to identify any bulk changes to the scaffold structure (Figure 8.18). Notably, 60wt% HA parts were relatively more fragile than equivalent 50wt% scaffolds. External outer struts for samples 50F6Y, 50V6Y, 60F6Y and 60V6Y were observed to be damaged, which suggests these post-processing treatments reduced mechanical integrity, and as a result the ease of handling was poorer.

Table 8.7: Summary of 3D printed green body scaffolds

HA content (wt%)	Printing direction (axis)	Post-processing method	Post-processing time (hrs)	Sample ID
50	X	N/A Printed	N/A	50PX
		Furnace dried	2	50F2X
			6	50F6X
		Vacuum dried	2	50V2X
			6	50V6X
50	Y	N/A Printed	N/A	50PY
		Furnace dried	2	50F2Y
			6	50F6Y
		Vacuum dried	2	50V2Y
			6	50V6Y
60	X	N/A Printed	N/A	60PX
		Furnace dried	2	60F2X
			6	60F6X
		Vacuum dried	2	60V2X
			6	60V6X
60	Y	N/A Printed	N/A	60PY
		Furnace dried	2	60F2Y
			6	60F6Y
		Vacuum dried	2	60V2Y
			6	60V6Y

The height and diameter, as well as weight of printed and post-processed green bodies were recorded. A larger variation was observed between the diameter and height of printed green bodies fabricated along the X-axis compared with those printed along the Y-axis (Figure 8.19). A reduction in the average height and diameter of all constructs was demonstrated between printed and dried samples. Generally, a decrease in sample weight was calculated for post-processed scaffolds compared with printed parts (Figure 8.20).

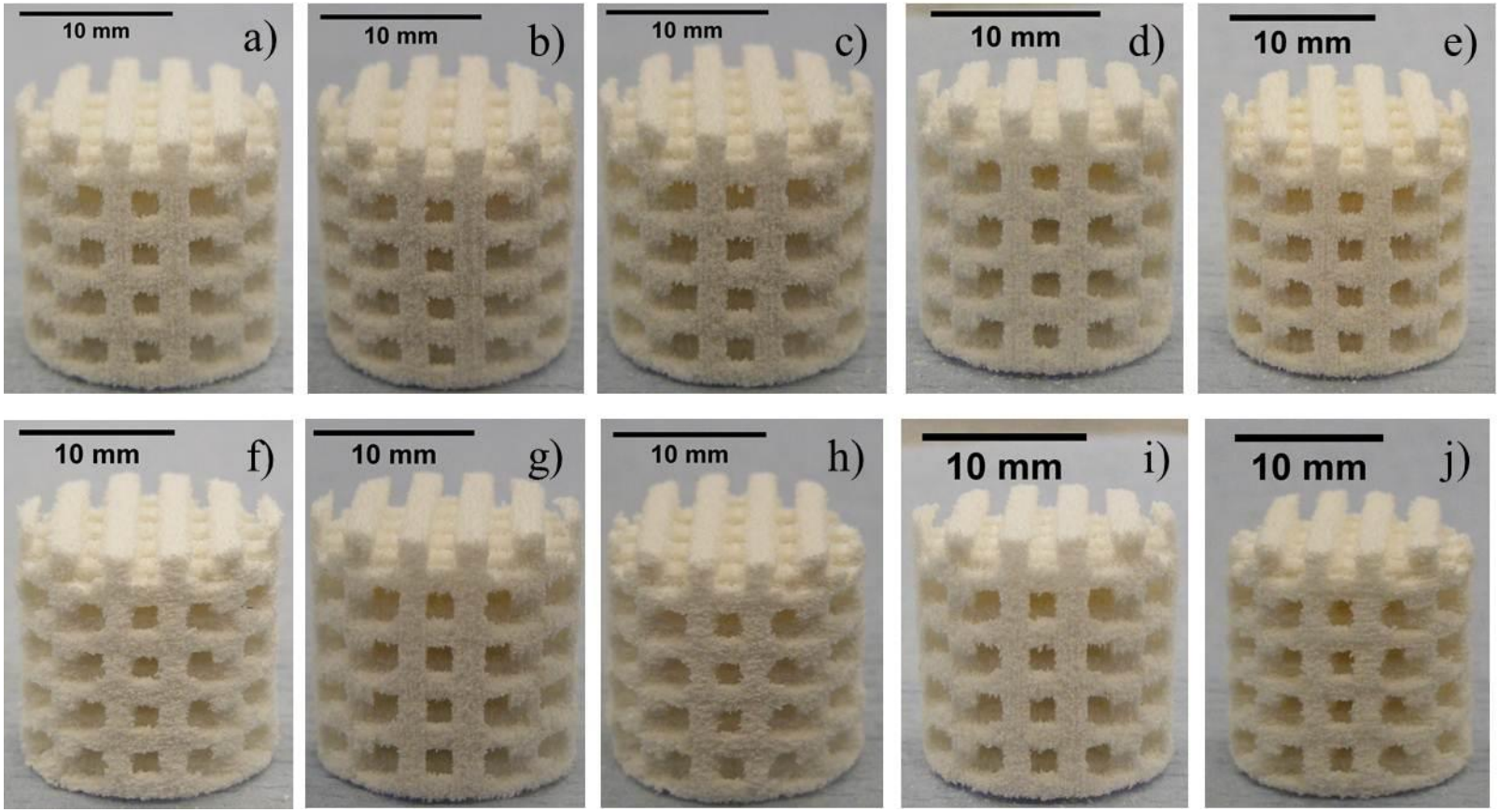

Figure 8.18: Dried 50wt% HA green scaffolds
(a) 50PX, (b) 50F2X, (c) 50F6X, (d) 50V2X, (e) 50V6X, (f) 50PY, (g) 50F2Y, (h) 50F6Y, (i) 50V2Y, and (j) 50V6Y

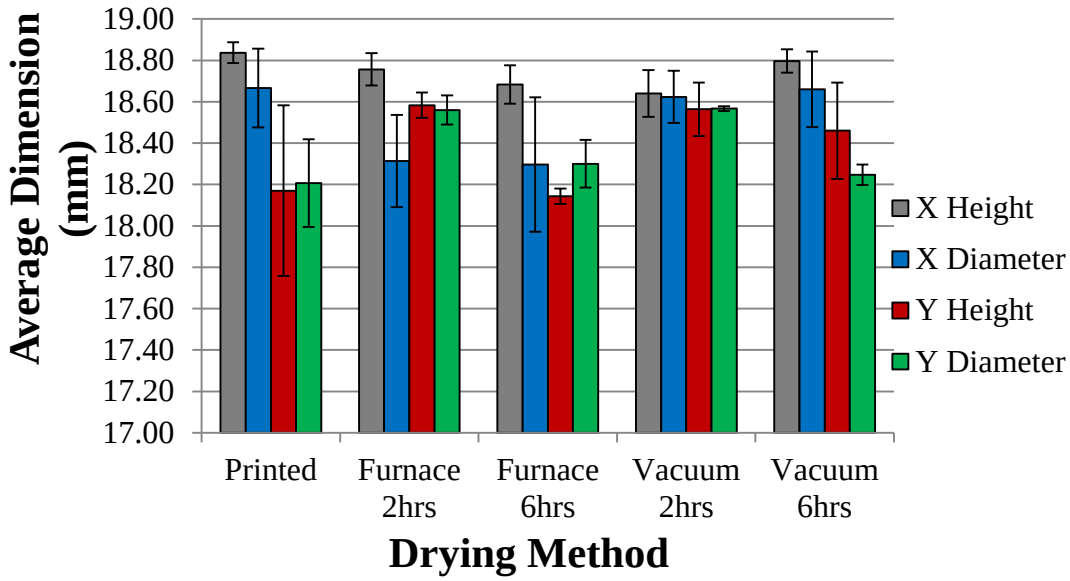

Figure 8.19: Influence of post-processing on size of 50wt% HA green body scaffolds

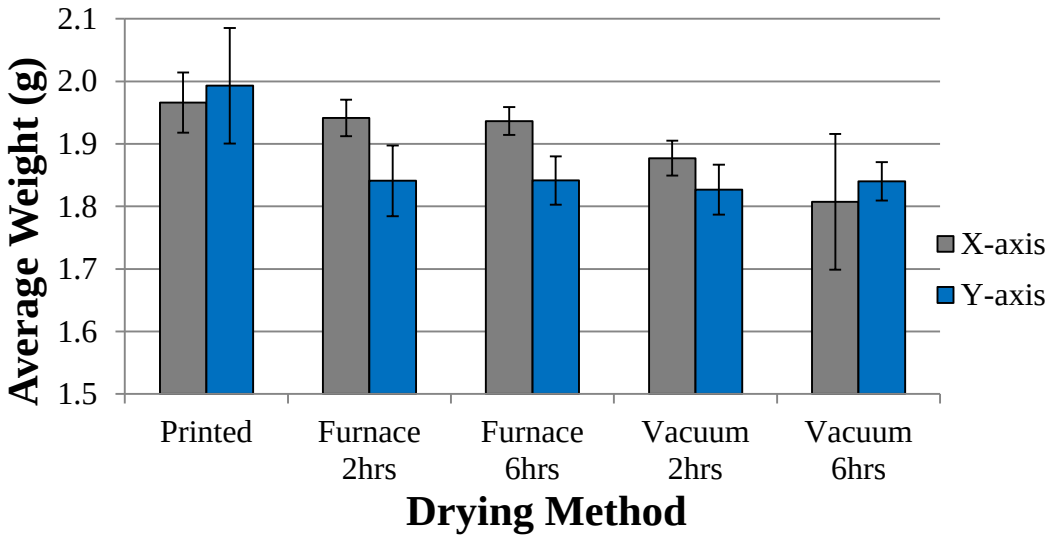

Figure 8.20: Influence of post-processing on weight of 50wt% HA green body scaffolds

Chemical composition

In comparison to respective precursor powders, the intensity of PO_4^{3-} bands were observed to increase for printed and dried green bodies (Figure 8.21). Correspondingly, only weak bands associated with PVOH were detected in precursor powders as well as dried green bodies. An increase in the O-H vibration intensity at 635cm^{-1} for printed and post-processed samples may be attributed to the composition of the commercial binder being largely water.

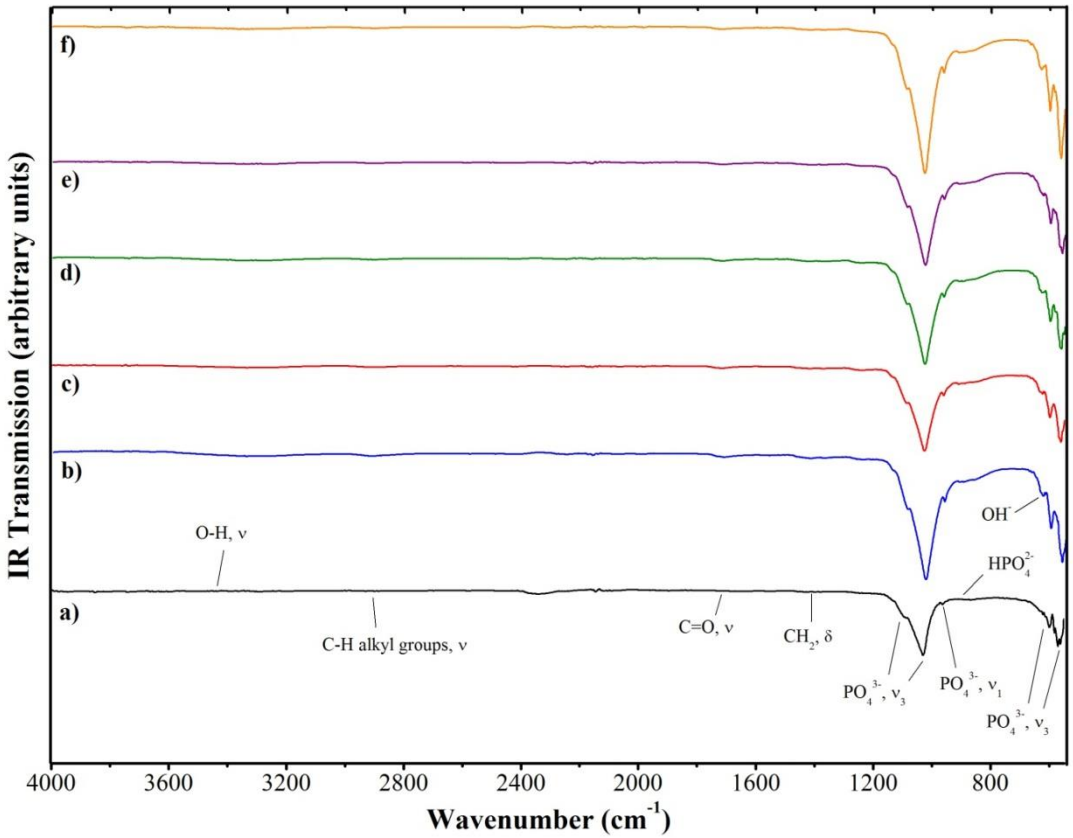

Figure 8.21: Influence of drying methods on composition of X-axis 50wt% HA green bodies (a) 50HA:50PVOH precursor, (b) 50PX, (c) 50F2X, (d) 50F6X, (e) 50V2X, and (f) 50V6X

Microstructural Development

The average range (i.e. mean ± one standard deviation) calculated for the height of pore channels was shown to overlap for all printed and post-processed green scaffolds (Figure 8.22). This suggests that the investigated drying methods did not significantly influence the size of scaffold features that were defined in the initial CAD model. A comparison of the average pore channel height for samples 50PX and 50PY, as well as 60PX and 60PY suggests that features perpendicular to the direction of spreading are distorted to some degree, since the X-axis dimension was smaller in both cases.

The width of designed struts for samples 50F6X, 60F6Y, 60V2X, 50V6X, 50V6Y, 60V6X, and 60V6Y were significantly (i.e. no overlap was exhibited between the range of mean ± one standard deviation) smaller compared with printed counterparts (Figure 8.23). This reduction suggests that a degree of construct shrinkage occurred as a result of the corresponding post-processing treatments.

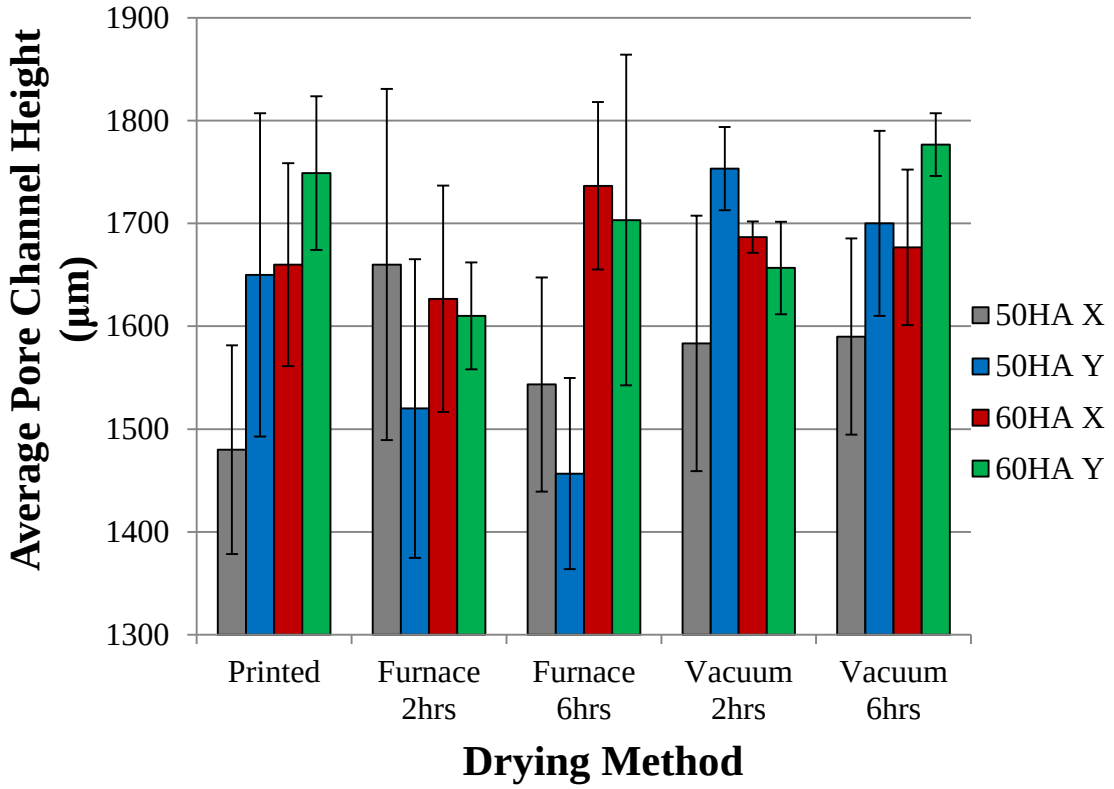

Figure 8.22: Influence of post-processing methods on the height of designed pore channels of 3D printed green scaffolds

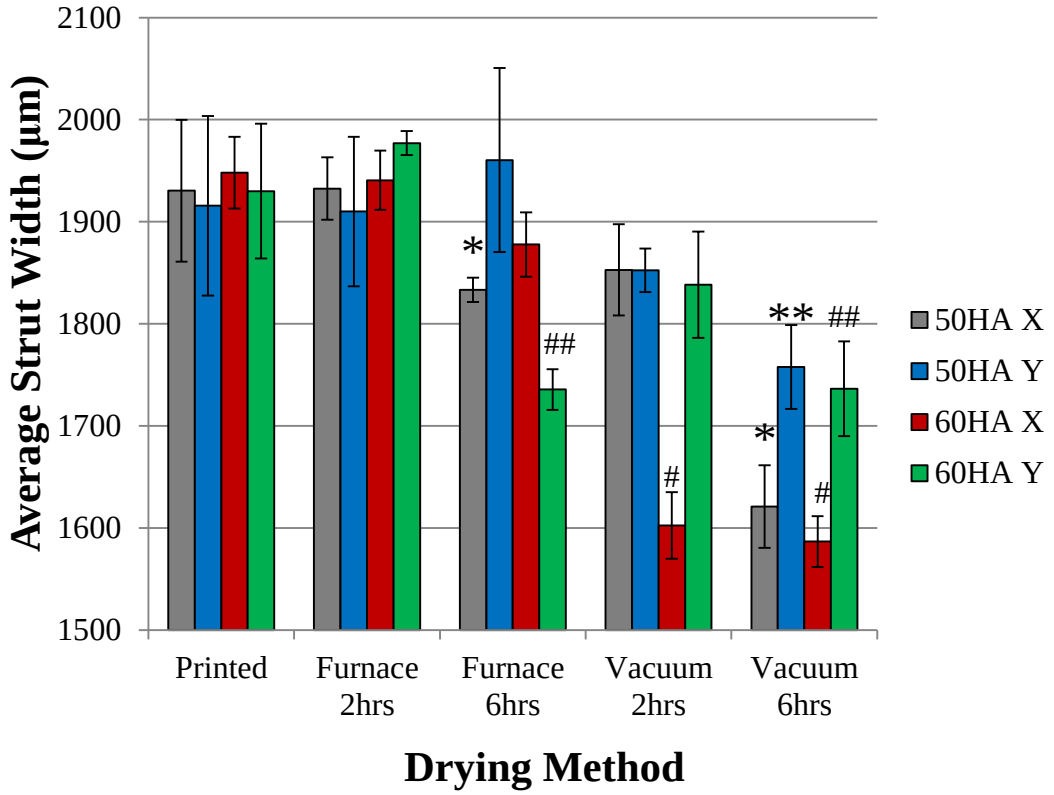

Figure 8.23: Influence of post-processing methods on strut width of 3D printed green scaffolds (significant difference observed compared with: *50PX, **50PY, #60PX, and ##60PY)

Reductions observed in the size of surface pores presents further evidence that post-processing treatments resulted in green part shrinkage (Figure 8.24). Surface pore size analysis suggests that vacuum drying for 2hrs has the most consistent marked effect since all samples exhibited a significant reduction compared with respective printed constructs. The average size of surface pores in 60wt% HA samples were demonstrated to be notably smaller in comparison to equivalent 50wt% HA scaffolds, which suggests that a larger fraction of smaller HA particles improves the packing efficiency of printed layers (Figure 8.6). The effect of drying processes on the average height of pore channels, width of struts, and size of surface pores is summarised in Table 8.8

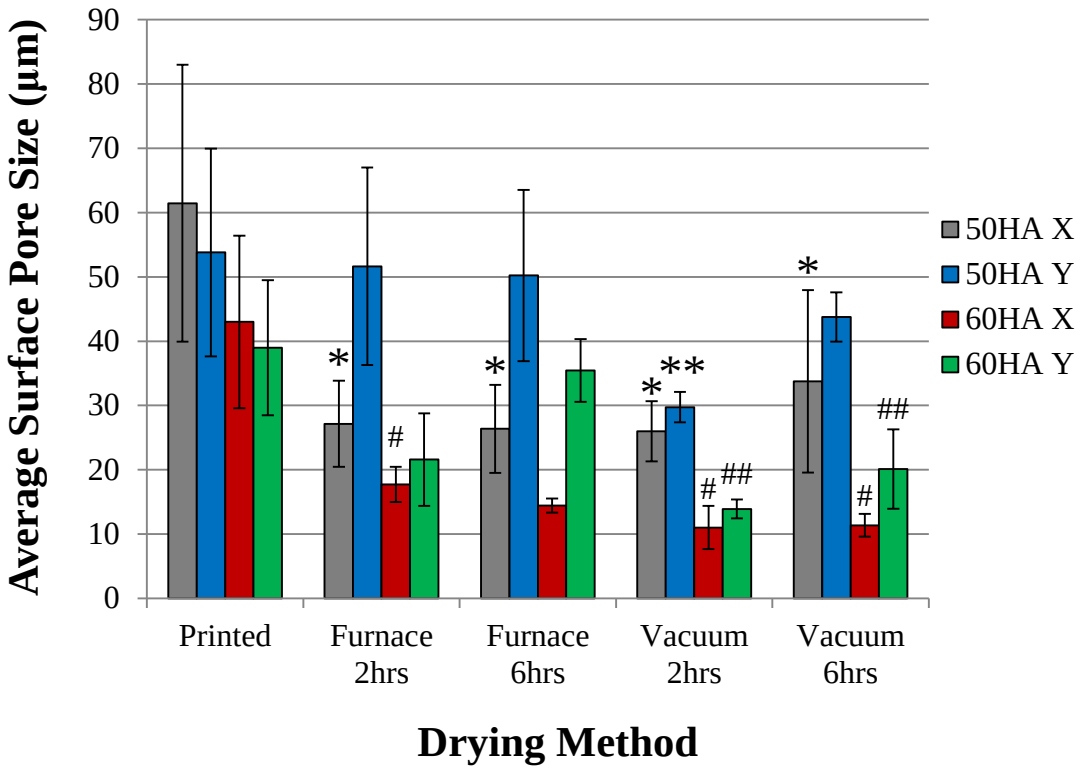

Figure 8.24: Influence of post-processing methods on average surface pore size of 3D printed green scaffolds (significant difference observed compared with: *50PX, **50PY, #60PX, and ##60PY)

Table 8.8: Effect of drying processes on the microstructure of 3D printed green scaffolds (n=6)

Sample	Average size (µm)		
	Strut width	Surface pores	Pore channel height
50PX	1931±70	61.5±21.5	1480±102
50F2X	1933±31	27.2±6.7	1660±171
50F6X	1833±12	26.4±6.8	1543±104
50V2X	1853±45	26.0±4.7	1583±124
50V6X	1621±40	33.8±14.2	1590±95
50PY	1916±88	53.8±16.2	1650±157
50F2Y	1910±73	51.7±15.4	1520±145
50F6Y	1960±90	50.2±13.3	1456±93
50V2Y	1853±21	29.7±2.4	1753±40
50V6Y	1758±41	43.8±3.8	1700±90
60PX	1948±35	43±13.4	1660±99
60F2X	1941±29	17.7±2.8	1627±110
60F6X	1878±32	14.4±1.1	1737±81
60V2X	1602±33	11.0±3.4	1687±15.3
60V6X	1587±25	11.4±1.8	1677±76
60PY	1930±66	39±10.5	1749±75
60F2Y	1977±12	21.6±7.2	1610±52
60F6Y	1736±20	35.5±4.9	1703±161
60V2Y	1838±52	13.9±1.5	1657±45
60V6Y	1736±47	20.1±6.2	1777±31

Typical micrographs showed the morphology of the designed struts and pore channels, as well as the surface topography. Generally, pore channels were shown to be free of loose powder and exhibited rough edges, which was also observed to be the case for strut extremities. This observation is due to the relationship between printing resolution and the maximum particle size and morphology, since these properties infer the packing efficiency of respective powders. Visualisation of scaffold surfaces revealed the presence of micropores as well as numerous topographical irregularities. Characteristic micrographs of scaffold struts, surfaces, and designed pore channels are shown in Figures 8.25 for constructs produced from the 50wt% HA precursor and printed along the X-axis.

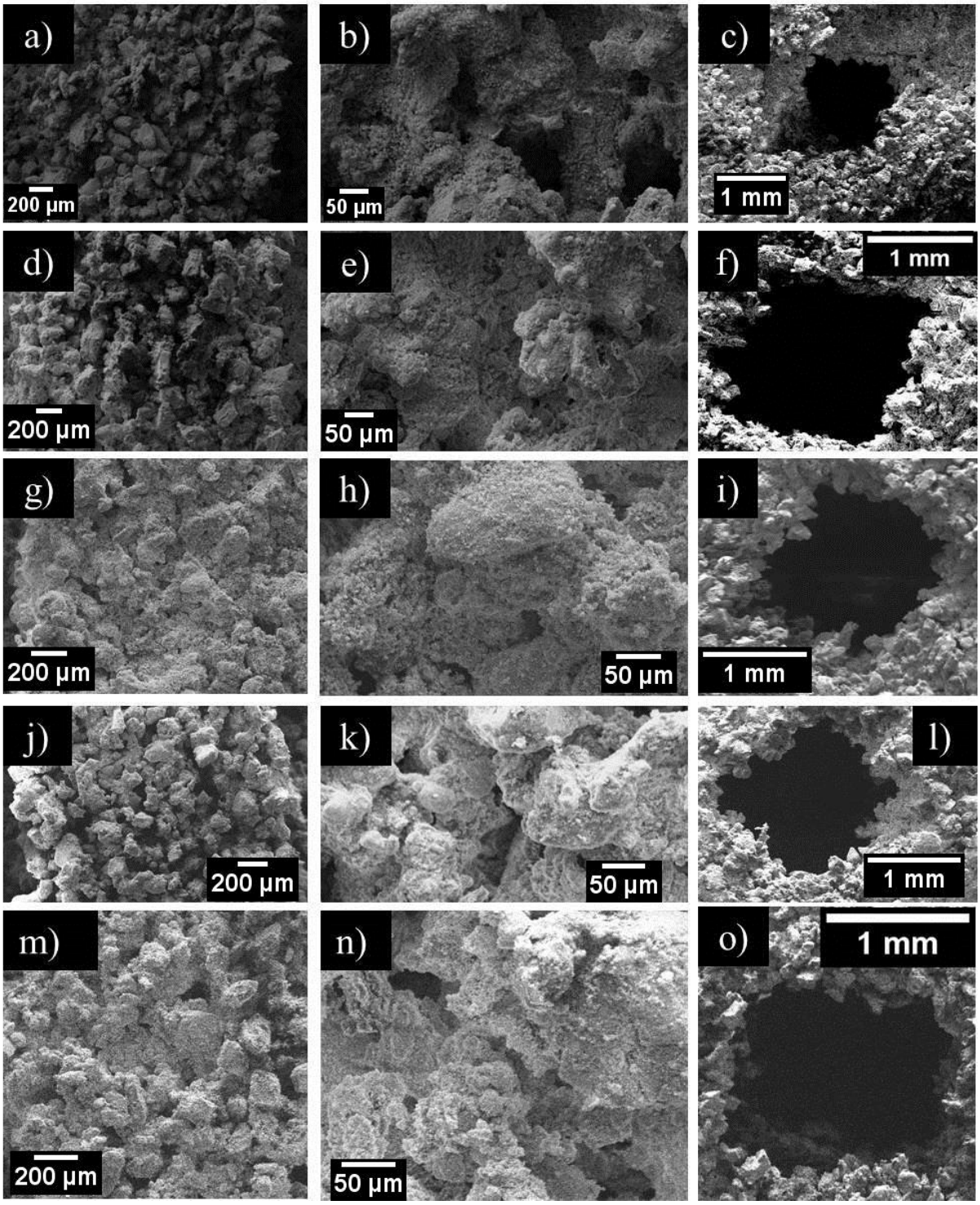

Figure 8.25: Micrographs of 50wt% HA green scaffolds printed along X-axis (a) 50PX strut, (b) 50PX surface, (c) 50PX pore channel, (d) 50F2X strut, (e) 50F2X surface, (f) 50F2X pore channel, (g) 50F6X strut, (h) 50F6X surface, (i) 50F6X pore channel, (j) 50V2X strut, (k) 50V2X surface, (l) 50V2X pore channel, (m) 50V6X strut, (n) 50V6X surface, and (o) 50V6X pore channel

Mechanical strength

The yield and ultimate compressive strengths of 50wt% HA scaffolds were remarkably higher than corresponding 60wt% HA samples (Figures 8.26 and 8.27). All drying processes were shown to improve the yield as well as ultimate compressive strength of X-axis samples compared with 50PX. However, this trend was not observed for all post-processed samples printed along the Y-axis, namely 50F2Y and 50V2Y exhibited lower strength values. Notably, 50PY, 50F6Y, and 50V6Y green bodies yielded as well as failed at higher compressive loads in comparison to equivalent samples printed along the X-axis. Thus suggesting drying via either method for 6hrs was particularly advantageous to the development of compressive strength of green scaffolds printed along the Y-axis.

In contrast, furnace and vacuum drying 50wt% HA constructs for 2hrs was observed to improve the yield and ultimate compressive strength of X-axis scaffolds but a reduction was seen for equivalent Y-axis samples compared with 50PX and 50PY, respectively. Analysis of the surface microstructure revealed larger pores in 50PX compared with 50PY but a relatively higher shrinkage rate was demonstrated after 2hrs of either drying treatment (Table 8.8).

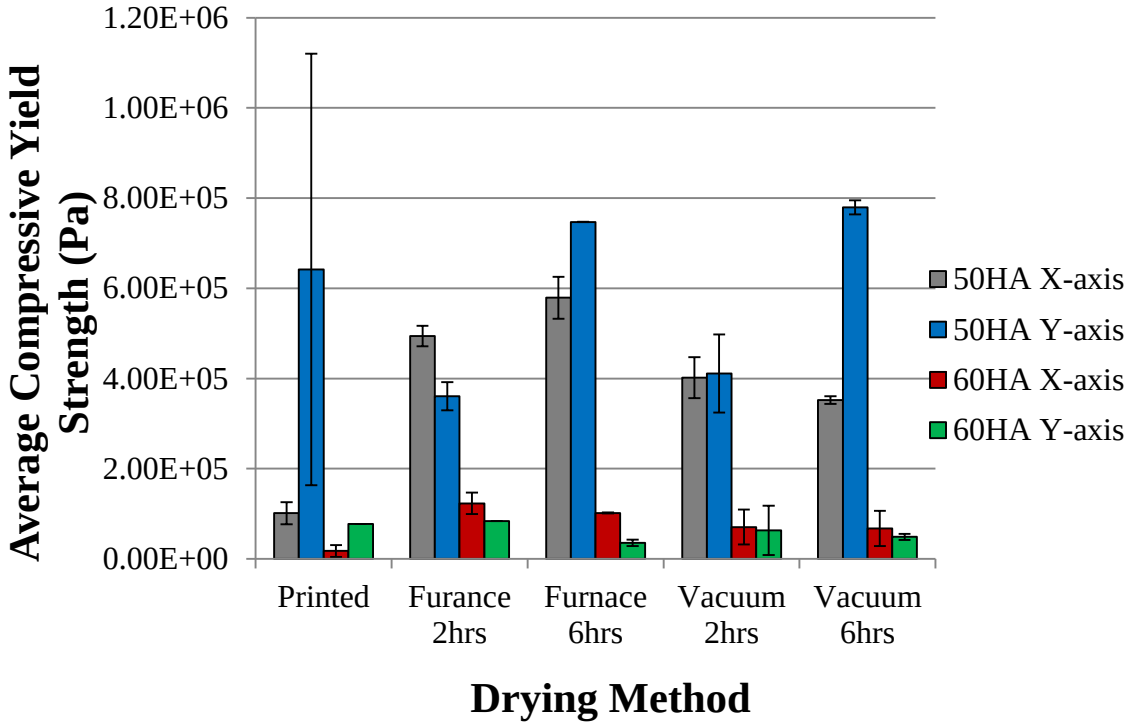

Figure 8.26: Average compressive yield strength of 50 and 60wt% HA 3D printed green scaffolds (n= 3)

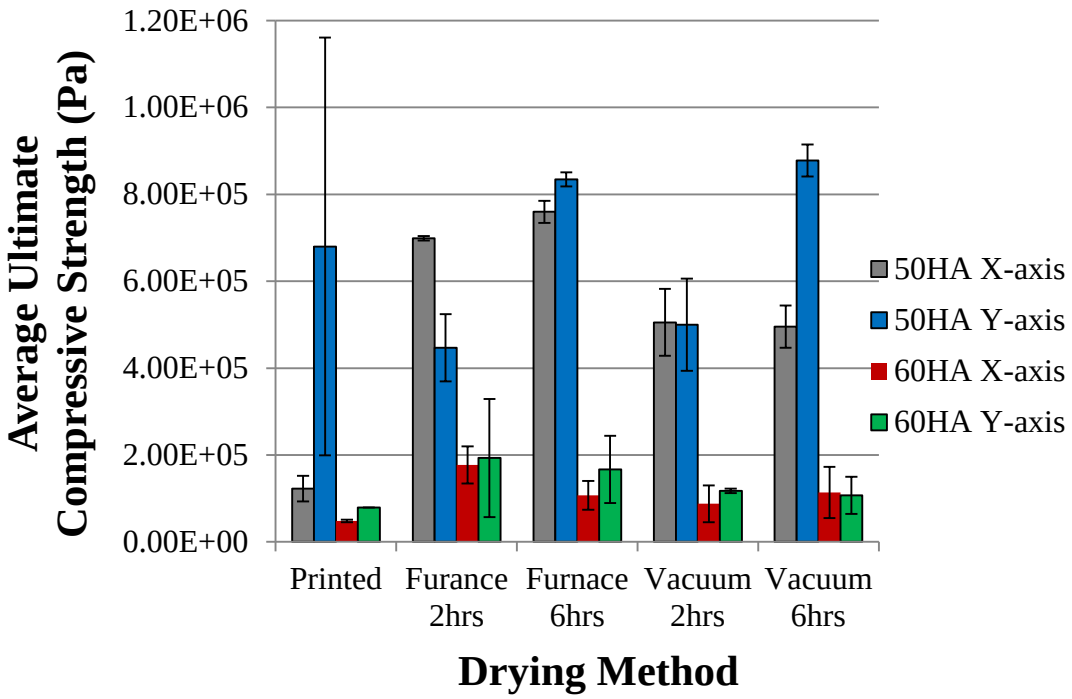

Figure 8.27: Average ultimate compressive strength of 50 and 60wt% HA green scaffolds (n= 3)

The average degree of strain at the onset of plastic deformation, and failure were calculated to be higher in Y-axis samples compared with corresponding constructs printed along the X-axis (Figures 8.28 and 8.29). Loading parallel to the printing axis, (i.e. X-axis samples) was observed to result in a relatively brittle and catastrophic failure mechanism compared with the higher plastic deformation seen for Y-axis samples (Figure 8.30). Therefore the direction of printing was found to be a key determinant of the part failure mechanism. It is recognised that a more dynamic loading pattern is to be expected in-vivo compared with the uniaxial testing reported in this thesis.

Drying treatments did not influence the yield or ultimate compressive strains developed in X-axis scaffolds. In comparison, post-processing treatments had a mildly positive influence on the yield strain of 60PX. It is plausible that PVOH particles became slightly molten at 60°C, resulting in improved infiltration of the structure, which is likely to strengthen layer bonding once parts were cooled after drying treatments. Post-processing techniques generally had a positive effect on the yield strain of 50wt% HA scaffolds printed along the Y-axis but a reduction in the ultimate strain was observed. Contrastingly, the opposite trend was largely demonstrated for corresponding 60wt% HA constructs.

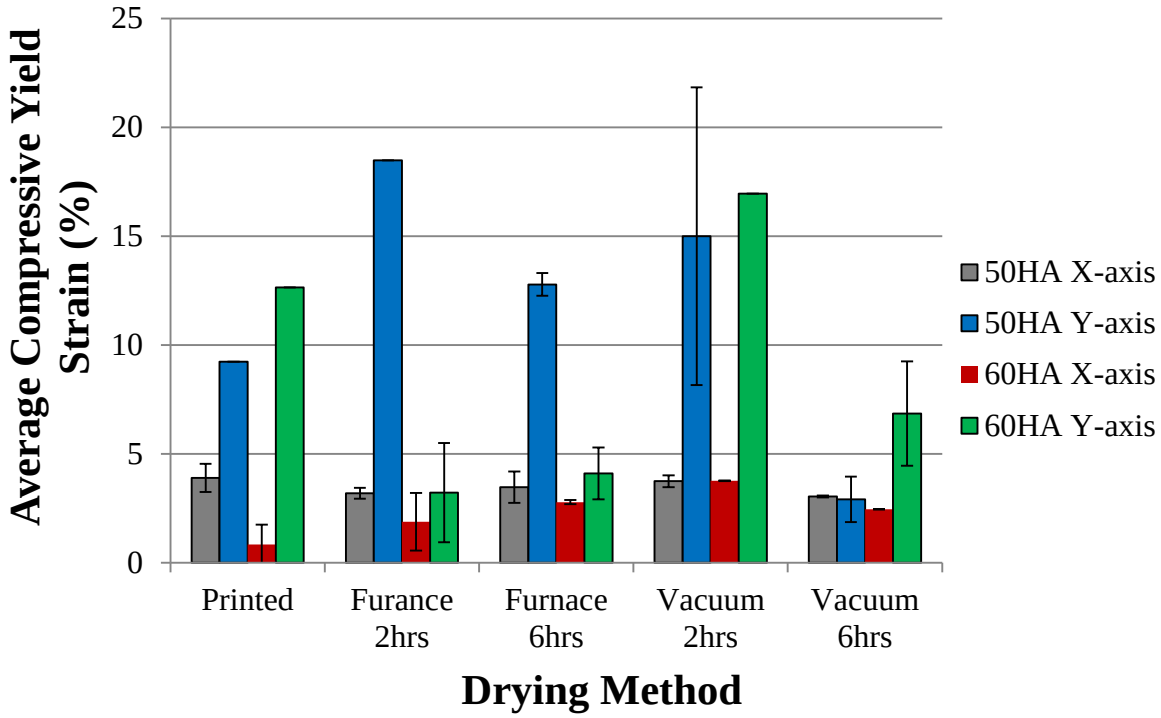

Figure 8.28: Average strain at onset of plastic deformation in 3D printed 50 and 60wt% HA green scaffolds under compressive loading (n= 3)

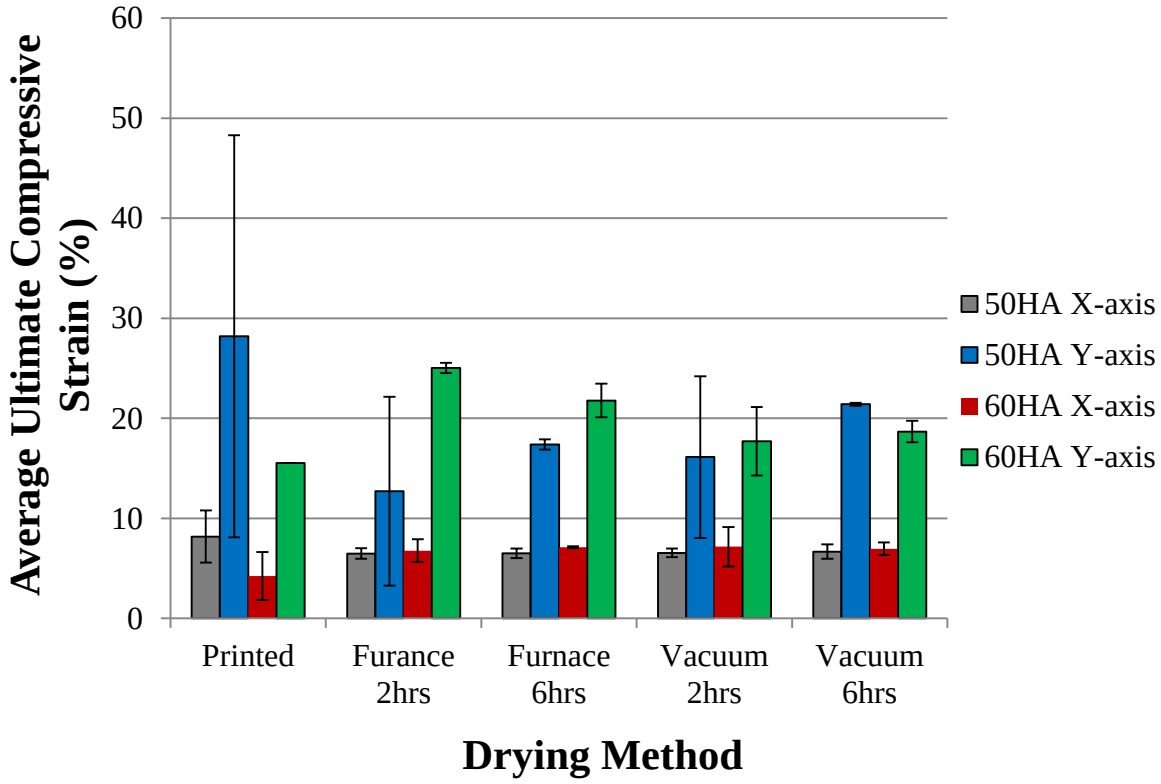

Figure 8.29: Average compressive strain of 3D printed 50 and 60wt% green scaffolds at failure (n= 3)

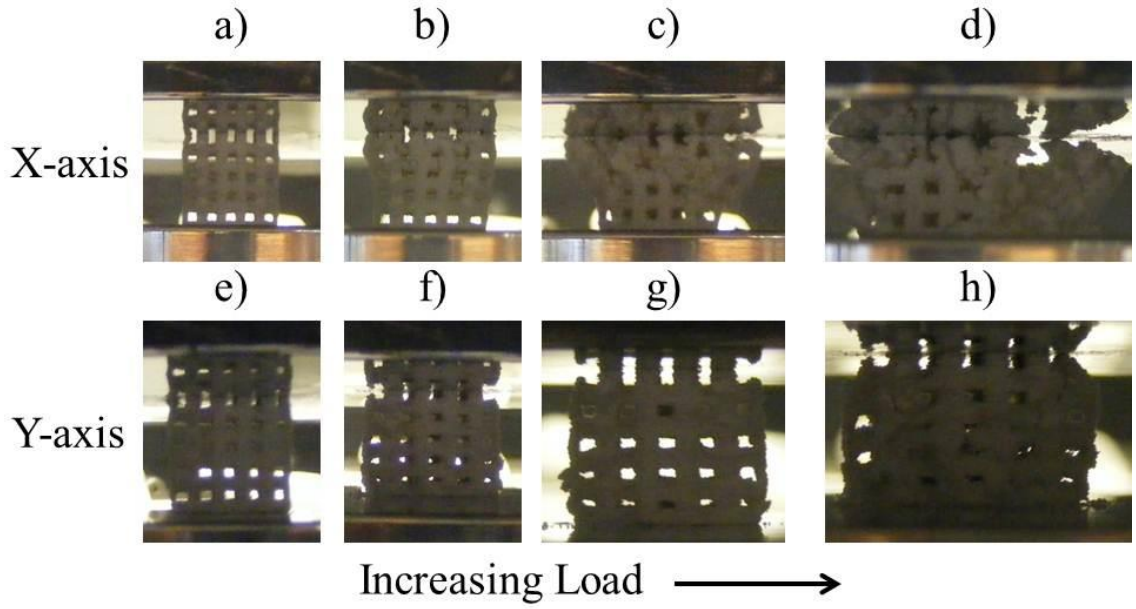

Figure 8.30: Typical failure mechanisms of printed 50wt% HA scaffolds (a – d) catastrophic failure of 50PX, and (e – h) plastic failure of 50PY

8.4.3 Sintered constructs

8.4.3.1 Stability of sintered scaffolds

TGA results revealed the majority of precursor weight loss occurred between 185 and 500°C. Heat treatment protocols (Table 8.9) were designed according to this information and the temperature (230°C) reported as the onset of PVOH molten state degradation [323]. Initially the feasibility of each protocol was tested on 50PX and 50PY samples.

To begin with, a sintering temperature of 800°C was investigated (HT1 – 3) and the most stable parts were found to be those heated at a rate of 1°C/min using a single stage protocol (HT2), i.e. without soaking at 230°C. However, these constructs were all difficult to handle and therefore in an effort to increase the consolidation of the HA construct a higher sintering temperature of 1300°C was investigated.

A reduction in the ramp rate from 10 to 1°C/min was observed to improve the stability of the sintered scaffold (HT4 and HT5). However, a further reduction to 0.5°C/min caused the structure to collapse between 250 and 800°C (HT6). Since failure occurred above 230°C it was concluded that the HA scaffolds were not consolidated fast enough after PVOH burn out. This attribution was confirmed by HT7, since a higher

ramp rate (1°C/min) above 230°C resulted in maintenance of mechanical integrity. A further improvement in mechanical strength was achieved when the dwell time at 230°C was removed and the ramp rate between 230 and 1300°C was increased to 2°C/min (HT8), which is explained in terms of a reduction in time between PVOH burn out and HA consolidation.

The effect of green body post-processing on the stability and structure of final sintered scaffolds was assessed using HT8 protocol (Figure 8.31). X-axis scaffolds were observed to exhibit some lateral expansion at the base of the structure, and the pore channels at the bottom of samples 50F2Y and 50F6Y were shown to be relatively smaller. Partial collapse of samples 50F2X and 50F6X occurred parallel to the direction of layer printing, which corresponds to the propagation of cracks along interlayer bonding that was shown to be the cause of failure in mechanical strength tests. Some instability was also noted for samples 50F2Y and 50F6Y. Overall, 50PX, 50PY, 50V6X, and 50V6Y were the easiest to handle, no defects were observed, and bulk shrinkage appeared to be uniform.

Table 8.9: Heat treatment protocols employed on 50wt% HA scaffolds (T= temperature, R= ramp rate, D= dwell time)

Protocol ID	Heat treatment stages									Comment
	T_0 (°C)	R_1 (°C/min)	T_1 (°C)	D_1 (hrs)	R_2 (°C/min)	T_2 (°C)	D_2 (hrs)	R_3 (°C/min)	T_3 (°C)	
HT1	30	1	230	1	1	800	1	1	30	Failure of parts occurred parallel to direction of printing
HT2		1	800	1	1	30	N/A			Scaffolds difficult to handle and some cracks observed Improvement in stability compared to HT1
HT3		10	800	1	10	30				More cracks observed compared to HT2
HT4		10	1300	1	10	30				Improved stability compared to HT3 Cracks observed parallel to direction of printing
HT5		1	1300	1	1	30				Some cracking and distortion of part shape observed Less shrinkage than HT4
HT6		0.5	1300	1	0.5	30				Scaffolds intact at 250°C Structure collapsed before 800°C
HT7		0.5	230	1	1	1300	1	1	30	No collapse of structure Few cracks observed
HT8		0.5	230	0	2	1300	1	2	30	Improved ease of handling compared with HT7 Cracks observed only in some samples (Figure 8.31)

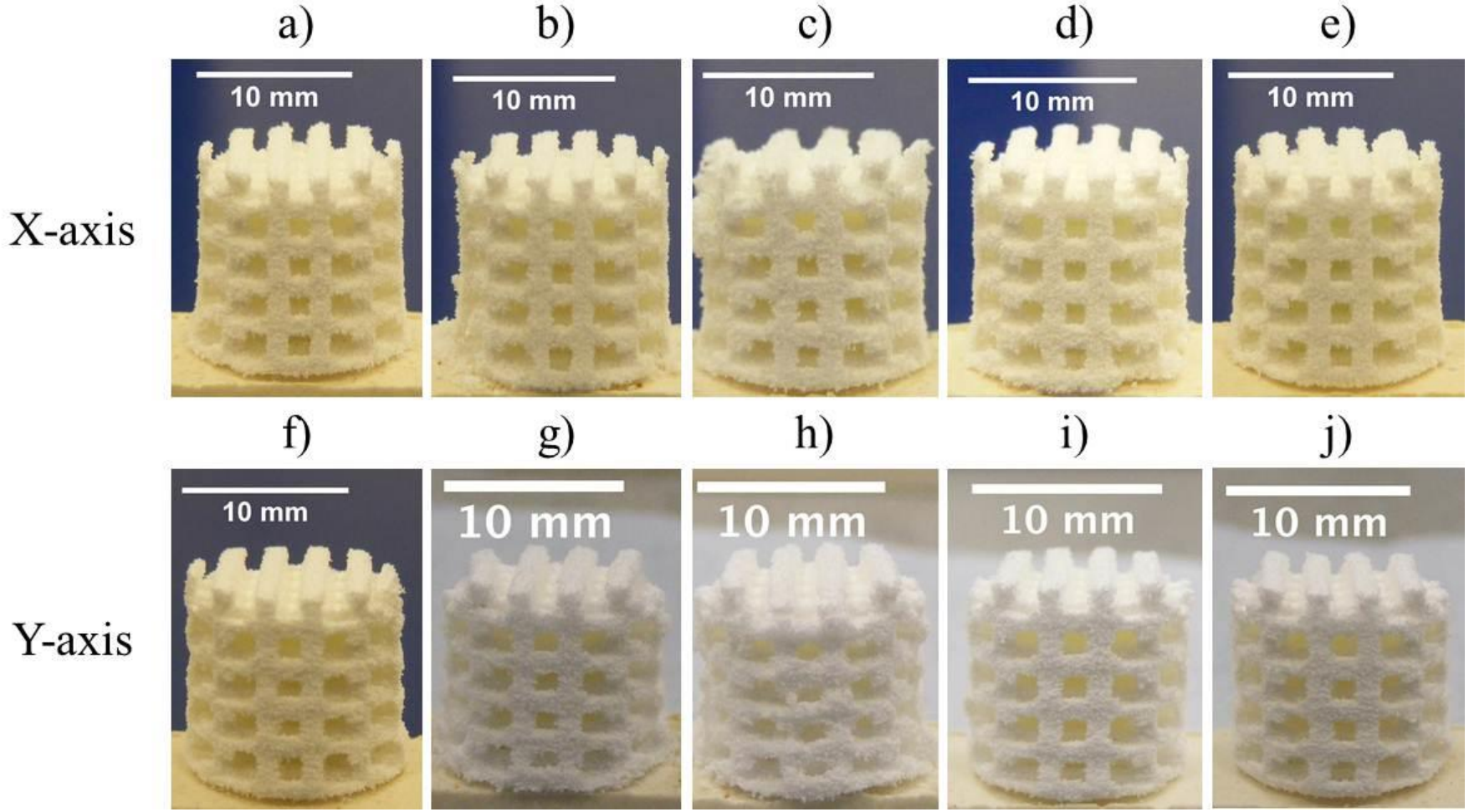

Figure 8.31: Sintered scaffolds heat treated using HT8 protocol (a) 50PX, (b) 50F2X, (c) 50F6X, (d) 50V2X, (e) 50V6X, (f) 50PY, (g) 50F2Y, (h) 50F6Y, (i) 50V2X, and (j) 50V6Y

8.4.3.2 Chemical composition of sintered scaffolds

Band/peak assignments corresponding to PVOH were not observed in 50wt% HA precursor powder after TGA analysis or X-axis scaffolds after sintering using protocol HT8 (Figure 8.32). In contrast, strong vibration bands corresponding to C-H alkyl groups were revealed in sintered Y-axis scaffolds (Figure 8.33), which signifies incomplete removal of PVOH. Furthermore, the appearance of bands between 1900 – 2300cm^{-1} were attributed to stretching of C≡C in low molecular weight alkynes, which have been reported as thermal degradation products of PVOH [324]. O-H vibration was also demonstrated in sintered Y-axis scaffolds 3600 – 3750cm^{-1}. Corresponding XRD patterns of as-supplied and sintered HA (1300°C) as well as 50 HA:50PVOH were illustrated in Figure 7.2.

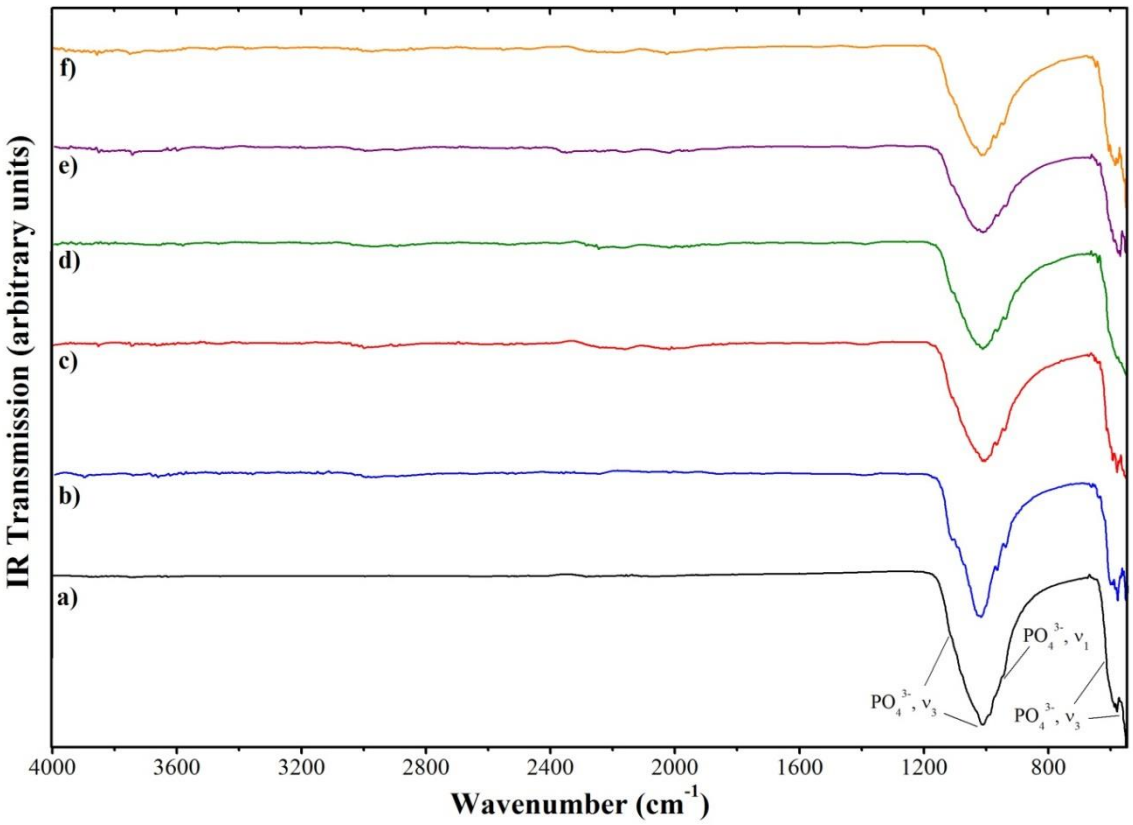

Figure 8.32: FTIR spectrum of 50wt% HA scaffolds printed along X-axis and sintered using HT8 (a) 50wt% HA precursor post TGA analysis, (b) 50PX, (c) 50F2X, (d) 50F6X, (e) 50V2X, and (f) 50V6X

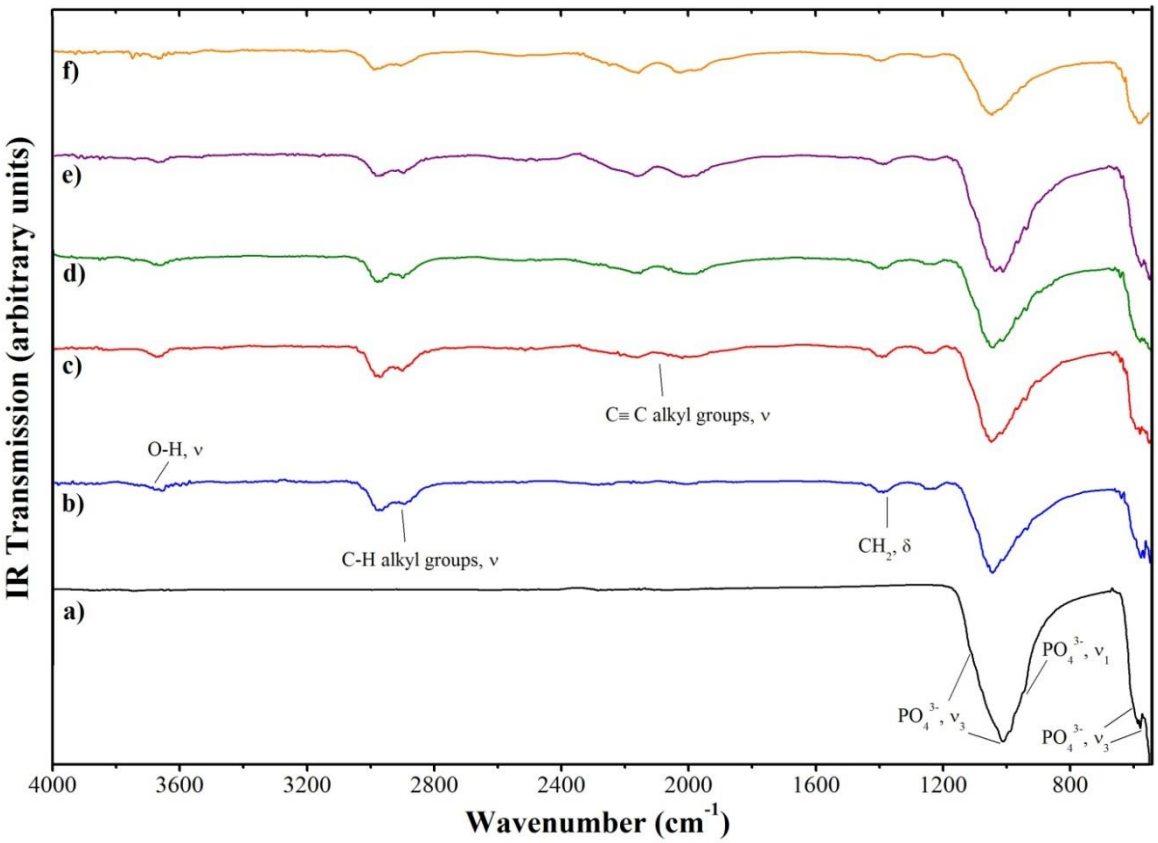

Figure 8.33: FTIR spectrum of 50wt% HA scaffolds printed along Y-axis and sintered using HT8 (a) 50wt% HA precursor post TGA analysis, (b) 50PY, (c) 50F2Y, (d) 50F6Y, (e) 50V2Y, and (f) 50V6Y

8.4.3.3 Shrinkage of sintered scaffolds

Average shrinkage of scaffold height was found to be greater than corresponding diameter reductions for all sintered X (Figure 8.34) and Y-axis (Figure 8.35) constructs. A larger shrinkage in height was observed in all Y-axis samples compared with equivalent X-axis scaffolds. Overall, a more uniform shrinkage was observed for X-axis constructs, i.e. shrinkage of average height and diameters were closer in value.

On average 55 and 54% weight loss was calculated for X and Y-axis samples, respectively. This corresponds approximately to the weight loss recorded for 50wt% HA precursor powder measured by TGA (55.15%), thus suggesting that PVOH content was removed from the construct.

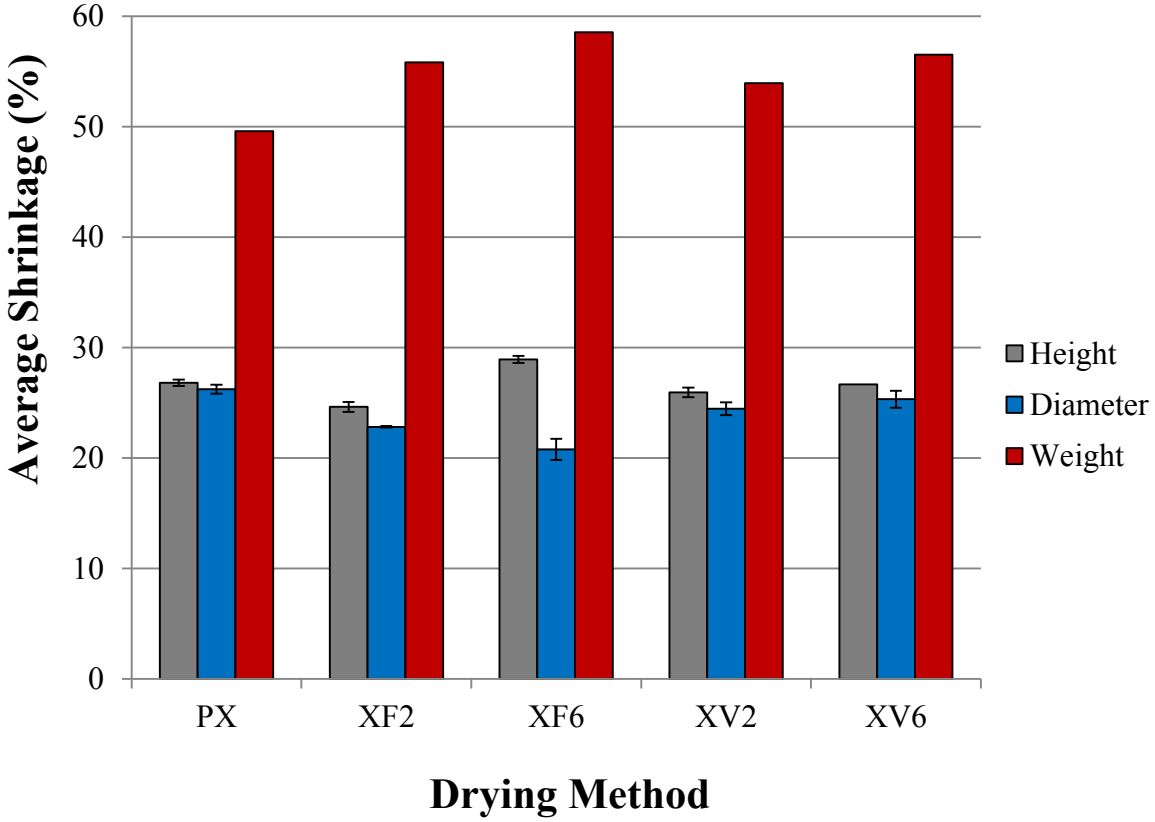

Figure 8.34: Bulk shrinkage of X-axis 50wt% HA scaffolds sintered using HT8 (n=3)

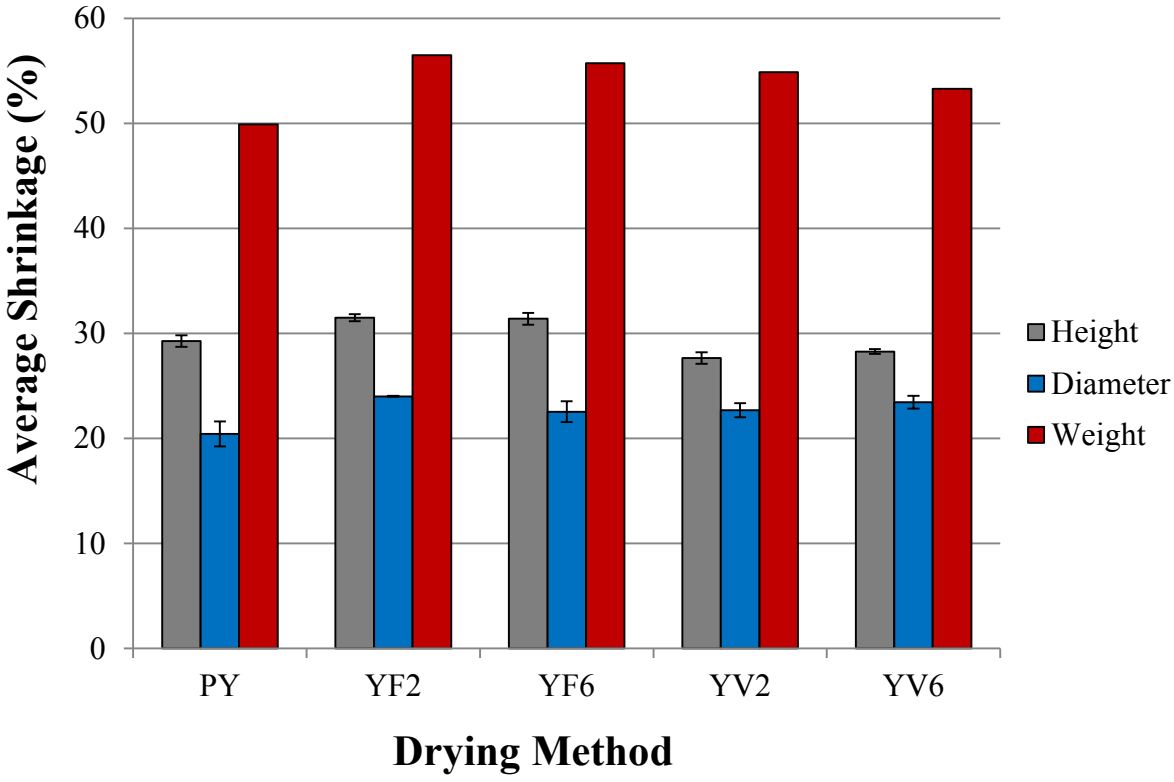

Figure 8.35: Bulk shrinkage of Y-axis 50wt% HA scaffolds sintered using HT8 (n=3)

8.4.3.4 Microstructure of sintered scaffolds

The effect of sintering on scaffold microstructure, specifically the shrinkage of designed pore channels, struts, and surface pores was evaluated (Table 8.10). A number of trends in pore channel height and strut width were observed: (1) 50PX, 50F2X and 50F6X shrank less than equivalent Y-axis samples, and (2) ranges (mean ± one standard deviation) for 50V2X and 50V2Y, as well as 50V6X and 50V6Y overlapped. The average surface pore size for sintered X-axis scaffolds was larger than corresponding Y-axis samples (Table 8.10). It is suggested that this observation explains why Y-axis constructs were demonstrated to contain residue of PVOH degradation products (Figure 8.33).

Shrinkage of pore channels, struts, and surface pores due to HT8 are illustrated in Figures 8.36 – 8.38, respectively. Pores, designed channels and surface, as well as struts of Y-axis constructs were observed to shrink more compared with X-axis scaffolds. Shrinkage of surface pores was shown to be substantially greater than pore channel height or strut width.

Table 8.10: Effect of HT8 protocol on microstructure of sintered 50wt% HA scaffolds

Sample	Average size (μm)		
	Pore channel height	Strut width	Surface pores
PX	1152±106	1587±41	3.2±1.0
PY	907±39	1357±53	1.8±0.5
F2X	1064±77	1498±41	3.0±1.6
F2Y	830±43	1105±102	1.8±0.2
F6X	1039±55	1161±116	3.2±1.2
F6Y	877±71	1014±14	2.0±0.1
V2X	1085±110	1181±53	2.3±0.5
V2Y	1122±26	1238±46	1.6±0.6
V6X	1015±36	1252±55	3.5±1.0
V6Y	1144±12	1304±5	3.0±0.8

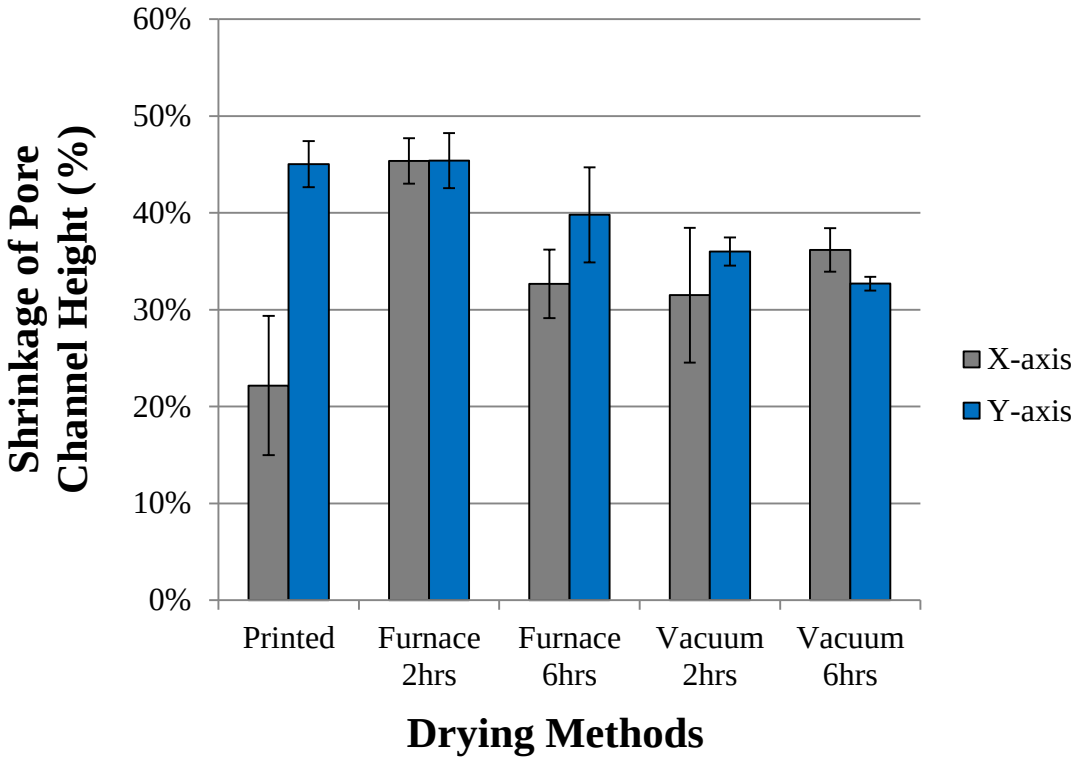

Figure 8.36: Shrinkage of pore channel height for sintered scaffolds compared with green bodies (n=3)

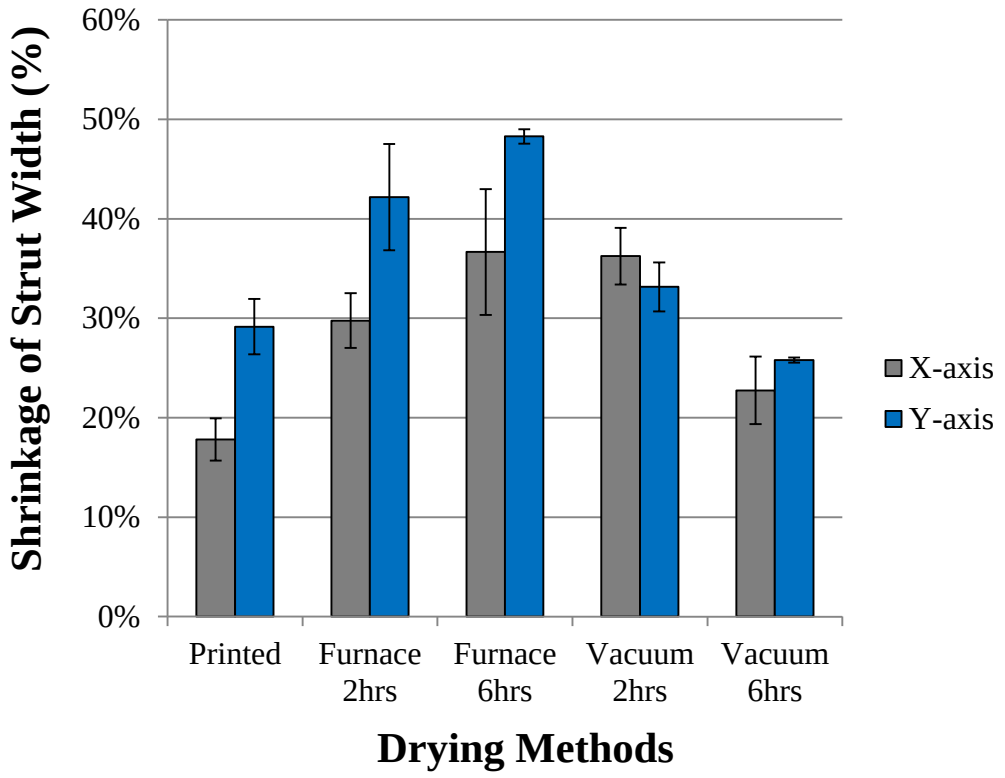

Figure 8.37: Shrinkage of strut width for sintered scaffolds compared with green bodies (n=3)

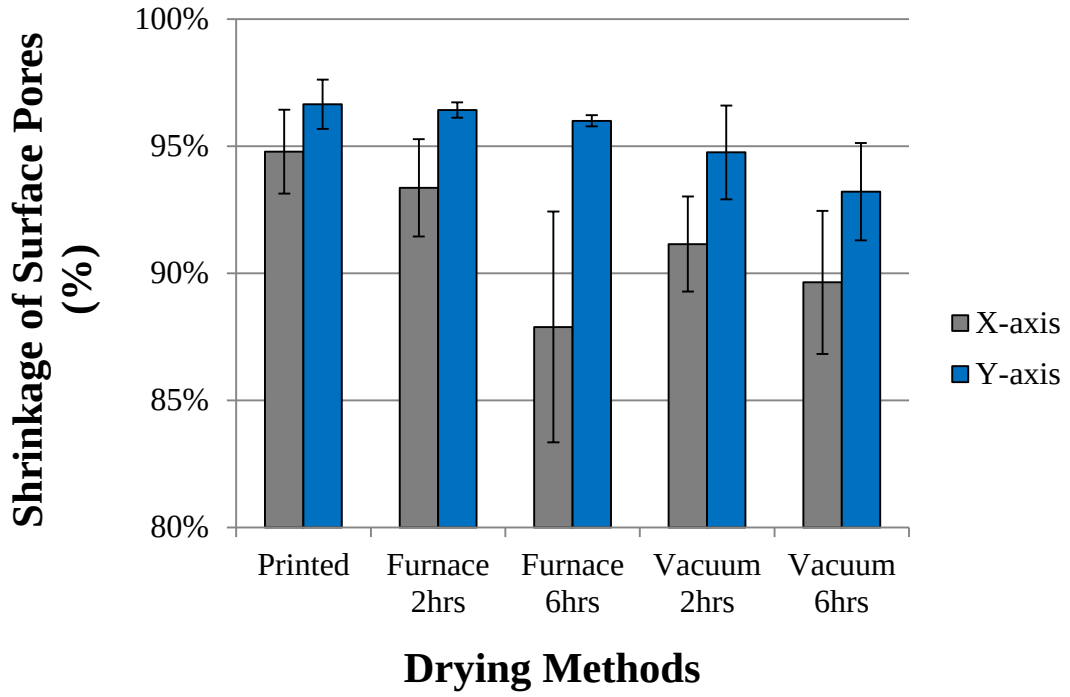

Figure 8.38: Shrinkage of surface pores for sintered scaffolds compared with green bodies (n=3)

Corresponding micrographs revealed the influence of HT8 on the surface topography of scaffolds. A degree of distortion of designed pore channels in X (Figure 8.39) and Y-axis (Figure 8.40) scaffolds was observed, indicating that uniform shrinkage did not occur. The surface topography of sintered constructs was shown to be distinctly different to green parts where larger PVOH particles were observed (Figure 8.25). In comparison, the surface of sintered scaffolds appeared to be consolidated HA particles arranged in a coralline like structure. Micropores (<5μm) were demonstrated within samples and it is suggested that this porosity is a result of consolidation of inherent surface pores observed in green scaffolds. Typically, the surface topography of sintered constructs appeared to be more regular than equivalent green parts, which is attributed to heat treatment causing consolidation of HA as well as removal of PVOH particulates.

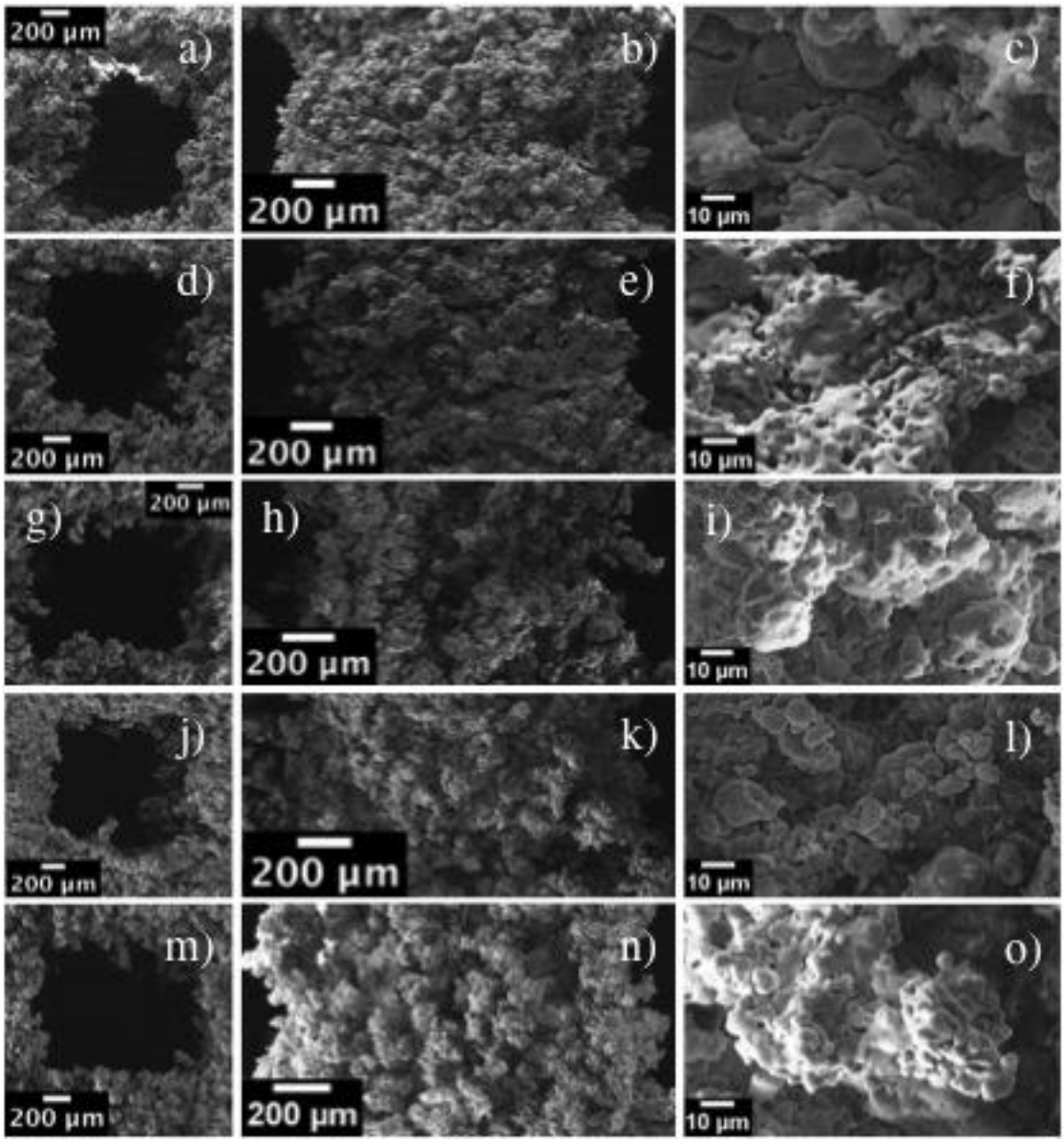

Figure 8.39: Micrographs of 50wt% HA sintered scaffolds printed along X-axis (a) 50PX pore channel, (b) 50PX strut, (c) 50PX surface, (d) 50F2X pore channel, (e) 50F2X strut, (f) 50F2X surface, (g) 50F6X pore channel, (h) 50F6X strut, (i) 50F6X surface, (j) 50V2X pore channel, (k) 50V2X strut, (l) 50V2X surface, (m) 50V6X pore channel, (n) 50V6X strut, and (o) 50V6X surface

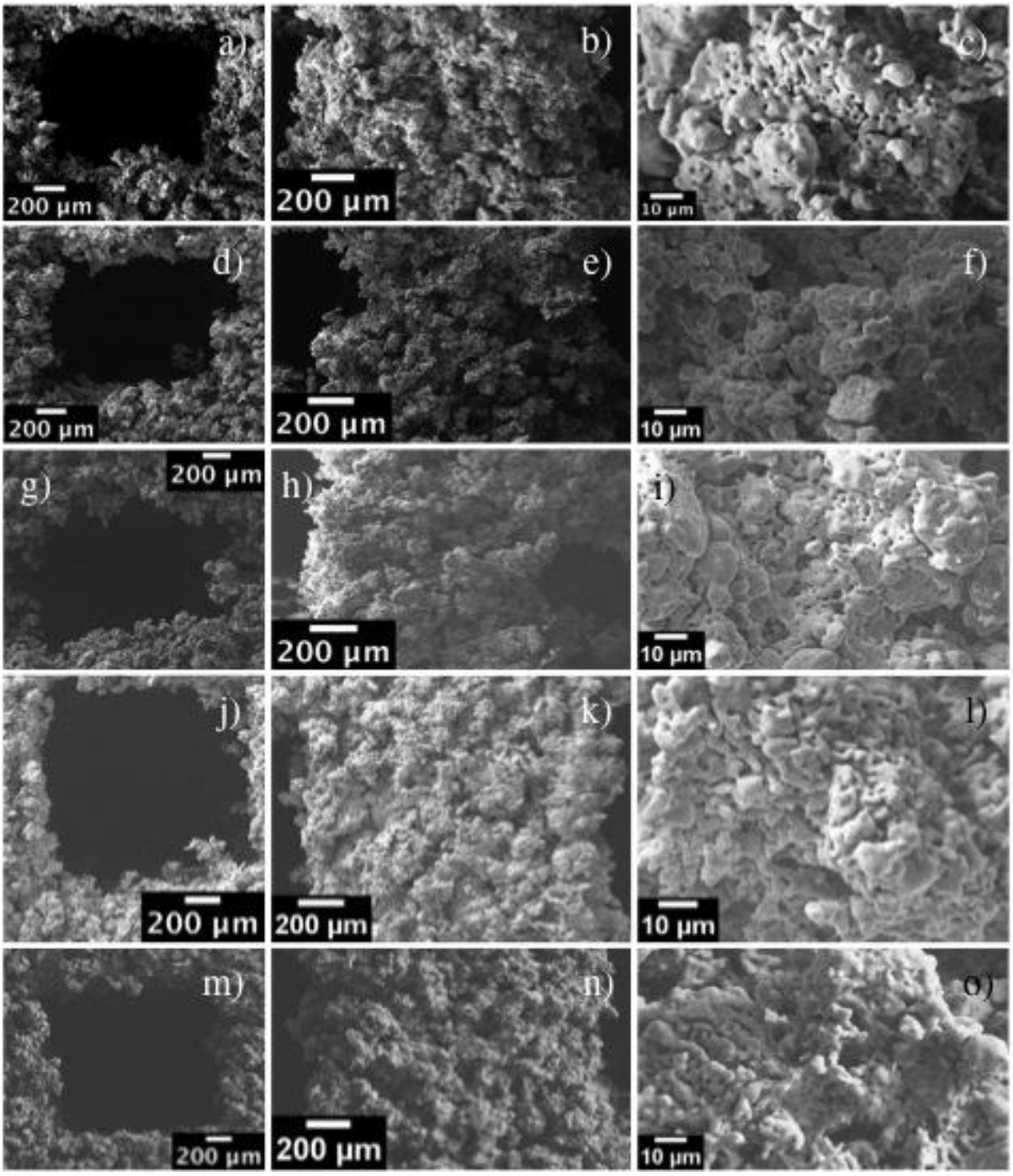

Figure 8.40: Micrographs of 50wt% HA sintered scaffolds printed along Y-axis (a) 50PY pore channel, (b) 50PY strut, (c) 50PY surface, (d) 50F2Y pore channel, (e) 50F2Y strut, (f) 50F2Y surface, (g) 50F6Y pore channel, (h) 50F6Y strut, (i) 50F6Y surface, (j) 50V2Y pore channel, (k) 50V2Y strut, (l) 50V2Y surface, (m) 50V6Y pore channel, (n) 50V6Y strut, and (o) 50V6Y surface

8.5 Discussion

Preliminary results presented in Chapter 7 established that HA:PVOH precursor powders with a maximum of 80wt% HA were printable. However, further printability assessments demonstrated the instability of 80HA:20PVOH and 70HA:30PVOH

scaffolds, which was attributed to poor interlayer bonding due to insufficient PVOH content (Table 8.6). Prior to printing the flowability of precursor powders was assessed by two funnel methods, and these results correlated with the observed printability, i.e. materials that recorded faster flow times and a lower angle of repose were more easily printed. This is explained in terms of improved powder flowability resulting in a higher degree of bed recoating, leading to less interparticulate voids, which contributes to stronger bonding between layers. Thus it is clear that precursor flowability contributes to mechanical stability and strength.

Clumping of powders with 60wt% or more HA was observed during spreadability analysis (Figure 8.10), which was attributed to the higher fraction of smaller HA particles in these precursors (Figure 8.6). This observation may also be a contributing factor in determining printability, since spreading of clumped powders was shown to disrupt the surface topography of the build bed. As a result reduced packing efficiency, corresponding to a higher void volume is likely. The Hausner ratio presents an assessment of the relative effect of interparticle interactions on flowability. Calculation of this value revealed that 90, 80, and 70wt% HA precursors were harder to settle compared with 50HA:50PVOH and raw stock materials, which may have contributed to the observed clumping behaviour and instability of green parts. As part of future studies it could be of interest to investigate any influence of particle surface charge on the flowability of powders and if it can be used to reduce clumping of precursors. If this property is found to be influential it would be important to consider the solvent system in which HA is produced since the results of Chapter 5 highlighted the variability of ZP according to the degree of solvent polarity.

Measurements of the width of powder and build beds were taken to assess spreadability, since these profiles were suggested to indicate powder flowability and bed stability. No significant differences were observed between precursors (Figure 8.9) and trends of these results did no match direct flowability or density measurements, which presented cohesive attributions. For these reasons it is concluded that this method cannot be used as a means to quantitatively distinguish the spreadability of powders. In contrast, comparison of the surface topography of beds observed after spreading different precursors was useful.

A notable difference in the average size of precursor powders was observed between SEM measurements (Table 8.4), and particle size analysis (Table 8.2). Thus, the

agglomeration behaviour of precursors, which was demonstrated in typical micrographs (Figure 8.11), is expected to be more prominent within the bulk sample than SEM analysis suggests. It is likely that the method used to prepared samples for SEM resulted in a reduction of agglomerates due to fine spreading of powders on stubs. If this is the case it can be concluded that agglomerates of HA and PVOH particles are only loosely bound together. This suggests that sieving powders prior to printing is a sufficient method to ensure the flowability of precursors is not compromised by any agglomeration that could occur as a result of mechanical mixing or storage.

A reported disadvantage of 3DP is the 'difficulty' involved in removing unbound powder from green bodies (Table 2.9). The novel combination of a commercial airbrush nozzle and a syringe needle (Figure 8.3) used in this project was proven to be an effective and time efficient way to remove loose powder from pore channels, as well as the surface of green bodies. The success of this method was attributed to the fine jet of compressed air, which could be blown at a controlled rate (Figure 8.17). Micrographs of green scaffolds demonstrated that pore channels were not occluded, and no surface damage was apparent (Figure 8.25). It should be noted that the interconnection of designed pore channels helped to facilitate the removal of loose powder, and the ease of de-powdering is expected to be more difficult for intricate or relatively complex structures.

The ease of handling green Y-axis 50 and 60wt% HA scaffolds was observed to reduce when structures were dried for 6hrs in a furnace or vacuum oven, which resulted in damage to external struts (Figure 8.18). In general, drying of scaffolds resulted in bulk shrinkage of height and diameter (Figure 8.19), as well as loss of weight (Figure 8.20). Notably a larger weight reduction was recorded for Y-axis samples compared with equivalent X-axis green bodies. Corresponding micrographs revealed no significant change in the height of pore channels due to post processing compared with printed constructs (Figure 8.25). This dimension was found to be smaller for printed X-axis samples compared with Y-axis constructs. Thus, it is suggested that the build bed is partially distorted as the counter-rotating roller spreads powder across and this affects dimensions parallel to the direction of spreading, which corresponds to the height of X-axis constructs.

Significant shrinkage of strut width occurred for samples 50F6X, 60F6Y, 60V2X, 50V6X, 50V6Y, 60V6X, and 60V6Y, which was attributed to these drying treatments causing consolidation of the structure (Figure 8.23). It is unlikely that consolidation of HA would occur at such a low temperature and since shrinkage was accompanied by weight loss (Figure 8.20) it is therefore suggested that this observation is associated with partial decomposition of PVOH. TGA analysis of precursors demonstrated 2.5%, and <0.5% weight loss of PVOH and HA at 60°C, respectively. Since no corresponding DTA peaks were observed this weight loss can be attributed to loss of non-bound surface water. Weight losses caused by post-processing treatments were greater than TGA reductions, thus it is probable that some thermal degradation of PVOH occurred as a result of dwelling scaffolds at 60°C for a prolonged period of time. A reduction in the size of surface pores was also revealed (Figure 8.24), and notably this effect was more consistent when a vacuum oven was used to dry constructs. If drying resulted in partial degradation of PVOH it may be suggested that these products were more readily removed under vacuum, which would explain the higher rate of consolidation. Overall, these observations infer that drying scaffolds resulted in microstructural shrinkage but the degree of consolidation was not large enough to affect the dimensions of non-solid features, i.e. pore channels.

The improved yield and compressive strength of 50wt% HA scaffolds compared with 60wt% HA constructs can be related to the higher flowability, and reduced interparticle interactions of the respective precursor powders. Hence, these differences are evidence of the critical influence of these precursor characteristics on mechanical integrity. Different trends in yield and ultimate compressive strength development were exhibited for X and Y-axis constructs (Figures 8.26 and 8.27). This suggests that the rate at which strength development occurred, due to drying, for these samples was different, and this is attributed to the size of surface pores. 50F2X, 50F6X, 50V2X, and 50V6X were observed to exhibit significant shrinkage of surface pores (i.e. a faster reduction in void volume compared to Y-axis samples), which can be associated with development of strength. Therefore it may be concluded that the rate of consolidation of surface pores is a critical factor in compressive strength development. However, since samples 50F6Y and 50V6Y exhibited higher ultimate strengths it is suggested that this is not the only factor that contributes to compressive strength. Hence, more specifically it is advocated that void volume influences the strength of

interlayer bonds. Strength testing demonstrated that failure occurred due to propagation of cracks along the boundaries between layers (Figure 8.30). The lower maximum yield and ultimate compressive strength of X-axis scaffolds, as well as the catastrophic failure mechanism observed advocate that interlayer bonding is weakest parallel to the direction of loading. Therefore, it is concluded that it is not merely the strength of interlayer bonding but also the direction of part loading that infers the bulk compressive strength of the printed scaffolds. Anisotropic strength of 3D printed parts is commonly reported in the literature [325]. In all cases Y-axis scaffolds exhibited a larger extension at yield (Figure 8.28) and failure (Figure 8.29), which corroborates the assertion that interlayer bonding is weaker under parallel compression loading, and are the areas where crack propagation is most likely to occur.

A range of heat treatment protocols were designed using TGA data as prerequisite information, since it detailed the burn out behaviour of PVOH. Ramp rate, number of heating stages and sintering temperature were found to determine the stability of sintered scaffolds (Table 8.9). Protocol HT8 resulted in the easiest to handle and most stable scaffolds, which was attributed to a reduction in the time between burn out of PVOH and consolidation of the remaining HA structure since a relatively fast ramp rate was used above 230°C. Some distortion, namely lateral expansion (X-axis samples) and variation in the size of pore channels (50F2Y and 50F6Y) were visually observed as a result of performing the HT8 sintering protocol. These observations are attributed to the solid base of scaffolds trapping evolving gases, which could have caused a build-up of pressure within the bottom of the structure. Partial collapse of constructs 50F2X and 50F6X along layer boundaries matched the typical failure mechanisms observed for X-axis green bodies (Figure 8.30).

FTIR analysis of structures sintered using HT8 revealed the presence of strong bands between 1900 and 2300cm^{-1} in all Y-axis samples, which are associated with low molecular weight alkynes that are known to be a thermal degradation product of PVOH. These results indicate incomplete removal of degradation products of PVOH, which are suggested to become trapped due to consolidation of the structure. Presence of surface pores would facilitate evolution of gaseous by-products and hence the influence of post-processing methods could be considered as detrimental to this process since they caused observed surface pores to shrink (Figure 8.24). Specifically, larger bulk shrinkage of the height of Y-axis samples compared with equivalent X-axis

scaffolds was demonstrated (Figures 8.34 and 8.35). In contrast, generally a comparable shrinkage of diameter, and weight reduction were observed between sintered X and Y-axis constructs. A larger degree of surface pore consolidation is a likely explanation as to why bands corresponding to thermal degradation products were revealed in FTIR spectra of sintered Y-axis samples (Table 8.10). It is unclear why the average weight loss (±1%), as a result of sintering, corresponded to losses demonstrated by TGA analysis of precursors but residue of PVOH degradation products were shown in FTIR spectra. Complete removal of PVOH degradation products by increasing the dwell time of structures at either 230 or 1300°C is plausible. However, since dwelling at 230°C was observed to reduce the stability of parts it would be preferable to soak at the higher temperature (Table 8.9).

These results advocate a trade-off between the effects of surface pore size on strength development, and the ability of thermal degradation products to evolve from the structure. In particular, the 3D interconnectivity of the inherent surface porosity would be crucial in facilitating gaseous removal, and since this property has not been characterised the degree of structural consolidation cannot be deemed as the only limitation. The greater relative uniformity of height and diameter shrinkage evidenced for X-axis scaffolds suggests these structures offer an improved 3D connectivity of the exhibited surface microporosity. CT scanning is recommended for future work to assess the degree of interconnectivity of micropores.

Overall, microstructural analysis of sintered scaffolds exposed a significant reduction in the height of pore channels, strut width, and surface pores compared with green scaffolds (Figure 8.36 – 8.38). Therefore, as expected, it can be concluded that sintering resulted in bulk and microstructural consolidation. The greater shrinkage demonstrated for Y-axis samples infers a higher mechanical strength of these sintered bodies compared with X-axis scaffolds since a greater degree of consolidation corresponds to a larger decrease in the volume of voids. However, as aforementioned this observation may also explain why PVOH degradation products were trapped within these samples, which could be detrimental to biocompatibility.

8.6 Conclusions

This chapter presents an assessment of the use of 3DP to manufacture bone tissue scaffolds from HA:PVOH precursors, and the experimental work completed highlights the potential, as well as the difficulties associated with this fabrication system. In summary, characterisation of precursor flowability strongly correlated with observed printability and can be deemed a vital prerequisite property since it influenced recoating of the build bed, which ultimately determined several critical physical criteria such as mechanical strength, microstructure, and porosity. Scaffolds produced from less flowable precursors (i.e. 60HA:40PVOH) were shown to be substantially weaker in compression and this was attributed to insufficient bonding between layers. Calculation of the Hausner ratio provided an indication of the influence of interparticle interactions on flowability, which helped explain the clumping behaviour observed in precursor powders with ≥60wt% HA.

Characterisation of green bodies provided valuable information that facilitated an understanding of the shrinkage behaviour observed as a result of sintering. Significant differences in microstructure were observed between green scaffolds printed along the X and Y-axes, which resulted in variation of mechanical strength, and influenced the effectiveness of the removal of degradation products of PVOH during sintering. Post-processing treatments were similarly shown to significantly impact mechanical properties, as well as the microstructure of green bodies. Compression tests highlighted that interlayer bonding was critical to bulk strength and when parts were loaded perpendicular to the direction of printing (i.e. parallel to the boundaries of interlayer bonding) catastrophic failure occurred.

A maximum average compressive strength of 0.85MPa was exhibited by 50wt% HA green parts printed along the Y-axis and dried for 6hrs in either a furnace or vacuum oven (50F6Y, 50V6Y), which falls within the range reported for cancellous bone (Table 2.2). In contrast, a maximum compressive strength of 0.75MPa was demonstrated for green parts printed along the X-axis (50F6X). In comparison to green parts, sintered scaffolds were less easy to handle and stability was more variable, thus their mechanical suitability for use as a bone tissue scaffold is questionable. Therefore, it is recommended that further work involve the investigation of composites of HA and biocompatible, as well as biodegradable polymers so that a

sintering protocol would not need to be employed. This would remove a number of the most prominent difficulties highlighted in this study, namely design of a heat treatment protocol that results in uniform shrinkage, and does not adversely affect chemical composition or mechanical integrity.

Microporosity as well as topographic surface features are known to be key determinants of the success of bone tissue implants [88, 108, 109]. Micrographs of typical green and sintered scaffolds revealed irregularities in the surface topography as well as the presence of surface microporosity, which is promising since these properties are known to be advantageous for osteoblast adhesion, capillary in growth (i.e. osteoconduction), and mechanical interlocking with native tissue (i.e. osteointegration). The size of pore channels in green as well as sintered scaffolds would be expected to expedite vascularisation of the scaffold, which has been shown to result in direct osteogenesis [87]. Since the observed sizes of pore channels were at the upper end of the recommended pore size it is proposed that the CAD model could be adapted to reduce this dimension, which is likely to improve mechanical strength. However, without reducing the size of precursor particles the accuracy of smaller parts is expected to be poorer since the resolution of the technique is limited by the maximum particle size of stock materials.

In conclusion, the scaffolds produced exhibited macro- and micropores within the reported optimum range for bone tissue scaffolds. The demonstrated rough surface topography is a promising inherent advantage of 3D printed parts, and the mechanical integrity of green constructs were shown to fall within the range of cancellous bone. These features are promising since they can improve osteogenesis, osteoconduction, and osteointegration in-vivo [20, 84, 92, 93, 108, 109]. To improve mechanical performance a reduction in the pore channel dimension is suggested. A number of underlying precursor characteristics were found to determine the above properties and therefore it is advocated that powder characterisations, such as those presented here, should be considered an essential part of the process of selecting stock materials.

Chapter 9

Conclusions

9. Conclusions

Despite being the current clinical ‘gold standard’ autologous bone grafts exhibit numerous short comings, including the need for two surgical procedures, pain associated with bone harvesting, limited supply and the risk of surgical complications. There is subsequently a need for alternative clinical strategies to repair or regenerate defective bone tissue. One such strategy is to implant a synthetic porous structure referred to as a scaffold. In order to elicit a favourable biological outcome ideally these constructs should emulate the chemical and physical structure of the native tissue. The strategy adopted in this work in order to achieve this was to consider the effect of synthesis methods and conditions on material properties and the translational of this understanding to the biological performance of the selected biomaterial. Fabrication and structural properties of the scaffold structure were also investigated.

Objectives for this project are listed in Chapter 1 and relevant literature was reviewed in Chapter 2. HA was selected as the candidate material due to the chemical and crystallographic similarity to bone mineral apatite. Chapters 3 – 6 present the experimental work performed with the aim of developing an understanding of how key reaction parameters affect material composition and ultimately biological suitability of HA. Results presented in Chapters 4 – 6 highlighted the sensitivity of the AP technique and demonstrated that changes to experimental conditions cannot be deemed trivial. In particular, pH and temperature conditions are vital reaction parameters that should be carefully considered since they were shown influence composition to a degree that determined the viability of MC3T3 cells. Promising improvements in the proliferative rate of osteoblast precursor cells were seen when CDHA was prepared in mixed solvent systems containing Toluene and/or Ethanolamine, and when theoretical substitutions of 10mol% Mg or 2mol% Zn were incorporated.

These results were followed by studies concerning the viability of fabricating a scaffold structure that exhibited key physical features of cancellous bone, such as compressive strength, porosity, and pore interconnectivity (Chapters 7 and 8). The feasibility of 3DP user defined porous, interconnected scaffold structures was investigated. Scaffolds were shown to exhibit desirable surface topographies,

microporosity, and an ultimate compressive strength at the lower end of the range reported for cancellous bone.

It is difficult to recommend an 'optimised' synthesis condition to use in combination with the reported 3DP fabrication method since without conducting further experimental work it is unclear whether combining promising conditions, for example Mg or Zn substitution and the use of Toluene in the solvent system, would further improve biological performance. Overall, compositions that were shown to enhance the proliferative rates of osteoblast precursor cells compared to the control (AP09) can be considered 'optimised' formulations that shall be the subject of future work. This chapter summarises the conclusions that can be drawn from the presented experimental findings.

9.1 Synthesis of HA

Of the three synthesis methods initially selected and experimentally investigated, AP was concluded to be the technique that enabled the production of materials that most closely met the defined product criteria: (1) phase pure HA, (2) particle size less than 1μm, (3) degree of control of crystallinity, and (4) ability to alter stoichiometry (Table 3.5). Hence this synthesis technique was taken forward for further study (Chapters 4 – 6).

9.1.1 Influence of pH, temperature and solute concentration

It is well known that pH conditions determine the CaP phase precipitated from a solution and this can be explained in terms of the varying solubility of this group of materials according to pH values (Figure 2.7). Hence, the formation of precipitates containing DCPA and DCPD under less alkali conditions (pH <10) merely confirms what is already reported in the literature. Similar to previous authors [12, 15, 165, 205-208], precipitates that exhibited XRD patterns which were matched to HA and no secondary phases were produced at a starting pH value greater than 10. However, concurrent FTIR analysis exposed the presence of non-apatitic HPO_4^{2-} and notably vibrational bands associated with DCPD were demonstrated for precipitates prepared in a solution initially adjusted to pH 10 and uncontrolled during crystallisation (AP07). This suggests that precipitates were not stoichiometric HA but instead CDHA.

Interestingly, as-synthesised samples that exhibited no discernible difference in XRD patterns could be distinguished by their thermal behaviour, which was determined by simultaneous DTA-TGA. Compositions prepared at an initial pH value of 10 and either uncontrolled (AP07) or controlled (AP10) during addition, exhibited a rapid endothermic loss of weight between 200 – 300°C. This behaviour was attributed respectively to the: (1) dehydration of DCPD to DCPA and subsequent condensation to β-$Ca_2P_2O_7$, and (2) weight loss of CDHA prepared via the hydrolysis of DCPA. An increase in reaction temperature also had a marked effect on composition which was again reflected in the observed weight loss behaviour. Samples prepared at a higher temperature (AP12) or at an uncontrolled pH value of 10 (AP07) notably did not exhibit a DTG peak between 700 and 800°C, which was demonstrated for all other samples. Additionally, a positive ZP was recorded for these compositions, which was shown to be inconsistent with other specimens that exhibited a negative surface charge, i.e. a deficiency of cations (CDHA).

A live/dead assay was used to assess the cytocompatibility of CDHA substrates. MC3T3 cells seeded on AP07 and AP12 were revealed to be non-viable after 1 and 3 days of culture, respectively. This was attributed to the excess acidity confirmed within these compositions by ZP measurements. In contrast, cells seeded onto all other substrates were observed to increase in number and change morphology from rounded to elongated, which is indicative of attachment, spreading and proliferation. A quantitative assessment of the ability of cytocompatible CDHA materials to support osteoblast proliferation was achieved by conducting MTT and Hoechst assays. Proliferative rates between 1 and 7 days were calculated and ANOVA tests were used to determine if the observed increase in cell number was statistically significant. Overall, the results of these cellular in-vitro tests advocate that the absolute value of pH and temperature strongly determine the viability of osteoblast precursor cells since these reaction parameters significantly affected material composition. Control of pH during synthesis was shown to be advantageous to cell proliferation and this is explained in terms of the ion speciation boundaries in solution (Figure 2.10).

Preparation of the respective phases under different pH conditions was not shown to influence the affinity of particles for cells. However, differences in the intracellular agglomeration behaviour of AP07 – AP10 were established and this was attributed to variation in the sign and value of surface charge. An elongated morphology was

observed for MC3T3 cells that internalised AP09 and AP10 particles. These results advocate that consideration of reaction conditions is important not only for the specific objectives of this thesis but also other applications, such as drug delivery.

9.1.2 Influence of solvent system

IR spectra and corresponding thermal analysis confirmed the presence of non-apatitic HPO_4^{2-} within precipitates prepared in mixed solvents systems containing Ethanolamine and/or Toluene with DI water suggesting AP13 – AP15 were CDHA. Despite this, XRD patterns of as-synthesised specimens were matched to HA alone. The degrees of peak broadening for materials prepared in systems containing Toluene were distinguishably broader. This is explained by the lower dielectric constant of Toluene resulting in a faster stabilisation of crystallites.

The solvent system was not shown to influence the sign of particle ZP measured in DI water at 25°C. However, the degree of negativity (i.e. the value of ZP) decreased for those samples precipitated in mixed solvent systems (AP13 – AP15). This indicates a reduction in colloidal stability and is believed to be due to a lower degree of deprotonation in less polar solvents systems. Lower repulsive charges could lead to particle flocculation, which might be detrimental in spreading of stock materials in the 3DP process. Therefore, it may be necessary to investigate the influence of particle surface charge on flowability as part of future work.

It was particularly important to test the viability of cells seeded on substrates prepared in Ethanolamine and/or Toluene since residues of these solvents would be cytotoxic. Live/dead assay results were encouraging and confirmed the viability of cells seeded on samples AP13 – AP15, which justifies selecting Ethanolamine due to its high volatility. In addition, cell number, measured by metabolic activity as well as DNA staining, was shown to significantly increase over a 7 day culture period. Cell results were promising in that, the proliferative rate of metabolically active osteoblasts seeded on CDHA substrates prepared in a mixed DI water and Toluene system (AP14) was more than double the control sample (AP09) that was prepared in pure DI water. This improved performance was linked to the 20% larger surface area exhibited by particles of AP14. In contrast, a greater increase in cell number measured by DNA staining was demonstrated on substrates prepared in a mixed DI water, Toluene and Ethanolamine solvent system (AP15). When these results were compared to corresponding

assessments (Chapter 4) it is suggested that a higher HPO_4^{2-} content, which is likely to result in a faster rate of dissolution due to the reduction in stoichiometry, is responsible for the observed relative increase in cell number.

In summary, Chapter 5 presents a novel experimental assessment of the influence of solvent polarity on the material properties of CDHA. The in-vitro tests performed exposed promising capabilities of substrates prepared in mixed solvent systems to support proliferation of osteoblast precursor cells to a higher degree than control samples. It is concluded that the solvent polarity should be carefully considered and potentially chosen according to the end application. It is recognised that further characterisations are necessary to improve the understanding of the underlying scientific reasons for the observed results, in particular surface roughness and dissolution.

9.1.3 Influence of divalent cations

XRF was used to confirm the presence as well as accuracy of Sr, Mg, or Zn substitutions and revealed a significantly greater accuracy of Sr (93%) doping compared with Mg (10.3%) and Zn (12%). This is attributed to the relative ionic sizes of Sr^{2+}, Mg^{2+} and Zn^{2+}, which are known to be 116, 75 and 65% the size of Ca^{2+}. Notably, XRF does not enabled differentiation of surface absorbed or lattice incorporation of ions; however the shifts observed for characteristic XRD peaks of HA are convincing evidence that additional cations were at least partially incorporated into the apatite structure. Calculation of Ca+Mx:P ratios revealed that AP16 – AP18 were not stoichiometric HA but exhibited ratios typical of CDHA, which is consistent with FTIR and DTA-TGA studies that demonstrated the presence of HPO_4^{2-}.

Remarkably, an 80% increase in the number of metabolically active cells observed between 1 and 7 days of culture was demonstrated on AP17 compared with the control CDHA specimen (AP07). This sample was shown to contain Mg as confirmed by XRF, thermally degraded to whitlockite below 600°C and exhibited a 45% smaller crystallite size. These chemical and physical variations due to the addition of Mg have been previously reported in the literature [129, 319]. Incorporation of Zn (AP18) was shown to facilitate a 40% higher degree of osteoblast proliferation. In addition to compositional variations evidenced by XRD, FTIR and DTA-TGA, a relatively low crystallinity and larger surface area were used to explain the improved proliferative

rate of MC3T3 cells seeded on samples that contained Mg (AP17) and Zn (AP18). Interestingly, the surface morphology of pellets immersed in SBF that contained additional divalent cations were indicative of a higher degree of surface degradation compared with other self-prepared CDHA. Hence, it was concluded that an assessment of dissolution rate should be included in future work.

9.1.4 Summary of HA synthesis work

Much research has been conducted in the area of synthesising CaPs, including HA. However, relatively few authors have combined the knowledge of material properties and biological performance of precursors [18]. It is more common to assess only the in-vitro or in-vivo performance of the entire scaffold structure. The overriding objective of Chapters 4 – 6 was to investigate a number of reaction parameters that have previously been reported (pH, temperature, solute concentration, divalent cation substitutions), as well as novel factors (Toluene and Ethanolamine), to influence material characteristics known to play a part in the response of bone cells. A number of in-vitro tests were used to determine any variations in the in-vitro performance of these various substrates. A range of characterisation techniques were performed and concurrent analysis contributed to the established knowledge regarding the effects of these reaction parameters. In particular, compositional and physical variations revealed by DTA-TGA, FTIR, ZP, and surface area measurements helped to shed light on the observed differences in biological performance.

Use of the live/dead assay is justified since results enabled a distinction to be made between cytotoxic and cytocompatible samples. Particularly, this assay pulled out the non-viability of MC3T3 cells on AP12, which was not achieved by the combination of the reported MTT assay and standard ANOVA testing. It is also important to consider the suitability of the MTT and Hoechst assays. Advantages of the MTT assay can be summarised as: precision, relatively fast processing time (since no washing steps are used), and the ability to quantitatively measure proliferation [291]. In comparison, Hoechst dyes, such as H33258 have been noted for their superior sensitivity and specificity for DNA. Furthermore, freezing of cultures enabled experiments to be analysed in a single batch thus reducing processing time. It is also suggested this helps to improve intra- and inter-experimental standardisation [326]. These assays are reported to be a more accurate estimation of cell number than, for example counting cells that include/exclude an appropriate dye or ALP estimation [327]. The advantages

listed above are considered justification of the selection and use of MTT and Hoechst assays to determine cell proliferation.

It is also possible to draw an overall conclusion regarding the applicability of the modified ANOVA test. This method was used and compared with *F* ratios calculated using the standard ANOVA test that is widely used in the literature to determine if the observed increase in cell number within data sets is statistical significant. The reported modified ANOVA test was formulated since lag cell growth, generally up to day 3 or 5, was observed for MTT and Hoechst assay results. Hence it was suggested that striping back the lag rate would help to differentiate between substrates that demonstrated different exponential growth phases. This assertion was confirmed since a number of substrates that exhibited relatively low proliferative rates were pulled out as non-significant using the modified ANOVA test. MC3T3 cells were shown to be non-viable on AP12 after day 3 using the live/dead assay however interestingly the standardised ANOVA test confirmed the increase in metabolically cells over the 7 day period as statistically significant. In contrast, the modified test identified this sample as non-significant since the *F* ratio calculated considered the full data set and hence crucial information was not lost. In addition, different proliferation trends were observed for some samples (e.g. AP13, AP17) and in these cases consideration of the full data set enabled such samples to be statistically distinguished. Overall, the ability to distinguish a number of samples using the modified ANOVA method was a useful tool for this project. Simultaneous application of both statistical tests highlights the importance of selecting a suitable statistical test to answer a specific experimental question. Knowledge of statistics is an important prerequisite to achieve this and ensure that the data is analysed as accurately as possible by setting appropriate hypotheses.

9.2 3DP of HA scaffolds for applications in bone tissue engineering

A number of inherent advantages of 3D printed scaffolds intended for use in the repair or replacement of bone were highlighted in the reviewed literature, for example surface roughness. The initial experimental study (Chapter 7) performed confirmed that these desirable characteristics could feasibly be fabricated from combinations of

as-received HA and ball milled PVOH. Specifically, precursors with a maximum HA content of 80wt% were primarily deemed as printable. However, a more detailed assessment revealed that scaffolds fabricated from 80HA:20PVOH and 70HA:30PVOH exhibited insufficient interlayer bonding, which caused inadequate part stability and ultimately structural failure.

A number of precursor characteristics were measured directly and indirectly in an effort to understand the structural differences between scaffolds printed from different HA:PVOH compositions. In particular, the ability of powders to flow was deemed critical since it determines the ability to recoat the build bed, which was shown to ultimately influence the resolution and mechanical strength of printed parts. Flowability was directly measured using two funnel tests: (1) flow time, and (2) angle of repose. These results were shown to correlate with observed printability. A higher fraction of smaller HA particles, established by particle size analysis, was shown to result in clumping of precursors that contained ≥60wt% HA. This behaviour reduced spreadability and caused disruptions in the topography of the build bed.

De-powdering of 3D printed constructs has been identified as a difficulty associated with this fabrication method [262]. Ultrasound and compressed air were investigated as methods to de-powder loose material from the surface and pore channels of printed scaffolds. Attachment of a syringe needle to the nozzle of a commercial airbrush system enabled a fine and controlled stream of air to be blown, which was shown to unclog pores and remove loose surface powder in a time efficient manner without damaging parts.

Post-processing of green scaffolds by drying in a furnace or vacuum oven for 2 or 6hrs was evidenced to result in bulk and microstructural shrinkage. These affects were shown to be more consistent when a vacuum oven was used. Since weight loss was also recorded, it was suggested that partial degradation of PVOH simultaneously occurred as a result of post-processing.

The mechanical strength of green scaffolds was tested under compressive loading and these results revealed a higher yield and ultimate compressive strength for 50wt% HA parts compared with those prepared from 60HA:40PVOH. This was explained in terms of the higher flowability and lower interparticulate interactions demonstrated for the 50HA:50PVOH precursor powder. Micrographs of green scaffolds revealed the

presence of micron sized surface pores, which were shown to consolidate as a result of drying. The rate of shrinkage of such voids was shown to infer the development rate, and ultimate strength of interlayer bonding. When parts were loaded parallel to the direction of layers crack propagation was shown to occur along these boundaries and led to catastrophic failure. Improvement in the ultimate strength and degree of strain exhibited for Y-axis scaffolds was attributed to the perpendicular application of compressive loading. Anisotropic behaviour of 3D printed parts is commonly reported in the literature [325].

An understanding of the burn out and high temperature behaviour of PVOH and HA precursors, respectively was useful in designing heat treatment protocols to sinter scaffolds as characterised by DTA-TGA. Residue of PVOH thermal degradation products were revealed in sintered Y-axis scaffolds and this was linked to the higher degree of bulk shrinkage, and consolidation of surface pores, which are suggested to facilitate evolution of gaseous by-products. Thus, it is concluded that there is a trade-off between the effect of surface pore size on strength and the ability to facilitate evolution of PVOH degradation products.

In summary, flowability of precursor materials was verified to be a critical prerequisite property to ensure mechanical stability, and was also shown to influence microstructure, as well as porosity. The difference in the mechanical strength as well as failure mechanisms of X and Y-axis printed scaffolds demonstrated that it is important to consider the direction of loading since interlayer bonding was shown to be weaker under parallel compressive forces. The maximum strength of X-axis green scaffolds was measured to be approximately 0.75MPa (50F6X) and for Y-axis samples dried for 6hrs in either a furnace or vacuum oven an ultimate compressive strength of 0.85MPa was exhibited, which falls within the range reported for cancellous bone. These results are considered promising and it is expected that the improvements proposed in Chapter 10 will assist in further optimisation. The key physical features exhibited by these 3D printed scaffolds, namely porosity, interconnected macropores, as well as surface microporosity and roughness, are expected to be favourable for osteogenesis, osteoconduction, and osteointegration of the structures in-vivo.

Chapter 10

Future work

10. Future work

The experimental work performed achieved the first four initial project objectives outlined in Chapter 1. However, it is difficult to conclude a single 'optimised' synthesis condition without conducting further experimental work due to the complexity of the crystallisation process. Enhanced biological performances were highlighted, in particular, for samples prepared in mixed DI water, Toluene and/or Ethanolamine systems, as well as substituted with Mg and Zn. Future work is suggested to include optimisation of the value of these conditions (i.e. the level of substitution and solvent system ratio) and an investigation of the effects of combining these two reaction parameters on material properties and ultimately the biological performance of substrates using the techniques reported in this thesis.

The development of osteoprecursor cells seeded on a biomaterial substrate is characterised by a sequence of events: (1) cell adhesion and spreading, (2) cell proliferation, (3) ECM biosynthesis, (4) ECM development and maturation, as well as (5) ECM mineralisation [328]. Since adhesion and spreading is considered a critical stage that influences the capacity of cells to proliferate and differentiate, visualisation of this process could provide complementary information to the results presented in this thesis [18, 329]. Additionally, analysis of the dissolution rate of substrates and characterisation of surface area, as well as roughness are proposed since these material characteristics are known to play a key role in mineralisation and cellular attachment, respectively. A combination of these additional material characterisations and SEM and/or confocal imaging of osteoblasts on substrates will assist in furthering the understanding gained from MTT and Hoechst assay results presented here.

This study highlighted the potential of 3DP to enable the fabrication of porous scaffold structures from HA:PVOH precursor materials. Structures were shown to exhibit advantageous properties, including surface microporosity, roughness, and the compressive strength of a number of green parts were demonstrated to fall within the reported range of cancellous bone. Complete removal of thermal degradation products of PVOH and the reduced ease of handling of sintered structures were notable difficulties associated with this system. Replacement of PVOH with a biocompatible polymer, such as PGA, PLA or PLGA, which does not need to be burnt out from the

structure, is thus recommended as a more suitable precursor system. Regardless, of the material system it is suggested that future work should include an assessment of the 3D interconnectivity of any microporosity since this property is a key determinant of the suitability of the scaffold for application in bone tissue engineering [103, 104]. Micro-CT analysis is an extremely valuable tool with analytical techniques that would enable an assessment of 3D interconnectivity as well as total porosity. Therefore characterisation of scaffolds using this technique is recommended and may shed light on any differences in the 3D microstructure of X and Y-axis scaffolds. It is also advised that the initial CAD model could be tailored, specifically the size of pore channels, to improve the mechanical strength of scaffolds.

In addition, further work is to be focused on translating the knowledge gained concerning synthesis of HA to 3DP of scaffold structures physically suitable for application in bone tissue engineering. It is likely that there will be constraints to this process since this project has highlighted a number of specific material properties that determine biological performance and several powder characteristics were shown to influence the physical attributes of the end product. It therefore may be sensible to select a range of 'optimised' synthesis conditions, produce bulk quantities, and characterise properties of these powders that were concluded to be critical to the success of 3DP, for example flowability, particle size distribution, as well as bulk and tapped density. These additional characterisations may enable selection of an 'optimal' synthesis condition that not only exhibits an enhanced biological performance but is also suitable for 3DP.

Surface charge is suggested to be an additional factor that could be influential in determining powder flowability. Powders that exhibit a lower surface charge are more likely to clump during spreading since repulsive forces determine colloidal stability. Characterisation of ZP in DI water, and more specifically a suspension of the binder solution at the temperature maintained during printing, is strongly recommended for printable powder compositions. In order to determine the surface chemistry of dried powders characterisation by XPS is also proposed.

References

[1] A. S. Posner, "Crystal chemistry of bone mineral," *Physiol Rev,* vol. 49, pp. 760-792, Oct 1969.
[2] S. Cazalbou, C. Combes, D. Eichert, *et al.*, "Adaptative physico-chemistry of bio-related calcium phosphates," *J Mater Chem,* vol. 14, pp. 2148-2153, 2004.
[3] W. Suchanek and M. Yoshimura, "Processing and properties of hydroxyapatite-based biomaterials for use as hard tissue replacement implants," *J Mater Res,* vol. 13, pp. 94-117, Jan 1998.
[4] C. J. Damien and J. R. Parsons, "Bone-Graft and Bone-Graft Substitutes - a Review of Current Technology and Applications," *J Appl Biomater,* vol. 2, pp. 187-208, Fal 1991.
[5] B. Cengiz, Y. Gokce, N. Yildiz, *et al.*, "Synthesis and characterization of hydroxyapatite nanoparticles," *Colloid Surface A,* vol. 322, pp. 29-33, Jun 5 2008.
[6] R. Murugan and S. Ramakrishna, "Aqueous mediated synthesis of bioresorbable nanocrystalline hydroxyapatite," *J Cryst Growth,* vol. 274, pp. 209-213, Jan 15 2005.
[7] A. E. Porter, N. Patel, J. N. Skepper, *et al.*, "Comparison of in vivo dissolution processes in hydroxyapatite and silicon-substituted hydroxyapatite bioceramics," *Biomaterials,* vol. 24, pp. 4609-4620, Nov 2003.
[8] T. J. Webster, R. W. Siegel, and R. Bizios, "Osteoblast adhesion on nanophase ceramics," *Biomaterials,* vol. 20, pp. 1221-1227, Jul 1999.
[9] T. J. Webster, C. Ergun, R. H. Doremus, *et al.*, "Enhanced osteoclast-like cell functions on nanophase ceramics," *Biomaterials,* vol. 22, pp. 1327-1333, Jun 2001.
[10] T. Leventouri, "Synthetic and biological hydroxyapatites: Crystal structure questions," *Biomaterials,* vol. 27, pp. 3339-3342, Jun 2006.
[11] E. Boanini, M. Gazzano, and A. Bigi, "Ionic substitutions in calcium phosphates synthesized at low temperature," *Acta Biomater,* vol. 6, pp. 1882-1894, Jun 2010.
[12] A. Afshar, M. Ghorbani, N. Ehsani, *et al.*, "Some important factors in the wet precipitation process of hydroxyapatite," *Mater Design,* vol. 24, pp. 197-202, May 2003.
[13] S. Bose and S. K. Saha, "Synthesis and characterization of hydroxyapatite nanopowders by emulsion technique," *Chem Mater,* vol. 15, pp. 4464-4469, 2003.
[14] E. Landi, G. Logroscino, L. Proietti, *et al.*, "Biomimetic Mg-substituted hydroxyapatite: from synthesis to in vivo behaviour," *J Mater Sci-Mater M,* vol. 19, pp. 239-247, Jan 2008.
[15] S. Raynaud, E. Champion, D. Bernache-Assollant, *et al.*, "Calcium phosphate apatites with variable Ca/P atomic ratio I. Synthesis, characterisation and thermal stability of powders," *Biomaterials,* vol. 23, pp. 1065-1072, Feb 2002.
[16] D. Tadic, F. Peters, and M. Epple, "Continuous synthesis of amorphous carbonated apatites," *Biomaterials,* vol. 23, pp. 2553-2559, Jun 2002.
[17] J. C. Elliott, *Structure and chemistry of the apatites and other calcium orthophosphates* vol. 4: Elsevier Amsterdam, 1994.
[18] W. Xue, J. L. Moore, H. L. Hosick, *et al.*, "Osteoprecursor cell response to strontium-containing hydroxyapatite ceramics," *J Biomed Mater Res A,* vol. 79, pp. 804-814, 2006.

[19] A. J. Salgado, O. P. Coutinho, and R. L. Reis, "Bone tissue engineering: State of the art and future trends," *Macromol Biosci,* vol. 4, pp. 743-765, Aug 9 2004.
[20] S. F. Yang, K. F. Leong, Z. H. Du, *et al.*, "The design of scaffolds for use in tissue engineering. Part 1. Traditional factors," *Tissue Eng,* vol. 7, pp. 679-689, Dec 2001.
[21] S. F. Yang, K. F. Leong, Z. H. Du, *et al.*, "The design of scaffolds for use in tissue engineering. Part II. Rapid prototyping techniques," *Tissue Eng,* vol. 8, pp. 1-11, Feb 2002.
[22] A. Macchetta, I. G. Turner, and C. R. Bowen, "Fabrication of HA/TCP scaffolds with a graded and porous structure using a camphene-based freeze-casting method," *Acta Biomater,* vol. 5, pp. 1319-1327, May 2009.
[23] D. W. Hutmacher, "Scaffolds in tissue engineering bone and cartilage," *Biomaterials,* vol. 21, pp. 2529-2543, Dec 2000.
[24] A. Chamay and P. Tschantz, "Mechanical Influences in Bone Remodeling - Experimental Research on Wolffs Law," *J Biomech,* vol. 5, pp. 173-&, 1972.
[25] L. D. You, J. H. Chen, C. Liu, *et al.*, "Boning up on Wolff's Law: Mechanical regulation of the cells that make and maintain bone," *J Biomech,* vol. 43, pp. 108-118, Jan 5 2010.
[26] R. O. Ritchie, J. W. Ager, and G. Balooch, "Fracture, aging, and disease in bone," *J Mater Res,* vol. 21, pp. 1878-1892, Aug 2006.
[27] J. P. Schmitz and J. O. Hollinger, "The Critical Size Defect as an Experimental-Model for Craniomandibulofacial Nonunions," *Clin Orthop Relat R,* pp. 299-308, Apr 1986.
[28] Healio. (Accessed 01/2012). Available: http://www.healio.com/orthopedics/trauma/news/online/%7B476C068B-5283-4E71-9DD5-CC851E809E3F%7D/Study-questions-definition-of-critical-sized-bone-defect
[29] M. S. Chapekar, "Tissue engineering: Challenges and opportunities," *J Biomed Mater Res,* vol. 53, pp. 617-620, Dec 5 2000.
[30] A. S. Greenwald, S. D. Boden, V. M. Goldberg, *et al.*, "Bone-graft substitutes: Facts, fictions, and applications," *J Bone Joint Surg Am,* vol. 83A, pp. 98-103, 2001.
[31] NHS. (Accessed 01/2012). Available: http://www.hesonline.nhs.uk/Ease/servlet/ContentServer?siteID=1937&categoryID=1243
[32] L. Kalichman, Z. Cohen, E. Kobyliansky, *et al.*, "Interrelationship between bone aging traits and basic anthropometric characteristics," *Am J Hum Biol,* vol. 14, pp. 380-390, May-Jun 2002.
[33] G. Livshits, D. Karasik, I. Otremski, *et al.*, "Genes play an important role in bone aging," *Am J Hum Biol,* vol. 10, pp. 421-438, 1998.
[34] G. M. Kiebzak, "Age-Related Bone Changes," *Exp Gerontol,* vol. 26, pp. 171-187, 1991.
[35] R. B. Mazess, "On Aging Bone Loss," *Clin Orthop Relat R,* pp. 239-252, 1982.
[36] J. E. South-Paul, "Osteoporosis: Part I. Evaluation and assessment," *Am Fam Physician,* vol. 63, pp. 897-904, Mar 1 2001.
[37] F. S. Kaplan, "Osteoporosis," *Women Health,* vol. 10, pp. 95-114, 1985.
[38] R. C. Lawrence, C. G. Helmick, F. C. Arnett, *et al.*, "Estimates of the prevalence of arthritis and selected musculoskeletal disorders in the United States," *Arthritis Rheum-Us,* vol. 41, pp. 778-799, May 1998.
[39] NHS, Accessed 01/2012.
[40] J. A. Kanis, L. J. Melton, C. Christiansen, *et al.*, "Perspective - the Diagnosis of Osteoporosis," *J Bone Miner Res,* vol. 9, pp. 1137-1141, Aug 1994.

[41] R. Altman, E. Asch, D. Bloch, *et al.*, "Development of Criteria for the Classification and Reporting of Osteoarthritis - Classification of Osteoarthritis of the Knee," *Arthritis Rheum-Us,* vol. 29, pp. 1039-1049, Aug 1986.
[42] J. Y. Rho, L. Kuhn-Spearing, and P. Zioupos, "Mechanical properties and the hierarchical structure of bone," *Med Eng Phys,* vol. 20, pp. 92-102, Mar 1998.
[43] L. J. Gibson, "The mechanical behaviour of cancellous bone," *J Biomech,* vol. 18, pp. 317-328, 1985.
[44] D. Carter and W. Hayes, "Fatigue life of compact bone—I effects of stress amplitude, temperature and density," *J Biomech,* vol. 9, pp. 27-34, 1976.
[45] (Accessed 01/2013). *Bone Structure*. Available: http://www.3bscientific.co.uk/Bone-Structure-Chart-V2050U,p_1207_16_61_2128.html
[46] X. D. Wang and Q. W. Ni, "Determination of cortical bone porosity and pore size distribution using a low field pulsed NMR approach," *J Orthop Res,* vol. 21, pp. 312-319, Mar 2003.
[47] G. Marotti, Lees, and Reeve, "A New Theory of Bone Lamellation," *Calcified Tissue Int,* vol. 53, pp. S47-S56, 1993.
[48] J. B. Park and J. D. Bronzino, *Biomaterials: principles and applications*: CRC, 2002.
[49] (Accessed 01/2013). Available: http://www.daviddarling.info/encyclopedia/B/bone.html
[50] G. a. G. Tortora, J, *Principles of anatomy and physiology*: John Wiley.
[51] K. A. Hing, "Bone repair in the twenty-first century: biology, chemistry or engineering?," *Philos T Roy Soc A,* vol. 362, pp. 2821-2850, Dec 15 2004.
[52] R. A. Robinson and M. L. Watson, "Collagen-crystal relationships in bone as seen in the electron microscope," *Anat Rec,* vol. 114, pp. 383-409, Nov 1952.
[53] S. Weiner and W. Traub, "Bone-Structure - from Angstroms to Microns," *Faseb J,* vol. 6, pp. 879-885, Feb 1 1992.
[54] L. J. Zhang and T. J. Webster, "Nanotechnology and nanomaterials: Promises for improved tissue regeneration," *Nano Today,* vol. 4, pp. 66-80, Feb 2009.
[55] J. L. Niu, "Hydrothermal synthesis of nano-crystalline hydroxyapatite," *Bioceramics, Vol 19, Pts 1 and 2,* vol. 330-332, pp. 247-250, 2007.
[56] S. Weiner and H. D. Wagner, "The material bone: Structure mechanical function relations," *Annu Rev Mater Sci,* vol. 28, pp. 271-298, 1998.
[57] S. V. Dorozhkin and M. Epple, "Biological and medical significance of calcium phosphates," *Angew Chem Int Edit,* vol. 41, pp. 3130-3146, 2002.
[58] D. Eichert, M. Salomé, M. Banu, *et al.*, "Preliminary characterization of calcium chemical environment in apatitic and non-apatitic calcium phosphates of biological interest by X-ray absorption spectroscopy," *Spectrochimica Acta Part B: Atomic Spectroscopy,* vol. 60, pp. 850-858, 2005.
[59] N. Vandecandelaere, C. Rey, and C. Drouet, "Biomimetic apatite-based biomaterials: on the critical impact of synthesis and post-synthesis parameters," *Journal of Materials Science: Materials in Medicine,* vol. 23, pp. 2593-2606, 2012.
[60] A. Bigi, E. Boanini, and M. Gazzano, "Ionic substitutions in calcium phosphates synthesized at low temperature," *Acta Biomater,* vol. 6, pp. 1882-1894, Jun 2010.
[61] F. P. Ross, "Cytokine regulation of osteoclast formation and function," *J Musculoskelet Neuronal Interact,* vol. 3, pp. 282-286; discussion 292-284, Dec 2003.
[62] A. M. Parfitt, "Morphometry of Bone-Resorption - Introduction and Overview," *Bone,* vol. 14, pp. 435-441, May-Jun 1993.

[63] S. A. Goldstein, "The Mechanical-Properties of Trabecular Bone - Dependence on Anatomic Location and Function," *J Biomech,* vol. 20, pp. 1055-1061, 1987.
[64] J. Y. Rho, M. C. Hobatho, and R. B. Ashman, "Relations of Mechanical-Properties to Density and Ct Numbers in Human Bone," *Med Eng Phys,* vol. 17, pp. 347-355, Jul 1995.
[65] C. E. Oxnard, "The Mechanical Adaptations of Bones - Currey,J," *Nature,* vol. 315, pp. 521-521, 1985.
[66] K. Choi, J. L. Kuhn, M. J. Ciarelli, *et al.,* "The Elastic-Moduli of Human Subchondral, Trabecular, and Cortical Bone Tissue and the Size-Dependency of Cortical Bone Modulus," *J Biomech,* vol. 23, pp. 1103-1113, 1990.
[67] E. D. Arrington, W. J. Smith, H. G. Chambers, *et al.,* "Complications of iliac crest bone graft harvesting," *Clin Orthop Relat R,* pp. 300-309, Aug 1996.
[68] K. Kaveh, R. Ibrahim, M. Z. Abu Bakar, *et al.,* "Bone Grafting and Bone Graft Substitutes," *J Anim Vet Adv,* vol. 9, pp. 1055-1067, 2010.
[69] M. Bongio, J. J. J. P. van den Beucken, S. C. G. Leeuwenburgh, *et al.,* "Development of bone substitute materials: from 'biocompatible' to 'instructive'," *J Mater Chem,* vol. 20, pp. 8747-8759, 2010.
[70] A. H. Burstein, D. T. Reilly, and M. Martens, "Aging of Bone Tissue - Mechanical-Properties," *J Bone Joint Surg Am,* vol. 58, pp. 82-86, 1976.
[71] J. H. McElhaney, "Dynamic response of bone and muscle tissue," *J Appl Physiol,* vol. 21, pp. 1231-1236, Jul 1966.
[72] D. T. Reilly and A. H. Burstein, "The elastic and ultimate properties of compact bone tissue," *J Biomech,* vol. 8, pp. 393-405, 1975.
[73] A. Rohlmann, H. Zilch, G. Bergmann, *et al.,* "Material Properties of Femoral Cancellous Bone in Axial Loading .1. Time Independent Properties," *Arch Orthop Traum Su,* vol. 97, pp. 95-102, 1980.
[74] R. Vincentelli and M. Grigorov, "The Effect of Haversian Remodeling on the Tensile Properties of Human Cortical Bone," *J Biomech,* vol. 18, pp. 201-&, 1985.
[75] D. L. Kopperdahl and T. M. Keaveny, "Yield strain behavior of trabecular bone," *J Biomech,* vol. 31, pp. 601-608, Jul 1998.
[76] T. L. Norman, S. V. Nivargikar, and D. B. Burr, "Resistance to crack growth in human cortical bone is greater in shear than in tension," *J Biomech,* vol. 29, pp. 1023-1031, Aug 1996.
[77] P. Zioupos and J. D. Currey, "Changes in the stiffness, strength, and toughness of human cortical bone with age," *Bone,* vol. 22, pp. 57-66, Jan 1998.
[78] T. L. Norman, D. Vashishth, and D. B. Burr, "Fracture-Toughness of Human Bone under Tension," *J Biomech,* vol. 28, pp. 309-320, Mar 1995.
[79] R. O. Ritchie, R. K. Nalla, J. J. Kruzic, *et al.,* "Effect of aging on the toughness of human cortical bone: evaluation by R-curves," *Bone,* vol. 35, pp. 1240-1246, Dec 2004.
[80] T. J. Cypher and J. P. Grossman, "Biological principles of bone graft healing," *J Foot Ankle Surg,* vol. 35, pp. 413-417, Sep-Oct 1996.
[81] H. S. Sandhu, H. S. Grewal, and H. Parvataneni, "Bone grafting for spinal fusion," *Orthop Clin N Am,* vol. 30, pp. 685-+, Oct 1999.
[82] J. D. Sipe, "Tissue engineering and reparative medicine," *Reparative Medicine: Growing Tissues and Organs,* vol. 961, pp. 1-9, 2002.
[83] F. R. A. J. Rose and R. O. C. Oreffo, "Bone tissue engineering: Hope vs hype," *Biochem Bioph Res Co,* vol. 292, pp. 1-7, Mar 22 2002.
[84] K. J. L. Burg, S. Porter, and J. F. Kellam, "Biomaterial developments for bone tissue engineering," *Biomaterials,* vol. 21, pp. 2347-2359, Dec 2000.

[85] P. Kessler, M. Thorwarth, A. Bloch-Birkholz, *et al.*, "Harvesting of bone from the iliac crest - comparison of the anterior and posterior sites," *Brit J Oral Max Surg,* vol. 43, pp. 51-56, Feb 2005.
[86] R. Z. Legeros, S. Lin, R. Rohanizadeh, *et al.*, "Biphasic calcium phosphate bioceramics: preparation, properties and applications," *J Mater Sci-Mater M,* vol. 14, pp. 201-209, Mar 2003.
[87] Y. Kuboki, H. Takita, D. Kobayashi, *et al.*, "BMP-induced osteogenesis on the surface of hydroxyapatite with geometrically feasible and nonfeasible structures: Topology of osteogenesis," *J Biomed Mater Res,* vol. 39, pp. 190-199, Feb 1998.
[88] J. R. Woodard, A. J. Hilldore, S. K. Lan, *et al.*, "The mechanical properties and osteoconductivity of hydroxyapatite bone scaffolds with multi-scale porosity," *Biomaterials,* vol. 28, pp. 45-54, Jan 2007.
[89] A. G. Mikos, G. Sarakinos, M. D. Lyman, *et al.*, "Prevascularization of Porous Biodegradable Polymers," *Biotechnol Bioeng,* vol. 42, pp. 716-723, Sep 5 1993.
[90] B. J. Story, W. R. Wagner, D. M. Gaisser, *et al.*, "In vivo performance of a modified CSTi dental implant coating," *Int J Oral Max Impl,* vol. 13, pp. 749-757, Nov-Dec 1998.
[91] S. F. Hulbert, F. A. Young, R. S. Mathews, *et al.*, "Potential of ceramic materials as permanently implantable skeletal prostheses," *J Biomed Mater Res,* vol. 4, pp. 433-456, Sep 1970.
[92] V. Karageorgiou and D. Kaplan, "Porosity of 3D biornaterial scaffolds and osteogenesis," *Biomaterials,* vol. 26, pp. 5474-5491, Sep 2005.
[93] V. Maquet and R. Jerome, "Design of macroporous biodegradable polymer scaffolds for cell transplantation," *Porous Materials for Tissue Engineering,* vol. 250, pp. 15-42, 1997.
[94] P. V. Giannoudis, H. Dinopoulos, and E. Tsiridis, "Bone substitutes: An update," *Injury,* vol. 36, pp. 20-27, Nov 2005.
[95] N. O. Engin and A. C. Tas, "Manufacture of macroporous calcium hydroxyapatite bioceramics," *J Eur Ceram Soc,* vol. 19, pp. 2569-2572, 1999.
[96] I. Sopyan, M. Mel, S. Ramesh, *et al.*, "Porous hydroxyapatite for artificial bone applications," *Sci Technol Adv Mat,* vol. 8, pp. 116-123, Jan-Mar 2007.
[97] M. C. von Doernberg, B. von Rechenberg, M. Bohner, *et al.*, "In vivo behavior of calcium phosphate scaffolds with four different pore sizes," *Biomaterials,* vol. 27, pp. 5186-5198, Oct 2006.
[98] C. E. Holy, M. S. Shoichet, and J. E. Davies, "Engineering three-dimensional bone tissue in vitro using biodegradable scaffolds: Investigating initial cell-seeding density and culture period," *J Biomed Mater Res,* vol. 51, pp. 376-382, 2000.
[99] S. Sanchez-Salcedo, D. Arcos, and M. Vallet-Regi, "Upgrading calcium phosphate scaffolds for tissue engineering applications," *Progress in Bioceramics,* vol. 377, pp. 19-42, 2008.
[100] Y. Kuboki, Q. M. Jin, and H. Takita, "Geometry of carriers controlling phenotypic expression in BMP-induced osteogenesis and chondrogenesis," *J Bone Joint Surg Am,* vol. 83A, pp. S105-S115, 2001.
[101] H. E. Gotz, M. Muller, A. Emmel, *et al.*, "Effect of surface finish on the osseointegration of laser-treated titanium alloy implants," *Biomaterials,* vol. 25, pp. 4057-4064, Aug 2004.
[102] K. Whang, K. E. Healy, D. R. Elenz, *et al.*, "Engineering bone regeneration with bioabsorbable scaffolds with novel microarchitecture," *Tissue Eng,* vol. 5, pp. 35-51, Spr 1999.

[103] D. J. Mooney, D. F. Baldwin, N. P. Suh, *et al.*, "Novel approach to fabricate porous sponges of poly(D,L-lactic-co-glycolic acid) without the use of organic solvents," *Biomaterials,* vol. 17, pp. 1417-1422, Jul 1996.
[104] C. K. Colton, "Implantable Biohybrid Artificial Organs," *Cell Transplant,* vol. 4, pp. 415-436, Jul-Aug 1995.
[105] J. J. Klawitter and S. F. Hulbert, "Application of porous ceramics for the attachment of load bearing internal orthopedic applications," *J Biomed Mater Res,* vol. 5, pp. 161-229, 1971.
[106] R. Lange, F. Luthen, U. Beck, *et al.*, "Cell-extracellular matrix interaction and physico-chemical characteristics of titanium surfaces depend on the roughness of the material," *Biomol Eng,* vol. 19, pp. 255-261, Aug 2002.
[107] P. T. de Oliveira, S. F. Zalzal, M. M. Beloti, *et al.*, "Enhancement of in vitro osteogenesis on titanium by chemically produced nanotopography," *J Biomed Mater Res A,* vol. 80A, pp. 554-564, 2007.
[108] J. E. Davies, "In vitro modeling of the bone/implant interface," *The Anatomical Record,* vol. 245, pp. 426-445, 1996.
[109] T. Albrektsson and C. Johansson, "Osteoinduction, osteoconduction and osseointegration," *Eur Spine J,* vol. 10, pp. S96-S101, Oct 2001.
[110] T. J. Webster, R. W. Siegel, and R. Bizios, "Nanoceramic surface roughness enhances osteoblast and osteoclast functions for improved orthopaedic/dental implant efficacy," *Scripta Mater,* vol. 44, pp. 1639-1642, May 18 2001.
[111] T. Q. Lee, M. I. Danto, and W. C. Kim, "Initial stability comparison of modular hip implants in synthetic femurs," *Orthopedics,* vol. 21, pp. 885-888, Aug 1998.
[112] C. Botelho, M. Lopes, I. Gibson, *et al.*, "Structural analysis of Si-substituted hydroxyapatite: zeta potential and X-ray photoelectron spectroscopy," *Journal of Materials Science: Materials in Medicine,* vol. 13, pp. 1123-1127, 2002.
[113] K. A. Athanasiou, C. F. Zhu, D. R. Lanctot, *et al.*, "Fundamentals of biomechanics in tissue engineering of bone," *Tissue Eng,* vol. 6, pp. 361-381, Aug 2000.
[114] R. Langer and J. P. Vacanti, "Tissue Engineering," *Science,* vol. 260, pp. 920-926, May 14 1993.
[115] Q. Hu, Z. Tan, Y. Liu, *et al.*, "Effect of crystallinity of calcium phosphate nanoparticles on adhesion, proliferation, and differentiation of bone marrow mesenchymal stem cells," *J Mater Chem,* vol. 17, pp. 4690-4698, 2007.
[116] P. J. Jiang, "Application of calcium phosphate based gels for encapsulation of therapeutic molecules," PhD, University of Birmingham, Accessed 01/2013.
[117] S. Loher, W. J. Stark, M. Maciejewski, *et al.*, "Fluoro-apatite and calcium phosphate nanoparticles by flame synthesis," *Chem Mater,* vol. 17, pp. 36-42, Jan 11 2005.
[118] D. Mohn, D. Ege, K. Feldman, *et al.*, "Spherical Calcium Phosphate Nanoparticle Fillers Allow Polymer Processing of Bone Fixation Devices with High Bioactivity," *Polym Eng Sci,* vol. 50, pp. 952-960, May 2010.
[119] R. Z. LeGeros, "Properties of osteoconductive biomaterials: Calcium phosphates," *Clin Orthop Relat R,* pp. 81-98, Feb 2002.
[120] T. Jones and M. Long, "Correlating in-vitro dissolution measurement methods used with bone void filler bioceramics," *Key Eng Mat,* vol. 254-2, pp. 261-264, 2004.
[121] M. Bohner, "Calcium orthophosphates in medicine: from ceramics to calcium phosphate cements," *Injury,* vol. 31, pp. S37-S47, Dec 2000.

[122] E. C. Victoria and F. D. Gnanam, "Synthesis and characterisation of biphasic calcium phosphate," *Trends in Biomaterials and Artificial Organs,* vol. 16, 2002.
[123] L. L. Hench and J. Wilson, "An introduction to bioceramics," *World Scientific, Sigapore,* pp. 1 - 24, 1993.
[124] J. E. Sojka and C. M. Weaver, "Magnesium Supplementation and Osteoporosis," *Nutr Rev,* vol. 53, pp. 71-74, Mar 1995.
[125] S. Wallach, "Effects of Magnesium on Skeletal Metabolism," *Magnesium Trace Elem,* vol. 9, pp. 1-14, Jan-Feb 1990.
[126] S. Kannan, J. H. G. Rocha, and J. M. F. Ferreira, "Synthesis and thermal stability of sodium, magnesium co-substituted hydroxyapatites," *J Mater Chem,* vol. 16, pp. 286-291, Jan 21 2006.
[127] S. R. Kim, J. H. Lee, Y. T. Kim, *et al.*, "Synthesis of Si, Mg substituted hydroxyapatites and their sintering behaviors," *Biomaterials,* vol. 24, pp. 1389-1398, Apr 2003.
[128] K. S. TenHuisen and P. W. Brown, "Effects of magnesium on the formation of calcium-deficient hydroxyapatite from CaHPO4 center dot 2H(2)O and Ca-4(PO4)(2)O," *J Biomed Mater Res,* vol. 36, pp. 306-314, Sep 5 1997.
[129] W. L. Suchanek, K. Byrappa, P. Shuk, *et al.*, "Preparation of magnesium-substituted hydroxyapatite powders by the mechanochemical-hydrothermal method," *Biomaterials,* vol. 25, pp. 4647-4657, Aug 2004.
[130] A. Bigi, G. Falini, E. Foresti, *et al.*, "Magnesium Influence on Hydroxyapatite Crystallization," *J Inorg Biochem,* vol. 49, pp. 69-78, Jan 1993.
[131] M. Okazaki, J. Takahashi, and H. Kimura, "Crystallographic Behavior of Mg-Containing Hydroxyapatites in Solutions at Physiological Ph," *J Dent Res,* vol. 68, pp. 666-666, Apr 1989.
[132] H. B. Pan, Z. Y. Li, W. M. Lam, *et al.*, "Solubility of strontium-substituted apatite by solid titration," *Acta Biomater,* vol. 5, pp. 1678-1685, Jun 2009.
[133] C. Capuccini, P. Torricelli, E. Boanini, *et al.*, "Interaction of Sr-doped hydroxyapatite nanocrystals with osteoclast and osteoblast-like cells," *J Biomed Mater Res A,* vol. 89A, pp. 594-600, Jun 1 2009.
[134] A. Bigi, E. Boanini, C. Capuccini, *et al.*, "Strontium-substituted hydroxyapatite nanocrystals," *Inorg Chim Acta,* vol. 360, pp. 1009-1016, Feb 15 2007.
[135] E. Shorr and A. C. Carter, "The usefulness of strontium as an adjuvant to calcium in the remineralization of the skeleton in man," *Bull Hosp Joint Dis,* vol. 13, pp. 59-66, Apr 1952.
[136] B. S. Moonga and D. W. Dempster, "Zinc Is a Potent Inhibitor of Osteoclastic Bone-Resorption in-Vitro," *J Bone Miner Res,* vol. 10, pp. 453-457, Mar 1995.
[137] M. Yamaguchi, "Role of zinc in bone formation and bone resorption," *J Trace Elem Exp Med,* vol. 11, pp. 119-135, 1998.
[138] N. R. Calhoun, J. C. Smith, and K. L. Becker, "Role of Zinc in Bone Metabolism," *Clin Orthop Relat R,* pp. 212-234, 1974.
[139] F. Z. Ren, R. L. Xin, X. Ge, *et al.*, "Characterization and structural analysis of zinc-substituted hydroxyapatites," *Acta Biomater,* vol. 5, pp. 3141-3149, Oct 2009.
[140] A. Bigi, E. Foresti, M. Gandolfi, *et al.*, "Inhibiting Effect of Zinc on Hydroxylapatite Crystallization," *J Inorg Biochem,* vol. 58, pp. 49-58, Apr 1995.
[141] F. Miyaji, Y. Kono, and Y. Suyama, "Formation and structure of zinc-substituted calcium hydroxyapatite," *Mater Res Bull,* vol. 40, pp. 209-220, Feb 15 2005.
[142] G. Daculsi, J. M. Bouler, and R. Z. LeGeros, "Adaptive crystal formation in normal and pathological calcifications in synthetic calcium phosphate and related

biomaterials," *International Review of Cytology - a Survey of Cell Biology, Vol 172*, vol. 172, pp. 129-191, 1997.
[143] S. Padilla, I. Izquierdo-Barba, and M. Vallet-Regi, "High Specific Surface Area in Nanometric Carbonated Hydroxyapatite," *Chem Mater,* vol. 20, pp. 5942-5944, Oct 14 2008.
[144] J. D. Pasteris, B. Wopenka, J. J. Freeman, *et al.*, "Lack of OH in nanocrystalline apatite as a function of degree of atomic order: implications for bone and biomaterials," *Biomaterials,* vol. 25, pp. 229-238, Jan 2004.
[145] R. Z. LeGeros, "Calcium phosphates in demineralization/remineralization processes," *Journal of Clinical Dentistry,* vol. 10, pp. 65-73, 1999.
[146] Y. Doi, T. Shibutani, Y. Moriwaki, *et al.*, "Sintered carbonate apatites as bioresorbable bone substitutes," *J Biomed Mater Res,* vol. 39, pp. 603-610, Mar 15 1998.
[147] E. G. Nordstrom and K. H. Karlsson, "Carbonate-Doped Hydroxyapatite," *J Mater Sci-Mater M,* vol. 1, pp. 182-184, Oct 1990.
[148] I. R. Gibson and W. Bonfield, "Novel synthesis and characterization of an AB-type carbonate-substituted hydroxyapatite," *J Biomed Mater Res,* vol. 59, pp. 697-708, Mar 15 2002.
[149] N. Patel, S. M. Best, W. Bonfield, *et al.*, "A comparative study on the in vivo behavior of hydroxyapatite and silicon substituted hydroxyapatite granules," *J Mater Sci-Mater M,* vol. 13, pp. 1199-1206, Dec 2002.
[150] F. Balas, J. Perez-Pariente, and M. Vallet-Regi, "In vitro bioactivity of silicon-substituted hydroxyapatites," *J Biomed Mater Res A,* vol. 66A, pp. 364-375, Aug 1 2003.
[151] M. Vallet-Regi and D. Arcos, "Silicon substituted hydroxyapatites. A method to upgrade calcium phosphate based implants," *J Mater Chem,* vol. 15, pp. 1509-1516, 2005.
[152] Y. Wang, S. Zhang, X. Zeng, *et al.*, "Osteoblastic cell response on fluoridated hydroxyapatite coatings," *Acta Biomater,* vol. 3, pp. 191-197, 2007.
[153] H. Qu and M. Wei, "The effect of fluoride contents in fluoridated hydroxyapatite on osteoblast behavior," *Acta Biomater,* vol. 2, pp. 113-119, 2006.
[154] S. Kannan, A. Rebelo, and J. M. F. Ferreira, "Novel synthesis and structural characterization of fluorine and chlorine co-substituted hydroxyapatites," *J Inorg Biochem,* vol. 100, pp. 1692-1697, Oct 2006.
[155] S. D. Cook, K. A. Thomas, J. F. Kay, *et al.*, "Hydroxyapatite-Coated Titanium for Orthopedic Implant Applications," *Clin Orthop Relat R,* pp. 225-243, Jul 1988.
[156] B. V. Rejda, J. G. J. Peelen, and K. D. Groot, "Tri-Calcium Phosphate as a Bone Substitute," *J Bioeng,* vol. 1, pp. 93-97, 1977.
[157] N. Kivrak and A. C. Tas, "Synthesis of calcium hydroxyapatite-tricalcium phosphate (HA-TCP) composite bioceramic powders and their sintering behavior," *J Am Ceram Soc,* vol. 81, pp. 2245-2252, Sep 1998.
[158] G. Daculsi, "Biphasic calcium phosphate concept applied to artificial bone, implant coating and injectable bone substitute," *Biomaterials,* vol. 19, pp. 1473-1478, Aug 1998.
[159] G. Lenart, G. Bidlo, and J. Pinter, "Some Basic Problems in Examination of Calcium Hydrogen Phosphates of Bone," *Clin Orthop Relat R,* pp. 263-&, 1972.
[160] Muenzenb.Kj and M. Gebhardt, "Brushite Octacalcium Phosphate, and Carbonate-Containing Apatite in Bone," *Clin Orthop Relat R,* pp. 271-273, 1973.
[161] M. D. Francis and N. C. Webb, "Hydroxyapatite Formation from a Hydrated Calcium Monohydrogen Phosphate Precursor," *Calc Tiss Res,* vol. 6, pp. 335-&, 1971.

[162] M. Bohner, H. P. Merkle, and J. Lemaitre, "In vitro aging of a calcium phosphate cement," *J Mater Sci-Mater M,* vol. 11, pp. 155-162, Mar 2000.
[163] L. Getter, Bienveni.P, J. M. Brady, *et al.*, "3 Biodegradable Calcium Phosphate Slurry Implants in Bone," *J Oral Surg,* vol. 30, pp. 263-&, 1972.
[164] E. Munting, A. A. Mirtchi, and J. Lemaitre, "Bone Repair of Defects Filled with a Phosphocalcic Hydraulic Cement - an in-Vivo Study," *J Mater Sci-Mater M,* vol. 4, pp. 337-344, May 1993.
[165] G. M. Cunniffe, F. J. O'Brien, S. Partap, *et al.*, "The synthesis and characterization of nanophase hydroxyapatite using a novel dispersant-aided precipitation method," *J Biomed Mater Res A,* vol. 95A, pp. 1142-1149, Dec 15 2010.
[166] P. P. Wang, C. H. Li, H. Y. Gong, *et al.*, "Effects of synthesis conditions on the morphology of hydroxyapatite nanoparticles produced by wet chemical process," *Powder Technol,* vol. 203, pp. 315-321, Nov 10 2010.
[167] E. Bouyer, F. Gitzhofer, and M. I. Boulos, "Morphological study of hydroxyapatite nanocrystal suspension," *J Mater Sci-Mater M,* vol. 11, pp. 523-531, Aug 2000.
[168] C. Kothapalli, M. Wei, A. Vasiliev, *et al.*, "Influence of temperature and concentration on the sintering behavior and mechanical properties of hydroxyapatite," *Acta Mater,* vol. 52, pp. 5655-5663, Nov 8 2004.
[169] D. M. Liu, T. Troczynski, and W. J. Tseng, "Water-based sol-gel synthesis of hydroxyapatite: process development," *Biomaterials,* vol. 22, pp. 1721-1730, Jul 2001.
[170] G. Bezzi, G. Celotti, E. Landi, *et al.*, "A novel sol-gel technique for hydroxyapatite preparation," *Mater Chem Phys,* vol. 78, pp. 816-824, Feb 28 2003.
[171] W. J. Weng, G. R. Han, P. Y. Du, *et al.*, "The effect of citric acid addition on the formation of sol-gel derived hydroxyapatite," *Mater Chem Phys,* vol. 74, pp. 92-97, Feb 1 2002.
[172] S. Pramanik, A. K. Agarwal, K. N. Rai, *et al.*, "Development of high strength hydroxyapatite by solid-state-sintering process," *Ceram Int,* vol. 33, pp. 419-426, 2007.
[173] R. R. Rao and T. S. Kannan, "Synthesis and sintering of hydroxyapatite-zirconia composites," *Mat Sci Eng C-Bio S,* vol. 20, pp. 187-193, May 31 2002.
[174] G. C. Koumoulidis, A. P. Katsoulidis, A. K. Ladavos, *et al.*, "Preparation of hydroxyapatite via microemulsion route," *J Colloid Interf Sci,* vol. 259, pp. 254-260, Mar 15 2003.
[175] H. F. Zhang and A. I. Cooper, "Synthesis and applications of emulsion-templated porous materials," *Soft Matter,* vol. 1, pp. 107-113, Jul 14 2005.
[176] G. K. Lim, J. Wang, S. C. Ng, *et al.*, "Processing of hydroxyapatite via microemulsion and emulsion routes," *Biomaterials,* vol. 18, pp. 1433-1439, Nov 1997.
[177] J. H. Yang, K. H. Kim, C. K. You, *et al.*, "Synthesis of spherical hydroxyapatite granules with interconnected pore channels using camphene emulsion," *J Biomed Mater Res B,* vol. 99B, pp. 150-157, Oct 2011.
[178] M. Yoshimura and K. Byrappa, "Hydrothermal processing of materials: past, present and future," *J Mater Sci,* vol. 43, pp. 2085-2103, Apr 2008.
[179] S. A. Manafi, B. Yazdani, M. R. Rahimiopour, *et al.*, "Synthesis of nano-hydroxyapatite under a sonochemical/hydrothermal condition," *Biomed Mater,* vol. 3, Jun 2008.
[180] A. A. Chaudhry, S. Haque, S. Kellici, *et al.*, "Instant nano-hydroxyapatite: a continuous and rapid hydrothermal synthesis," *Chem Commun,* pp. 2286-2288, 2006.

[181] X. Y. Guo and P. Xiao, "Effects of solvents on properties of nanocrystalline hydroxyapatite produced from hydrothermal process," *J Eur Ceram Soc,* vol. 26, pp. 3383-3391, 2006.
[182] S. H. Rhee, "Synthesis of hydroxyapatite via mechanochemical treatment," *Biomaterials,* vol. 23, pp. 1147-1152, Feb 2002.
[183] Y. J. Wang, C. Lai, K. Wei, *et al.*, "Investigations on the formation mechanism of hydroxyapatite synthesized by the solvothermal method," *Nanotechnology,* vol. 17, pp. 4405-4412, Sep 14 2006.
[184] S. Y. Zhang, C. Lai, K. Wei, *et al.*, "Kinetic studies on the synthesis of hydroxyapatite nanowires by solvothermal methods," *Aust J Chem,* vol. 60, pp. 99-104, 2007.
[185] M. G. Ma and J. F. Zhu, "Solvothermal Synthesis and Characterization of Hierarchically Nanostructured Hydroxyapatite Hollow Spheres," *Eur J Inorg Chem,* pp. 5522-5526, Dec 2009.
[186] C. Yang, P. P. Yang, W. X. Wang, *et al.*, "Solvothermal synthesis and characterization of Ln (Eu3+, Tb3+) doped hydroxyapatite," *J Colloid Interf Sci,* vol. 328, pp. 203-210, Dec 1 2008.
[187] S. Sasikumar and R. Vijayaraghavan, "Synthesis and Characterization of Bioceramic Calcium Phosphates by Rapid Combustion Synthesis," *J Mater Sci Technol,* vol. 26, pp. 1114-1118, Dec 2010.
[188] S. Sasikumar and R. Vijayaraghavan, "Solution combustion synthesis of bioceramic calcium phosphates by single and mixed fuels - A comparative study," *Ceram Int,* vol. 34, pp. 1373-1379, Aug 2008.
[189] A. C. Tas, "Combustion synthesis of calcium phosphate bioceramic powders," *J Eur Ceram Soc,* vol. 20, pp. 2389-2394, Dec 2000.
[190] L. B. Kong, J. Ma, and F. Boey, "Nanosized hydroxyapatite powders derived from coprecipitation process," *J Mater Sci,* vol. 37, pp. 1131-1134, Mar 15 2002.
[191] L. Y. Cao, C. B. Zhang, and H. F. Huang, "Synthesis of hydroxyapatite nanoparticles in ultrasonic precipitation," *Ceram Int,* vol. 31, pp. 1041-1044, 2005.
[192] T. S. B. Narasaraju and D. E. Phebe, "Some physico-chemical aspects of hydroxylapatite," *J Mater Sci,* vol. 31, pp. 1-21, Jan 1 1996.
[193] M. J. Phillips, J. A. Darr, Z. B. Luklinska, *et al.*, "Synthesis and characterization of nano-biomaterials with potential osteological applications," *J Mater Sci-Mater M,* vol. 14, pp. 875-882, Oct 2003.
[194] M. G. S. Murray, J. Wang, C. B. Ponton, *et al.*, "An Improvement in Processing of Hydroxyapatite Ceramics," *J Mater Sci,* vol. 30, pp. 3061-3074, Jun 15 1995.
[195] P. G. Koutsoukos, "Current Knowledge of Calcium Phosphate Chemistry and in Particular Solid Surface-Water Interface Interactions," *http://www.nhm.ac.uk/research-curation/research/projects/phosphate-recovery/Nordwijkerhout/Koutsoukos.pdf*
[196] E. Eanes, I. Gillessen, and A. Posner, "Intermediate states in the precipitation of hydroxyapatite," *Nature,* vol. 208, pp. 365-367, 1965.
[197] H. Newesely, "Changes in crystal types of low solubility calcium phosphates in the presence of accompanying ions," *Arch Oral Biol,* vol. 6, pp. 174-180, 1961.
[198] F. Betts and A. Posner, "An X-ray radial distribution study of amorphous calcium phosphate," *Mater Res Bull,* vol. 9, pp. 353-360, 1974.
[199] J. De Rooij, J. Heughebaert, and G. Nancollas, "A pH study of calcium phosphate seeded precipitation," *J Colloid Interf Sci,* vol. 100, pp. 350-358, 1984.

[200] Y. B. Li, D. X. Li, and Z. Z. Xu, "Synthesis of hydroxyapatite nanorods assisted by Pluronics," *J Mater Sci*, vol. 44, pp. 1258-1263, Mar 2009.
[201] H. F. Zhang, M. Liu, H. S. Fan, *et al.*, "An efficient method to synthesize carbonated nano hydroxyapatite assisted by poly(ethylene glycol)," *Mater Lett*, vol. 75, pp. 26-28, May 15 2012.
[202] Y. K. Liu, W. Z. Wang, Y. J. Zhang, *et al.*, "A simple route to hydroxyapatite nanofibers," *Mater Lett*, vol. 56, pp. 496-501, Oct 2002.
[203] J. W. Wang and L. L. Shaw, "Morphology-enhanced low-temperature sintering of nanocrystalline hydroxyapatite," *Adv Mater*, vol. 19, pp. 2364-+, Sep 3 2007.
[204] Y. M. Sung, J. C. Lee, and J. W. Yang, "Crystallization and sintering characteristics of chemically precipitated hydroxyapatite nanopowder," *J Cryst Growth*, vol. 262, pp. 467-472, Feb 15 2004.
[205] M. R. Saeri, A. Afshar, M. Ghorbani, *et al.*, "The wet precipitation process of hydroxyapatite," *Mater Lett*, vol. 57, pp. 4064-4069, Aug 2003.
[206] C. Garcia, C. Paucar, J. Gaviria, *et al.*, "Effect of some physical-chemical variables in the synthesis of hydroxyapatite by the precipitation route," *Bioceramics, Vol 17*, vol. 284-286, pp. 47-50, 2005.
[207] L. M. Rodriguez-Lorenzo and M. Vallet-Regi, "Controlled crystallization of calcium phosphate apatites," *Chem Mater*, vol. 12, pp. 2460-2465, Aug 2000.
[208] P. N. Kumta, C. Sfeir, D. H. Lee, *et al.*, "Nanostructured calcium phosphates for biomedical applications: novel synthesis and characterization," *Acta Biomater*, vol. 1, pp. 65-83, Jan 2005.
[209] Y. X. Pang and X. Bao, "Influence of temperature, ripening time and calcination on the morphology and crystallinity of hydroxyapatite nanoparticles," *J Eur Ceram Soc*, vol. 23, pp. 1697-1704, Sep 2003.
[210] N. Monmaturapoj, "Nano-size hydroxyapatite powders preparation by wet-chemical precipitation route," *Journal of Metals, Materials and Minerals*, vol. 18, pp. 15-20, 2008.
[211] A. Slosarczyk, E. Stobierska, Z. Paszkiewicz, *et al.*, "Calcium phosphate materials prepared from precipitates with various calcium:phosphorus molar ratios," *J Am Ceram Soc*, vol. 79, pp. 2539-2544, Oct 1996.
[212] S. Raynaud, E. Champion, and D. Bernache-Assollant, "Calcium phosphate apatites with variable Ca/P atomic ratio II. Calcination and sintering," *Biomaterials*, vol. 23, pp. 1073-1080, Feb 2002.
[213] Y. Hakuta, H. Ura, H. Hayashi, *et al.*, "Effects of hydrothermal synthetic conditions on the particle size of gamma-AlO(OH) in sub and supercritical water using a flow reaction system," *Mater Chem Phys*, vol. 93, pp. 466-472, Oct 15 2005.
[214] K. Sue, K. Kimura, and K. Arai, "Hydrothermal synthesis of ZnO nanocrystals using microreactor," *Mater Lett*, vol. 58, pp. 3229-3231, Oct 2004.
[215] Y. Mao, T. J. Park, F. Zhang, *et al.*, "Environmentally friendly methodologies of nanostructure synthesis," *Small*, vol. 3, pp. 1122-1139, Jul 2007.
[216] C. J. Tredwin, "Sol-gel derived hydroxyapatite, fluorhydroxyapatite and fluorapatite coatings for titanium implants," UCL (University College London), 2009.
[217] A. McIntosh and W. Jablonski, "X-ray diffraction powder patterns of calcium phosphates," *Anal Chem*, vol. 28, pp. 1424-1427, 1956.
[218] T. Yasue, Suzuki, T., Arai, Y., "Dehydration and condensation of calcium hydrogenphosphate dihydrate," *J Chem Soc Jpn*, pp. 494-500, 1983 1983.
[219] A. Mortier, J. Lemaitre, and P. G. Rouxhet, "Temperature-programmed characterization of synthetic calcium-deficient phosphate apatites," *Thermochim Acta*, vol. 143, pp. 265-282, 1989.

[220] A. Osaka, Y. Miura, K. Takeuchi, *et al.*, "Calcium Apatite Prepared from Calcium Hydroxide and Orthophosphoric Acid," *J Mater Sci-Mater M,* vol. 2, pp. 51-55, Jan 1991.
[221] K. F. Leong, C. M. Cheah, and C. K. Chua, "Solid freeform fabrication of three-dimensional scaffolds for engineering replacement tissues and organs," *Biomaterials,* vol. 24, pp. 2363-2378, Jun 2003.
[222] D. W. Hutmacher, J. T. Schantz, C. X. F. Lam, *et al.*, "State of the art and future directions of scaffold-based bone engineering from a biomaterials perspective," *J Tissue Eng Regen M,* vol. 1, pp. 245-260, Jul-Aug 2007.
[223] A. M. Le Ray, H. Gautier, J. M. Bouler, *et al.*, "A new technological procedure using sucrose as porogen compound to manufacture porous biphasic calcium phosphate ceramics of appropriate micro- and macrostructure," *Ceram Int,* vol. 36, pp. 93-101, Jan 2010.
[224] A. G. Mikos, A. J. Thorsen, L. A. Czerwonka, *et al.*, "Preparation and Characterization of Poly(L-Lactic Acid) Foams," *Polymer,* vol. 35, pp. 1068-1077, 1994.
[225] Y. X. Liu, J. H. Kim, D. Young, *et al.*, "Novel template-casting technique for fabricating beta-tricalcium phosphate scaffolds with high interconnectivity and mechanical strength and in vitro cell responses," *J Biomed Mater Res A,* vol. 92A, pp. 997-1006, Mar 1 2010.
[226] F. J. O'Brien, B. A. Harley, I. V. Yannas, *et al.*, "The effect of pore size on cell adhesion in collagen-GAG scaffolds," *Biomaterials,* vol. 26, pp. 433-441, Feb 2005.
[227] Q. Fu, M. N. Rahaman, F. Dogan, *et al.*, "Freeze casting of porous hydroxyapatite scaffolds. I. Processing and general microstructure," *J Biomed Mater Res B,* vol. 86B, pp. 125-135, Jul 2008.
[228] J. R. Jones and L. L. Hench, "Effect of surfactant concentration and composition on the structure and properties of sol-gel-derived bioactive glass foam scaffolds for tissue engineering," *J Mater Sci,* vol. 38, pp. 3783-3790, Sep 15 2003.
[229] X. Li, X. P. Wang, H. R. Chen, *et al.*, "Hierarchically porous bioactive glass scaffolds synthesized with a PUF and P123 cotemplated approach," *Chem Mater,* vol. 19, pp. 4322-4326, Aug 21 2007.
[230] J. Zarzycki, "Past and present of sol-gel science and technology," *J Sol-Gel Sci Techn,* vol. 8, pp. 17-22, 1997.
[231] J. R. Jones, L. M. Ehrenfried, and L. L. Hench, "Optimising bioactive glass scaffolds for bone tissue engineering," *Biomaterials,* vol. 27, pp. 964-973, Oct 2006.
[232] Q. Z. Z. Chen, I. D. Thompson, and A. R. Boccaccini, "45S5 Bioglass (R)-derived glass-ceramic scaffolds for bone tissue engineering," *Biomaterials,* vol. 27, pp. 2414-2425, Apr 2006.
[233] E. Cunningham, N. Dunne, G. Walker, *et al.*, "Hydroxyapatite bone substitutes developed via replication of natural marine sponges," *J Mater Sci-Mater M,* vol. 21, pp. 2255-2261, Aug 2010.
[234] B. Chen, T. Zhang, J. Zhang, *et al.*, "Microstructure and mechanical properties of hydroxyapatite obtained by gel-casting process," *Ceram Int,* vol. 34, pp. 359-364, Mar 2008.
[235] P. Sepulveda, J. G. P. Binner, S. O. Rogero, *et al.*, "Production of porous hydroxyapatite by the gel-casting of foams and cytotoxic evaluation," *J Biomed Mater Res,* vol. 50, pp. 27-34, Apr 2000.
[236] F. P. W. Melchels, J. Feijen, and D. W. Grijpma, "A review on stereolithography and its applications in biomedical engineering," *Biomaterials,* vol. 31, pp. 6121-6130, Aug 2010.

[237] T. M. G. Chu, D. G. Orton, S. J. Hollister, *et al.*, "Mechanical and in vivo performance of hydroxyapatite implants with controlled architectures," *Biomaterials,* vol. 23, pp. 1283-1293, Mar 2002.
[238] J. W. Choi, R. Wicker, S. H. Lee, *et al.*, "Fabrication of 3D biocompatible/biodegradable micro-scaffolds using dynamic mask projection microstereolithography," *J Mater Process Tech,* vol. 209, pp. 5494-5503, Aug 1 2009.
[239] M. Heule, S. Vuillemin, and L. J. Gauckler, "Powder-based ceramic meso- and microscale fabrication processes," *Adv Mater,* vol. 15, pp. 1237-1245, Aug 5 2003.
[240] J. M. Williams, A. Adewunmi, R. M. Schek, *et al.*, "Bone tissue engineering using polycaprolactone scaffolds fabricated via selective laser sintering," *Biomaterials,* vol. 26, pp. 4817-4827, Aug 2005.
[241] Y. Shanjani, Y. X. Hu, R. M. Pilliar, *et al.*, "Mechanical characteristics of solid-freeform-fabricated porous calcium polyphosphate structures with oriented stacked layers," *Acta Biomater,* vol. 7, pp. 1788-1796, Apr 2011.
[242] K. H. Tan, C. K. Chua, K. F. Leong, *et al.*, "Scaffold development using selective laser sintering of polyetheretherketone-hydroxyapatite biocomposite blends," *Biomaterials,* vol. 24, pp. 3115-3123, Aug 2003.
[243] K. H. Tan, C. K. Chua, K. F. Leong, *et al.*, "Fabrication and characterization of three-dimensional poly(ether-ether-ketone)/-hydroxyapatite biocomposite scaffolds using laser sintering," *P I Mech Eng H,* vol. 219, pp. 183-194, May 2005.
[244] J. Will, R. Melcher, C. Treul, *et al.*, "Porous ceramic bone scaffolds for vascularized bone tissue regeneration," *J Mater Sci-Mater M,* vol. 19, pp. 2781-2790, Aug 2008.
[245] C. T. Wu, Y. X. Luo, G. Cuniberti, *et al.*, "Three-dimensional printing of hierarchical and tough mesoporous bioactive glass scaffolds with a controllable pore architecture, excellent mechanical strength and mineralization ability," *Acta Biomater,* vol. 7, pp. 2644-2650, Jun 2011.
[246] I. Zein, D. W. Hutmacher, K. C. Tan, *et al.*, "Fused deposition modeling of novel scaffold architectures for tissue engineering applications," *Biomaterials,* vol. 23, pp. 1169-1185, Feb 2002.
[247] J. T. Schantz, A. Brandwood, D. W. Hutmacher, *et al.*, "Osteogenic differentiation of mesenchymal progenitor cells in computer designed fibrin-polymer-ceramic scaffolds manufactured by fused deposition modeling," *J Mater Sci-Mater M,* vol. 16, pp. 807-819, Sep 2005.
[248] E. Sachlos and J. T. Czernuszka, "Making tissue engineering scaffolds work. Review: the application of solid freeform fabrication technology to the production of tissue engineering scaffolds," *Eur Cell Mater,* vol. 5, pp. 29-39; discussion 39-40, Jun 30 2003.
[249] W. Y. Yeong, C. K. Chua, K. F. Leong, *et al.*, "Rapid prototyping in tissue engineering: challenges and potential," *Trends Biotechnol,* vol. 22, pp. 643-652, Dec 2004.
[250] P. B. Malafaya and R. L. Reis, "Porous bioactive composites from marine origin based in chitosan and hydroxylapatite particles," *Bioceramics 15,* vol. 240-2, pp. 39-42, 2003.
[251] J. S. Mao, L. G. Zhao, Y. J. Yin, *et al.*, "Structure and properties of bilayer chitosan-gelatin scaffolds," *Biomaterials,* vol. 24, pp. 1067-1074, Mar 2003.
[252] K. K. Mallick, "Freeze Casting of Porous Bioactive Glass and Bioceramics," *J Am Ceram Soc,* vol. 92, pp. S85-S94, Jan 2009.

[253] M. M. Pereira, J. R. Jones, and L. L. Hench, "Bioactive glass and hybrid scaffolds prepared by sol-gel method for bone tissue engineering," *Adv Appl Ceram,* vol. 104, pp. 35-42, Feb 2005.
[254] I. Sopyan and J. Kaur, "Preparation and characterization of porous hydroxyapatite through polymeric sponge method," *Ceram Int,* vol. 35, pp. 3161-3168, Dec 2009.
[255] E. Saiz, L. Gremillard, G. Menendez, *et al.*, "Preparation of porous hydroxyapatite scaffolds," *Mat Sci Eng C-Bio S,* vol. 27, pp. 546-550, Apr 2007.
[256] H. R. Ramay and M. Q. Zhang, "Preparation of porous hydroxyapatite scaffolds by combination of the gel-casting and polymer sponge methods," *Biomaterials,* vol. 24, pp. 3293-3302, Aug 2003.
[257] J. T. Tian and J. M. Tian, "Preparation of porous hydroxyapatite," *J Mater Sci,* vol. 36, pp. 3061-3066, 2001.
[258] M. Lombardi, V. Naglieri, J. M. Tulliani, *et al.*, "Gelcasting of dense and porous ceramics by using a natural gelatine," *J Porous Mat,* vol. 16, pp. 393-400, Aug 2009.
[259] F. Z. Zhang, T. Kato, M. Fuji, *et al.*, "Gelcasting fabrication of porous ceramics using a continuous process," *J Eur Ceram Soc,* vol. 26, pp. 667-671, 2006.
[260] M. J. Rosen, "Frontmatter," in *Surfactants and Interfacial Phenomena*, ed: John Wiley & Sons, Inc., 2004, pp. i-xiii.
[261] S. J. Hollister, "Porous scaffold design for tissue engineering," *Nat Mater,* vol. 4, pp. 518-524, Jul 2005.
[262] M. M. Savalani and R. A. Harris, "Layer manufacturing for in vivo devices," *P I Mech Eng H,* vol. 220, pp. 505-520, May 2006.
[263] R. A. Levy, T. M. G. Chu, J. W. Halloran, *et al.*, "CT-generated porous hydroxyapatite orbital floor prosthesis as a prototype bioimplant," *Am J Neuroradiol,* vol. 18, pp. 1522-1525, Sep 1997.
[264] T. M. G. Chu, J. W. Halloran, S. J. Hollister, *et al.*, "Hydroxyapatite implants with designed internal architecture," *J Mater Sci-Mater M,* vol. 12, pp. 471-478, 2001.
[265] C. K. Chua, S. M. Chou, and T. S. Wong, "A study of the state-of-the-art rapid prototyping technologies," *Int J Adv Manuf Tech,* vol. 14, pp. 146-152, 1998.
[266] A. Butscher, M. Bohner, C. Roth, *et al.*, "Printability of calcium phosphate powders for three-dimensional printing of tissue engineering scaffolds," *Acta Biomater,* vol. 8, pp. 373-385, Jan 2012.
[267] M. Nebelung and B. Lang, "Flowability of Ceramic Bulk Materials Part 2: Interaction of primary particle properties and flowability," *Cfi-Ceram Forum Int,* vol. 86, pp. E35-E38, Apr 2009.
[268] D. Schulze, "Flowability of Bulk Solids - Definition and Measuring Principles," *Chem-Ing-Tech,* vol. 67, pp. 60-68, Jan 1995.
[269] S. A. Mohammed, E. C. Abdullah, D. Geldart, *et al.*, "Measuring powder flowability with a modified Warren Spring cohesion tester," *Particuology,* vol. 9, pp. 148-154, Apr 2011.
[270] E. Sachs, M. Cima, J. Cornie, *et al.*, "Three-Dimensional Printing: The Physics and Implications of Additive Manufacturing," *CIRP Annals - Manufacturing Technology,* vol. 42, pp. 257-260, 1993.
[271] A. Park, B. Wu, and L. G. Griffith, "Integration of surface modification and 3D fabrication techniques to prepare patterned poly(L-lactide) substrates allowing regionally selective cell adhesion," *J Biomat Sci-Polym E,* vol. 9, pp. 89-110, 1998.

[272] J. K. Sherwood, S. L. Riley, R. Palazzolo, *et al.*, "A three-dimensional osteochondral composite scaffold for articular cartilage repair," *Biomaterials,* vol. 23, pp. 4739-4751, Dec 2002.
[273] A. Butscher, M. Bohner, S. Hofmann, *et al.*, "Structural and material approaches to bone tissue engineering in powder-based three-dimensional printing," *Acta Biomater,* vol. 7, pp. 907-920, Mar 2011.
[274] A. Khalyfa, S. Vogt, J. Weisser, *et al.*, "Development of a new calcium phosphate powder-binder system for the 3D printing of patient specific implants," *J Mater Sci-Mater M,* vol. 18, pp. 909-916, May 2007.
[275] T. D. Roy, J. L. Simon, J. L. Ricci, *et al.*, "Performance of hydroxyapatite bone repair scaffolds created via three-dimensional fabrication techniques," *J Biomed Mater Res A,* vol. 67A, pp. 1228-1237, Dec 15 2003.
[276] T. D. Roy, J. L. Simon, J. L. Ricci, *et al.*, "Performance of degradable composite bone repair products made via three-dimensional fabrication techniques," *J Biomed Mater Res A,* vol. 66A, pp. 283-291, Aug 1 2003.
[277] D. W. Hutmacher, T. Schantz, I. Zein, *et al.*, "Mechanical properties and cell cultural response of polycaprolactone scaffolds designed and fabricated via fused deposition modeling," *J Biomed Mater Res,* vol. 55, pp. 203-216, May 2001.
[278] S. J. Kalita, S. Bose, H. L. Hosick, *et al.*, "Development of controlled porosity polymer-ceramic composite scaffolds via fused deposition modeling," *Mat Sci Eng C-Bio S,* vol. 23, pp. 611-620, Oct 15 2003.
[279] Y. Zhao, Y. Zhang, F. Ning, *et al.*, "Synthesis and cellular biocompatibility of two kinds of HAP with different nanocrystal morphology," *J Biomed Mater Res B,* vol. 83B, pp. 121-126, Oct 2007.
[280] X. Y. Guo, J. E. Gough, P. Xiao, *et al.*, "Fabrication of nanostructured hydroxyapatite and analysis of human osteoblastic cellular response," *J Biomed Mater Res A,* vol. 82A, pp. 1022-1032, Sep 15 2007.
[281] G. Balasundaram, M. Sato, and T. J. Webster, "Using hydroxyapatite nanoparticles and decreased crystallinity to promote osteoblast adhesion similar to functionalizing with RGD," *Biomaterials,* vol. 27, pp. 2798-2805, May 2006.
[282] F. C. M. Driessens, "Formation and stability of calcium phosphates in relation to the phase composition of the mineral in calcified tissue," in *Bioceramics of calcium phosphate*, K. DeGroot, Ed., ed Florida: CRC Press, 1983, pp. 1 - 33.
[283] L. J. Jha, S. M. Best, J. C. Knowles, *et al.*, "Preparation and characterization of fluoride-substituted apatites," *J Mater Sci-Mater M,* vol. 8, pp. 185-191, Apr 1997.
[284] J. Barralet, S. Best, and W. Bonfield, "Carbonate substitution in precipitated hydroxyapatite: An investigation into the effects of reaction temperature and bicarbonate ion concentration," *J Biomed Mater Res,* vol. 41, pp. 79-86, Jul 1998.
[285] J. E. Barralet, S. M. Best, and W. Bonfield, "Preparation and Sintering of Carbonate-Substituted Apatite," *Bioceramics, Vol 6,* pp. 179-184, 1993.
[286] R. Z. LeGeros, C. B. Bleiwas, M. Retino, *et al.*, "Zinc effect on the in vitro formation of calcium phosphates: Relevance to clinical inhibition of calculus formation," *American Journal of Dentistry,* vol. 12, pp. 65-71, Apr 1999.
[287] H. Aoki, *Science and medical applications of hydroxyapatite*: Ishiyaku Euroamerica, 1991.
[288] M. H. Santos, M. Oliveira, L. P. F. Souza, *et al.*, "Synthesis control and characterization of hydroxyapatite prepared by wet precipitation process," *Materials Research,* vol. 7, pp. 625-630, 2004.
[289] T. Kokubo and H. Takadama, "How useful is SBF in predicting in vivo bone bioactivity?," *Biomaterials,* vol. 27, pp. 2907-2915, May 2006.

[290] R. Shu, R. McMullen, M. Baumann, *et al.*, "Hydroxyapatite accelerates differentiation and suppresses growth of MC3T3-E1 osteoblasts," *J Biomed Mater Res A,* vol. 67, pp. 1196-1204, 2003.
[291] T. Mosmann, "Rapid colorimetric assay for cellular growth and survival: Application to proliferation and cytotoxicity assays," *J Immunol Methods,* vol. 65, pp. 55-63, 1983.
[292] N. Seaton and J. Walton, "A new analysis method for the determination of the pore size distribution of porous carbons from nitrogen adsorption measurements," *Carbon,* vol. 27, pp. 853-861, 1989.
[293] R. L. Williams, M. J. Hadley, P. Jiang, *et al.*, "Thiol modification of silicon-substituted hydroxyapatite nanocrystals facilitates fluorescent labelling and visualisation of cellular internalisation," *J. Mater. Chem. B,* 2013.
[294] S. Zhang, F. Cui, S. Liao, *et al.*, "Synthesis and biocompatibility of porous nano-hydroxyapatite/collagen/alginate composite," *Journal of Materials Science: Materials in Medicine,* vol. 14, pp. 641-645, 2003.
[295] M. P. Hofmann, A. M. Young, U. Gbureck, *et al.*, "FTIR-monitoring of a fast setting brushite bone cement: effect of intermediate phases," *J Mater Chem,* vol. 16, pp. 3199-3206, 2006.
[296] L. Yubao, C. Klein, J. De Wijn, *et al.*, "Shape change and phase transition of needle-like non-stoichiometric apatite crystals," *Journal of Materials Science: Materials in Medicine,* vol. 5, pp. 263-268, 1994.
[297] R. N. Panda, M. F. Hsieh, R. J. Chung, *et al.*, "FTIR, XRD, SEM and solid state NMR investigations of carbonate-containing hydroxyapatite nano-particles synthesized by hydroxide-gel technique," *J Phys Chem Solids,* vol. 64, pp. 193-199, Feb 2003.
[298] D. M. Liu, "Fabrication and characterization of porous hydroxyapatite granules," *Biomaterials,* vol. 17, pp. 1955-1957, Oct 1996.
[299] M. Uota, H. Arakawa, N. Kitamura, *et al.*, "Synthesis of high surface area hydroxyapatite nanoparticles by mixed surfactant-mediated approach," *Langmuir,* vol. 21, pp. 4724-4728, 2005.
[300] M. Bailey, S. Coe, D. Grant, *et al.*, "Accurate determination of the Ca: P ratio in rough hydroxyapatite samples by SEM-EDS, PIXE and RBS—a comparative study," *X-Ray Spectrometry,* vol. 38, pp. 343-347, 2009.
[301] A. Banerjee, A. Bandyopadhyay, and S. Bose, "Hydroxyapatite nanopowders: Synthesis, densification and cell–materials interaction," *Materials Science and Engineering: C,* vol. 27, pp. 729-735, 2007.
[302] V. Sokolova, O. Rotan, J. Klesing, *et al.*, "Calcium phosphate nanoparticles as versatile carrier for small and large molecules across cell membranes," *J Nanopart Res,* vol. 14, pp. 1-10, 2012.
[303] L. Chen, J. M. Mccrate, J. C. Lee, *et al.*, "The role of surface charge on the uptake and biocompatibility of hydroxyapatite nanoparticles with osteoblast cells," *Nanotechnology,* vol. 22, p. 105708, 2011.
[304] M. Motskin, D. Wright, K. Muller, *et al.*, "Hydroxyapatite nano and microparticles: correlation of particle properties with cytotoxicity and biostability," *Biomaterials,* vol. 30, pp. 3307-3317, 2009.
[305] U. Mayr-Wohlfart, J. Fiedler, K. P. Günther, *et al.*, "Proliferation and differentiation rates of a human osteoblast-like cell line (SaOS-2) in contact with different bone substitute materials," *J Biomed Mater Res,* vol. 57, pp. 132-139, 2001.
[306] N. Ayobian-Markazi, T. Fourootan, and M. Kharazifar, "Comparison of cell viability and morphology of a human osteoblast-like cell line (SaOS-2) seeded on

various bone substitute materials: an in vitro study," *Dental research journal,* vol. 9, p. 86, 2012.
[307] G. S. Stein and J. B. Lian, "Molecular mechanisms mediating proliferation/differentiation interrelationships during progressive development of the osteoblast phenotype," *Endocrine Reviews,* vol. 14, pp. 424-442, 1993.
[308] J. De Heer, "The principle of Le Chatelier and Braun," *J Chem Educ,* vol. 34, p. 375, 1957.
[309] M. Bohner and J. Lemaitre, "Can bioactivity be tested in vitro with SBF solution?," *Biomaterials,* vol. 30, pp. 2175-2179, 2009.
[310] H. Pan, X. Zhao, B. W. Darvell, *et al.*, "Apatite-formation ability–Predictor of "bioactivity"?," *Acta Biomater,* vol. 6, pp. 4181-4188, 2010.
[311] N. Ribeiro, S. Sousa, and F. Monteiro, "Influence of crystallite size of nanophased hydroxyapatite on fibronectin and osteonectin adsorption and on MC3T3-E1 osteoblast adhesion and morphology," *J Colloid Interf Sci,* vol. 351, pp. 398-406, 2010.
[312] J. Morgan, K. R. Holtman, J. C. Keller, *et al.*, "In vitro mineralization and implant calcium phosphate-hydroxyapatite crystallinity," *Implant Dent,* vol. 5, pp. 264-271, 1996.
[313] J. de Bruijin, J. Flach, K. De Groot, *et al.*, "Analysis of the bony interface with various types of hydroxyapatite in vitro," *Cells and Materials(USA),* vol. 3, pp. 115-127, 1993.
[314] J. D. Termine, H. K. Kleinman, S. W. Whitson, *et al.*, "Osteonectin, a bone-specific protein linking mineral to collagen," *Cell,* vol. 26, pp. 99-105, 1981.
[315] J. Sodek, B. Ganss, and M. McKee, "Osteopontin," *Critical Reviews in Oral Biology & Medicine,* vol. 11, pp. 279-303, 2000.
[316] S. H. Maxian, T. Di Stefano, M. C. Melican, *et al.*, "Bone cell behavior on Matrigel®-coated Ca/P coatings of varying crystallinities," *J Biomed Mater Res,* vol. 40, pp. 171-179, 1998.
[317] T. Yuasa, Y. Miyamoto, K. Ishikawa, *et al.*, "Effects of apatite cements on proliferation and differentiation of human osteoblasts in vitro," *Biomaterials,* vol. 25, pp. 1159-1166, 2004.
[318] R. Z. LeGeros, "Calcium phosphates in oral biology and medicine," *Monographs in oral science,* vol. 15, pp. 1-201, 1990.
[319] N. Kanzaki, K. Onuma, G. Treboux, *et al.*, "Inhibitory effect of magnesium and zinc on crystallization kinetics of hydroxyapatite (0001) face," *J Phys Chem B,* vol. 104, pp. 4189-4194, May 4 2000.
[320] S. Rowles, "The precipitation of whitlockite from aqueous solutions," *Bull Soc Chim Fr,* vol. 1968, p. 802, 1968.
[321] D. Laurencin, N. Almora-Barrios, N. H. de Leeuw, *et al.*, "Magnesium incorporation into hydroxyapatite," *Biomaterials,* vol. 32, pp. 1826-1837, Mar 2011.
[322] B. Leukers, H. Gulkan, S. H. Irsen, *et al.*, "Hydroxyapatite scaffolds for bone tissue engineering made by 3D printing," *J Mater Sci-Mater M,* vol. 16, pp. 1121-1124, Dec 2005.
[323] B. J. Holland and J. N. Hay, "The thermal degradation of poly(vinyl alcohol)," *Polymer,* vol. 42, pp. 6775-6783, 2001.
[324] Z. Peng, L. X. Kong, and S. D. Li, "Thermal properties and morphology of a poly (vinyl alcohol)/silica nanocomposite prepared with a self-assembled monolayer technique," *J Appl Polym Sci,* vol. 96, pp. 1436-1442, 2005.

[325] C. Lee, S. Kim, H. Kim, *et al.*, "Measurement of anisotropic compressive strength of rapid prototyping parts," *J Mater Process Tech*, vol. 187, pp. 627-630, 2007.
[326] R. Rage, J. Mitchen, and G. Wilding, "DNA fluorometric assay in 96-well tissue culture plates using Hoechst 33258 after cell lysis by freezing in distilled water," *Anal Biochem*, vol. 191, pp. 31-34, 1990.
[327] J. Rao and W. R. Otto, "Fluorimetric DNA assay for cell growth estimation," *Anal Biochem*, vol. 207, pp. 186-192, 1992.
[328] G. Stein and J. Lian, "Molecular mechanisms mediating developmental and hormone-regulated expression of genes in osteoblasts: an integrated relationship of cell growth and differentiation," *Cellular and molecular biology of bone*, vol. 1, pp. 47-95, 1993.
[329] K. Anselme, "Osteoblast adhesion on biomaterials," *Biomaterials*, vol. 21, pp. 667-681, 2000.
[330] A. Serotec. (Accessed 09/2013). Available: http://www.abdserotec.com/alamarblue-faqs.html

Appendix A - modified ANOVA test

A typical distribution observed for MTT assay is displayed in Figure A.1. Typically an ANOVA test analyses the variance (σ^2) from the mean (μ) within and between data sets (Figure A.2).

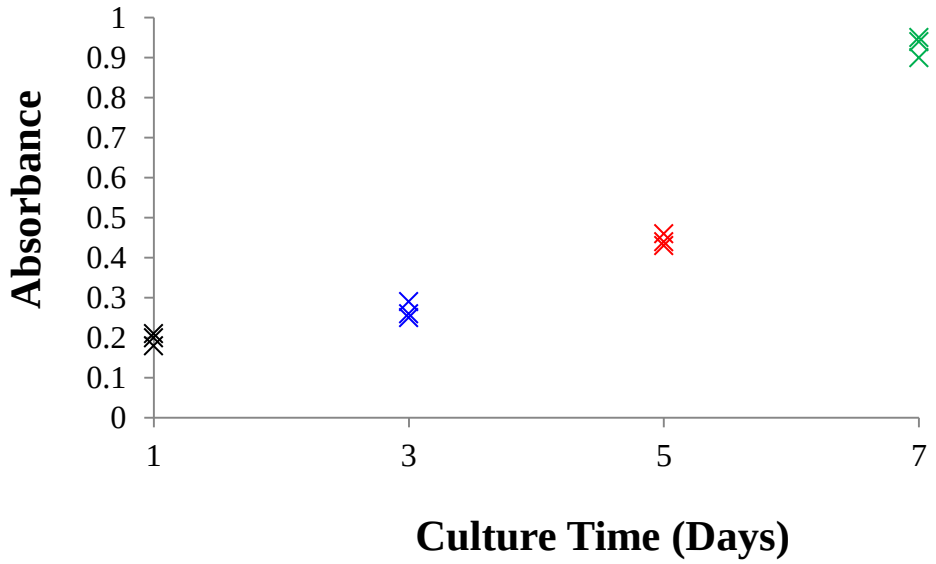

Figure A.1: Example of MTT assay data set

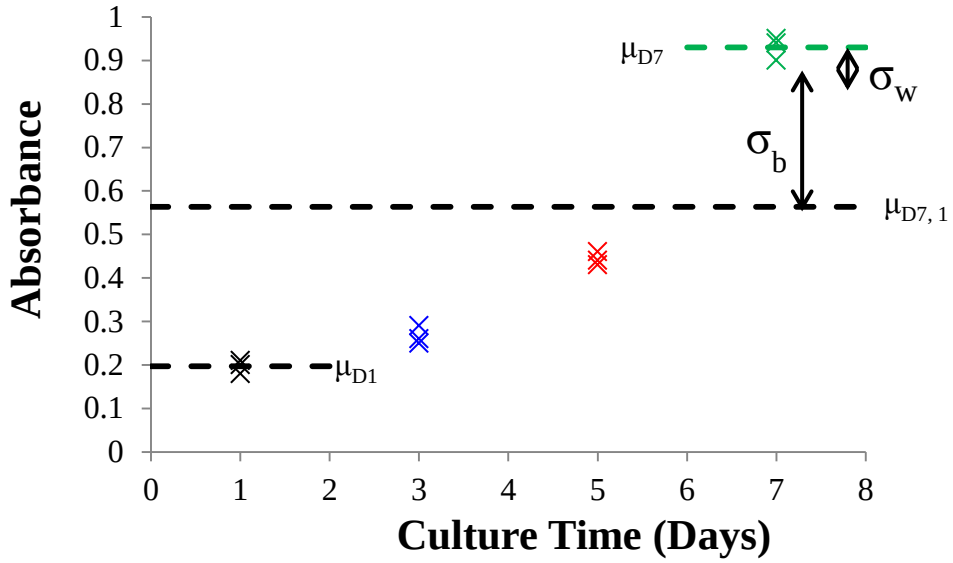

Figure A.2: ANOVA test analysis
μ_{D1} = mean day 1, μ_{D7} = mean day 7, $\mu_{D7,1}$ = mean days 1 and 7, σ_b = σ between sets, σ_w = σ within set

In order to take account of the lag growth phase typically observed for mammalian cells the ANOVA test was modified so that the variance was calculated from a linear trend line (Figure A.3). Linear regression was performed between either days 1 to 3 or days 1 to 5, which were suggested to be the lag phases in experimental data. Thus this modified method enables lag growth to be calculated and effectively strips it back from the experimental data, making the analysis of the exponential proliferation phase more rigorous and less sensitive to individual erroneous measurements and outliers. Figure A.4 demonstrates the well-established phases of mammalian cell growth.

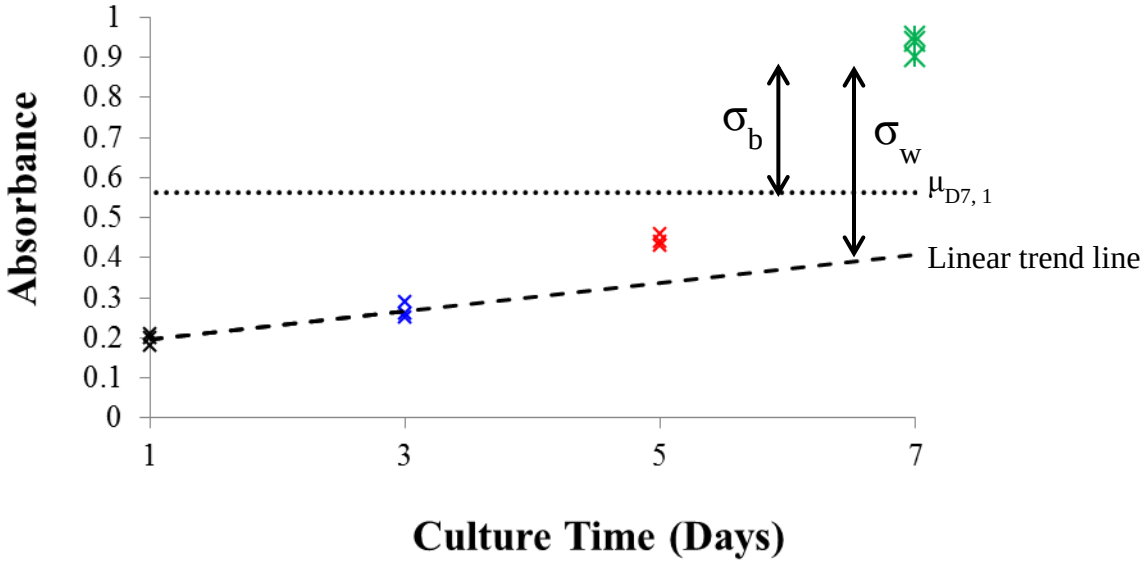

Figure A.3: Typical linear regression performed in modified ANOVA test
$\mu_{D7,1}$ = mean days 1 and 7, σ_b = σ between sets, σ_w = σ within set

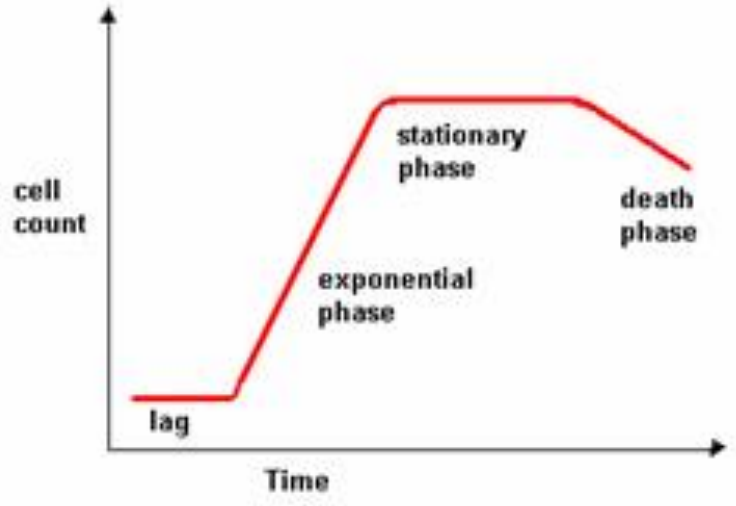

Figure A.4: Standard cell growth curve [330]